



Heat transfer in turbulent pipe flows with variable fluid properties

Author Name: Lorenzo Sufrà

Supervisor: Ao.Univ.-Prof. Dipl.-Ing. Dr.techn. Helfried Steiner

A thesis presented for the degree of
Doctor of Philosophy

Institute of Fluid Mechanics and Heat Transfer
Graz University of Technology

Graz, January, 2022

Affidavit
Eidesstattliche Erklärung

I declare that I have authored this thesis independently, that I have not used other than the declared sources/resources, and that I have explicitly indicated all material which has been quoted either literally or by content from the sources used. The text document uploaded to TUGRAZonline is identical to the present doctoral thesis.

Ich erkläre an Eides statt, dass ich die vorliegende Arbeit selbstständig verfasst, andere als die angegebenen Quellen/Hilfsmittel nicht benutzt, und die den benutzten Quellen wörtlich und inhaltlich entnommenen Stellen als solche kenntlich gemacht habe. Das in TUGRAZonline hochgeladene Textdokument ist mit der vorliegenden Dissertation identisch.

Datum

Unterschrift

Abstract

An extensive numerical investigation of heat transfer in turbulent pipe flows with significant variation in fluid properties and molecular Prandtl number Pr well beyond unity was carried out using highly resolved Direct Numerical Simulation (DNS). The feedback of the temperature on the momentum transfer in fully developed pipe flow under alternatively heated and cooled wall conditions turned out to significantly modulate the turbulent motion in the region close to the wall, where the same thermal reference conditions were assumed for all cases. The DNS based results were further used to assess the predictive capabilities of three popular subgrid-scale (sgs) models commonly used in Large Eddy Simulation (LES). The Standard Smagorinsky Model (SMAG) delivered excessive turbulent sgs heat flux near the wall, resulting in overestimated heat transfer rates. The Coherent Structure Model (CSM) and the Wall Local Adapting Eddy Viscosity Model (WALE), on the contrary, generally yielded accurate predictions, without the need for further modification, especially when tested in presence of markedly varying material properties.

Lastly, the turbulent heat transfer was investigated in a pipe experiencing a circular axisymmetric abrupt expansion, which causes the separation of the dynamic boundary layer. DNS using air at constant molecular Prandtl number $Pr = 0.7$ and a mixture of glyserol-water 50/50 Vol% with $Pr = 10$, was carried out to predict the transfer of momentum and heat in the separation region. Constant fluid properties were assumed for the case associated with air, whereas a temperature depending molecular viscosity was assumed for the coolant. The enhanced turbulent mixing caused by the sudden variation in the pipe diameter turned out to enhance the local heat transfer rate four to five times as compared with analogous thermally fully developed conditions at the same reference Prandtl and bulk Reynolds numbers. Additionally, the DNS results served as a benchmark for the assessment of the CSM sgs model, which proved to adequately enhance the turbulent transfer of heat in the separated region, yielding results in good agreement with the target DNS.

Keywords: Forced convective heat transfer, material property variation, pipe flows, turbulence near heated/cooled walls, LES, DNS, subgrid-scale modelling.

Kurzfassung

Die Wärmeübertragung in turbulenten Rohrströmungen mit stark variierenden Stoffeigenschaften und weit über eins liegenden technisch relevanten Prandtlzahlen wurde mithilfe von räumlich und zeitlich hoch aufgelösten Direkten Numerischen Simulationen (DNS) untersucht. Die unterschiedliche Änderung der Stoffwerte in Abhängigkeit vom Temperaturverlauf nahe der beheizten bzw. gekühlten Wand zeigte durchwegs einen signifikanten nicht zu vernachlässigenden Einfluss auf den Impuls- und Wärmetransport. Die DNS-basierten Ergebnisse wurden zusätzlich für die Validierung drei populärer Ansätze zur Modellierung der nicht aufgelösten turbulenten Feinstruktur („subgrid-scale“, kurz „sgs“) in der Large Eddy Simulation (LES) genutzt. Das Standard Smagorinsky Modell (SMAG) lieferte generell einen stark überhöhten sgs-Beitrag zum turbulenten Wärmefluss, mit daraus folgender Überschätzung des gesamten Wärmeübergangs. Im Gegensatz dazu erwiesen sich das Coherent Structure Modell (CSM) und das Wall Local Adapting Eddy Viscosity Modell (WALE) als sehr vorhersagegenaue Turbulenzmodelle ohne spezielle Anpassungen oder Modifikationen in deren ursprünglichen Formulierungen.

Zusätzlich zur dynamisch und thermisch voll entwickelter Strömung wurde ebenso die Wärmeübertragung in turbulenten Rohrströmungen mit plötzlicher Durchmessererweiterung numerisch untersucht, wo die abrupte Vergrößerung des Strömungsquerschnitts eine massive Ablösung der Strömungsgrenzschicht hervorruft. Luft mit konstanten Stoffeigenschaften und eine Mischung aus Wasser und Glycerin 50/50 Vol% mit temperaturabhängiger dynamischer Viskosität wurden als Arbeitsfluide betrachtet.

Die intensivere turbulente Mischbewegung infolge der Ausbildung einer starken Scherschicht zwischen der Kernströmung und dem abgelösten Wandbereich im abrupt erweiterten Querschnitt erhöhte den lokalen Wärmeübergangskoeffizienten auf ein bis zu fünffaches des Vergleichswerts bei vollständig entwickelter Strömung mit denselben Reynolds - und Prandtlzahlen. Die Konfiguration mit plötzlicher Querschnittserweiterung wurde ebenso mittels LES simuliert, um die Vorhersagegenauigkeit des CSM sgs-Modells gegen die DNS-Resultate eingehend zu validieren. Die vom CSM-Modell gelieferten Beiträge für die nicht aufgelöste turbulente Feinstruktur führten auch bei dieser komplexen durch starke Ablösung geprägten Strömungssituation zu sehr guter Übereinstimmung mit den DNS-Daten.

Danksagung

Die folgenden Zeilen sind meiner persönlichen Danksagung an die Personen gewidmet, ohne deren Unterstützung der Erfolg dieser Arbeit nicht möglich gewesen wäre.

In Erstlinie möchte ich mich mit Professor Steiner für seine ständige und geduldige Betreuung bedanken, der mich vom Anfang an in diesem wissenschaftlichen Projekt begleitete. Meine große Dankbarkeit möchte ich auch Professor Brenn aussprechen, der mit seinem Beitrag als Institutsvorstand die Qualität dieser Arbeit ohne Zweifel erhöht hat.

Zusätzlich bin ich dankbar FFG und AVL List für die konkrete Unterstützung und für die Beteiligung an diesem Projekt. Diesbezüglich sind die Herren Andreas Ennemoser, Heinz Petutschnig, Branislav Basara und Sanjin Šarić herzlich für ihr Mitwirken gedankt.

Ein tiefer Dank richtet sich an meine Familie aus, die ihre Unterstützung trotz der schwierigen Zeiten nie abgezogen haben, und, insbesondere, an Dario.

Das Arbeiten am Institut wäre ebenso nicht so angenehm und produktiv gewesen, ohne die Präsenz aller meiner netten Kollegen im ISW. Unter denen möchte ich Christoph Irrenfried explizit für seine Verfügbarkeit (insbesondere in den ersten Monaten 2017) bedanken, und Dino Zrnic für die schöne Zeit, die wir außer dem Arbeitsplatz verbracht haben.

Schließend, unter den Personen, die mich tief unterstützt haben, möchte ich auch meine Freunde in Mailand erwähnen und Elisa.

Graz, 24.01.2022

Lorenzo Sufrà

Contents

1	Introduction	17
1.1	Motivation and Objectives	18
1.2	State of the Art	19
2	Problem description	27
2.1	Heat transfer in wall bounded turbulent flows	27
2.2	Governing equations	30
2.3	Turbulent pipe flow in fully developed conditions	31
2.3.1	Dynamically fully developed conditions	32
2.3.2	Thermally fully developed conditions	34
2.3.3	Non-dimensional formulation	37
2.3.4	Thermal Boundary conditions	39
2.4	Turbulent flow in a pipe with an abrupt circular expansion	41
2.4.1	Thermal boundary conditions in the downstream pipe	42
2.5	Fluid material properties	43
3	Methodology	45
3.1	Direct numerical simulation of turbulent flows	45
3.2	Large Eddy Simulation of turbulent flows	46
3.2.1	Spatial filtering	47
3.2.2	Subgrid-scale (sgs) models	49
3.2.3	<i>A priori</i> LES	51
3.2.4	<i>A posteriori</i> LES	54
3.3	Experiments on fully developed heated pipe flow	54
4	Numerical procedure	57
4.1	Computational domains	57
4.2	Spatial discretization	58
4.3	Temporal discretization	60
5	DNS of fully developed turbulent pipe flow	68
5.1	Considered DNS cases	68
5.2	Validation and spatial resolution	69
5.2.1	Assessment against reference DNS data	72
5.2.2	Assessment against experiments	72
5.3	First order statistics	75

5.3.1	Variation of local material properties	75
5.3.2	Axial velocity	79
5.3.3	Enthalpy difference	81
5.4	Higher order statistics	82
5.4.1	Turbulent velocity fluctuations	82
5.4.2	Laminar and turbulent shear stress	85
5.4.3	Budgets for turbulent kinetic energy and shear stress	88
5.4.4	Turbulent enthalpy fluctuations	93
5.4.5	Laminar and turbulent heat flux	94
5.4.6	Budget for enthalpy difference variance and heat flux	96
5.5	Turbulent Prandtl number	99
5.6	Effect of thermal boundary conditions	100
6	LES of fully developed turbulent pipe flow	107
6.1	<i>A priori</i> LES and assessment of numerical error	107
6.2	<i>A posteriori</i> LES	117
6.2.1	First order statistics	118
6.2.2	Second order statistics	122
6.2.3	Assessment in strongly heated condition	126
7	<i>A posteriori</i> LES of turbulent flow in pipe with abrupt circular expansion	129
7.1	Momentum transfer in separated flow condition	132
7.2	Heat transfer in separated flow condition	138
8	Summary and Conclusions	147
	Appendix	150

List of Figures

2.1	Effect of Reynolds number on turbulent dynamic boundary layer	28
2.2	Effect of Prandtl number on thermal boundary layer	29
2.3	Fully developed pipe flow domain	31
2.4	Cooled (a) and heated (b) fully developed pipe flow	35
2.5	Geometry of conjugate heat transfer problem	41
2.6	Sketch of a turbulent flow in a pipe with a sudden circular expansion . . .	42
2.7	Setting with isothermal boundary condition in the downstream pipe	43
2.8	Setting with isoflux thermal boundary condition in the downstream pipe .	43
2.9	Variation of fluid properties with temperature	44
3.1	Spectrum of a turbulent signal as function of wave number	47
3.2	One-dimensional spatial filtering procedure in LES	47
3.3	Grid filtering in <i>a priori</i> LES	52
3.4	Experimental facility	54
3.5	Details of the test section in the experimental facility	55
4.1	Geometrical sketches of the computational domains for attached turbulent pipe flow (left side) and detached turbulent pipe flow with abrupt circular expansion (right side)	57
4.2	Axial decompositions for MPI parallel domain distributions	58
4.3	Staggered polar grid for DNS and LES of periodic pipe flow	60
4.4	Two opposite cells near the centerline	67
5.1	Spatial resolution normalized with the Kolmogorov length scale η_K and Batchelor length scale η_B for the DNS at $Re_\tau = 360, 500, 750$ and $Pr_w = 10$ under cooled conditions. Δr , $r\Delta\varphi$ and Δz represent the grid size in radial, azimuthal and axial directions, respectively	71
5.2	Mean axial velocity and <i>rms</i> of radial, azimuthal and axial velocity compo- nents against data of Wu and Moin (2008) with constant fluid properties .	72
5.3	Skin friction coefficient C_f vs bulk Reynolds number Re_b	73
5.4	Heat transfer coefficient Nu vs bulk Reynolds number	74
5.5	Averaged local material properties for DHH750 and DC360, dashed line representing constant fluid properties added as reference	76
5.6	Wall normal variation of $\langle Re \rangle$ at three different reference friction Reynolds numbers $Re_\tau = 360, 500, 750$, and reference Prandtl number $Pr_w = 10$. . .	78
5.7	Wall normal variation of $\langle Pr \rangle$ at three different reference friction Reynolds number $Re_\tau = 360, 500, 750$ and $Pr_w = 10$	79

5.8	Averaged axial velocity profile at reference friction Reynolds number $Re_\tau = 360, 500, 750$	80
5.9	Averaged enthalpy difference profile at reference friction Reynolds numbers $Re_\tau = 360, 500, 750$	81
5.10	<i>Rms</i> -value of the turbulent fluctuating velocity component in radial direction for heated and cooled cases at $Re_\tau = 360, 500, 750$	82
5.11	<i>Rms</i> -value of turbulent fluctuating velocity component in azimuthal direction for heated and cooled cases at $Re_\tau = 360, 500, 750$	83
5.12	<i>Rms</i> -value of turbulent fluctuating velocity component in axial direction for heated and cooled cases at $Re_\tau = 360, 500, 750$	84
5.13	Turbulent kinetic energy k^+ for heated and cooled cases at $Re_\tau = 360, 500, 750$ 84	
5.14	Turbulent and laminar contribution to total shear stress at reference friction Reynolds number $Re_\tau = 360, 500, 750$ for different wall heat fluxes	86
5.15	Mean shear rate at reference friction Reynolds numbers $Re_\tau = 360, 500, 750$	87
5.16	Turbulent $\langle \rho^* w'^+ w'^+ \rangle$ -budget for heated and cooled cases at $Re_\tau = 360$. .	89
5.17	Turbulent $\langle \rho^* u'^+ u'^+ \rangle$ -budget for heated and cooled cases at $Re_\tau = 360$. . .	90
5.18	Turbulent k^+ -budget for heated and cooled cases at $Re_\tau = 360$	92
5.19	<i>Rms</i> -value of enthalpy difference χ_{rms}^+ for heated and cooled cases at $Re_\tau = 360, 500, 750$	94
5.20	Turbulent and laminar contribution to total heat fluxes at reference wall friction Reynolds number $Re_\tau = 360, 500, 750$	95
5.21	Turbulent $\langle \rho \chi'^2 \rangle$ -budget for heated and cooled cases at $Re_\tau = 360$	97
5.22	Budget of the turbulent radial heat flux $q_{turb}^+ = \langle \rho^* u'^+ \chi'^+ \rangle$ for heated and cooled cases at $Re_\tau = 360$	99
5.23	Turbulent Prandtl number Pr_T for heated and cooled cases at $Re_\tau = 360, 500, 750$	100
5.24	<i>Rms</i> -value of enthalpy difference as predicted by D360, N360, CHT360 at $Re_\tau = 360$ for constant fluid properties.	101
5.25	Averaged enthalpy difference and turbulent heat flux as predicted for D360, N360, CHT360 at $Re_\tau = 360$ using constant fluid properties.	102
5.26	Instantaneous temperature contours from DNS using c.f.p. with different thermal boundary conditions: a) isothermal, b) conjugate Heat Transfer, c) isoflux	103
5.27	Turbulent heat flux and <i>rms</i> -value of enthalpy difference as predicted for the cases NH360, DH360, C360 at $Re_\tau = 360$ for variable fluid properties. .	104
5.28	Averaged axial velocity and enthalpy difference profile as predicted for the cases NH360, DH360 and NC360, DC360 at $Re_\tau = 360$ for variable fluid properties.	105
5.29	Turbulent Prandtl number Pr_T obtained for the different thermal wall b.c.s at $Re_\tau = 360$, assuming constant and variable fluid properties.	106
6.1	Budgets of the averaged advective divergence terms for the axial momentum transport comparing the WALE, CSM and SMAG subgrid-scale model contributions for different $Re_\tau = 360/500, Pr = 10/20$	109

6.2	Budgets of the averaged advective divergence terms for the heat transport comparing the WALE, CSM and SMAG subgrid-scale model contributions for different $Re_\tau = 360/500$, $Pr = 10/20$	111
6.3	<i>Rms</i> -values of the numerical error β_w and the <i>a priori</i> sgs-contribution α_w for axial momentum equation at different Re_τ and Pr numbers	112
6.4	<i>Rms</i> -values of the numerical error β_θ and the <i>a priori</i> sgs-contribution α_θ for energy transport equation at different Re_τ and Pr numbers	113
6.5	Cross correlation coefficient $\langle \rangle^*$ between numerical error and resolved contribution (red line), resolved and sgs model contribution (blue line), resolved and sgs model contribution (green line) for $Re_\tau = 360/500$ and $Pr = 10/20$	114
6.6	Radial variation of the subgrid-scale Prandtl number as computed from the filtered DNS data Pr_{sgs} at different Re_τ and Pr numbers	115
6.7	Radial variation of the Smagorinsky model coefficient C^{SMAG} , C^{DNS} , and Coherent Structure Model coefficient C^{CSM} as computed from the filtered DNS data, at different friction Reynolds numbers $Re_\tau = 360/500$	116
6.8	Sgs eddy viscosity predicted by CSM, WALE and SMAG sgs models compared against the <i>a priori</i> eddy viscosity retrieved from the filtered DNS data at $Re_\tau = 360/500$	116
6.9	Diagonal components of Taylor micro scale tensor λ_{ij} as obtained from DNS and compared against LES grid sizes in radial, azimuthal and axial direction	119
6.10	Averaged axial velocity (first row) and averaged enthalpy difference profile (second row) predicted by LES for variable fluid properties in heated/cooled conditions (DH360/DC360) and constant material properties (D360) as compared against correspondent DNS results at $Re_\tau = 360$	120
6.11	Averaged subgrid-scale eddy viscosities predicted by CSM, WALE, SMAG at $Re_\tau = 360$	121
6.12	Resolved and total turbulent fluxes of momentum from CSM, WALE and SMAG compared against DNS for $Re_\tau = 360$	122
6.13	Resolved and total turbulent fluxes of heat from CSM, WALE and SMAG compared against DNS for $Re_\tau = 360$	123
6.14	<i>Rms</i> -values of fluctuating velocity components and enthalpy difference predicted by LES with SMAG, CSM, WALE and DNS at $Re_\tau = 360$, heated variable fluid properties case DH360	125
6.15	<i>Rms</i> -values of fluctuating velocity components and enthalpy difference predicted by LES with SMAG, CSM, WALE and DNS at $Re_\tau = 360$, cooled variable fluid properties case DC360	125
6.16	<i>Rms</i> -values of fluctuating velocity component and enthalpy difference as predicted by LES with SMAG, CSM, WALE and DNS at $Re_\tau = 360$, constant fluid property case D360	126
6.17	Averaged axial velocity component and enthalpy difference as predicted by LES with SMAG, CSM, WALE and DNS at $Re_\tau = 500$, strongly heated case with variable fluid properties (DHH500)	127
6.18	<i>Rms</i> -values of fluctuating velocity components and enthalpy difference as predicted by LES with SMAG, CSM, WALE and DNS at $Re_\tau = 500$, strongly heated case with variable fluid properties (DHH500)	127

6.19	Resolved and total turbulent fluxes of momentum and heat from LES with CSM, WALE and SMAG compared against DNS at $Re_\tau = 500$, strongly heated case with variable fluid properties (DHH500)	128
7.1	Axial resolution in LES given in inlet wall units	131
7.2	Axial resolution in DNS given in inlet wall units	131
7.3	Contours of ratio Ψ obtained for the DNS with air	132
7.4	Wall normal variation of molecular kinematic viscosity with wall distance $y^* = 0.5 - r/D$ at selected positions z/H as predicted by DNS and LES using glysantine-water as working fluid	133
7.5	Sagittal view of istantaneous contours of spanwise velocity component predicted by DNS for air	134
7.6	Sagittal view of istantaneous contours of wall normal velocity component predicted by DNS for air	134
7.7	Sagittal view of istantaneous contours of axial velocity component predicted by DNS for air	135
7.8	Axial variation of skin friction coefficient past the step in the downstream pipe as predicted by DNS, LES with CSM sgs model, and LES without sgs model	136
7.9	Wall normal variation of turbulent sher stress normalized with the turbulent kinetic energy in the downstream pipe past the step as predicted by DNS and LES with CSM sgs model for air	136
7.10	Wall normal variation of turbulent shear stress past the step in the downstream pipe as predicted by DNS, LES with CSM sgs model for glysantine-water	137
7.11	Wall normal variation of sgs eddy viscosity relative to molecular viscosity in the downstream pipe as predicted by LES with CSM sgs model for air	138
7.12	Sagittal view of istantaneous non-dimensional temperature field predicted by the DNS for air	139
7.13	Sagittal view of istantaneous non-dimensional temperature field predicted by the DNS for glysantine-water	139
7.14	Wall normal variation of rms -value of non-dimensional temperature along the downstream pipe as predicted by DNS for air (red line) and glysantine-water (black line)	140
7.15	Wall normal variation of radial turbulent heat flux past the step in the downstream pipe obtained from DNS and LES with CSM sgs model for air	141
7.16	Wall normal variation of radial turbulent heat flux past the step in the downstream pipe obtained from DNS and LES with CSM sgs model for glysantine-water	141
7.17	Wall normal variation of modelled sgs radial heat flux in the downstream pipe obtained from LES with CSM sgs model for glysantine-water and air	142
7.18	Axial variation of local Nusselt number Nu^* in the downstream pipe obtained from DNS, LES with CSM sgs model and LES without sgs model	143
7.19	Averaged $\langle T_w \rangle, \langle T_b \rangle$ along axial coordinate z in the downstream pipe for air	144
7.20	Averaged $\langle q_w \rangle, \langle T_b \rangle$ along axial coordinate z in the downstream pipe for glysantine-water	144

7.21	Axial variation of averaged temperature $\langle T \rangle / T_w$ along the downstream pipe as predicted by DNS for air (red line) and glyserine-water (black line) . . .	145
7.22	Axial variation of averaged wall-to-bulk temperature difference $\Delta T = \langle T_w \rangle - \langle T_b \rangle$ in the downstream pipe obtained from DNS, LES with CSM sgs model	146

List of Tables

2.1	Coefficients used in Fig. 2.9	44
5.1	DNS test cases with variable fluid properties	69
5.2	Grid size in DNS	70
5.3	Geometrical and physical parameters used in the <i>conjugate heat transfer</i> analysis	101
6.1	LES test cases	117
6.2	Grid size in LES/DNS	117
6.3	Wall skin friction coefficient C_f and Nusselt number Nu	121
7.1	Thermal conditions adopted for the considered working fluids	130
7.2	Grid resolution in the radial and azimuthal directions for DNS/LES	130

Nomenclature

Abbreviations

DNS Direct Numerical Simulation

LES Large Eddy Simulation

Nu Nusselt Number

Pr Prandtl number

Re Reynolds number

Ri Richardson number

Greek Letters

χ enthalpy difference [$\frac{J}{kg}$]

η_B Batchelor length scale [m]

η_K Kolmogorov length scale [m]

λ thermal conductivity [$\frac{W}{m K}$]

μ molecular viscosity [$\frac{kg}{m s}$]

ν_T non-dimensional eddy viscosity

ρ density [$\frac{kg}{m^3}$]

τ non-dimensional stress tensor

θ temperature difference [K]

φ azimuthal coordinate

Latin Letters

A_λ fluid property coefficient [$\frac{W}{m K}$]

A_μ fluid property coefficient [$Pa s$]

A_ρ fluid property coefficient [$\frac{kg}{m^3}$]

A_{c_p}	fluid property coefficient [$\frac{J}{kg\ K}$]
a_T	non-dimensional eddy diffusivity
B_λ	fluid property coefficient [$\frac{W}{m\ K^2}$]
B_μ	fluid property coefficient [K]
B_ρ	fluid property coefficient [$\frac{kg}{m^3\ K}$]
B_{c_p}	fluid property coefficient [$\frac{J}{kg\ K^2}$]
c_p	specific heat capacity [$\frac{J}{kg\ K}$]
C_μ	fluid property coefficient [K]
C_f	skin friction coefficient
D	Downstream pipe diameter [m]
d	upstream pipe diameter [m]
\mathbb{G}	non-dimensional velocity gradient tensor
h	specific enthalpy [$\frac{J}{kg}$]
k	turbulent kinetic energy [$\frac{m^2}{s^2}$]
\dot{m}	mass flow rate [$\frac{kg}{s}$]
\mathbf{q}	heat flux vector [$\frac{W}{m^2}$]
R	pipe radius [m]
r	radial coordinate [m]
\mathbb{S}	non-dimensional strain tensor
T	temperature [K]
t	non-dimensional time
\mathbf{U}	velocity vector [m/s]
\mathbb{W}	non-dimensional vorticity tensor
y	wall normal coordinate [m]
z	axial coordinate [m]

Operators

$\hat{(\)}$	density-weighted quantity
$\langle \ \rangle$	ensemble average

∇ non-dimensional Nabla operator

$\overline{(\)}$ Favre filtered quantity

$\widetilde{(\)}$ spatially filtered quantity

Superscripts and Subscripts

$(\)^*$ non-dimensional quantity rescaled with its reference wall value

$(\)^+$ non-dimensional quantity in wall units

$(\)_w$ quantity evaluated at the wall

$(\)_{sgs}$ subgrid scale quantity

Chapter 1

Introduction

In various engineering applications the forced convection of heat and momentum is of paramount importance for a reliable industrial design process. Ranging from fairly small-scale applications, as found in automotive cooling systems of combustion engines, electric motors, or rechargeable batteries, to large heat exchanging devices in power plants, the generally utilized turbulent heat transfer mechanism is often accompanied by a strong variation in local material properties. This is particularly the case for turbulent flows using working fluids at high molecular Prandtl number well beyond unity, for which the near wall temperature gradients are typically very steep. Due to their acknowledged technical relevance, these flows have been receiving progressively larger attention within the scientific and CFD (Computational Fluid Dynamics) community, as the constantly growing computational power makes nowadays numerical simulations a valuable alternative to the experimental approach for a qualitative and quantitative investigation of turbulent flow.

Nevertheless, some intrinsic difficulties arise when the demand on accuracy in the simulation of such kind of flows is increased, as the pronounced near wall temperature gradients coupled with possibly intense turbulent regimes, make the computational costs significantly rise to meet the required spatial high resolution. This issue becomes even more relevant, when the large temperature differences occurring in the heated or cooled flow field require to account for real temperature-depending material properties, which naturally introduces a back-coupling of the heat transfer on the momentum transfer.

In pace with a possibly strong local variation of the molecular transfer coefficients, additional complexities arise, when turbulence modelling is involved. The concept of RANS (Reynolds Averaged Navier Stokes) has been established as an efficient and computationally cheap standard approach, when the spatial resolution of the domain is too coarse for a direct computation of all relevant small scales without the aid of modelling, as done in DNS (Direct Numerical Simulation). However, RANS modelling approaches do lack of universality and are often very case-specific, as the employed turbulence models are frequently tuned for a limited range of flow conditions or geometries. In the past years, the concept of LES (Large Eddy Simulation) gained increasing attention as a possible alternative to RANS, provided that a sufficient spatial resolution is ensured. Many subgrid-scale (sgs) models have been developed for closing the unresolved turbulent fluxes in the LES equations. These closure models were mostly designed for momentum transfer under the assumption of equilibrium between production and dissipation of turbulent kinetic energy, which, however, may not be necessarily satisfied in real circumstances. Despite the

generally attempted small relative influence of the sgs model on the numerical description of the resolved eddies, a straight-forward extension of standard sgs modelling approaches to turbulent flows at high molecular Prandtl number, still poses some questions concerning essentially the model's applicability in different flow regimes and the tuning of parameters, such as the subgrid-scale Prandtl number Pr_{sgs} .

1.1 Motivation and Objectives

The first objective of this thesis is to deliver a comprehensive insight into heat transfer for wall bounded turbulent pipe flows at high molecular Prandtl number close to 10 in fully developed attached and separated conditions, using a specific 50/50 Vol% mixture of Glysantine and water as working fluid. Appropriate constitutive laws for the fluid properties involved in heat and momentum transfer phenomena will be considered in order to account for a feedback of the temperature on the momentum transfer. Results obtained by alternatively considering and neglecting the aforementioned dependency on local temperature will be discussed. The coupling of momentum and heat transfer through molecular viscosity is indeed in most of the available literature neglected, since the simulated conditions often give rise to fairly limited temperature differences which allow for such simplification for the considered fluids. However, when the temperature induced variation of viscosity becomes considerable, this approach may lead to a substantially wrong prediction of both momentum and heat transfer. Accounting for such a thermal back-coupling represents without any doubt an increased cost under the computational standpoint, which is a further reason why such interaction is hardly addressed in the literature, particularly in DNS studies on heat transfer.

More specifically, the present topics will be addressed by analyzing two different flow conditions: fully developed periodic turbulent flow in a straight pipe representing attached boundary layer type equilibrium flow, and a non-equilibrium separated flow in a pipe with an abrupt axisymmetric expansion. For these two configurations the modulation of turbulence and heat transfer is closely investigated with the aid of well resolved DNS, which will be further used as benchmark for LES assessment. Furthermore, the numerical results obtained for the periodic pipe flow will be supported by an experimental campaign on an in-house test facility to provide useful validation data for the acquired numerical results.

The second objective of this thesis will address subgrid-scale turbulence modelling in the context of LES, where the previously acquired DNS results will serve as reference for different turbulence regimes and thermal loads. An extensive assessment of a selection of popular well established sgs models will be carried out, with a major focus on the prediction of heat transfer in presence of a feedback on momentum through temperature-dependent material properties. Most of the available sgs models have been indeed calibrated and tuned essentially for momentum transfer in fully turbulent conditions, assuming equilibrium between production and dissipation of turbulent kinetic energy. Little attention has been paid to their performance in the modelling of heat transfer, especially in moderate turbulent regimes, considering temperature depending material properties, or even under non-developed flows.

The thesis is structured as follows:

- The available literature addressing the main topics of the thesis is carefully reviewed in Chapter 1.
- Chapter 2 presents the general mathematical formulation for describing the heat and momentum transfer in turbulent pipe flows.
- In Chapter 3, the methods and strategies used to analyze turbulent heat and momentum transfer in the considered operating conditions are presented. This includes in particular a description of the employed turbulence modelling concepts. An overview of the experimental setup used for additional validation of the numerical results is presented as well.
- In Chapter 4, the detailed numerical solution of the governing equations for the considered test cases is presented. This part essentially describes the numerics used in self-sustained predictive DNS and *a posteriori* LES simulations, as well as non-predictive *a priori* LES based on the analysis of spatially filtered DNS data (*a priori* test).
- Chapter 5 analyzes the results obtained from DNS in fully developed turbulent pipe flows, under the influence of heated/cooled wall conditions with/without temperature-dependent material properties.
- In Chapter 6, the predictive capabilities of three popular LES sgs models are assessed against DNS results for the fully developed pipe flow cases.
- In Chapter 7, the performance of the Coherent Structure Model (CSM) sgs model is assessed against DNS in turbulent heated pipe flow with an abrupt circular expansion.
- A summary and the conclusions are given in Chapter 8. The relevance of temperature-dependent material properties in momentum and heat transfer is summarized, and the strengths/weaknesses of the existing subgrid-scale modelling concepts used in LES are highlighted for both attached and separated flow conditions.

1.2 State of the Art

The early attempts to approach numerically heated or cooled turbulent wall bounded flows were generally restricted to consider only moderate Reynolds numbers (Re) and near-unity molecular Prandtl numbers (Pr), as the available computational power at that time prevented to carry out simulations on grids fine enough to represent the pronounced near wall temperature and velocity gradients, as well as the large variety of thermal scales arising when Pr increases well beyond unity. Additionally, the dependence of fluid's thermophysical properties on temperature was initially neglected, partially because of the additional numerical complexity, and partially due to the fairly small variation of the material properties of the considered low Prandtl number fluids in the investigated temperature range.

The majority of the numerical studies on wall bounded turbulent flows considered isothermal conditions without heat transfer. As for the methods, DNS represents the most accurate computational tool to investigate turbulent flows, although the computational demand is in many cases so high that only rather simple geometries can be treated. As

a consequence, DNS of wall bounded flows are often performed in simplified generic configurations like straight channels or pipes, avoiding cumbersome geometrical complexities, and assuming periodicity in the flow's structure along at least one spatial direction. The reliability of DNS as a valuable research tool for investigating in much detail turbulent flow fields, has been acknowledged throughout the past years, as these computational studies in general yielded very good agreement with the available experimental data. Pioneering works in the early application of the DNS approach were carried out by Kim *et al.* (1987) for planar channel flow at a friction Reynolds number $Re_\tau = 360$, and later by Moser *et al.* (1999) for higher Re_τ up to 395. The authors of these works provided DNS results of periodic channel flows which were well supported by comparison with experimental data. Their database is still considered nowadays as a valuable reference for assessment of codes or numerical results. Later on, the literature was extended by further DNS studies, also considering simplified generic configurations, such as a periodic channel or pipe flows, where the flow is assumed fully developed and statistically homogeneous in two directions. The advection of a scalar in a turbulent motion was computationally investigated in various follow-up DNS studies. Kim and Moin (1989) and Kasagi *et al.* (1992) simulated the advection of temperature as a passive scalar in a streamwise and spanwise periodic channel flow at $Re_\tau = 180$ (based on the channel's half width) with $Pr = 0.025, 0.71, 2$ and $Re_\tau = 150$ with $Pr = 0.71$, respectively. These works examined the low and higher order statistics for a turbulent scalar field. Later on, Kawamura *et al.* (1999) conducted similar numerical investigations but for an increased $Re_\tau = 395$. All of the three mentioned works provided a very close insight into the turbulent transport of a passive scalar, as which temperature might be considered in a first approximation, and clearly showed the tendency of thermal and velocity's fluctuations to become tightly correlated, as Pr approaches unity. The observed close similarity between the dynamic and thermal turbulent structures, is often referred to as *Reynolds analogy*. Concerning the modelling of turbulent thermal scales, the three aforementioned works did not reveal a substantial sensitivity of an important modelling parameter, namely the turbulent Prandtl number (Pr_T), on the molecular Prandtl number in the near wall region.

Further studies of DNS with passive scalar transport in periodic channel flow pointed out that an enhanced molecular Pr may affect Pr_T and finally lead to the breakdown of *Reynolds analogy*. In this regard, Na and Hanratty (2000) came to the conclusion that the thermal turbulent diffusivity does not scale with the wall distance like the eddy viscosity (y^{+3}) in the limit of $y^+ \rightarrow 0$, when Pr significantly exceeds unity. In particular, the authors of argued that the dampening effect of the wall, acting primarily on high wave number temperature fluctuations, is by far more pronounced as compared to the wall dampening of wall-normal velocity fluctuations.

Aside from the effect of high molecular Prandtl numbers, a second possible factor, which may lead to the breakdown of *Reynolds analogy*, resides in the posture of different thermal boundary conditions. Accounting for the heat conduction in the solid wall surrounding a heated pipe or a channel flow, may affect the extent and intensity of the thermal fluctuations which develop in the near wall region of the fluid phase. The modulation of the near wall thermal fluctuations is indeed influenced by both geometrical and the thermophysical properties of the boundaries, such as the thickness of the solid wall and the effusivity of the solid material. These aspects are thoroughly addressed in the works of Tiselj *et al.* (2001) and Tiselj and Cizelj (2012), where the heat conduction in the solid

wall is accounted for by means of a DNS with a conjugated heat transfer. The solution of the conjugate heat transfer problem basically also includes the two asymptotic limits for the thermal boundary conditions, being the isothermal boundary condition and the isoflux boundary condition, respectively. The first is associated with zero fluctuations in temperature, while the latter assumes zero fluctuations for the heat flux. The prescription of either of them leads to a different near wall behaviour of Pr_T . This result is confirmed also in the work of Piller (2005), who investigated the transport of heat in cylindrical pipe flow at $Pr = 0.7$, assuming alternatively *isoflux*, *isothermal* and mixed thermal boundary conditions.

Lastly, the effect of temperature-dependent material properties is identified as a third possibly relevant mechanism for altering the turbulent transport of momentum and heat. This is especially an issue, when large temperature differences come together with strongly temperature sensitive fluid properties governing the momentum transfer. The vast majority of the available studies mainly focused the momentum transfer, as being altered by the temperature-dependent material properties. Little attention, on the contrary, has been devoted to heat transfer, especially when fluids with high molecular Prandtl numbers are considered. Patel *et al.* (2015) show that the variable density and viscosity in turbulent heated wall bounded flow can be incorporated into an universal description by introducing a semilocal scaling which, for the constant fluid property case, simply reduces to the classical plus-unit $(+)$ scaling. Using this newly proposed scaling approach, the statistics up to 2^{nd} order reasonably collapse. Zonta *et al.* (2012) considered a periodic planar channel heated and cooled on the top and bottom wall, respectively. The temperature difference between both walls was imposed high enough to induce a pronounced viscosity variation across the channel's height. The authors of this work made the basically counterintuitive observation, that turbulence is enhanced in the cold region of flow domain, namely in proximity of the cold wall, where viscosity is increased, and dampened near the hot wall, where viscosity is reduced. A corresponding trend was seen in the budget of the turbulent kinetic energy (TKE) as compared against the constant fluid property case, exhibiting an increased production term and reduced dissipation rate term near the cold wall and viceversa near the hot wall.

The influence of a pronounced back-coupling on momentum transfer induced by temperature distribution in presence of strongly varying thermophysical properties has been later on investigated in Lee *et al.* (2013) for a turbulent boundary layer of water at reference $Pr = 5.4$ along an isothermally heated wall. The effect of stratified viscosity as function temperature was examined with a special focus on the resulting skin friction coefficient. The authors of this work observed a maximum drop in the skin friction coefficient by 26% as compared to the constant fluid property case. Turbulence intensity turned out to decrease owing to the weakened Reynolds shear stresses, which in turn are responsible for the decrease in the TKE production term in the buffer layer.

Further to the modulation of turbulence through a pronounced variation of thermophysical transport properties, the effect of buoyancy due to stratification of density has been also acknowledged as a possibly important source of alteration of the near wall turbulent activity. Turbulent stably and unstably stratified flows manifest in many industrial applications, like cooling in nuclear reactors and fuel injection in internal combustion engines, and in environmental processes, such as nocturnal boundary layers and oceans streams.

The influence of buoyancy in stably stratified turbulent flows is thoroughly addressed

in Zonta and Soldati (2018), where the shear Richardson number Ri_τ is identified as a key parameter to distinguish between weakly/moderate and strongly stratified turbulence. In the former regime the effect of buoyant forces is confined to large distances from the wall, leaving the canonical near wall sustained turbulent activity untouched, whereas in the latter case the near wall conditions are severely affected by the buoyant action leading to the coexistence of laminar and turbulent flow patterns. The study by Garg *et al.* (2000) analogously classifies turbulent channel flows in stably stratified conditions based on Ri_τ , distinguishing in particular buoyancy affected, buoyancy controlled and buoyancy dominated flows. Buoyancy affected flows retain a near wall turbulent activity similar to the one of unstratified flows, as consistently observed by Zonta and Soldati (2018). Turbulent intensity is generally inhibited, especially in the outer region remote from the wall. Buoyancy controlled flows show a peculiar asymmetry with respect to the channel's mid line, where eventually the upper or lower half of the channel intermittently relaminarizes for some time. Lastly, in buoyancy dominated flows the turbulence is completely suppressed by stratification.

The complex interaction of buoyancy and turbulence in mixed convection was also investigated in Bae *et al.* (2005) and in Pirozzoli *et al.* (2017). Bae *et al.* (2005) showed that the turbulence budgets are greatly affected by buoyancy in a vertical supercritical heated flow at inlet bulk Reynolds number $Re_b \approx 5400$ and inlet bulk Prandtl number $Pr_b \approx 3.04$. It is demonstrated that buoyancy amplifies turbulence production in downward flows, while dampens it in upward flows. This peculiar behaviour is essentially induced by the strong buoyant forces, which arise close to the wall due to the significant drop of the local density supporting or counteracting the upwards or downwards motion of the main flow, respectively. Pirozzoli *et al.* (2017) investigated planar horizontal Poiseuille flows in unstably stratified conditions compared against the non-buoyant unstratified case. They inspect qualitatively the development of distinct patterns in form of rollers, extending in the streamwise direction of the main flow. They observe large meandering streamwise coherent structures at bulk Richardson number $Ri_b \approx 1$, whereas for ranges of Ri_b from 0.01 to 0.001, a progressive disappearing of such structures is observed, tending towards purely forced convection conditions ($Ri_b = 0$). The role of the bulk Richardson number Ri_b for the onset of buoyancy-altered turbulence is also addressed in the study of Sekimoto *et al.* (2011), who performed DNS of air at $Re_b \approx 6400$ and $Pr_b \approx 0.7$ in a horizontal square duct heated from the bottom wall. In this work, the global transport parameters, namely the Nusselt number Nu and the skin friction coefficient C_f , are shown to become insensitive to the bulk Richardson number for $Ri_b < 0.025$.

Aside from the computationally expensive fundamental DNS studies, the method of Large Eddy Simulation (LES) has been progressively getting more attention among scientists dealing with heat transfer in turbulent flows. Especially in moderate turbulent regimes, the widely used well established Reynold-Averaged Navier Stokes (RANS) approach often fails to describe accurately turbulent flow field, as major RANS modelling assumptions based on fully developed high Reynolds number conditions are violated. Due to this limitation, RANS-like approaches appear as less suited for the accurate prediction of heat transfer in such conditions as well, especially when a thermal back-coupling induced by temperature-dependent material properties is considered. As opposed to RANS, LES approach represents a more reliable tool for this kind of numerical investigations, as the

influence of the subgrid-scale closure model on the main flow structure is limited to the smaller scales, so that the effect of the intrinsic modelling error may be more confined. On the other hand, LES modelling for turbulent flows at high molecular Pr requires a significantly higher spatial resolution, in order to properly describe the thin thermal boundary layer near the wall, increasing by far the computational cost and the sensitivity to numerical errors. Additionally, LES approach for heat transfer is not exempted from modelling uncertainties. The often used assumption of $Pr_{sgs} \approx 0.9$ for relating subgrid-scale transport coefficients of momentum and heat is certainly simple but not universal.

The modelling capabilities of different sgs modelling approaches as well as the role of the numerical error in LES have been systematically examined in the framework of *a priori* tests. Abba *et al.* (2003) carried out an extensive analysis on several sgs models and assessed their performance by comparing the total kinetic energy dissipation provided by the models to that of a filtered reference DNS. The authors additionally formulate a new improved tensorial model, which does not rely on the traditional *Boussinesq*-type eddy viscosity approach, producing a fair agreement with the dissipation computed with filtered DNS data. Vreman *et al.* (1995) compare in a planar 2D mixing layer the contribution of the sgs model against the estimated numerical error, which arises from the spatial discretization of the convective non linear terms in Navier-Stokes equations. The authors conclude that the use of 2nd-order spatial discretization scheme together with a coarse mesh size leads to a pronounced rise in the numerical error, which may considerably exceed contribution of the sgs model. The role of the numerical error is addressed as well by Brandt (2006), where the author presents a strategy based on explicit test filtering of the governing equations for LES in order to gain higher accuracy and reduce the amount of error introduced by the discretization of the convective terms. Salvetti and Banerjee (1995) assessed selected popular sgs models against DNS by comparing the modelled sgs stresses with the unresolved *a priori* stresses retrieved from the filtered DNS data. They additionally propose a modified dynamic model capable to give very good agreement between all modelled sgs stress components and the filtered unresolved stress tensor components from the DNS.

The number of *a posteriori* LES for subgrid-scale model assessment is rather large, as they basically represent the ultimate benchmark test for evaluating the predictive capability, computational feasibility, and numerical stability of the models. A common goal in LES is to provide simple and efficient closure models, which could be readily used in real and complex geometries. This is indeed a reason for the rather widespread use of the *Boussinesq*-type sgs eddy viscosity models, as their implementation is easy, they are computationally cheap, and often do not require special features of the flow configuration, such as homogeneity in one or more directions to perform a statistical averaging of the strongly fluctuating model parameters. The first eddy-viscosity type model was developed by Smagorinsky (1963) for applications in atmospheric flows. This model represents the very starting point for further more refined modelling efforts and is still widely used, mainly owing to its robustness and simplicity. Some important drawbacks are however envisaged in the need for an artificial near wall correction when internal flows are simulated, and in the need for choosing an appropriate model coefficient, which turned out to be markedly dependent on the kind of flow considered. A significant improvement to the original Smagorinsky model was brought about by the introduction of the dynamic procedure by Germano *et al.* (1991), further refined by Lilly (1992), which enabled the local

evaluation of the model coefficient based on the local turbulent flows conditions. Despite the clear improvement provided by the local determination of the model parameter, the dynamic procedure still requires some averaging along homogeneous directions or a clipping of eddy viscosity to positive values, in order to prevent instabilities in the *a posteriori* computations. Therefore, the applicability of such models remains limited to simple mostly generic test cases involving one or more statistically homogeneous directions required for averaging. Nicoud and Ducros (1999) developed an eddy viscosity model (Wall Adapting Local Eddy viscosity, WALE) based on both the resolved strain and vorticity tensors, and able to provide the correct scaling of sgs eddy viscosity without the aid of *ad hoc* wall damping functions. The model turned out to perform in a very satisfactory way in various internal flow configurations, and is nowadays implemented as a standard sgs model in many CFD software packages, like Ansys FLUENT, or OpenFOAM. Similarly, the sgs model developed by Kobayashi (2005) targets the need for a correct near wall scaling of eddy viscosity without the use of damping dependent on wall distance, which might be difficult to define in complex flows geometries. Facing this objective, Kobayashi (2005) developed a formulation which does not rely neither on any geometry-related quantity, such as the distance from the nearest wall, nor on any dynamic procedure for the calculation of a model parameter. The formulation only uses resolved flow-related quantities instead, like the total dissipation and the second invariant velocity gradient tensor, both locally evaluated. The model, termed Coherent Structure Model (CSM), essentially extends the original Standard Smagorinsky model (SMAG) introducing a variable model coefficient, which vanishes in relaminarized flow. The CSM approach was proven to give fairly accurate results for both attached boundary layer type flow as well as more complex separated flows conditions, as shown in Kobayashi *et al.* (2008).

To the knowledge of the author, the number of studies dealing with LES of turbulent heated flow with relevant fluid property variation is rather limited. One reason for the scarcity of these studies is the lack of reference DNS data for a systematic model assessment. Additionally, the molecular Pr for which most studies have been performed was mostly assumed near or exactly unity, as typically met with gases like air. Dailey *et al.* (1999) (1999) considered a planar channel flow, where the fluid is heated from both sides at different uniform wall temperatures. In this work the Standard Smagorinsky sgs model corrected with a Van-Driest wall damping function is compared against a dynamic Smagorinsky sgs model, in which the sgs modelling parameters are obtained using the dynamic procedure introduced by Germano *et al.* (1991). For both models an overestimated mean velocity profile is observed and, surprisingly, the Standard Smagorinsky model outperforms its dynamic counterpart when the grid resolution is refined. Later, Dailey *et al.* (2003) performed an LES of turbulent channel flow of air (at constant $Pr = 0.71$) heated from the walls with a constant wall heat flux. The dynamic Smagorinsky model was employed for subgrid-scale closure and the results were compared against the DNS of Kim *et al.* (1987) at constant fluid properties. Especially under high wall heating condition, the authors experienced rather an increase in bulk velocity as compared to the reference DNS results. Correspondingly, a drop in the resolved contribution to the radial turbulent flux of momentum and heat flux has been observed. In more recent years Serra *et al.* (2012a), Serra *et al.* (2012b) considered LES of heated channel flow of air at wall friction Reynolds number $Re_\tau = 189$ and 395. The ratio between the uniform upper wall and uniform lower wall temperature, denoted by T2 and T1, respectively, was prescribed as input thermal

boundary conditions. The considered temperature ratios varied between $T_2/T_1 = 1.01$ and 2. The assessment was carried out against the available DNS data of Nicoud (1998) for a ratio $T_2/T_1 = 1.01$ and $Re_\tau = 180$, whereas the simulations at higher $Re_\tau = 395$ were compared against data of Moser *et al.* (1999) neglecting fluid properties variation. The WALE model developed by Nicoud and Ducros (1999) was used for subgrid-scale closure. The authors showed that at lower temperature ratio, the effect of varying fluid properties can be neglected, as the discrepancy with results obtained from LES with constant fluid properties is quite reduced. However, when the temperature ratio T_2/T_1 is increased, the change in viscosity and heat conductivity modulates the turbulence in a significant way. An interesting finding of this study concerns the benefit of including a dynamic procedure for the computation of Pr_{sgs} . The authors concluded from their results that the dynamic computation of Pr_{sgs} does not bring a significant advantage in terms of additional modelling accuracy. The LES study of Inagaki *et al.* (2012) introduced a hybrid timescale between the timescales of the velocity and thermal fields, through which the subgrid-scale thermal eddy diffusivity is modelled without the need for the introduction of a subgrid-scale Prandtl number Pr_{sgs} . The authors showed the capabilities of newly proposed model in planar channel flow, uniformly heated at the walls, and provided results in good agreement with DNS of Kim and Moin (1989) at molecular Prandtl numbers $Pr = 0.71, 2$.

As opposed to attached and fully developed turbulent heated flows in periodic pipe or channel geometries, much less attention has been generally paid to DNS/LES of detached separated flows like the flow over a backward-facing step or through channels with abrupt expansion including heat transfer. This is certainly due to the significantly higher computational cost associated with the more complex geometry, but also due to the harder parametrization of the considered flow conditions, which reduces the universal applicability of actually obtained findings. Most of the available DNS studies on separated flow, consider a backward-facing step in a channel or in a pipe, assuming relatively low upstream Reynolds numbers (based on the step height) which vary between 3000 and 10000, such as in the work of Le *et al.* (1997); Barri *et al.* (2010); Kopera *et al.* (2017); Pont-Vilchez *et al.* (2019). These numerical studies provide useful information concerning the required spatial resolution to adequately resolve the finest relevant scales of motions in such kind of flow. The shown results are generally in good agreement with the available experimental data. Nevertheless, heat transfer is not addressed, as the main focus is on momentum transfer in detached conditions. The vast majority of these isothermal DNS studies considered detached flows past a backward facing step in a planar channel geometry, where the statistical homogeneity in spanwise direction is exploited with the adoption of appropriate periodic boundary conditions, as it is commonly done in DNS of attached turbulent flows. Turbulent flow in pipes with an abrupt expansion was approached with DNS and LES by rather few authors, such as, by Wagner and Friedrich (1995), or Friedrich *et al.* (2001). The expansion ratio between the upstream and downstream diameter considered in these studies is 1.2 and the inlet conditions are taken from a precursor DNS at friction Reynolds number $Re_\tau = 360$ in Friedrich *et al.* (2001), and bulk Reynolds number $Re_B = 6950$ in Wagner and Friedrich (1995) based on the upstream pipe diameter. The moderate expansion ratio and the fairly coarse spatial resolution employed in both works somehow limits the possibility to draw very general conclusions from the results. Nevertheless, the authors demonstrated by comparing their DNS results with LES results obtained with a standard

Smagorinsky model that the turbulent energy transfer cannot be properly described by traditional eddy viscosity models, like the Standard Smagorinsky model, as the complex secondary flow occurring past the step results in the relative enhancement of the Reynolds stress components. The increased anisotropy of the turbulent motion is typically not captured by standard linear eddy viscosity approaches, which in turn influences the predicted production of turbulent kinetic energy.

Experimental studies of heated turbulent flow in pipes with a sudden expansion at moderate inlet bulk Reynolds number with air as working fluid were carried out by Baughn *et al.* (1984, 1989) and Zemanick and Dougall (1970). Downstream of the step all the authors observe an increase of heat transfer rate up to a factor ten as compared to the theoretical heat transfer rate predicted by well-established empirical correlations formula in fully developed conditions. The exact extent of heat transfer enhancement is strongly influenced by the upstream bulk Reynolds number and by the step height. Considering a inlet bulk Reynolds number $Re_b \approx 5000$ and expansion ratios between inlet and outlet pipe's diameters $r = 0.533, 0.54$, respectively, Baughn *et al.* (1984) and Zemanick and Dougall (1970) basically examined very similar experimental conditions, but their results are still not in good agreement. The discrepancy in the measured maximum heat transfer rate as well as its position along the downstream pipe is notable. For the considered range of low Reynolds number and Prandtl numbers well beyond unity, practically no numerical studies of DNS/LES can be found for use in a further comparison or validation. On the other hand, a couple of RANS studies on heat transfer with separated flows in pipes with abrupt expansions appeared in literature over the past years, especially at high inlet bulk Reynolds number, due to the large number of experimental data in such conditions. Among these, the study by Prud'homme and Elghobashi (1986), provides reasonable agreement with the experiments of Zemanick and Dougall (1970) at downstream bulk Reynolds number $Re = 4186$ and $Re = 9620$. Kim and Lee (1994) compared the performance of Reynolds stress model and a standard $k-\epsilon$ model, and assessed their results against the experiments of Baughn *et al.* (1989). In this study the superior performance of Reynolds stress model is confirmed also in such a separated flow. The poor performance of $k-\epsilon$ model in the prediction of maximum heat transfer rate and its position along the downstream pipe is highlighted.

As a final remark, it is noted that turbulent heat transfer with relevant back-coupling on the momentum still represents quite a scarcely explored field of research, especially when moderate Reynolds numbers are considered. With this regard, this thesis work intends to additionally enrich the state of art of numerical investigation on turbulent heat transfer and provide at the same time a valuable reference for further developments in this field.

Chapter 2

Problem description

This chapter intends to provide a mathematical description of heat transfer in turbulent pipe flow, which is heated or cooled through the surrounding walls without any internal additional source of energy. The heat transfer rate is strongly influenced by the flow regime, whether it stays laminar or turns into turbulent, and even within the turbulent regime, marked differences are to be encountered. The considered different flow configurations and operating conditions need therefore to be discussed in advance, in order to provide a comprehensive overview of the physical mechanism relevant for the process. Afterwards, the governing equations of a heated/cooled flow will be introduced and consequently applied to the considered test cases.

2.1 Heat transfer in wall bounded turbulent flows

The chaotic, random nature of turbulent fluctuating motion basically excludes a fully deterministic description of the flow. Due to this fundamental problem, a statistical approach is generally used instead, which describes the essential features of the flow in terms of ensemble averages.

An ensemble average of an arbitrary fluctuating quantity $\phi = \phi(\mathbf{x}, t)$ in turbulent flow represents the average over N statistically independent samples, realized for the same operating conditions:

$$\langle \phi(\mathbf{x}, t) \rangle_N = \frac{1}{N} \sum_{i=1}^N \phi_i(\mathbf{x}, t). \quad (2.1)$$

In the limit of an infinite number of samples $N \rightarrow \infty$, Eq. (2.1) returns the statistical average of variable ϕ , often referred to as Reynolds average:

$$\lim_{N \rightarrow \infty} \langle \phi(\mathbf{x}, t) \rangle_N = \langle \phi(\mathbf{x}, t) \rangle. \quad (2.2)$$

If the fluctuating process ϕ is statistically stationary, all its statistical moments are invariant with respect to an arbitrary translation in time. If a time averaging procedure over an infinitely extended time window is considered, Reynolds average and time average operators are equivalent:

$$\bar{\phi} = \lim_{\Delta T \rightarrow \infty} \frac{1}{\Delta T} \int_0^{\Delta T} \phi(\tilde{t}) d\tilde{t} = \langle \phi(\mathbf{x}) \rangle. \quad (2.3)$$

In consistence with the introduction of the Reynolds average operator $\overline{(\)}$, the instantaneous realization ϕ can be decomposed into an averaged and fluctuating component:

$$\phi = \overline{\phi} + \phi', \quad (2.4)$$

where the fluctuating contribution has zero mean, $\overline{\phi'} = 0$.

In this way it is possible to extract meaningful statistics of any random variable related to a turbulent flow, provided that the number of samples or averaging time in the ensembles is large enough to guarantee a converged statistics.

Introducing ψ as an additional random quantity, and its fluctuating component as $\psi' = \psi - \overline{\psi}$, the definition of a 2nd order statistical moment $\overline{\phi'\psi'}$ reads

$$\overline{\phi'\psi'} = \overline{(\phi - \overline{\phi})(\psi - \overline{\psi})}. \quad (2.5)$$

Additionally, the *rms*-values will be denoted with the subscript $(\)_{rms}$ and represent a special case of Eq. (2.5), where ϕ and ψ correspond to the same variable

$$\phi_{rms} = \sqrt{\overline{(\phi - \overline{\phi})(\phi - \overline{\phi})}}. \quad (2.6)$$

Wall bounded turbulent flows are by definition enclosed by at least one or more solid surfaces, which inherently prevents isotropic turbulence conditions to establish. The presence of a non-moving wall results in a stronger dampening of the velocity fluctuations in the wall-normal direction. If the flows remains attached, a thin region termed turbulent boundary layer, or dynamic boundary layer, develops in the proximity of the solid surface, where the advective mixing due to fluctuations is strongly decreased in favour of an enhanced viscous stress contribution and a correspondingly steepened velocity gradient near the wall associated with no-slip boundary condition.

As the characteristic Reynolds number increases, the thickness of the dynamic boundary layer is reduced, confining the effect of viscosity progressively closer to the surface and making the near wall velocity gradient accordingly steeper. This tendency is sketched in Fig. 2.1.

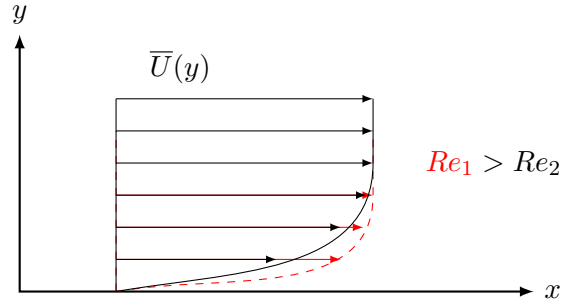


Figure 2.1: Effect of Reynolds number on turbulent dynamic boundary layer

In a heated or cooled turbulent flow, enthalpy is advected by fluctuating velocity, and in the immediate vicinity of the wall a thin layer, called thermal boundary layer, develops where the temperature profile changes from the core level to the conditions prescribed at the

wall. The temperature gradient at the wall and the thickness of the thermal boundary layer is strongly influenced by the fluid properties molecular viscosity μ , specific heat capacity c_p , and heat conductivity λ of the considered fluid. These three thermophysical fluid properties can be rearranged in a non-dimensional number called the molecular Prandtl number Pr , which is defined as:

$$Pr = \frac{\nu}{a} = \frac{\mu c_p}{\lambda}, \quad (2.7)$$

where ν denotes the kinematic viscosity $\nu = \frac{\mu}{\rho}$, and $a = \frac{\lambda}{\rho c_p}$ the thermal diffusivity.

Owing to its definition, Pr depends only on material properties of the working fluid. Therefore, it may undergo spatial variations inside the flow field as a result of compressibility or temperature dependence. Pr characterizes the ratio between the diffusion of momentum, represented by the molecular viscosity, and the conduction of heat, represented by the thermal diffusivity. In turbulent flows subject to heating or cooling through a wall heat flux q_w , as depicted in Fig. 2.2, a higher Pr always results in a steeper near-wall temperature gradient and a decreased thickness of the thermal boundary layer δ_{th} :

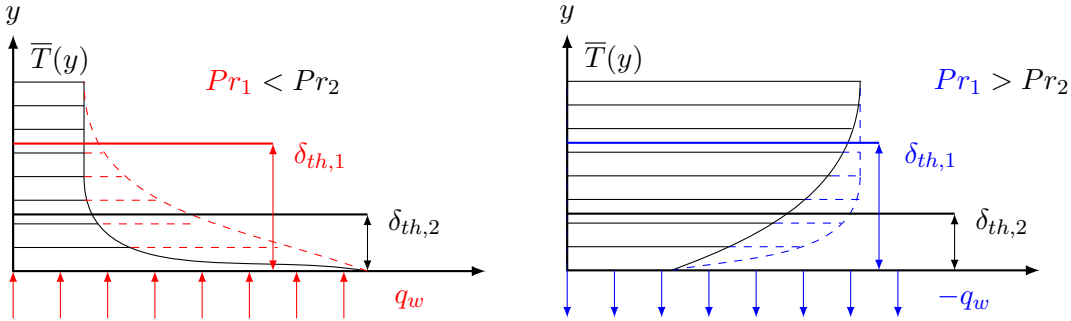


Figure 2.2: Effect of Prandtl number on thermal boundary layer

In fluids with $Pr \approx 1$, like air, the rate of transfer of momentum and heat are most closely related, and the thickness of the thermal boundary layer δ_{th} is comparable with the thickness of momentum boundary layer δ . In a wall bounded turbulent flow of such kind, this indicates, that the turbulent thermal structures develop in space similarly to the turbulent structures of momentum. This feature is generally called *Reynolds analogy*, referring to the close analogy or coherence between the transport of momentum and heat.

However, in several fluids of practical engineering interest (such as oil, coolant, or simply water) $Pr \gg 1$, and therefore the *Reynolds analogy* breaks down. The thermal turbulent structures spatially extend much smaller, as compared to those of momentum and the thickness of the thermal boundary layer is significantly reduced.

In many engineering applications, turbulent flows are bounded by complex wall geometries, which may induce a separation of the boundary layer, and the breakdown of statistical homogeneity in one or more spatial directions. This expectedly does not only affect the turbulent momentum transfer but also has a clear effect on heat transfer. Such separation typically occurs in the case of a turbulent flow past a cylindrical backward facing step, like in a straight pipe which undergoes a sudden expansion, increasing the pipe diameter in the downstream region. The separation of the boundary layer past the step

induces a region of recirculation which in turn enhances the advective turbulent heat transfer, as a consequence of the increased turbulent kinetic energy triggered by the separation (Kim and Lee (1994)). The extent of the separated flow region is dictated by the upstream conditions as well as by geometrical parameters. As no boundary layer is present anymore, no spatial coherence between momentum and thermal structures may be assumed even at Pr close to unity (breakdown of the *Reynolds analogy*).

2.2 Governing equations

The numerical investigation of turbulent flows undergoing a heating or cooling process starts out from the conservation equations for mass, momentum (Navier-Stokes equations) and energy, which read in the most general compressible case:

$$\frac{\partial \rho}{\partial t} + \nabla \cdot (\rho \mathbf{U}) = 0 \quad (2.8)$$

$$\frac{\partial(\rho \mathbf{U})}{\partial t} + \nabla \cdot (\rho \mathbf{U} \mathbf{U}) + \nabla P = \nabla \cdot \boldsymbol{\tau} \quad (2.9)$$

$$\frac{\partial(\rho h)}{\partial t} + \nabla \cdot (\rho \mathbf{U} h) = \frac{\partial P}{\partial t} + \mathbf{U} \cdot \nabla P - \nabla \cdot \mathbf{q} + \psi \quad (2.10)$$

Equations (2.8), (2.9) and (2.10) are solved for the velocity vector field \mathbf{U} , density ρ and specific enthalpy h . In the most general case, where thermodynamics due to compressibility is accounted for, they form a fully coupled system which needs a further mathematical closure through the introduction of two additional equations of state in the form

$$P = f(\rho, h) \quad (2.11)$$

$$T = f(P, h), \quad (2.12)$$

where T is the temperature of the fluid. The tensorial term appearing on the right hand side of Eq. (2.9) denotes the viscous stress tensor. For a Newtonian fluid it reads

$$\boldsymbol{\tau} = \mu(T) [\nabla \mathbf{U}^T + \nabla \mathbf{U} - \frac{2}{3} (\nabla \cdot \mathbf{U}) \mathbb{I}] = 2\mu(T) [\mathbb{S} - \frac{1}{3} \nabla \cdot \mathbf{U} \mathbb{I}], \quad (2.13)$$

where the dynamic viscosity of the fluid $\mu(T)$ is assumed dependent on temperature T , \mathbb{I} is the identity tensor and \mathbb{S} the symmetric part of the velocity gradient tensor $\nabla \mathbf{U}$:

$$\mathbb{S} = \frac{1}{2} [\nabla \mathbf{U} + (\nabla \mathbf{U})^T]. \quad (2.14)$$

In Eq. (2.10), the divergence term on the right hand side involves the conductive heat flux

$$\mathbf{q} = -\lambda(T) \nabla T, \quad (2.15)$$

where $\lambda(T)$ represents the thermal conductivity of the fluid with an assumed dependence on T . Lastly, again referring to the right hand side of Eq. (2.10), ψ denotes the dissipation term due to viscous forces, written as

$$\psi = \boldsymbol{\tau} : \nabla \mathbf{U}. \quad (2.16)$$

In the present work the flow will be treated as incompressible (low Mach number flow), while a dependence of the thermophysical properties ρ , λ , μ , and c_p on temperature is retained. The assumption of incompressibility allows for a simplification of conservation equation of energy rewritten as

$$\frac{(\partial \rho h)}{\partial t} + \nabla \cdot (\rho \mathbf{U} h) = -\nabla \cdot \mathbf{q}, \quad (2.17)$$

where the specific enthalpy is a function of T computed as

$$h = \int_{T_{ref}}^T c_p(T) dT. \quad (2.18)$$

In Eq. (2.18), T_{ref} represents a reference state temperature, at which a certain specific reference enthalpy is given. As the flow is incompressible, the coupling between its thermal state, as described by Eq. (2.17), and momentum is solely carried by the constitutive material laws for density $\rho = \rho(T)$, specific heat $c_p(T)$, and molecular viscosity $\mu = \mu(T)$ as function of local temperature T . The thermodynamic equations of state, as generally represented by Eqs. (2.11) and (2.12), are therefore effectively reduced to a law for thermal dilatation $\rho(T)$ in such incompressible case.

2.3 Turbulent pipe flow in fully developed conditions

The geometry representing the computational domain for the numerical simulation of turbulent pipe flow in fully developed conditions is schematically sketched in Fig. 2.3.

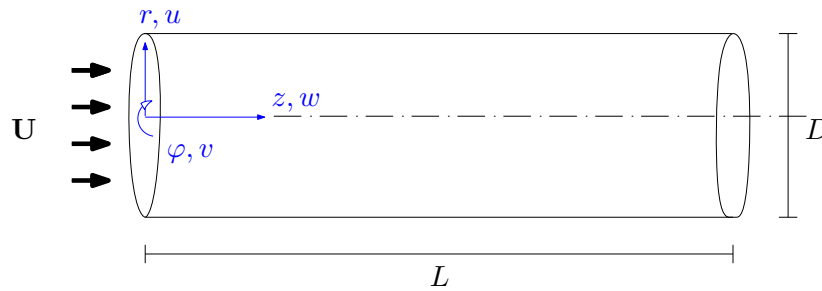


Figure 2.3: Fully developed pipe flow domain

The flow through the straight pipe with diameter D and length L is described in terms of polar coordinates r, φ, z , denoting the radial distance from the centerline of the pipe, the azimuthal angle, and the axial distance from an inlet section, respectively. u, v, w , denote the radial, azimuthal and axial velocity components, respectively.

The fully developed pipe flow is characterized by its statistical invariance with respect to the axial and azimuthal coordinates z, φ , respectively. As a consequence, the statistics can only depend on the radial coordinate r , and the flow is said to be statistically one dimensional.

The governing equations for mass, momentum and specific enthalpy, generally given in Eq. (2.8), (2.9) and (2.17) respectively, are rewritten in cylindrical coordinates as

$$\frac{\partial \rho}{\partial t} + \frac{1}{r} \frac{\partial(r\rho u)}{\partial r} + \frac{1}{r} \frac{\partial(\rho v)}{\partial \varphi} + \frac{\partial(\rho w)}{\partial z} = 0 \quad (2.19)$$

$$\begin{aligned} \frac{\partial(\rho u)}{\partial t} + \frac{1}{r} \frac{\partial(r\rho u u)}{\partial r} + \frac{1}{r} \frac{\partial(\rho u v)}{\partial \varphi} + \frac{\partial(\rho u w)}{\partial z} - \frac{\rho v v}{r} = \\ - \frac{\partial p}{\partial r} + \frac{1}{r} \frac{\partial(r\tau_{rr})}{\partial r} + \frac{1}{r} \frac{\partial\tau_{r\varphi}}{\partial \varphi} - \frac{\tau_{\varphi\varphi}}{r} + \frac{\partial\tau_{rz}}{\partial z} \end{aligned} \quad (2.20)$$

$$\begin{aligned} \frac{\partial(\rho v)}{\partial t} + \frac{1}{r} \frac{\partial(r\rho v u)}{\partial r} + \frac{1}{r} \frac{\partial(\rho v v)}{\partial \varphi} + \frac{\partial(\rho v w)}{\partial z} + \frac{\rho u v}{r} = \\ - \frac{1}{r} \frac{\partial p}{\partial \varphi} + \frac{1}{r} \frac{\partial(r\tau_{\varphi r})}{\partial r} + \frac{\tau_{\varphi r}}{r} + \frac{1}{r} \frac{\partial\tau_{\varphi\varphi}}{\partial \varphi} + \frac{\partial\tau_{\varphi z}}{\partial z} \end{aligned} \quad (2.21)$$

$$\begin{aligned} \frac{\partial(\rho w)}{\partial t} + \frac{1}{r} \frac{\partial(r\rho w u)}{\partial r} + \frac{1}{r} \frac{\partial(\rho w v)}{\partial \varphi} + \frac{\partial(\rho w w)}{\partial z} = \\ - \frac{\partial p}{\partial z} + \frac{1}{r} \frac{\partial(r\tau_{zr})}{\partial r} + \frac{1}{r} \frac{\partial\tau_{z\varphi}}{\partial \varphi} + \frac{\partial\tau_{zz}}{\partial z} \end{aligned} \quad (2.22)$$

$$\begin{aligned} \frac{\partial(\rho h)}{\partial t} + \frac{1}{r} \frac{\partial(r\rho h u)}{\partial r} + \frac{1}{r} \frac{\partial(\rho h v)}{\partial \varphi} + \frac{\partial(\rho h w)}{\partial z} = \\ - \frac{1}{r} \frac{\partial(rq_r)}{\partial r} - \frac{1}{r} \frac{\partial q_\varphi}{\partial \varphi} - \frac{\partial q_z}{\partial z} \end{aligned} \quad (2.23)$$

2.3.1 Dynamically fully developed conditions

The assumption of fully developed dynamic conditions implies the independence of all momentum statistics of the axial and azimuthal directions, and time. Additionally, the averaged velocity components \bar{u}, \bar{v} are zero. Applying the Reynolds average operator $(\bar{\cdot})$ to the conservation equations of momentum (2.20)-(2.22), they are reduced to

$$\frac{1}{r} \frac{\partial(r\overline{\rho u^2})}{\partial r} - \frac{\overline{\rho v^2}}{r} = -\frac{\partial \bar{p}}{\partial r} \quad (2.24)$$

$$\frac{1}{r} \frac{\partial(r\overline{\rho w u} - r\bar{\tau}_{zr})}{\partial r} = -\frac{\partial \bar{p}}{\partial z} \quad (2.25)$$

The first integration of Eq.(2.24) along the radial coordinate results in

$$\bar{p} = p_w - \overline{\rho u^2} - \int_r^R \frac{\overline{\rho u^2} - \overline{\rho v^2}}{r} dr. \quad (2.26)$$

Since $\overline{\rho u^2} \neq f(z)$ and $\overline{\rho v^2} \neq f(z)$ due to fully developed conditions, the derivation of Eq. (2.26) with respect to z proves that the mean axial pressure gradient $\frac{\partial \bar{p}}{\partial z}$ is independent of r

$$\frac{\partial \bar{p}}{\partial z} = \frac{dp_w}{dz} \neq f(r). \quad (2.27)$$

Due to this radial invariance of the mean axial pressure gradient, Eq. (2.25) can be radially integrated to

$$\overline{\rho w u} - \bar{\tau}_{rz} = -\frac{r}{2} \frac{\partial \bar{p}}{\partial z}. \quad (2.28)$$

By evaluating Eq. (2.28) at the wall ($r = D/2$), a relation between the wall shear stress $\bar{\tau}_{rz}|_{r=D/2} = \mu_w \frac{\partial \bar{w}}{\partial r}|_w = -\tau_w$ and the mean pressure gradient $\frac{\partial \bar{p}}{\partial z}$ which drives the flow in the pipe can be derived as follows:

$$-\frac{4}{D} \tau_w = \frac{\partial \bar{p}}{\partial z}. \quad (2.29)$$

Eq. (2.29) can be integrated along the coordinate z in order to derive an expression for the axial variation of the averaged pressure $\bar{p} = \bar{p}_w$

$$\bar{p} = -\frac{4\tau_w}{D} z + f(r). \quad (2.30)$$

The integration of Eq. (2.30) over an arbitrary section of the pipe, introduces the cross-sectional averaged pressure, defined as

$$\langle \bar{p} \rangle_A = -\frac{4\tau_w}{D} z + \frac{1}{R^2} \int_0^R f(r) dr 2\pi = -\frac{4\tau_w}{D} z + \langle \bar{p} \rangle_{inlet}. \quad (2.31)$$

The local pressure p can be splitted into a cross-sectional average defined in Eq. (2.31) as linearly dependent on z , and the instantaneous deviation from there, such that

$$p(r, \varphi, z, t) = \pi(r, \varphi, z, t) + \langle \bar{p} \rangle_A. \quad (2.32)$$

The decomposition expressed by Eq. (2.32) can be inserted in the conservation equations of momentum, which yields

$$\begin{aligned} \frac{\partial(\rho u)}{\partial t} + \frac{1}{r} \frac{\partial(r \rho u u)}{\partial r} + \frac{1}{r} \frac{\partial(\rho u v)}{\partial \varphi} + \frac{\partial(\rho u w)}{\partial z} - \frac{\rho v v}{r} = \\ -\frac{\partial \pi}{\partial r} + \frac{1}{r} \frac{\partial(r \tau_{rr})}{\partial r} + \frac{1}{r} \frac{\partial(r \tau_{r\varphi})}{\partial \varphi} - \frac{\tau_{\varphi\varphi}}{r} + \frac{\partial \tau_{rz}}{\partial z} \end{aligned} \quad (2.33)$$

$$\begin{aligned} \frac{\partial(\rho v)}{\partial t} + \frac{1}{r} \frac{\partial(r \rho v u)}{\partial r} + \frac{1}{r} \frac{\partial(\rho v v)}{\partial \varphi} + \frac{\partial(\rho v w)}{\partial z} + \frac{\rho u v}{r} = \\ -\frac{1}{r} \frac{\partial \pi}{\partial \varphi} + \frac{1}{r} \frac{\partial(r \tau_{\varphi r})}{\partial r} + \frac{\tau_{\varphi r}}{r} + \frac{1}{r} \frac{\partial \tau_{\varphi\varphi}}{\partial \varphi} + \frac{\partial \tau_{\varphi z}}{\partial z} \end{aligned} \quad (2.34)$$

$$\begin{aligned} \frac{\partial(\rho w)}{\partial t} + \frac{1}{r} \frac{\partial(r \rho w u)}{\partial r} + \frac{1}{r} \frac{\partial(\rho w v)}{\partial \varphi} + \frac{\partial(\rho w w)}{\partial z} = \\ -\frac{\partial \pi}{\partial z} + \frac{4}{D} \tau_w + \frac{1}{r} \frac{\partial(r \tau_{zr})}{\partial r} + \frac{1}{r} \frac{\partial \tau_{z\varphi}}{\partial \varphi} + \frac{\partial \tau_{zz}}{\partial z} \end{aligned} \quad (2.35)$$

2.3.2 Thermally fully developed conditions

In a flow through a straight pipe undergoing a constant heating or cooling induced by a positive or negative mean wall heat flux \bar{q}_w , the wall and fluid bulk temperatures T_w and T_b , respectively, are continuously increasing or decreasing along the axial direction z . As the material properties of the fluid are function of temperature, this circumstance would consequently violate any assumption of periodicity and fully developed conditions, as the cross-sectional mean temperature (or equivalently the bulk temperature) at the end of the pipe will always lead to material properties, which are different from the corresponding values at the entrance. Fully developed conditions can be still assumed, if the temperature difference between the pipe entrance and exit is sufficiently small, so that the temperature-dependent axial variation of the mean material properties can be neglected. The last assumption is of particular importance for the molecular viscosity, which in liquids generally exhibits the strongest relative variation with respect to its reference value.

The thermally fully developed conditions shall be tackled by first introducing a bulk enthalpy $h_b(z)$, defined as

$$h_b(z) = \frac{1}{\dot{m}} \int_A \rho(r, \varphi, z, t) w(r, \varphi, z, t) h(r, \varphi, z, t) dA \quad (2.36)$$

and a mean wall enthalpy \bar{h}_w . In Eq. (2.36), \dot{m} represents the mass flow rate over a cross section $A = D\pi^2/4$, which is computed as

$$\dot{m} = \int_A \rho w dA. \quad (2.37)$$

For the considered heating or cooling with constant mean wall heat flux $\pm\bar{q}_w$, the flow is thermally fully developed if

$$\frac{\partial(\bar{h}_w - h_b(z))}{\partial z} = 0, \quad (2.38)$$

implying a constant difference between \bar{h}_w and h_b along the axis of the pipe. Due to the constant wall heat flux, both the wall and bulk enthalpy, linearly increase or decrease along the axial coordinate z of the pipe, according to the sign of the imposed wall heat flux, as schematically represented in Fig. 2.4.

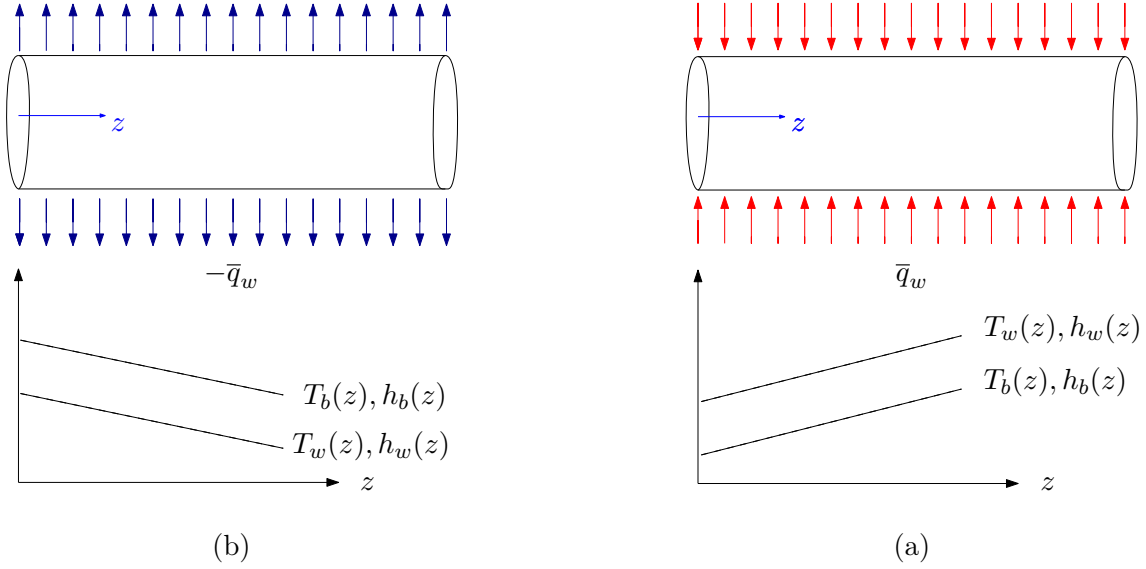


Figure 2.4: Cooled (a) and heated (b) fully developed pipe flow

Due to the neglect of the axial variation of the mean material properties, the relation (2.38) can be rewritten in terms of a axial derivative of the bulk-to-wall temperature difference

$$\frac{\partial(\bar{T}_w - T_b(z))}{\partial z} = 0. \quad (2.39)$$

The conditions (2.38) and (2.39) allow for a reformulation of Eq. (2.17), introducing the local enthalpy difference χ and local temperature difference θ with respect to their wall values

$$\chi(r, \varphi, z, t) = \bar{h}_w(z) - h(r, \varphi, z, t), \quad (2.40)$$

$$\theta(r, \varphi, z, t) = \bar{T}_w(z) - T(r, \varphi, z, t). \quad (2.41)$$

Using the new variables χ and θ , the transport equation for enthalpy becomes

$$\begin{aligned} \rho \frac{\partial \chi}{\partial t} + \rho \frac{1}{r} \frac{\partial(r\chi u)}{\partial r} + \rho \frac{1}{r} \frac{\partial(\chi v)}{\partial \varphi} + \rho \frac{\partial(\chi w)}{\partial z} - \rho \chi \nabla \cdot \mathbf{U} = \\ \frac{1}{r} \frac{\partial}{\partial r} \left(r \lambda \frac{\partial \theta}{\partial r} \right) + \frac{1}{r} \frac{\partial}{\partial \varphi} \left(\frac{\lambda}{r} \frac{\partial \theta}{\partial \varphi} \right) + \frac{\partial}{\partial z} \left(\lambda \frac{\partial \theta}{\partial z} \right) + \rho w \frac{d\bar{h}_w}{dz} \end{aligned} \quad (2.42)$$

As follows from Eqs. (2.38) and (2.39), equation (2.42) may be solved for χ and θ using periodic boundary conditions

$$\begin{aligned} \chi(r, \varphi, z) &= \chi(r, \varphi, z + L), \\ \theta(r, \varphi, z) &= \theta(r, \varphi, z + L). \end{aligned} \quad (2.43)$$

The fully developed thermal state associated with Eq. (2.38) also implies a constant relative bulk enthalpy difference $\chi_b = \text{const}$, and we may write

$$\frac{dh_b}{dz} = \frac{d\bar{h}_w}{dz}. \quad (2.44)$$

Relation (2.44) can be further used to express the forcing term in Eq. (2.42) in terms of the known mean wall heat flux. Referring to a energy balance applied to a infinitesimal cylinder of length dz , it can be stated

$$\dot{m} \left(\frac{dh_b}{dz} dz \right) = \bar{q}_w D \pi dz, \quad (2.45)$$

which further leads to

$$\frac{dh_b}{dz} = \frac{\bar{q}_w D \pi}{\dot{m}}. \quad (2.46)$$

Making use of relation (2.46) the transport equation for enthalpy difference χ can be finally formulated as:

$$\begin{aligned} & \frac{\partial \chi}{\partial t} + \frac{1}{r} \frac{\partial(r\chi u)}{\partial r} + \frac{1}{r} \frac{\partial(\chi v)}{\partial \varphi} + \frac{\partial(\chi w)}{\partial z} - \chi \nabla \cdot \mathbf{U} = \\ & \frac{1}{\rho} \left[\frac{1}{r} \frac{\partial}{\partial r} \left(r \lambda \frac{\partial \theta}{\partial r} \right) + \frac{1}{r} \frac{\partial}{\partial \varphi} \left(\lambda \frac{\partial \theta}{\partial \varphi} \right) + \frac{\partial}{\partial z} \left(\lambda \frac{\partial \theta}{\partial z} \right) \right] + w \frac{\bar{q}_w D \pi}{\dot{m}} \end{aligned} \quad (2.47)$$

Equation (2.47) is solved for χ , which is used to compute the local temperature $T(r, \varphi, z, t)$ as lower boundary of the integral

$$\chi(r, \varphi, z, t) = \int_{T(r, \varphi, z, t)}^{\langle T_w \rangle} c_p(\tilde{T}) d\tilde{T}. \quad (2.48)$$

In the integral (2.48) a mean value of the wall temperature $\langle T_w \rangle$, defined as

$$\langle T_w \rangle = \frac{1}{2} (T_{w,in} + T_{w,out}), \quad (2.49)$$

is used as upper boundary in consistence with the neglect of axial variation of mean material properties. $T_{w,in}$ and $T_{w,out}$ represent the inlet and outlet averaged wall temperature, respectively.

In the present formulation $T_{w,out}$ is prescribed, and $T_{w,in}$ is retrieved from $T_{w,out}$ by introducing a domain average specific heat capacity $\langle c_p \rangle$, which is used to further rewrite Eq. (2.39) as

$$\frac{dT_w}{dz} = \frac{dT_b}{dz} = \frac{dh_b}{\langle c_p \rangle dz}. \quad (2.50)$$

Using Eq. (2.46) and integrating along Eq. (2.50) along z leads to

$$T_w(z) = T_{w,out} + (z - L) \frac{\bar{q}_w D \pi}{\langle c_p \rangle \dot{m}}, \quad (2.51)$$

which, evaluated at $z = 0$, yields $T_{w,in} = T_{w,out} - L \frac{\bar{q}_w D \pi}{\langle c_p \rangle \dot{m}}$.

For the considered heated and cooled cases with varying material properties, the wall temperature at the exit of the pipe is always assumed as a common reference temperature

$$T_{ref} = T_w(z = L) = T_{w,out} = 344.77 \text{ K}. \quad (2.52)$$

2.3.3 Non-dimensional formulation

In the considered fully developed turbulent heated or cooled pipe flow, associated with periodic axial boundary conditions, the governing equations introduced in Eqs. (2.33), (2.34), (2.35) and (2.47) can be rewritten as a universal non-dimensional formulation by rescaling all variables, coordinates and material properties. For the latter, the following reference material properties are introduced

$$\mu_0 = \mu(T_{ref}), \quad \lambda_0 = \lambda(T_{ref}), \quad c_{p,0} = c_p(T_{ref}), \quad \rho_0 = \rho(T_{ref}), \quad (2.53)$$

using the wall temperature at the exit of the pipe as reference, as stated in Eq. (2.52). Further scales used as reference are the friction velocity w_τ , the friction temperature T_τ , and a friction enthalpy h_τ , defined as

$$w_\tau = \sqrt{\frac{\tau_0}{\rho_0}}, \quad T_\tau = \frac{\bar{q}_w}{\rho_0 c_{p,0} w_\tau}, \quad h_\tau = c_{p,0} T_\tau, \quad (2.54)$$

respectively. Using these scales, the following non-dimensional variables can be defined

$$\begin{aligned} u_i^+ &= \frac{u_i}{w_\tau}, & \chi^+ &= \frac{\chi}{h_\tau}, & \theta^+ &= \frac{\theta}{T_\tau}, \\ q_i^+ &= \frac{q_i}{q_w}, & \tau_{ij}^+ &= \frac{\tau_{ij}}{\tau_w}, & \dot{m}^+ &= \frac{\dot{m}}{\rho_w w_\tau D^2 \pi}, & \pi^+ &= \frac{\pi}{\rho w_\tau^2}. \end{aligned}$$

Correspondingly, the spatial and temporal coordinates, and the differential operators are non-dimensionalized to

$$r^* = \frac{r}{D}, \quad z^* = \frac{z}{D}, \quad t^* = \frac{t w_\tau}{D}, \quad \nabla^* = D \nabla,$$

respectively. The proposed rescaling produces the following non-dimensional representation of Eqs. (2.19), (2.33), (2.34), (2.35), (2.47)

- non-dimensional mass conservation equation:

$$\frac{\partial \rho^*}{\partial t^*} + \frac{1}{r^*} \frac{\partial(r^* \rho^* u^+)}{\partial r^*} + \frac{1}{r^*} \frac{\partial(\rho^* v^+)}{\partial \varphi} + \frac{\partial(\rho^* w^+)}{\partial z^*} = 0 \quad (2.55)$$

- non-dimensional momentum conservation equation in r -direction:

$$\begin{aligned} \frac{\partial(\rho^* u^+)}{\partial t^*} + \frac{1}{r^*} \frac{\partial(r^* \rho^* u^+ u^+)}{\partial r^*} + \frac{1}{r^*} \frac{\partial(\rho^* u^+ v^+)}{\partial \varphi} + \frac{\partial(\rho^* u^+ w^+)}{\partial z^*} - \frac{\rho^* v^+ v^+}{r^*} = \\ - \frac{\partial \pi^+}{\partial r^*} + \frac{1}{Re_\tau} \left[\frac{1}{r^*} \frac{\partial(r^* \tau_{rr}^+)}{\partial r^*} + \frac{1}{r^*} \frac{\partial(r^* \tau_{r\varphi}^+)}{\partial \varphi} - \frac{\tau_{\varphi\varphi}^+}{r^*} + \frac{\partial \tau_{rz}^+}{\partial z^*} \right] \end{aligned} \quad (2.56)$$

- non-dimensional momentum conservation equation in φ -direction:

$$\begin{aligned} \frac{\partial(\rho^* v^+)}{\partial t^*} + \frac{1}{r^*} \frac{\partial(r^* \rho^* v^+ u^+)}{\partial r^*} + \frac{1}{r^*} \frac{\partial(\rho^* v^+ v^+)}{\partial \varphi} + \frac{\partial(\rho^* v^+ w^+)}{\partial z^*} + \frac{\rho^* u^+ v^+}{r^*} = \\ - \frac{1}{r^*} \frac{\partial \pi^+}{\partial \varphi} + \frac{1}{Re_\tau} \left[\frac{1}{r^*} \frac{\partial(r^* \tau_{\varphi r}^+)}{\partial r^*} + \frac{\tau_{\varphi r}^+}{r^*} + \frac{1}{r^*} \frac{\partial \tau_{\varphi\varphi}^+}{\partial \varphi} + \frac{\partial \tau_{\varphi z}^+}{\partial z^*} \right] \end{aligned} \quad (2.57)$$

- non-dimensional momentum conservation equation in z -direction:

$$\begin{aligned} \frac{\partial(\rho^* w^+)}{\partial t^*} + \frac{1}{r^*} \frac{\partial(r^* \rho^* w^+ u^+)}{\partial r^*} + \frac{1}{r^*} \frac{\partial(\rho^* w^+ v^+)}{\partial \varphi} + \frac{\partial(\rho^* w^+ w^+)}{\partial z^*} = \\ -\frac{\partial \pi^+}{\partial z^*} + 4 + \frac{1}{Re_\tau} \left[\frac{1}{r^*} \frac{\partial(r^* \tau_{zr}^+)}{\partial r^*} + \frac{1}{r^*} \frac{\partial \tau_{z\varphi}^+}{\partial \varphi} + \frac{\partial \tau_{zz}^+}{\partial z^*} \right] \end{aligned} \quad (2.58)$$

- non-dimensional transport equation for the enthalpy difference:

$$\begin{aligned} \frac{\partial \chi^+}{\partial t^*} + \frac{1}{r^*} \frac{\partial(r^* \chi^+ u^+)}{\partial r^*} + \frac{1}{r^*} \frac{\partial(\chi^+ v^+)}{\partial \varphi} + \frac{\partial(\chi^+ w^+)}{\partial z^*} - \chi^+ (\nabla^* \cdot \mathbf{U}^+) = \\ \frac{1}{\rho^* Pr_w Re_\tau} \left[\frac{1}{r^*} \frac{\partial}{\partial r^*} (r^* q_r^+) + \frac{1}{r^*} \frac{\partial}{\partial \varphi} \left(\frac{\lambda^*}{r^*} \frac{\partial \theta^+}{\partial \varphi} \right) + \frac{\partial}{\partial z^*} \left(\lambda^* \frac{\partial \theta^+}{\partial z^*} \right) \right] + \frac{w^+}{\dot{m}^*} \end{aligned} \quad (2.59)$$

In Eq. (2.56), (2.57), (2.58) the non-dimensional stress tensor components appear on the right hand side of the three governing equations for momentum under the sign of divergence. These viscous stress tensor components are defined in cylindrical coordinates as follows:

$$\tau_{rr}^+ = \mu^* \left[2 \frac{\partial u^+}{\partial r^*} - \frac{2}{3} (\nabla^* \cdot \mathbf{U}^+) \right] \quad (2.60)$$

$$\tau_{\varphi r}^+ = \tau_{r\varphi}^+ = \mu^* \left[r^* \frac{\partial}{\partial r^*} \left(\frac{v^+}{r^*} \right) + \frac{1}{r^*} \frac{\partial u^+}{\partial \varphi} \right] \quad (2.61)$$

$$\tau_{zr}^+ = \tau_{rz}^+ = \mu^* \left[\frac{\partial w^+}{\partial r^*} + \frac{\partial u^+}{\partial z^*} \right] \quad (2.62)$$

$$\tau_{\varphi\varphi}^+ = \mu^* \left[2 \left(\frac{1}{r^*} \frac{\partial v^+}{\partial \varphi} + \frac{u^+}{r^*} \right) - \frac{2}{3} (\nabla^* \cdot \mathbf{U}^+) \right] \quad (2.63)$$

$$\tau_{z\varphi}^+ = \tau_{\varphi z}^+ = \mu^* \left[\frac{\partial v^+}{\partial z^*} + \frac{1}{r^*} \frac{\partial w^+}{\partial \varphi} \right] \quad (2.64)$$

$$\tau_{zz}^+ = \mu^* \left[2 \frac{\partial w^+}{\partial z^*} - \frac{2}{3} (\nabla^* \cdot \mathbf{U}^+) \right] \quad (2.65)$$

Analogously, in Eq. (2.59), the non-dimensional conductive heat flux components appearing on the right hand side of the governing equation for the non-dimensional enthalpy difference are defined as follows:

$$q_r^+ = -\lambda^* \frac{\partial \theta^+}{\partial r^*}, \quad (2.66)$$

$$q_\varphi^+ = -\frac{\lambda^*}{r^*} \frac{\partial \theta^+}{\partial \varphi}, \quad (2.67)$$

$$q_z^+ = -\lambda^* \frac{\partial \theta^+}{\partial z^*}. \quad (2.68)$$

The non-dimensional wall friction Reynolds and Prandtl numbers are defined as

$$Re_\tau = \frac{\rho_w D w_\tau}{\mu_w}, \quad (2.69)$$

$$Pr_w = \frac{\mu_w c_{p,w}}{\lambda_w}, \quad (2.70)$$

respectively. They are always based on the wall conditions, specified by the wall temperature at the exit $T_{w,out} = T_{ref}$ used as a reference state. Assuming always the same reference temperature T_{ref} ensures a consistent and meaningful comparison between the different heated and cooled cases.

Lastly, the introduction of non-dimensional $()^+$ - units and the definition of Re_τ and Pr_w , given in Eq. (2.69) and Eq. (2.70), respectively, additionally allows to express the wall shear stress and wall heat flux in terms of skin friction coefficient C_f and the Nusselt number Nu as

$$C_f = \frac{2}{\rho_b^* U_b^{+2}}, \quad (2.71)$$

$$Nu = \frac{Pr_w Re_\tau}{\theta_b^+}. \quad (2.72)$$

The quantities U_b^+ , ρ_b^* , θ_b^+ , defined as

$$\begin{aligned} U_b^+ &= 8 \int_{r^*=0}^{0.5} \langle w^+ \rangle r^* dr^*, \\ \rho_b^* &= 4 \frac{\dot{m}^*}{U_b^+}, \\ \theta_b^+ &= \frac{2}{\bar{c}_p^* \dot{m}^*} \int_{r^*=0}^{0.5} \langle \rho^* w^+ \chi^+ \rangle r^* dr^* \quad \text{with} \quad \bar{c}_p^* = \frac{2}{\dot{m}^*} \int_{r^*=0}^{0.5} \langle \rho^* c_p^* w^+ \rangle r^* dr^*, \end{aligned} \quad (2.73)$$

identify the non-dimensional bulk velocity, bulk density, and bulk temperature difference, respectively.

2.3.4 Thermal Boundary conditions

At the physical wall $r = D/2$, basically three thermal boundary conditions are possible.

Dirichlet thermal boundary condition

This boundary condition prescribes fixed value for the temperature, and equivalently, enthalpy at the wall as $T = T_w$ and $h = h_w$, which remain constant in time. As such, this thermal boundary condition will be referred to as *isothermal*. The Dirichlet thermal boundary condition can be reformulated in terms of the corresponding non-dimensional temperature and enthalpy difference as

$$\theta_w^+ = 0, \quad \chi_w^+ = 0, \quad (2.74)$$

respectively. Accordingly, the fluctuations in enthalpy difference and temperature are zero at the wall boundary, $\chi_w^{+'} = 0$ and $\theta_w^{+'} = 0$, while the instantaneous wall heat flux fluctuates $q_w^{+'} \neq 0$.

Von Neumann thermal boundary condition

The wall heat flux is imposed as invariant in time, while the wall values of the temperature and enthalpy fluctuate. As such, this thermal boundary condition is termed as *isoflux* boundary condition.

Due to Fourier's law, the prescription of a fixed wall heat flux is equivalent to the posture of a fixed constant wall temperature gradient (or enthalpy gradient), written as

$$q_w = \bar{q}_w = - \left(\lambda \frac{\partial T}{\partial r} \right) \Big|_{r=D/2} = \text{const.} \quad (2.75)$$

and equivalently

$$- \left(\frac{\lambda}{c_p} \frac{\partial h}{\partial r} \right) \Big|_{r=D/2} = \text{const.} \quad (2.76)$$

This implies zero fluctuations for the wall heat flux and constitutive derivatives, such that $q'_w = 0$, $\frac{\partial T'}{\partial r} \Big|_{r=D/2} = 0$, $\frac{\partial h'}{\partial r} \Big|_{r=D/2} = 0$ whereas the fluctuations $T' \neq 0$, $h' \neq 0$ are non-zero. Prescribing only the wall gradient is basically not sufficient for specifying the temperature field. This ill-posedness is removed by setting the average wall temperature and enthalpy difference to zero, $\langle \theta_w \rangle_{\varphi,z} = 0$, $\langle \chi_w \rangle_{\varphi,z} = 0$. The Von Neumann boundary condition can be finally summarized in non-dimensionalized representation as follows:

$$\begin{cases} \left(\frac{1}{c_p^*} \frac{\partial \chi^+}{\partial r^*} \right) \Big|_{r^*=1/2} = Re_\tau Pr_w, \\ \langle \chi_w^+ \rangle_{\varphi,z} = 0 \end{cases} \quad (2.77)$$

or equivalently

$$\begin{cases} \frac{\partial \theta^+}{\partial r^*} \Big|_{r^*=1/2} = Re_\tau Pr_w. \\ \langle \theta_w^+ \rangle_{\varphi,z} = 0 \end{cases} \quad (2.78)$$

Coupled solution between solid and fluid phase

In this case the thermal boundary condition at the wall is provided by the solution of a conduction problem solved in the neighbouring solid wall with thickness d , heat capacity c_s , heat conductivity λ_s and density ρ_s . The outer wall of the solid layer is assumed as adiabatic, whereas the inner one represents the interface between the solid and the fluid, where the thermal interface conditions are imposed. The solid layer is internally heated with a homogeneously distributed volumetric heat source \dot{q} , whose strength is specified in consistence with the mean wall heat flux \bar{q}_w , actually applied to the fluid phase. The coupled solution of the fluid and solid phase, as sketched in Fig. 2.5, is usually termed *Conjugate heat transfer analysis*.

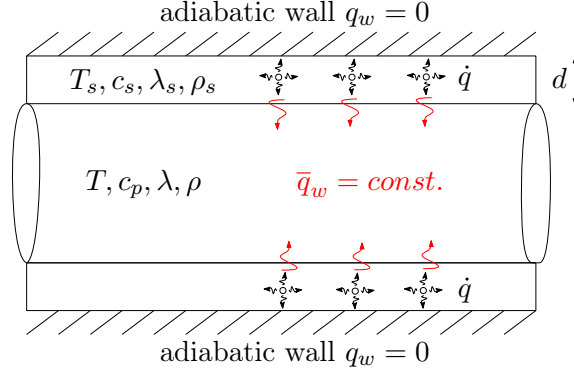


Figure 2.5: Geometry of conjugate heat transfer problem

Introducing the non dimensional parameter $K = \sqrt{\frac{\rho c_p \lambda}{\rho_s c_s \lambda_s}}$ (thermal activity ratio), $G = \frac{\alpha}{\alpha_s}$ (thermal diffusivity ratio), $d^* = \frac{d}{D}$ (non-dimensional thickness of the solid wall), the conduction problem in the solid wall may be non-dimensionalized to

$$\left\{ \begin{aligned} \frac{\partial \theta_s^+}{\partial t^*} &= \frac{1}{Gr_r Pr_w} \nabla^{*2} \theta_s^+ - \frac{K}{\sqrt{G} d^* (1 + d^*)} \end{aligned} \right. \quad (2.79)$$

$$\left\{ \begin{aligned} \theta_s^+ \Big|_{r^*=0.5} &= \theta^+ \Big|_{r^*=0.5} \end{aligned} \right. \quad (2.80)$$

$$\left\{ \begin{aligned} K \sqrt{G} \frac{\partial \theta_s^+}{\partial r^*} \Big|_{r^*=0.5} &= \frac{\partial \theta^+}{\partial r^*} \Big|_{r^*=0.5} \end{aligned} \right. \quad (2.81)$$

which is solved for the non-dimensional temperature difference $\theta_s^+ = \frac{T_s - T_w(z)}{T_\tau}$. The last term of the right hand side in Eq. (2.79), represents the non-dimensional internal heat source, whereas Eqs. (2.80)-(2.81) represent the continuity constraint of temperature and heat flux across the solid-fluid interface at $r^* = 0.5$.

2.4 Turbulent flow in a pipe with an abrupt circular expansion

When a fully developed turbulent pipe flow experiences a sudden change in its wall boundaries, for instance, due to an abrupt increase in the pipe diameter, the statistical homogeneity in the axial direction is lost. In this case, the statistical average operator $\langle \rangle$ will be therefore applied only in time and in azimuthal direction:

$$\langle \rangle = \overline{(\quad)} = \langle \rangle_{\varphi, t} \quad (2.82)$$

The flow through a pipe with an abrupt expansion is basically an axisymmetric representative of the widely investigated planar flow over 90° backward facing steps with homogeneous spanwise direction. The sharp corner triggers a separation of the dynamic boundary layer, the formation of a shear dominated region, where intense turbulent mixing occurs, and the formation of a recirculating bubble beneath, as exemplarily sketched in Fig. 2.6.

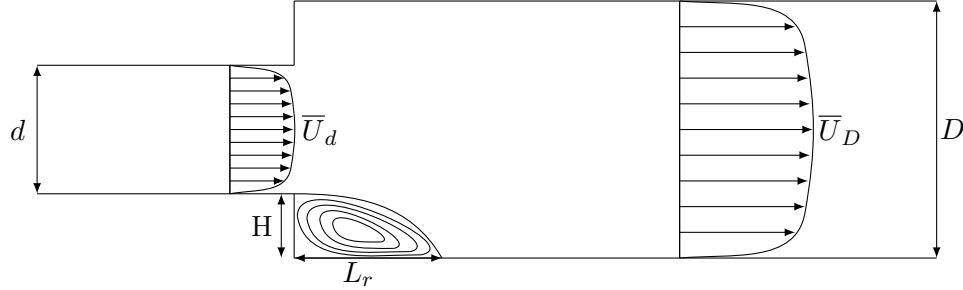


Figure 2.6: Sketch of a turbulent flow in a pipe with a sudden circular expansion

Downstream of the separation bubble the flow reattaches and, if the pipe is sufficiently long, fully developed and equilibrium conditions can be reached again. The reattachment length spanning the separated backflow region is typically measured in multiples of step heights $H = (D - d)/2$. The extension of the reattachment length L_r is strongly influenced by the step height H and by the inlet bulk Reynolds number Re_d . More specifically, it is acknowledged that the higher Re_d , the shorter the reattachment length. On the contrary, a higher step height H usually leads to an increased L_r in the downstream pipe, with a further enhancement of the recirculating motion after the step (Baughn *et al.* (1989), Chieng and Launder (1980), Zemanick and Dougall (1970)).

2.4.1 Thermal boundary conditions in the downstream pipe

The investigation of the heat transfer in the turbulent flow past an abrupt expansion of a pipe was carried out in the present work considered two different thermal boundary conditions. In the first setting a mixture of glysantine and water at 50/50 Vol% with temperature-depending molecular viscosity $\mu(T)$ is used as operating fluid. The remaining material properties, namely density ρ , the heat conductivity λ and the specific heat coefficient at constant pressure c_p are fixed at their corresponding reference values at $T_w = 344 \text{ K}$. As sketched in Fig. 2.7, a uniform constant inlet temperature profile $T_i = 331 \text{ K}$ is imposed at the inlet cross-section and at the wall of the upstream pipe. Hence, no temperature gradient in the wall-normal direction can be established in the upstream region of the narrow pipe.

At the wall of the downstream pipe, a uniform wall temperature $T_w > T_i$ is prescribed. At the outlet cross-section a zero axial temperature gradient is applied.

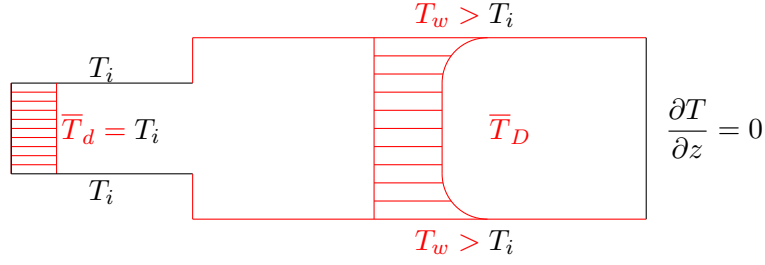


Figure 2.7: Setting with isothermal boundary condition in the downstream pipe

Using the isothermal boundary condition through the posture of a fixed uniform T_w in the downstream pipe enables the definition of a constant reference wall Prandtl number $Pr_w = 10$ for the considered working fluid.

The second thermal boundary setting considered used air with constant material properties at molecular Prandtl number $Pr = 0.7$ as working fluid. A uniform constant temperature $T_i = 311\text{ K}$ is applied again both at the cross-inlet section and at the wall of the narrow upstream pipe. Different from the first setting above, a uniform fixed heat flux q_w is applied at the wall of the downstream pipe (isoflux thermal boundary condition), as sketched in Fig. 2.8. At the outlet section, a zero axial temperature gradient is applied again.

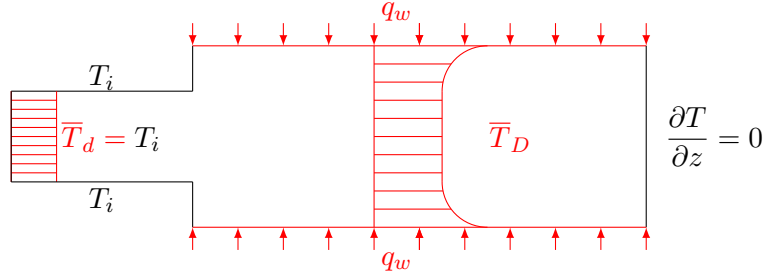


Figure 2.8: Setting with isoflux thermal boundary condition in the downstream pipe

2.5 Fluid material properties

In many engineering applications the convective heat transfer is carried by liquid coolant with high molecular Prandtl number. A 50/50 Vol% mixture of water and glyserine is assumed as working fluid for all numerical and experimental investigations in the present work, whenever real fluid behaviour is accounted for.

The relevant material properties, being the heat conductivity λ , the specific heat capacity c_p , the fluid density ρ and the molecular viscosity μ , are assumed as dependent only on the temperature. Their functional dependencies, which have been derived by fitting experimental data in the considered range of temperatures, as shown in Fig. 2.9 with the coefficients listed in Table 2.1, may bring further difficulties under the computational standpoint. The variation of temperature occurring in some region of the flow field might induce a significant change in material properties, which in turn, particularly through the

molecular viscosity μ , may strongly influence momentum transfer, so that it is harder to reach a stable converged numerical simulation.

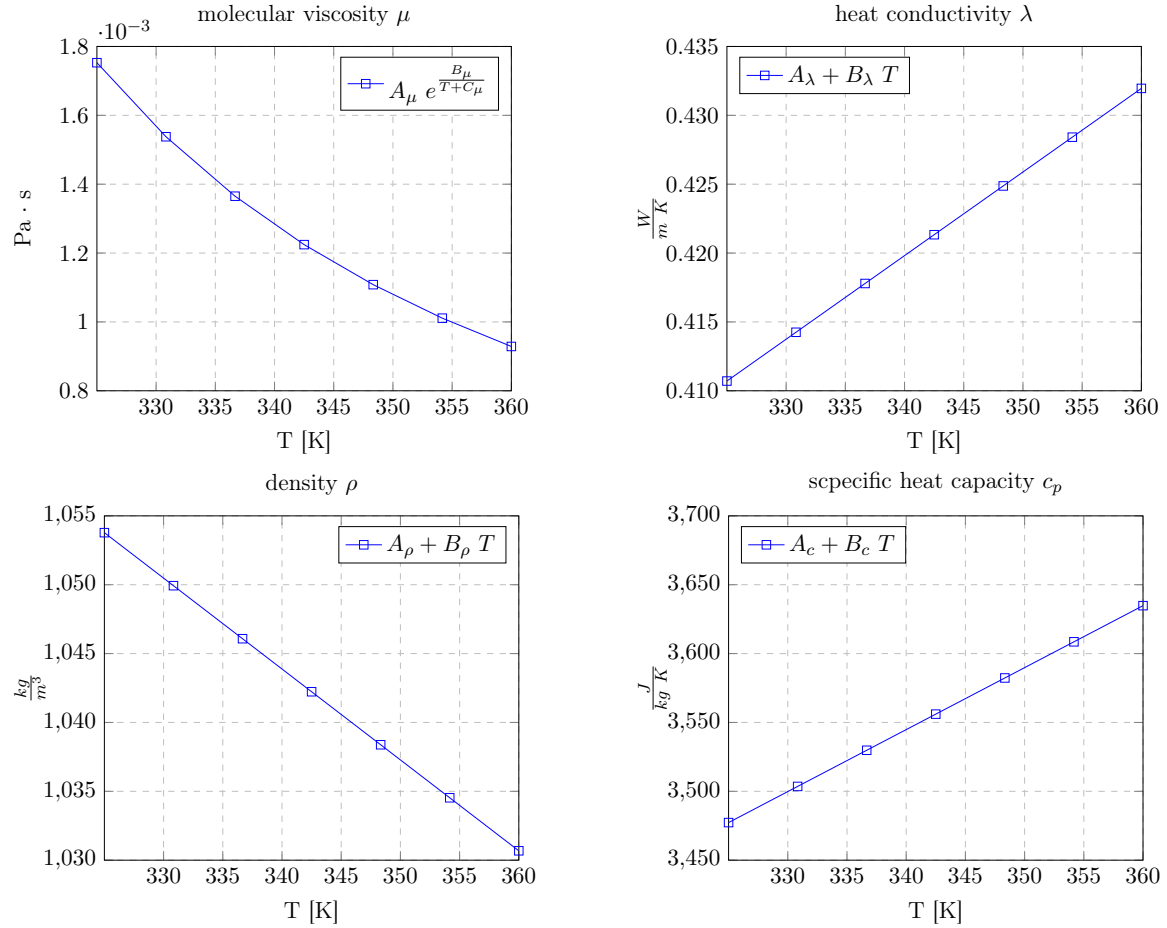


Figure 2.9: Variation of fluid properties with temperature

Table 2.1: Coefficients used in Fig. 2.9

	A	B	C
ϱ	1268.28 $[\frac{\text{kg}}{\text{m}^3}]$	-0.66 $[\frac{\text{kg}}{\text{m}^3 \text{K}}]$	
λ	0.2134 $[\frac{\text{W}}{\text{m K}}]$	$6.1 \cdot 10^{-4}$ $[\frac{\text{W}}{\text{m K}^2}]$	
c_p	2014.8 $[\frac{\text{J}}{\text{kg K}}]$	45.0 $[\frac{\text{J}}{\text{kg K}^2}]$	
μ	$1.1 \cdot 10^{-4}$ $[\frac{\text{kg}}{\text{m s}}]$	325.85 $[\text{K}]$	-207.30 $[\text{K}]$

Chapter 3

Methodology

This chapter is devoted to the description of the methods and the simulation techniques used to investigate computationally the turbulent heat transfer at high molecular Prandtl number in fully developed and non-developed conditions. Additionally, a complementary overview of the experimental setup used for the validation of DNS and LES results will be given.

3.1 Direct numerical simulation of turbulent flows

Any turbulent flow is characterized by a wide range of scales of the turbulent structures, often referred to as eddies, which differ in size and lifetime. The higher the characteristic Reynolds number of the flow, the more pronounced the scale separation, which will occur between the larger and the smaller eddies. In a Direct Numerical Simulation (DNS) the entire spectrum of relevant scales is resolved by using accurate time and space discretization schemes and a grid fine enough to capture appropriately the smallest eddies. Therefore, no turbulence model is needed, as the turbulent motion of the flow field is captured in its entirety. In a turbulent flow as described by a DNS the larger eddies are typically responsible for carrying most of the kinetic energy in the flow field. The turbulent energy cascades down from the larger eddies to the smaller and smaller ones inside the so called inertial subrange, until they get finally dissipated into heat due to viscous forces, in accordance to the concept of energy cascade developed by Richardson.

The length scale η_K at which turbulent energy dissipation occurs is termed Kolmogorov scale, defined as

$$\eta_K \sim \left(\frac{\nu^3}{\epsilon} \right)^{1/4}, \quad (3.1)$$

where ν is the kinematic viscosity and ϵ the dissipation rate of turbulent kinetic energy. Equivalently, in frequency space, the wave number associated with the Kolmogorov scale is defined as

$$k_\eta = 2\pi/\eta_K. \quad (3.2)$$

A fully resolved DNS by definition should employ a grid size Δ , which is sufficiently small to resolve all the scales arising in the turbulent field down to η_K . However, in many studies in the literature, a grid size $\Delta \approx 5 - 10 \eta_K$ is still considered as acceptable to resolve

the relevant portion of the small scale motion, such that the simulations are regarded as spatially resolved. For the case of isotropic turbulence, where no walls are present, it can be shown (Pope (2000)) that the minimum number of grid points needed to capture all relevant scales as $N \approx Re_D^{9/4}$. For typical Reynolds number in aerodynamical application, $Re_D > 10^5$, the number of points would be excessively high to perform DNS, especially with complex geometries. Therefore, a computationally much cheaper turbulence modelling approach like RANS is preferred in such case.

When heat transfer is considered as well, some further relevant thermal scales come into play. In particular, the smallest relevant scales arising in the turbulent thermal field may be related to η_K through the molecular thermal diffusivity α . This argumentation, proposed by Batchelor (1959), leads to the definition of the Batchelor length scale η_B as the smallest thermal scale written as

$$\eta_B = \frac{\eta_K}{\sqrt{Pr}}. \quad (3.3)$$

For DNS of turbulent flows with high molecular Prandtl number ($Pr \gg 1$), the requirement for the grid resolution evidently becomes more stringent to capture the smallest turbulent thermal scales.

3.2 Large Eddy Simulation of turbulent flows

In a typical turbulent energy spectrum, as the one exemplarily depicted in Fig. 3.1, some relevant regions and length scales, or equivalently wave numbers, are to be recognized. The integral length scale l denotes the length scale of the larger eddies, which carry the major part of kinetic energy of the flow field and are generally strongly anisotropic, as they are markedly influenced by the boundaries (like possibly walls) of the flow.

In the inertial subrange, the rate at which energy is transferred from larger to smaller eddies is driven by the advective exchange of momentum. The rate of this energy transfer is determined by the turbulent kinetic energy dissipation rate ϵ . The extension of the inertial subrange in the turbulent spectra becomes larger, as the characteristic Reynolds number of the flow increases, enhancing in this way the scale separation. The upper limit of the inertial subrange is marked by the Kolmogorov length scale η_K , beyond which the spectral energy decays rapidly, as the turbulent kinetic energy is dissipated due to the dominance of the viscous forces.

As opposed to DNS, Large Eddy Simulations (LES) of turbulent flows applies a grid size $\Delta \gg \eta_K$, which implicitly determines the size of the smallest resolvable eddies, introducing in this way a cut-off wave number k_Δ well below k_η , where the dissipative range of the spectrum begins. The cut-off wave number represents therefore the upper limit of the spectrum, which can be directly resolved with the adopted grid size. In LES terminology, the resolved larger structures in a turbulent field are usually termed *resolved* scales, whereas the smaller structures of motions, whose size falls below the grid size, are designated as *unresolved* scales, or subgrid-scale components.

In order to describe the missed dynamic effect of the small unresolved eddies on the resolved flow field and on the larger eddies, a subgrid-scale (sgs) model is adopted in LES. The sgs model is essentially intended to provide an appropriate amount of turbulent kinetic energy dissipation, which is associated with the exchange of momentum with the unresolved

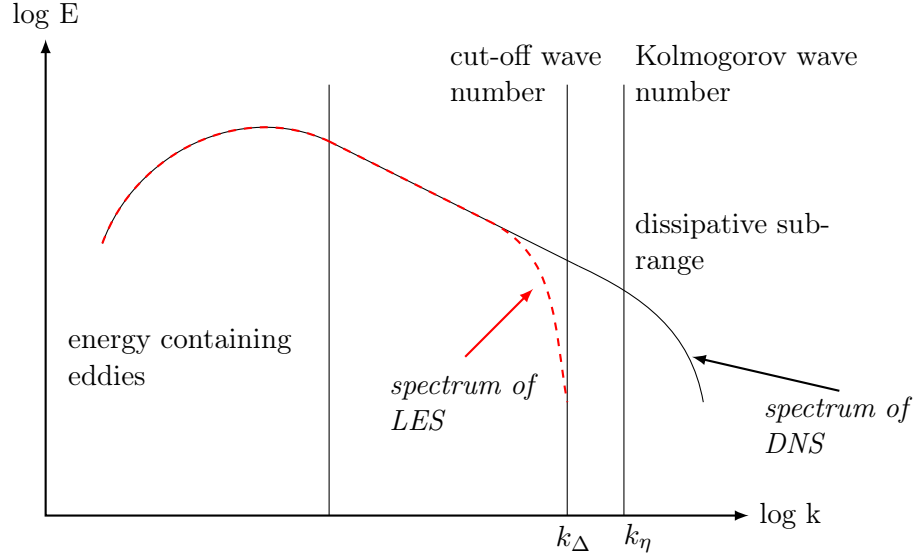


Figure 3.1: Spectrum of a turbulent signal as function of wave number

eddies and among them. Formally, the mathematical formulation, which enables LES to solve only for the largest scales of motion and model the contribution of the unresolved eddies, is based on a spatial filtering procedure.

3.2.1 Spatial filtering

The spatial filtering performed in LES is based on the convolution with a kernel function $G(\mathbf{x}, \xi)$, which would yield for an arbitrary quantity $\phi(\mathbf{x}, t)$ its filtered counterpart $\tilde{\phi}(\mathbf{x}, t)$

$$\tilde{\phi}(\mathbf{x}, t) = \int_D G(\mathbf{x}, \xi) \phi(\mathbf{x} - \xi, t) d\xi. \quad (3.4)$$

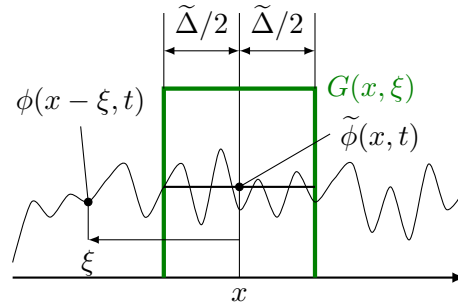


Figure 3.2: One-dimensional spatial filtering procedure in LES

Typically, normalized kernel functions are used, such that

$$\int_D G(\mathbf{x}, \xi) d\xi = 1 \quad (3.5)$$

which essentially prevents that the filtering procedure violates any conservation principle. In this study G will be assumed as a homogeneous top-hat kernel, which is constant within its local support and zero elsewhere. As exemplarily shown in Fig. 3.2 for a simple spatially one-dimensional filtering, the kernel function would read

$$\begin{cases} G(x, \xi) = \frac{1}{\tilde{\Delta}} & \text{for } \xi \in \left[x - \frac{\tilde{\Delta}}{2}, x + \frac{\tilde{\Delta}}{2} \right] \\ G(x, \xi) = 0 & \text{else.} \end{cases} \quad (3.6)$$

When dealing with variable density flow it is useful to introduce the concept of density-weighted, or Favre, filtering in order to avoid unclosed terms in the governing equations, which would arise from the turbulent fluctuating density. The Favre filtered representation of an arbitrary variable ϕ is defined as

$$\bar{\phi} = \frac{\widetilde{\rho\phi}}{\widetilde{\rho}}, \quad (3.7)$$

where $\widetilde{(\)}$ represents again the spatial filtering procedure already introduced in Eq. (3.4). Due to the weak variation of the density with temperature in the presently considered operating liquid, the difference between the density-weighted (Favre) to the unweighted filtering, (3.4), is negligibly small, so that $\bar{\phi} \approx \widetilde{\phi}$.

Applying the Favre filtering on the conservation equations, Eqs. (2.8)-(2.10), their filtered representations solved in LES can be finally expressed as

$$\frac{\partial \widetilde{\rho}}{\partial t} + \nabla \cdot (\widetilde{\rho} \bar{\mathbf{U}}) = 0 \quad (3.8)$$

$$\frac{\partial (\widetilde{\rho} \bar{\mathbf{U}})}{\partial t} + \nabla \cdot (\widetilde{\rho} \bar{\mathbf{U}} \bar{\mathbf{U}}) = -\nabla \bar{P} + \nabla \cdot (\widetilde{\boldsymbol{\tau}} - \boldsymbol{\tau}_{sgs}) \quad (3.9)$$

$$\frac{\partial (\widetilde{\rho} \bar{h})}{\partial t} + \nabla \cdot (\widetilde{\rho} \bar{h} \bar{\mathbf{U}}) = \nabla \cdot (-\widetilde{\mathbf{q}} - \mathbf{q}_{sgs}) \quad (3.10)$$

The filtered viscous stress tensor appearing in Eq. (3.9) is defined as:

$$\widetilde{\boldsymbol{\tau}} = 2\mu \left(\widetilde{\mathbf{S}} - \frac{2}{3} \mathbb{I} \nabla \cdot \widetilde{\mathbf{U}} \right), \quad (3.11)$$

where the resolved strain rate tensor $\widetilde{\mathbf{S}} = \frac{1}{2}(\nabla \widetilde{\mathbf{U}} + (\nabla \widetilde{\mathbf{U}})^T)$ has been used.

The filtered conductive heat flux occurring in Eq. (3.10) reads

$$\widetilde{\mathbf{q}} = -\lambda \nabla \widetilde{T}. \quad (3.12)$$

It is noted, that the fluctuations of the density and material properties induced by the turbulent fluctuating temperature have been neglected in these filtered molecular flux terms.

$\boldsymbol{\tau}_{sgs}$ and \mathbf{q}_{sgs} define the unresolved subgrid-scale (sgs) stress tensor and heat flux vector, respectively, arising from the spatial filtering of the non-linear advection terms:

$$\boldsymbol{\tau}_{sgs} = \widetilde{\rho} (\bar{\mathbf{U}} \bar{\mathbf{U}} - \bar{\mathbf{U}} \bar{\mathbf{U}}), \quad (3.13)$$

$$\mathbf{q}_{sgs} = \widetilde{\rho} (\bar{\mathbf{U}} \bar{h} - \bar{\mathbf{U}} \bar{h}). \quad (3.14)$$

They represent the unclosed terms in the filtered governing equations for LES, for which a subgrid-scale (sgs) model is needed.

3.2.2 Subgrid-scale (sgs) models

Concerning the modelling of the unresolved scales in momentum, the most common approach is based on the *Boussinesq* hypothesis, which assumes the deviatoric part of the subgrid-scale stress tensor to be perfectly aligned with the resolved strain rate tensor $\tilde{\mathbf{S}}$ as proportional to a scalar quantity, called subgrid-scale (sgs) eddy viscosity ν_{sgs} , in perfect analogy with the viscous stress tensor, such that

$$\tau_{sgs}^d = \tau_{sgs} - \frac{1}{3} \mathbb{I} \, tr[\tau_{sgs}] = -2 \nu_{sgs} \tilde{\mathbf{S}}. \quad (3.15)$$

A similar approach is usually adopted for modelling the subgrid-scale heat flux \mathbf{q}_{sgs} by assuming the latter as perfectly aligned with the the local temperature gradients (*gradient-diffusion* Ansatz), as proportional to a subgrid-scale eddy diffusivity a_{sgs} , such that

$$\frac{\mathbf{q}_{sgs}}{\tilde{\rho} \tilde{c}_p} = -a_{sgs} \nabla \tilde{T} = -\frac{\nu_{sgs}}{Pr_{sgs}} \nabla \tilde{T}, \quad (3.16)$$

where the local eddy diffusivity is related to the local eddy viscosity through the subgrid-scale Prandtl number defined as $Pr_{sgs} = \frac{\nu_{sgs}}{a_{sgs}}$.

It is commonly desired, that the modelled eddy-viscosity ν_{sgs} is, on the one side able to contribute appropriately to the overall dissipation of subgrid-scale kinetic energy, and on the other side, inherently reflects the natural damping of the turbulent motion near the solid walls. Concerning the second feature, the Van Driest (Van Driest (1956)) wall-damping function is often adopted, in order to decrease artificially the sgs eddy viscosity in the vicinity of the wall, if the model formulation for ν_{sgs} is not able to do it by itself. The Van-Driest wall-damping function, generally applied in LES, reads

$$f(y^+) = \left(1 - e^{(-\frac{y^+}{25})} \right), \quad (3.17)$$

where $y^+ = \frac{y w_\tau}{\nu}$ represents the non-dimensional distance from the wall in $()^+$ units.

In the course of past years the sgs models based on the *Boussinesq* hypothesis have become very popular, essentially due to the simplicity of their implementation, which is attractive when LES is used in real technical applications associated with complex geometries. In the following three well established sgs models of this kind will be considered and assessed, namely the Wall-Adapting Local Eddy viscosity model (WALE), as presented in Nicoud and Ducros (1999), the Coherent Structure model (CSM), developed by Kobayashi (2005), and lastly the classical Standard Smagorinsky model (SMAG) as defined in Smagorinsky (1963). All three sgs models build their Ansatz for the sgs eddy viscosity in a similar fashion, based on the same dimensional arguments, relating a subgrid-length scale squared l_{sgs}^2 to a subgrid-time scale t_{sgs} :

$$\nu_{sgs} \approx \frac{l_{sgs}^2}{t_{sgs}} \quad (3.18)$$

- SMAG: The classical Standard Smagorinsky model uses the filter width $\tilde{\Delta}$ as a natural choice for l_{sgs} , whereas the norm of the resolved strain $\|\tilde{\mathbf{S}}\| = \sqrt{2 \tilde{S}_{ij} \tilde{S}_{ij}}$ is used as inverse of the subgrid-time scale t_{sgs} , so that ν_{sgs} reads

$$\nu_{sgs} = (C\tilde{\Delta})^2 \sqrt{2 \tilde{\mathbf{S}}_{ij} \tilde{\mathbf{S}}_{ij}}. \quad (3.19)$$

The model constant C is unfortunately a non-universal parameter. It can be theoretically derived assuming that production of subgrid-scale energy equals the dissipation (energy equilibrium) in homogeneous isotropic turbulence, where it becomes $C = 0.18$. For wall bounded flow this value is known to generate an excessive model contribution, and therefore, a commonly accepted choice is rather $C = 0.1$. Since near the physical walls the vanishing of eddy viscosity is not ensured by the formulation (3.19), the constant C in Eq. (3.19) is multiplied by the Van Driest damping function introduced in Eq. (3.17), so that the dampened eddy viscosity decays with the square of the normal distance from the wall, $\nu_{sgs} \sim y^2$ for $y \rightarrow 0$. As such, the model parameter

$$C^{SMAG} = \left[C \left(1 - e^{(-\frac{y^+}{25})} \right) \right]^2, \quad (3.20)$$

can be introduced in the final formulation of the sgs eddy viscosity for SMAG as

$$\nu_{sgs}^{SMAG} = C^{SMAG} \tilde{\Delta}^2 \sqrt{2 \tilde{\mathbf{S}}_{ij} \tilde{\mathbf{S}}_{ij}}. \quad (3.21)$$

- CSM: The Coherent Structure Model defines the sgs eddy viscosity similar to SMAG, written as

$$\nu_{sgs}^{CSM} = C^{CSM} \tilde{\Delta}^2 \sqrt{2 \tilde{\mathbf{S}}_{ij} \tilde{\mathbf{S}}_{ij}}. \quad (3.22)$$

However, a non-constant model parameter $C^{CSM} = C^{CSM}(\mathbf{x}, t)$ is used to ensure a vanishing sgs eddy viscosity in the vicinity of solid walls, without the need for additional *ad hoc* wall damping functions. The parameter C^{CSM} is actually computed as

$$C^{CSM} = \frac{1}{22} (1 - F_{cs}) |F_{cs}|^{1.5}, \quad (3.23)$$

where F_{cs} represents the coherent structure function obtained as

$$F_{cs} = \frac{\widetilde{\mathbf{W}}_{ij} \widetilde{\mathbf{W}}_{ij} - \tilde{\mathbf{S}}_{ij} \tilde{\mathbf{S}}_{ij}}{\widetilde{\mathbf{W}}_{ij} \widetilde{\mathbf{W}}_{ij} + \tilde{\mathbf{S}}_{ij} \tilde{\mathbf{S}}_{ij}}. \quad (3.24)$$

F_{cs} depends on both the resolved strain tensor $\tilde{\mathbf{S}}$ and on the resolved vorticity tensor $\widetilde{\mathbf{W}} = \frac{1}{2}(\nabla \tilde{\mathbf{U}} - (\nabla \tilde{\mathbf{U}})^T)$. It goes to zero near solid walls, producing a scaling of the subgrid-scale eddy viscosity with wall distance given as $\nu_{sgs} \sim y^3$ for $y \rightarrow 0$.

- WALE: This approach models ν_{sgs} as

$$\nu_{sgs}^{WALE} = (C_w \tilde{\Delta})^2 \frac{(\tilde{\mathbf{S}}_{ij}^d \tilde{\mathbf{S}}_{ij}^d)^{3/2}}{(\tilde{\mathbf{S}}_{ij}^d \tilde{\mathbf{S}}_{ij}^d)^{5/4} + (\tilde{\mathbf{S}}_{ij} \tilde{\mathbf{S}}_{ij})^{5/2}}, \quad (3.25)$$

where $\tilde{\mathbb{S}}^d$ represents the traceless part of the square of the velocity gradient tensor

$$\tilde{\mathbb{S}}^d = \frac{1}{2}(\tilde{\mathbb{G}}\tilde{\mathbb{G}} + (\tilde{\mathbb{G}}, \tilde{\mathbb{G}})^T) - \frac{1}{3}\mathbb{I}tr(\tilde{\mathbb{G}}\tilde{\mathbb{G}}), \quad \text{with} \quad \tilde{\mathbb{G}} = \nabla \tilde{\mathbf{U}} \quad (3.26)$$

and C_w is a model constant set to 0.35. ν_{sgs} scales with wall distance $y \rightarrow 0$ as $\nu_{sgs} \sim y^3$.

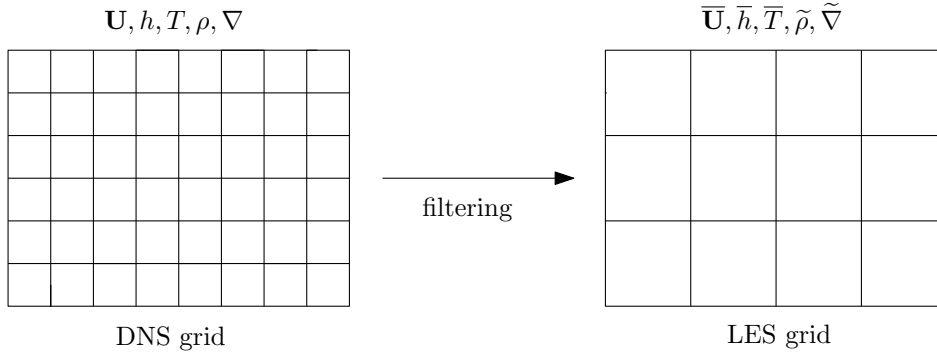
The grid-filter width is always defined as $\tilde{\Delta} = (\tilde{\Delta}_1 \tilde{\Delta}_2 \tilde{\Delta}_3)^{1/3}$ dependent on the mesh size in the three coordinate directions.

3.2.3 *A priori* LES

In this section the numerical procedure applied in the *a priori* test, or equivalently *a priori* LES, will be presented. The *a priori* LES is basically no self-sustained predictive simulation (commonly termed *a posteriori* LES) but rather analyzes an existing previously computed DNS database, which is considered as highly accurate, providing a fully resolved description. In an *a priori* test, an instantaneous field of velocity or temperature, previously computed in DNS on a very fine grid, is spatially filtered with a filter function G , as described by Eq. (3.4). The difference of the filtered fully resolved non-linear convective fluxes to their counterparts obtained with the filtered flow variables gives a good estimate for the subgrid-scale contributions (*a priori* subgrid-scale fluxes), which would have to be provided by appropriate subgrid-scale models in predictive (*a posteriori*) LES. Using only frozen flow fields provided by DNS, the dynamic effect of the sgs model on the temporal evolution of the solution is lost, as no governing set of equations for instationary turbulent flow is really solved in time. On the other hand, the advantage of the *a priori* test is that delivering the DNS based *a priori* subgrid-scale fluxes provides some kind of target values for these unclosed terms to be compared against corresponding predictions from subgrid-scale models. Additionally, the effect of the numerical error, which would be introduced in a predictive *a posteriori* LES, due to the adoption of a coarse LES-grid can be systematically analyzed, provided that the reference DNS results have been sufficiently accurately computed.

Spatial filtering

The aim of the filtering is to retain only the larger scales in the flow field and sieve out the smaller eddies, so as to mimic the solution of a predictive *a posteriori* LES performed on a coarse LES grid. The determination of the *a priori* sgs fluxes is schematically shown in Fig. 3.3.



a priori sgs fluxes

$$\begin{aligned}\tau_{sgs}^{DNS} &= \tilde{\rho}(\overline{\mathbf{U} \mathbf{U}} - \overline{\mathbf{U}} \overline{\mathbf{U}}), \\ \mathbf{q}_{sgs}^{DNS} &= \tilde{\rho}(\overline{\mathbf{U} h} - \overline{\mathbf{U}} \overline{h})\end{aligned}$$

Figure 3.3: Grid filtering in *a priori* LES

Assuming a top-hat filter kernel, the filtering procedure basically computes a local volumetric average of any unfiltered quantity by integrating it with an appropriate numerical quadrature rule over a spatial support, whose size is defined by the filter width $\tilde{\Delta}$, expressed as multiples of the initial grid size of DNS $N\Delta$. In one spatial dimension, this implies for the filtered variable $\tilde{\phi}_i$ at considered grid-point x_i

$$\tilde{\phi}_i = \sum_{j=-N/2}^{N/2} \alpha_j \phi_{i+j}, \quad (3.27)$$

where the weights α_i are given by higher-order Newton-Cotes formulas. E.g. for a LES grid being twice as coarse as the DNS grid, where $\tilde{\Delta} = 2\Delta$, this approach would result in the Simpson integration rule

$$\tilde{\phi}_i = \frac{1}{6}(\phi_{i+1} + 4\phi_i + \phi_{i-1}). \quad (3.28)$$

The 1D spatial filtering procedure defined by Eq. (3.27) can be straightforwardly extended in 3D as

$$\tilde{\phi}_{i,j,k} = \sum_{m=-\frac{N}{2}}^{\frac{N}{2}} \sum_{n=-\frac{N}{2}}^{\frac{N}{2}} \sum_{p=-\frac{N}{2}}^{\frac{N}{2}} \alpha_m \beta_n \gamma_p \phi_{i+m,j+n,k+p}, \quad (3.29)$$

where the indexes m, n, p denote the points covered by the filter width $\tilde{\Delta}$ along the coordinate directions. Filtering the non-linear advective terms, the *a priori* representations of the sgs fluxes τ_{sgs} and \mathbf{q}_{sgs} according to Eqs. (3.13) - (3.14) can be directly evaluated from DNS based quantities.

Aside from the closure problem of the unresolved small scale motion, a further issue arises from the larger numerical error on the coarse LES grid. The discretized representation of the differential operator represented by $\tilde{\nabla}$ on the coarse LES grid inherently reduces

the accuracy of the description of the advective flux balances. This numerical error contribution is estimated as proposed by Vreman *et al.* (1995) and Brandt (2006) under the assumption that the DNS solution is accurate enough to be assumed as representative of the theoretical exact solution. Following this proposal, the unclosed non-linear terms arising from the filtered momentum and heat fluxes can be decomposed into three contributions

$$\underbrace{\nabla \cdot (\tilde{\rho} \overline{\mathbf{U}\mathbf{U}})}_{A_{\mathbf{U}}} = \underbrace{\tilde{\nabla} \cdot (\tilde{\rho} \overline{\mathbf{U}} \overline{\mathbf{U}})}_{\overline{A}_{\mathbf{U}}} + \underbrace{\tilde{\nabla} \cdot (\tilde{\rho} \overline{\mathbf{U}\mathbf{U}} - \tilde{\rho} \overline{\mathbf{U}} \overline{\mathbf{U}})}_{\alpha_{\mathbf{U}}} + \underbrace{\nabla \cdot (\tilde{\rho} \overline{\mathbf{U}\mathbf{U}}) - \tilde{\nabla} \cdot (\tilde{\rho} \overline{\mathbf{U}\mathbf{U}})}_{\beta_{\mathbf{U}}}, \quad (3.30)$$

$$\underbrace{\nabla \cdot (\tilde{\rho} \overline{\mathbf{U}h})}_{A_{\theta}} = \underbrace{\tilde{\nabla} \cdot (\tilde{\rho} \overline{\mathbf{U}} \overline{h})}_{\overline{A}_{\theta}} + \underbrace{\tilde{\nabla} \cdot (\tilde{\rho} \overline{\mathbf{U}h} - \tilde{\rho} \overline{\mathbf{U}} \overline{h})}_{\alpha_{\theta}} + \underbrace{\nabla \cdot (\tilde{\rho} \overline{\mathbf{U}h}) - \tilde{\nabla} \cdot (\tilde{\rho} \overline{\mathbf{U}h})}_{\beta_{\theta}}. \quad (3.31)$$

The decompositions (3.30) and (3.31) represent budgets for the divergence of momentum and heat flux, $A_{\mathbf{U}}$ and A_{θ} , as they would appear in the filtered governing equations for LES. On the right hand side, the terms $\overline{A}_{\mathbf{U}}$ and \overline{A}_{θ} denote the resolved contributions to the advective fluxes of momentum and enthalpy, computed on the LES-grid with the corresponding operator $\tilde{\nabla}$. The second terms on the right hand side, denoted by $\alpha_{\mathbf{U}}$ and α_{θ} , represent the *a priori* representations of the sgs flux contributions to momentum and enthalpy, respectively. Lastly, the terms $\beta_{\mathbf{U}}$ and β_{θ} are the contributions due to the numerical error caused by the adoption of the operator $\tilde{\nabla}$ on the coarse LES-grid. These error terms are estimated by comparing discretized representation of the divergence on the coarse LES-grid against that on the fine DNS grid, associated with the operator ∇ .

Using the *a priori* representation of τ_{sgs} and \mathbf{q}_{sgs} , a DNS based *a priori* eddy viscosity ν_{sgs}^{DNS} and DNS based *a priori* thermal eddy diffusivity a_{sgs}^{DNS} can be obtained as

$$\nu_{sgs}^{DNS} = -\frac{\langle \tau_{sgs}^d : \tilde{\mathbf{S}} \rangle}{2 \langle \tilde{\mathbf{S}} : \tilde{\mathbf{S}} \rangle}, \quad (3.32)$$

$$a_{sgs}^{DNS} = -\frac{\langle \mathbf{q}_{sgs} / (\rho c_p) \cdot \tilde{\nabla} \tilde{T} \rangle}{\langle \tilde{\nabla} \tilde{T} \cdot \tilde{\nabla} \tilde{T} \rangle}, \quad (3.33)$$

A contraction with the filtered strain rate tensor $\tilde{\mathbf{S}}$ and temperature gradient $\tilde{\nabla} \tilde{T}$ was used here to yield scalar representations of both coefficients. The operator $\langle \cdot \rangle$ denotes the spatial averaging along the homogenous directions. The determination of ν_{sgs}^{DNS} can be further used to compute *a priori* representations of underlying model parameters, like the model coefficient for Smagorinsky-type models obtained as

$$C^{DNS} = \frac{\nu_{sgs}^{DNS}}{2\tilde{\Delta}^2 \sqrt{\tilde{\mathbf{S}}_{ij} \tilde{\mathbf{S}}_{ij}}}. \quad (3.34)$$

Consequently, using the *a priori* values obtained by Eqs. (3.32) and (3.33), respectively, of ν_{sgs}^{DNS} and a_{sgs}^{DNS} , the *a priori* representation of Pr_{sgs} is computed as

$$Pr_{sgs}^{DNS} = \frac{\nu_{sgs}^{DNS}}{a_{sgs}^{DNS}}. \quad (3.35)$$

3.2.4 *A posteriori* LES

As opposed to the *a priori* LES, which is only based on frozen instantaneous flow fields from DNS, the *a posteriori* LES solves the filtered governing equations described by Eqs. (3.8)-(3.10) discretized in time and space, using some numerical scheme, so as to predict the instantaneous flow field at each discrete instant of time. The governing equations are solved for the filtered variables with the aid of sgs models for the unresolved stress tensor and heat flux. The results may be afterwards statistically averaged in time and in space along any homogeneous directions, if the considered problem involves some spatial homogeneity.

In the present work, the *a posteriori* LES follows the concept of implicit filtering. In contrast to the concept of explicit filtering, where the governing equations are explicitly filtered using a known filter function, the implicit filtering is solely based on the filtering effect, inherently arising from the numerical discretization scheme on the LES grid. Therefore, the filter function and the effective filter width associated with the numerical discretization scheme and solution algorithm are basically unknown. The filter width can be still related to the adopted mesh size, such that $\tilde{\Delta} \sim \Delta_i$, using estimates like

$$\tilde{\Delta} = (\Delta_1 \Delta_2 \Delta_3)^{1/3} \quad , \quad \text{or} \quad \tilde{\Delta} = (\Delta_1^2 + \Delta_2^2 + \Delta_3^2)^{1/2}. \quad (3.36)$$

The first Ansatz in Eq. (3.36) is used in the present work.

3.3 Experiments on fully developed heated pipe flow

The extensive computational investigations of turbulent heated pipe flows using a mixture of glysantine-water was assisted by an experimental campaign providing useful validation for some of the analyzed test cases in both DNS and LES. The present section provides a description of the experimental setup used for this purpose.

The experimental campaign has been carried out on a facility schematically depicted in Fig. 3.4.

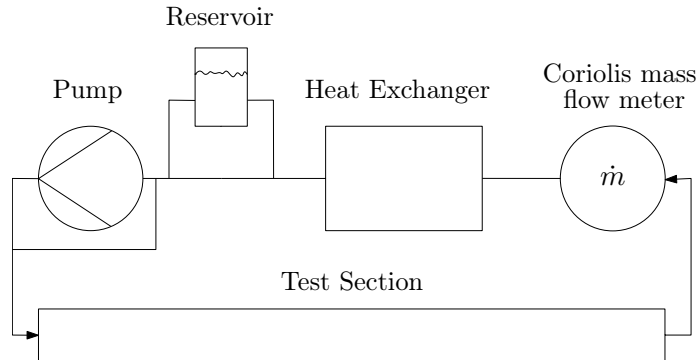


Figure 3.4: Experimental facility

The loop contains a reservoir, which stores large part of the working fluid and has some heating rods inside to control the temperature level of the circulating liquid. The centrifugal pump downstream, sets the fluid into motion. Downstream of the pump the

fluid moves into a cylindrical pipe test section, where the heat transfer experiments, which are essentially based on the temperature measurements, are carried out. Here the fluid is uniformly heated through the surrounding wall. A more detailed description of the heated test section will be given below. Downstream of the test section a mass flow meter measures the mass flow rate. It is noted that the mass flow rate is controlled by the pump speed and the opening of the bypass valve. The fluid exiting the test section is finally passed through a heat exchanger, where its temperature decreased back down to the level at the entrance into the heated test section.

A detailed view of the test section is provided in Fig. 3.5. The test section essentially consists of three main parts: an entrance region, a heated section and, lastly, a thermal equalization section.

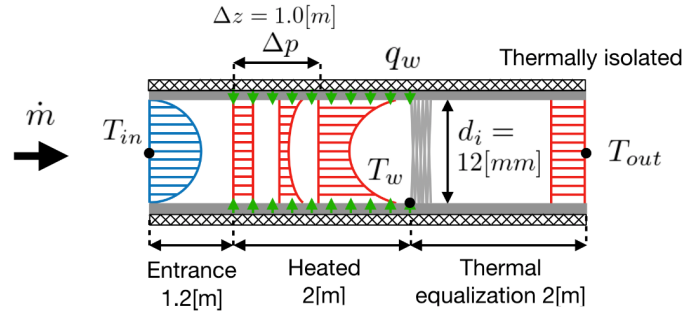


Figure 3.5: Details of the test section in the experimental facility

The whole section is thermally insulated through a Kapton layer and an outer jacket of insulating foam, so as to ensure adiabatic conditions at the outer surface. In the entrance region, no heating from the wall is provided and the isothermal flow can reach a dynamically fully developed state. Downstream of the hydraulic entrance region, a uniform wall heating is applied on the pipe inner surface by means of electric resistance heating, as electric current at low voltage is introduced into the pipe wall by a welding transformer. The heated section has a total length $L = 2m$, so as to ensure thermally fully developed conditions near the downstream end. The material of the pipe is stainless steel (14011). Once the fluid exits the heated section it is passed through the thermal equalization section, where it is supposed to reach a radially uniform enthalpy equivalent to a bulk temperature T_{out} , also referred to as "mixing temperature". The uniform bulk temperatures T_{in} and T_{out} are measured with probes placed at the centerline of the pipe. Since the thermal equalization section has been efficiently insulated, the measured exit value T_{out} is also assumed as bulk temperature of the thermally fully developed flow at the very end of the heated section.

The setup described above enables a direct measurement of the following quantities:

- mass flow rate \dot{m}
- pressure drop in the heated section Δp along the axial distance between the pressure probes $\Delta z = 1m$
- inlet bulk temperature T_{in}
- outlet bulk temperature T_{out}

- wall temperature at the end of the heated test section T_w

The bulk Reynolds number Re_b is specified using the measured T_{out} , which lets determine the required bulk fluid properties at the end of the heated test section, such that

$$Re_b = \frac{4 \dot{m}}{\mu(T_{out}) \pi d_i}, \quad (3.37)$$

where d_i represents the inner pipe diameter.

The wall molecular Prandtl number Pr_w which is used for parametrization of both the experimental and computational cases, can be determined as well based on the measurement of T_w at the end of the heated section:

$$Pr_w = \frac{\mu(T_w) c_p(T_w)}{\lambda(T_w)}. \quad (3.38)$$

The averaged wall heat flux and wall shear stress are acquired indirectly from the measured temperature difference $T_{out} - T_{in}$, pressure drop Δp and mass flow rate \dot{m} . Accordingly, the wall heat flux q_w , wall shear stress τ_w are obtained as

$$q_w = \frac{\dot{m} \hat{c}_p (T_{out} - T_{in})}{\pi d_i L_{heated}}, \quad (3.39)$$

$$\tau_w = \frac{d_i \Delta p}{4 \Delta z}, \quad (3.40)$$

respectively, with the bulk velocity being determined from

$$U_b = \frac{4 \dot{m}}{\rho(T_{out}) \pi d_i^2}. \quad (3.41)$$

L_{heated} represents the axial length of the heated portion of the test section, \hat{c}_p is the average specific heat capacity of the fluid along the heated section and is computed at temperature $(T_{out} + T_{in})/2$.

Following from Eqs. (3.39) and (3.40) the main outputs of the present experimental setup, recast into non-dimensional form, are the heat transfer coefficient (or Nusselt number Nu) and the skin friction coefficient (C_f), obtained as

$$Nu = \frac{q_w d_i}{\lambda(T_w) (T_w - T_{out})}, \quad (3.42)$$

$$C_f = \frac{2 \tau_w}{\rho(T_{out}) U_b^2}. \quad (3.43)$$

Chapter 4

Numerical procedure

4.1 Computational domains

In the course of this thesis we will address wall bounded turbulent flows in straight cylindrical pipe geometries, where the boundary layer either remains attached to the wall along the entire extension of the pipe or gets detached due to a step-like change in the wall geometry, as it is in case of a pipe with an abrupt circular expansion. In both cases it is convenient to use cylindrical coordinates (r, φ, z) for describing the flow field. Figure 4.1 schematically presents the two geometries, which define the spatial domains for the computational analysis in the further sections. r, φ and z denote the coordinates in radial, azimuthal and axial directions, whereas u, v, w the corresponding velocity components, respectively.

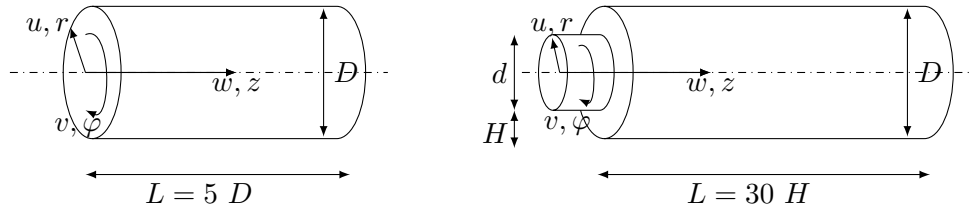


Figure 4.1: Geometrical sketches of the computational domains for attached turbulent pipe flow (left side) and detached turbulent pipe flow with abrupt circular expansion (right side)

On the left side of the two sketched geometries in Fig. 4.1, the flow is assumed dynamically and thermally fully developed, so that axial periodicity may be imposed at the inlet and at the exit cross-section. Under the statistical point of view, homogeneity is established in the axial and azimuthal direction.

On the right side of Fig. 4.1, the second geometry considered for the numerical analysis is shown. Here the flow passes through an upstream pipe of diameter d , which suddenly expands in a stepwise fashion, causing a separation of the flow and a region of intense mixing. The separated flow reattaches in downstream pipe of diameter D and length $L = 30H$ after some axial distance from the step. Ideally, in a sufficiently long downstream pipe, the flow will certainly recover fully developed conditions associated with statistical homogeneity in the axial direction. Statistical homogeneity in azimuthal direction is retained in

both the upstream and downstream pipe.

For both geometries the simulations are carried out using parallel processing architectures. To this end, the domain is always divided into axial subdomains, where the individual processes parallelly solve the governing equations in the assigned portion of the domain. The information exchange between the subdomain interfaces and between the outlet / inlet cross sections is based on MPI communications, as sketched in Fig. 4.2.

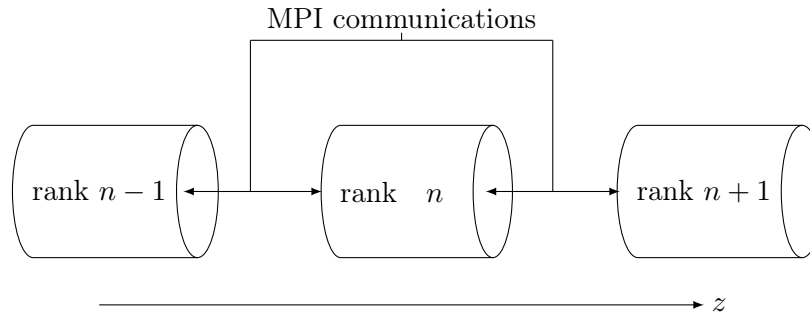


Figure 4.2: Axial decompositions for MPI parallel domain distributions

All computations of the turbulent periodic pipe flows, as schematically represented in Fig. 4.1 (left), were carried out with a dedicated FORTRAN in-house code with DNS/LES capabilities. On the other hand, the computations of the turbulent flows in a pipe with an abrupt circular expansion (Fig. 4.1, on the right), were performed with the open source software OpenFOAM, where the thermophysical model of the considered fluid was additionally implemented for this purpose. Some more details on the spatial and temporal discretization used in the in-house DNS/LES-code are given in the subsections below. The PISO-algorithm, which was applied to solve the incompressible Navier-Stokes equations in OpenFOAM is described in the Appendix.

4.2 Spatial discretization

The numerical method employed for simulating the turbulent flows in the considered domains is the Finite Volume Method (FVM). According to the FVM, the physical domain is discretized in space by means of a number of small finite volume elements, over which each of the governing conservation equations is integrated. Considering a single cell in the computational mesh, consisting of a given finite control volume V_c , different strategies in the spatial allocation of the variables might be followed. If all flow variables are located at the same position, namely at the cell center of V_c , the grid is termed *collocated*. Alternatively, only the scalar quantities, such as the pressure, the fluid properties and the enthalpy, might be located at the cell center, whereas the velocity components are defined at the cell faces. In this latter case, the approach is called *staggered* grid. For the computations performed in the cylindrical and periodic fully developed pipe flow of LES and DNS a staggered formulation is adopted, whereas the simulations performed in pipe with abrupt axisymmetric expansion step adopt a cell-centered collocated discretization.

The general unsteady transport equation of any flow-related tensorial variable $\phi = \phi(\mathbf{x}, t)$, which is advected by velocity \mathbf{U} and diffused based on Fick's law involving an effective diffusivity coefficient Γ_{eff} , can be expressed as:

$$\underbrace{\frac{\partial(\phi)}{\partial t}}_I + \underbrace{\nabla \cdot (\mathbf{U}\phi)}_{II} = \underbrace{\nabla \cdot (\Gamma_{eff} \nabla \phi)}_{III}. \quad (4.1)$$

In Eq. (4.1), I represents the rate of change of ϕ per unit of volume in time, II the advection by velocity, and III the transport due to diffusion, where the effective diffusivity coefficient $\Gamma_{eff} = \Gamma + \Gamma_T$ includes a laminar and turbulent component following from a gradient diffusion Ansatz for turbulence modelling. The finite volume discretization of Eq. (4.1) is derived by integrating Eq. (4.1) over the control volume V_c :

$$\int_{V_c} \frac{\partial(\phi)}{\partial t} dV + \int_{V_c} \nabla \cdot (\mathbf{U}\phi) dV = \int_{V_c} (\nabla \cdot \Gamma_{eff} \nabla \phi) dV. \quad (4.2)$$

Assuming $V_c \neq f(t)$, the term I can be expressed as

$$\int_{V_c} \frac{\partial(\phi)}{\partial t} dV = \frac{\partial \phi_c}{\partial t} V_c, \quad (4.3)$$

where ϕ_c corresponds to the volume average over the control volume V_c :

$$\phi_c = \frac{1}{V_c} \int_{V_c} \phi dV. \quad (4.4)$$

The integral of II over the same control volume is exactly transformed into a surface integral by applying the Gauss theorem:

$$\int_{V_c} \nabla \cdot (\mathbf{U}\phi) dV = \int_{S_c} (\mathbf{U}\phi \cdot d\mathbf{S}) = \sum_j (\mathbf{n}_j \cdot \mathbf{U}_j \phi_j) S_j, \quad (4.5)$$

where \mathbf{n}_j is the unit normal vector on the face area S_j .

The computation of the right-hand of Eq. (4.5) side represents a net flux balance accross all j faces which enclose the control volume V_c . In order to evaluate this term numerically, a proper representation of the face-fluxes is needed. Usually, the face values ϕ_j are approximated by interpolation between two volume averages of ϕ belonging to adjacent cells, which renders a 2^{nd} -order accurate approximation in space.

The term III can be treated in a similar fashion by converting the integral of a divergence into the sum of j diffusive fluxes accross the control volume's surface:

$$\int_{V_c} \nabla \cdot (\Gamma_{eff} \nabla \phi) dV = \int_{S_c} (\Gamma_{eff} \nabla \phi) \cdot d\mathbf{S} = \sum_j \mathbf{n}_j \cdot (\Gamma_{eff} \nabla \phi)_j S_j. \quad (4.6)$$

The face-fluxes $(\Gamma_{eff} \nabla \phi)_j$ are similarly obtained by interpolation of volume averaged quantities belonging to adjacent cells.

The discretized representation of Eq. (4.2) finally reads

$$\frac{\partial \phi_c}{\partial t} V_c + \sum_j (\mathbf{n}_j \cdot \mathbf{U}_j \phi_j) S_j - \sum_j \mathbf{n}_j \cdot (\Gamma_{eff} \nabla \phi)_j S_j = 0. \quad (4.7)$$

In the present work, the DNS simulations of fully developed heated/cooled turbulent pipe flows are computed using a 4th order accurate discretization for the approximation of the face-fluxes, as done in Lemos *et al.* (2012), whereas all LES and the DNS of turbulent heated flows in pipe with abrupt expansions were carried out using a 2nd order accurate interpolation scheme for the face-fluxes.

Staggered grid in polar geometry

The DNS and LES of the periodic pipe flow were carried out using a polar discretization of the spatial domain. The polar grid is uniformly discretized in axial and in the azimuthal direction, whereas the radial direction has been refined in vicinity of the wall and the centerline, so as to properly describe the near wall boundary layer with sufficient accuracy on one side, and on the other side, to ensure good accuracy also in proximity of the centerline singularity. The sketch on the left side of Fig. 4.3 gives a view on the cross-sectional discretization used in DNS/LES of periodic heated and cooled pipe flow.

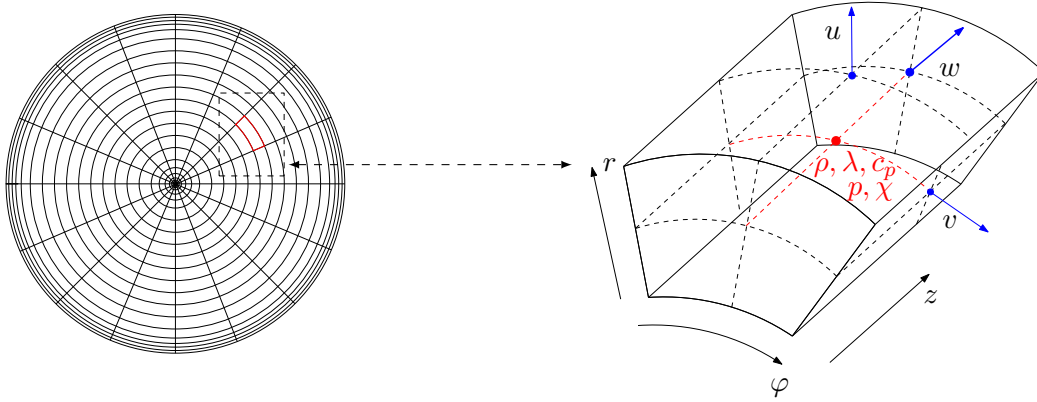


Figure 4.3: Staggered polar grid for DNS and LES of periodic pipe flow

A control volume of the staggered grid is sketched on the right side of Fig. 4.3. The position of three velocity components u , v , w are defined at the cell face centers, whereas all scalar quantities like pressure p , density ρ , or enthalpy difference χ are defined at the center of the volume.

4.3 Temporal discretization

The governing equations describing the unsteady turbulent motion need to be discretized in time using an appropriate integration scheme, which should meet the demands on accuracy, stability, and computational efficiency. The numerical time integration strategies adopted for the considered geometries, namely a straight periodic pipe and a pipe with an abrupt circular expansion, are different, as they are managed by two different solvers, and will be therefore described separately.

In the DNS of turbulent periodic pipe flow, a semi-implicit Adams-Bashforth scheme was adopted to discretize the non-dimensional governing equations (2.56)-(2.59) in time. The method uses an implicit Crank-Nicholson discretization scheme in one spatial direction, while the remaining two directions are discretized in time using the explicit Adams-Bashforth scheme. The method splits the time integration into two steps. At first, an intermediate solution is computed from the momentum equations, neglecting the contribution of the pressure. As a result, the intermediate solution is not mass conservative. In a second step the conservation of mass is enforced applying a pressure correction. The pressure is obtained from the solution of a Poisson equation. This method is generally called fractional step method Chorin (1968).

The global truncation error is of order $\mathcal{O}(\Delta t^2)$, which can be seen as a good compromise between accuracy and computational costs. For this reason this scheme has been often adopted also in other DNS studies, such as in Kim *et al.* (1987).

The integration procedure considers an alternating implicit/explicit treatment of advective and diffusive terms of the governing conservation equations. To this end, Eq. (4.1) is recast in non-dimensional form as

$$\begin{aligned} \frac{\partial(\phi)}{\partial t^*} + \underbrace{\frac{1}{r^*} \frac{\partial(r^* \phi u^+)}{\partial r^*}}_{(ADV)_r} + \underbrace{\frac{1}{r^*} \frac{\partial(\phi v^+)}{\partial \varphi}}_{(ADV)_\varphi} + \underbrace{\frac{\partial(\phi w^+)}{\partial z^*}}_{(ADV)_z} = \\ \underbrace{\frac{1}{r^*} \frac{\partial(r^* \Gamma_{eff}^* \nabla \phi)}{\partial r^*}}_{(DIFF)_r} + \underbrace{\frac{1}{r^*} \frac{\partial(\Gamma_{eff}^* \nabla \phi)}{\partial \varphi}}_{(DIFF)_\varphi} + \underbrace{\frac{\partial(\Gamma_{eff}^* \nabla \phi)}{\partial z^*}}_{(DIFF)_z}, \end{aligned} \quad (4.8)$$

where the terms (ADV) and $(DIFF)$ denote the advective and diffusive net fluxes of the scalar quantity ϕ , respectively, with the subscripts $()_r$, $()_\varphi$, $()_z$ denoting their spatial discretization. Γ_{eff}^* is a non-dimensional representation of the total diffusion coefficient, rescaled with an appropriate reference value. The radial direction is integrated implicitly near the wall within $r_{sw}^* < r < 0.5$. Near the centerline within $0 \leq r^* \leq r_{sw}^*$, the azimuthal direction is integrated implicitly, while the radial direction is discretized explicitly. The switching of the implicit treatment between radial and the azimuthal directions, is summarized below:

$$\begin{aligned} \frac{(\phi)^{n+1} - (\phi)^n}{\Delta t} + \frac{1}{2} [(ADV)_r - (DIFF)_r]^{n+1} = \\ - \frac{1}{2} [(ADV)_r - (DIFF)_r]^n \\ + \frac{3}{2} [(DIFF)_\varphi - (ADV)_\varphi + (DIFF)_z - (ADV)_z]^{n-1} \\ - \frac{1}{2} [(DIFF)_\varphi - (ADV)_\varphi + (DIFF)_z - (ADV)_z]^n \quad \text{for } r_{sw}^* < r < 0.5 \end{aligned} \quad (4.9)$$

$$\begin{aligned}
& \frac{(\phi)^{n+1} - (\phi)^n}{\Delta t} + \frac{1}{2} [(ADV)_\varphi - (DIFF)_\varphi]^{n+1} = \\
& - \frac{1}{2} [(ADV)_\varphi - (DIFF)_\varphi]^{n+1} \\
& + \frac{3}{2} [(DIFF)_r - (ADV)_r + (DIFF)_z - (ADV)_z]^{n-1} \\
& - \frac{1}{2} [(DIFF)_r - (ADV)_r + (DIFF)_z - (ADV)_z]^n \quad \text{for } 0 < r < r_{sw}^*
\end{aligned} \tag{4.10}$$

Integration of the thermal field

The aforementioned time discretization procedure is first applied to integrate the equation for the non-dimensional enthalpy difference χ^+ , as expressed by Eq. (2.59). The corresponding formulation reads

- $r_{sw}^* < r^* < 0.5$

$$\begin{aligned}
& \frac{(\chi^+)^{n+1} - (\chi^+)^n}{\Delta t^*} + \left[\frac{1}{r^*} \frac{\partial(r^* \chi^+ u^+)}{\partial r^*} - \frac{1}{Pr_w Re_{\tau,w}} \frac{1}{r^*} \frac{\partial(r^* q_r^+)}{\partial r^*} \right]^{n+1} - [\chi^+ \nabla^* \cdot \mathbf{U}^+]^n = \\
& + \frac{3}{2} \left[-\frac{1}{r^*} \frac{\partial(\chi^+ v^+)}{\partial \varphi} - \frac{\partial(\chi^+ w^+)}{\partial z^*} + \frac{1}{Pr_w Re_{\tau,w}} \left(\frac{1}{r^*} \frac{\partial(q_\varphi^+)}{\partial \varphi} + \frac{\partial(q_z^+)}{\partial z^*} \right) \right]^n \\
& - \frac{1}{2} \left[-\frac{1}{r^*} \frac{\partial(\chi^+ v^+)}{\partial \varphi} - \frac{\partial(\chi^+ w^+)}{\partial z^*} + \frac{1}{Pr_w Re_{\tau,w}} \left(\frac{1}{r^*} \frac{\partial(q_\varphi^+)}{\partial \varphi} + \frac{\partial(q_z^*)}{\partial z^*} \right) \right]^{n-1} \\
& + \left[\frac{w^+}{\dot{m}^*} \right]^n
\end{aligned} \tag{4.11}$$

- $0 < r^* < r_{sw}^*$

$$\begin{aligned}
& \frac{(\chi^+)^{n+1} - (\chi^+)^n}{\Delta t^*} + \left[\frac{1}{r^*} \frac{\partial(\chi^+ v^+)}{\partial \varphi} - \frac{1}{Pr_w Re_{\tau,w}} \frac{1}{r^*} \frac{\partial(q_\varphi^+)}{\partial \varphi} \right]^{n+1} - [\chi^+ \nabla^* \cdot \mathbf{U}^+]^n = \\
& + \frac{3}{2} \left[-\frac{1}{r^*} \frac{\partial(r^* \chi^+ u^+)}{\partial r^*} - \frac{\partial(\chi^+ w^+)}{\partial z^*} + \frac{1}{Pr_w Re_{\tau,w}} \left(\frac{1}{r^*} \frac{\partial(r^* q_r^+)}{\partial r^*} + \frac{\partial(q_z^+)}{\partial z^*} \right) \right]^n \\
& - \frac{1}{2} \left[-\frac{1}{r^*} \frac{\partial(r^* \chi^+ u^+)}{\partial r^*} - \frac{\partial(\chi^+ w^+)}{\partial z^*} + \frac{1}{Pr_w Re_{\tau,w}} \left(\frac{1}{r^*} \frac{\partial(r^* q_r^+)}{\partial r^*} + \frac{\partial(q_z^*)}{\partial z^*} \right) \right]^{n-1} \\
& + \left[\frac{w^+}{\dot{m}^*} \right]^n
\end{aligned} \tag{4.12}$$

The new prediction of enthalpy difference χ^{+n+1} is used to update the temperature field $T^{n+1} = T(\chi^{n+1})$, using the integral described by Eq. (2.48).

Prediction of velocity field

As a second step in the time integration procedure, the mass fluxes $(\rho u, \rho v, \rho w)$ are advanced in time by solving Eqs. (2.56)-(2.58) neglecting pressure. This is called *predictor* step. As a result of this operation, the intermediate solution denoted by $()^\dagger$ of the three mass fluxes is not mass conservative.

- $r_{sw}^* < r^* < 0.5$

$$\begin{aligned}
& \frac{(\rho^* u^+)^\dagger - (\rho^* u^+)^n}{\Delta t^*} + \\
& \frac{1}{2} \left[\frac{1}{r^*} \frac{\partial(r^* \rho^* u^+ u^+)}{\partial r^*} \right]^n + \frac{1}{2} \left[\frac{1}{r^*} \frac{\partial(r^* \rho^* u^+ u^+)}{\partial r^*} \right]^\dagger - \frac{1}{Re_\tau} \left[\frac{1}{r^*} \frac{\partial(r^* \tau_{rr}^+)}{\partial r^*} \right]^\dagger = \\
& + \frac{3}{2} \left[-\frac{1}{r^*} \frac{\partial(\rho^* u^+ v^+)}{\partial \varphi} + \frac{\rho^* (v^+)^2}{r^*} - \frac{\partial(\rho^* u^+ w^+)}{\partial z^*} + \frac{1}{Re_\tau} \left(\frac{1}{r^*} \frac{\partial \tau_{r\varphi}^+}{\partial \varphi} - \frac{\tau_{\varphi\varphi}^+}{r^*} + \frac{\partial \tau_{rz}^+}{\partial z^*} \right) \right]^n \\
& - \frac{1}{2} \left[-\frac{1}{r^*} \frac{\partial(\rho^* u^+ v^+)}{\partial \varphi} + \frac{\rho^* (v^+)^2}{r^*} - \frac{\partial(\rho^* u^+ w^+)}{\partial z^*} + \frac{1}{Re_\tau} \left(\frac{1}{r^*} \frac{\partial \tau_{r\varphi}^+}{\partial \varphi} - \frac{\tau_{\varphi\varphi}^+}{r^*} + \frac{\partial \tau_{rz}^+}{\partial z^*} \right) \right]^{n-1}
\end{aligned} \tag{4.13}$$

$$\begin{aligned}
& \frac{(\rho^* v^+)^\dagger - (\rho^* v^+)^n}{\Delta t^*} + \\
& \frac{1}{2} \left[\frac{1}{r^*} \frac{\partial(r^* \rho^* v^+ u^+)}{\partial r^*} \right]^n + \frac{1}{2} \left[\frac{1}{r^*} \frac{\partial(r^* \rho^* v^+ u^+)}{\partial r^*} \right]^\dagger - \frac{1}{Re_\tau} \left[\frac{1}{r^*} \frac{\partial(r^* \tau_{r\varphi}^+)}{\partial r^*} \right]^* = \\
& + \frac{3}{2} \left[-\frac{1}{r^*} \frac{\partial(\rho^* v^+ v^+)}{\partial \varphi} - \frac{\rho^* v^+ u^+}{r^*} - \frac{\partial(\rho^* v^+ w^+)}{\partial z^*} + \frac{1}{Re_\tau} \left(\frac{1}{r^*} \frac{\partial \tau_{\varphi\varphi}^+}{\partial \varphi} + \frac{\tau_{\varphi r}^+}{r^*} + \frac{\partial \tau_{\varphi z}^+}{\partial z^*} \right) \right]^n \\
& - \frac{1}{2} \left[-\frac{1}{r^*} \frac{\partial(\rho^* v^+ v^+)}{\partial \varphi} - \frac{\rho^* v^+ u^+}{r^*} - \frac{\partial(\rho^* v^+ w^+)}{\partial z^*} + \frac{1}{Re_\tau} \left(\frac{1}{r^*} \frac{\partial \tau_{\varphi\varphi}^+}{\partial \varphi} + \frac{\tau_{\varphi r}^+}{r^*} + \frac{\partial \tau_{\varphi z}^+}{\partial z^*} \right) \right]^{n-1}
\end{aligned} \tag{4.14}$$

$$\begin{aligned}
& \frac{(\rho^* w^+)^\dagger - (\rho^* w^+)^n}{\Delta t^*} + \\
& \frac{1}{2} \left[\frac{1}{r^*} \frac{\partial(\rho^* w^+ v^+)}{\partial \varphi} \right]^n + \frac{1}{2} \left[\frac{1}{r^*} \frac{\partial(\rho^* w^+ v^+)}{\partial \varphi} \right]^\dagger - \frac{1}{Re_\tau} \left[\frac{1}{r^*} \frac{\partial \tau_{z\varphi}^+}{\partial \varphi} \right]^* = \\
& + \frac{3}{2} \left[-\frac{1}{r^*} \frac{\partial(r \rho^* w^+ u^+)}{\partial r^*} - \frac{\partial(\rho^* w^+ w^+)}{\partial z^*} + \frac{1}{Re_\tau} \left(\frac{1}{r^*} \frac{\partial(r \tau_{zr}^+)}{\partial r^*} + \frac{\partial \tau_{zz}^+}{\partial z^*} \right) \right]^n \\
& - \frac{1}{2} \left[-\frac{1}{r^*} \frac{\partial(r \rho^* w^+ u^+)}{\partial r^*} - \frac{\partial(\rho^* w^+ w^+)}{\partial z^*} + \frac{1}{Re_\tau} \left(\frac{1}{r^*} \frac{\partial(r \tau_{zr}^+)}{\partial r^*} + \frac{\partial \tau_{zz}^+}{\partial z^*} \right) \right]^{n-1} + 4
\end{aligned} \tag{4.15}$$

- $0 < r^* < r_{sw}^*$

$$\begin{aligned}
& \frac{(\rho^* u^+)^\dagger - (\rho^* u^+)^n}{\Delta t^*} + \\
& \frac{1}{2} \left[\frac{1}{r^*} \frac{\partial(\rho^* u^+ v^+)}{\partial \varphi} \right]^n + \frac{1}{2} \left[\frac{1}{r^*} \frac{\partial(\rho^* u^+ v^+)}{\partial \varphi} \right]^\dagger - \frac{1}{Re_\tau} \left[\frac{1}{r^*} \frac{\partial \tau_{r\varphi}}{\partial \varphi} \right]^\dagger = \\
& + \frac{3}{2} \left[-\frac{1}{r^*} \frac{\partial(r^* \rho^* u^+ u^+)}{\partial r^*} + \frac{\rho^* (v^+)^2}{r^*} - \frac{\partial(\rho^* u^+ w^+)}{\partial z^*} + \frac{1}{Re_\tau} \left(\frac{1}{r^*} \frac{\partial(r^* \tau_{rr}^+)}{\partial r^*} - \frac{\tau_{\varphi\varphi}^+}{r^*} + \frac{\partial \tau_{rz}^+}{\partial z^*} \right) \right]^n \\
& - \frac{1}{2} \left[-\frac{1}{r^*} \frac{\partial(r^* \rho^* u^+ u^+)}{\partial r^*} + \frac{\rho^* (v^+)^2}{r^*} - \frac{\partial(\rho^* u^+ w^+)}{\partial z^*} + \frac{1}{Re_\tau} \left(\frac{1}{r^*} \frac{\partial(r^* \tau_{rr}^+)}{\partial r^*} - \frac{\tau_{\varphi\varphi}^+}{r^*} + \frac{\partial \tau_{rz}^+}{\partial z^*} \right) \right]^{n-1}
\end{aligned} \tag{4.16}$$

$$\begin{aligned}
& \frac{(\rho^* v^+)^\dagger - (\rho^* v^+)^n}{\Delta t^*} + \\
& \frac{1}{2} \left[\frac{1}{r^*} \frac{\partial(\rho^* v^+ v^+)}{\partial \varphi} \right]^n + \frac{1}{2} \left[\frac{1}{r^*} \frac{\partial(\rho^* v^+ v^+)}{\partial \varphi} \right]^\dagger - \frac{1}{Re_\tau} \left[\frac{1}{r^*} \frac{\partial \tau_{\varphi\varphi}}{\partial \varphi} \right]^\dagger = \\
& + \frac{3}{2} \left[-\frac{1}{r^*} \frac{\partial(r^* \rho^* v^+ u^+)}{\partial r^*} - \frac{\rho^* v^+ u^+}{r^*} - \frac{\partial(\rho^* v^+ w^+)}{\partial z^*} + \frac{1}{Re_\tau} \left(\frac{1}{r^*} \frac{\partial(r^* \tau_{\varphi r}^+)}{\partial r^*} + \frac{\tau_{\varphi r}^+}{r^*} + \frac{\partial \tau_{\varphi z}^+}{\partial z^*} \right) \right]^n \\
& - \frac{1}{2} \left[-\frac{1}{r^*} \frac{\partial(r^* \rho^* v^+ u^+)}{\partial r^*} - \frac{\rho^* v^+ u^+}{r^*} - \frac{\partial(\rho^* v^+ w^+)}{\partial z^*} + \frac{1}{Re_\tau} \left(\frac{1}{r^*} \frac{\partial(r^* \tau_{\varphi r}^+)}{\partial r^*} + \frac{\tau_{\varphi r}^+}{r^*} + \frac{\partial \tau_{\varphi z}^+}{\partial z^*} \right) \right]^{n-1}
\end{aligned} \tag{4.17}$$

$$\begin{aligned}
& \frac{(\rho^* w^+)^\dagger - (\rho^* w^+)^n}{\Delta t^*} + \\
& \frac{1}{2} \left[\frac{1}{r^*} \frac{\partial(\rho^* w^+ v^+)}{\partial \varphi} \right]^n + \frac{1}{2} \left[\frac{1}{r^*} \frac{\partial(\rho^* w^+ v^+)}{\partial \varphi} \right]^\dagger - \frac{1}{Re_\tau} \left[\frac{1}{r^*} \frac{\partial \tau_{z\varphi}^+}{\partial \varphi} \right]^\dagger = \\
& + \frac{3}{2} \left[-\frac{1}{r^*} \frac{\partial(r^* \rho^* w^+ u^+)}{\partial r^*} - \frac{\partial(\rho^* w^+ w^+)}{\partial z^*} + \frac{1}{Re_\tau} \left(\frac{1}{r^*} \frac{\partial(r^* \tau_{zr}^+)}{\partial r^*} + \frac{\partial \tau_{zz}^+}{\partial z^*} \right) \right]^n \\
& - \frac{1}{2} \left[-\frac{1}{r^*} \frac{\partial(r^* \rho^* w^+ u^+)}{\partial r^*} - \frac{\partial(\rho^* w^+ w^+)}{\partial z^*} + \frac{1}{Re_\tau} \left(\frac{1}{r^*} \frac{\partial(r^* \tau_{zr}^+)}{\partial r^*} + \frac{\partial \tau_{zz}^+}{\partial z^*} \right) \right]^n + 4
\end{aligned} \tag{4.18}$$

Correction of velocity field

After the prediction step, a Poisson equation for the pressure π must be solved in order to provide the needed correction to enforce mass conservation at the new time step. As starting point, we recall that the fractional step procedure is based on the splitting of the total change of the mass fluxes in time Δt into

$$\frac{(\)^{n+1} - (\)^n}{\Delta t} = \frac{(\)^{n+1} - (\)^\dagger}{\Delta t} + \frac{(\)^\dagger - (\)^n}{\Delta t}. \tag{4.19}$$

The first term on the right hand side represents the corrector step written as

$$\begin{aligned}(\rho^* u^+)^{n+1} &= (\rho^* u^+)^{\dagger} - \Delta t^* \frac{\partial \pi^{*n+1}}{\partial r^*}, \\(\rho^* v^+)^{n+1} &= (\rho^* v^+)^{\dagger} - \Delta t^* \frac{1}{r^*} \frac{\partial \pi^{*n+1}}{\partial \varphi}, \\(\rho^* w^+)^{n+1} &= (\rho^* w^+)^{\dagger} - \Delta t^* \frac{\partial \pi^{*n+1}}{\partial z^*}.\end{aligned}\tag{4.20}$$

Solving the Navier-Stokes equations in the incompressible limit of low Mach number flow, the pressure is obtained by enforcing continuity at each time. For the considered case where a temperature-dependent variation of the density is considered, the mass conservation at time t^{n+1} reads

$$\frac{\partial(\rho^*)^{n+1}}{\partial t^*} = -\frac{1}{r^*} \frac{\partial r^* (\rho^* u^+)^{n+1}}{\partial r^*} - \frac{1}{r^*} \frac{\partial(\rho^* v^+)^{n+1}}{\partial \varphi} - \frac{\partial(\rho^* w^+)^{n+1}}{\partial z^*}.\tag{4.21}$$

The right-hand side of represents the divergence of the corrected mass fluxes at time level t^{n+1} and the left-hand side the time derivative of density. Since the density depends on temperature only, its temporal change can be obtained from the time derivative of the enthalpy difference at time t^{n+1} , whose new value is already known from the prior solution of Eq. (4.11) and (4.12) as

$$\frac{\partial(\rho^*)^{n+1}}{\partial t^*} = \left(\frac{\partial \rho^*}{\partial T^+} \frac{\partial T^+}{\partial \chi^+} \frac{\partial \chi^+}{\partial t^*} \right)^{n+1} \approx \frac{1}{\rho_0} \left(\frac{B_\rho T_\tau}{(c_p^*)^n} \right) \frac{\partial(\chi^+)^{n+1}}{\partial t^*},\tag{4.22}$$

where the coefficient B_ρ is retrieved from the polynomial representation of the constitutive law of ρ in Table 2.1 and the term $\frac{\partial(\chi^+)^{n+1}}{\partial t^*}$ is numerically approximated as discrete increment $\frac{(\chi^+)^{n+1} - (\chi^+)^n}{\Delta t^*}$ using Eqs. (4.11) and (4.12). Taking the divergence of Eq. (4.20) the Poisson equation for $(\pi^*)^{n+1}$ is obtained as

$$\begin{aligned}\frac{1}{r^*} \frac{\partial}{\partial r^*} \left(\frac{r^* \partial(\pi^*)^{n+1}}{\partial r^*} \right) + \frac{1}{r^{*2}} \frac{\partial^2(\pi^*)^{n+1}}{\partial \varphi^2} + \frac{\partial^2(\pi^*)^{n+1}}{\partial z^{*2}} = \\ \frac{1}{\Delta t^*} \left[\frac{1}{r^*} \frac{\partial r^* (\rho^* u^+)^{\dagger}}{\partial r^*} + \frac{1}{r^*} \frac{\partial(\rho^* v^+)^{\dagger}}{\partial \varphi} + \frac{\partial(\rho^* w^+)^{\dagger}}{\partial z^*} + \frac{\partial(\rho^*)^{n+1}}{\partial t^*} \right].\end{aligned}\tag{4.23}$$

For the fully developed pipe flow the numerical solution of Eq. (4.23) takes benefit from the spatial homogeneity in axial and azimuthal direction, so that a fast Fourier Transform (FFT) may be applied, which reduces the original formulation to a 1D problem, solved in spectral space for $j_{max} \times k_{max}$ Fourier modes $\hat{\pi}_{\alpha,\beta}^{*n+1} = f(r^*)$, for $\alpha = 1, \dots, j_{max}$ and $\beta = 1, \dots, k_{max}$:

$$\frac{1}{r^*} \left(r^* \frac{\partial \hat{\pi}_{\alpha,\beta}^{*n+1}}{\partial r^*} \right) + \Lambda_{\alpha,\beta} \hat{\pi}_{\alpha,\beta}^{*n+1} = R \hat{H} S.\tag{4.24}$$

The term $\Lambda_{\alpha,\beta}$ corresponds to the spatial eigenvalue of the problem and $R \hat{H} S$ is the FFT of the right hand side of Eq. (4.23). Once each Fourier transform $\hat{\pi}_{\alpha,\beta}^{*n+1}$ is obtained by means of Gaussian elimination, the solution is transformed back to physical space with an inverse fast Fourier transform (IFFT).

Boundary conditions

Inlet and outlet

As the straight pipe is periodic in axial direction, all flows variables u, v, w, p, χ to be solved are mapped directly from the outlet onto the inlet section, associated with $z^* = 5$ and $z^* = 0$, respectively, so that

$$\begin{aligned} u^+(r^*, \varphi, 0) &= u^+(r^*, \varphi, 5) \\ v^+(r^*, \varphi, 0) &= v^+(r^*, \varphi, 5) \\ w^+(r^*, \varphi, 0) &= w^+(r^*, \varphi, 5) \\ \chi^+(r^*, \varphi, 0) &= \chi^+(r^*, \varphi, 5) \end{aligned} \quad (4.25)$$

and, similarly, the periodicity in the azimuthal direction implies

$$\begin{aligned} u^+(r^*, 0, z^*) &= u^+(r^*, 2\pi, z^*), \\ v^+(r^*, 0, z^*) &= v^+(r^*, 2\pi, z^*), \\ w^+(r^*, 0, z^*) &= w^+(r^*, 2\pi, z^*), \\ \chi^+(r^*, 0, z^*) &= \chi^+(r^*, 2\pi, z^*). \end{aligned} \quad (4.26)$$

Centerline

The mathematical formulation of the governing equations written in polar coordinates inherently involves a singularity, when the radial coordinate r vanishes at the centerline. Here, the boundary conditions for the azimuthal and axial components of velocity, and for the enthalpy difference read

$$\begin{aligned} \left. \frac{\partial v^+}{\partial r^*} \right|_{r^*=0} &= 0, \\ \left. \frac{\partial w^+}{\partial r^*} \right|_{r^*=0} &= 0, \\ \left. \frac{\partial \chi^+}{\partial r^*} \right|_{r^*=0} &= 0, \end{aligned} \quad (4.27)$$

respectively, whereas the radial velocity component is imposed as the arithmetic mean between the face values of two cells adjacent to the centerline and azimuthally displaced by π

$$u^+(r^* = 0, \varphi, z, t) = \frac{1}{2} [u^+(\Delta r^*, \varphi, z, t) + u^+(\Delta r^*, \varphi + \pi, z, t)], \quad (4.28)$$

where Δr^* denotes the radial extension of the first cell near the centerline, as sketched in Fig. (4.4).

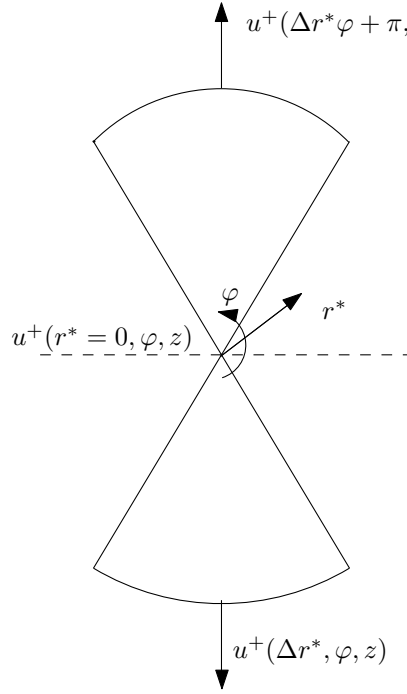


Figure 4.4: Two opposite cells near the centerline

Wall boundary

At the wall a no-slip and no-penetration boundary conditions are imposed for the velocity, written as

$$\begin{aligned} u^+|_{r^*=0} &= 0, \\ v^+|_{r^*=0} &= 0, \\ w^+|_{r^*=0} &= 0. \end{aligned} \tag{4.29}$$

The enthalpy difference, χ^+ , is imposed according to the three possible thermal wall boundary conditions explained in subsection 2.3.4.

Chapter 5

DNS of fully developed turbulent pipe flow

In this section the results of DNS obtained for the fully developed pipe flow configuration are presented, analyzed, and also critically assessed against available reference data. Firstly, the results are discussed and compared against analogous test cases assuming constant fluid properties. Identical reference conditions in terms of friction Reynolds number Re_τ and wall molecular Prandtl number Pr_w are assumed. In this part of the analysis, a validation against available experimental results and DNS from other authors will be performed and the effect of temperature depending material properties on the heat and momentum transfer is carefully analyzed. The analysis will be additionally extended by some further test cases imposing enhanced wall heating conditions, capable of triggering more pronounced variations in fluid properties, hence amplifying the possible back-coupling between heat and momentum transfer.

Secondly, the influence of different thermal boundary conditions on the near wall turbulence of the thermal field is investigated. Three different thermal boundary conditions were employed: a Dirichlet (*isothermal*), a Von Neumann (*isoflux*) boundary condition and, lastly, a conjugate heat transfer solution, in which the computation of the thermal field in the flow is coupled with the solution of the conductive heat transfer in the surrounding solid wall with a given thickness.

5.1 Considered DNS cases

All the DNS simulations of fully developed pipe flow were carried out for the same straight pipe geometry, whose details have been already described in section 4.1. The wall temperature at the outlet of the pipe, which defines the thermal reference conditions, is always assumed the same, being $T_{w,out} = 344.77 \text{ K}$. For the considered operating liquid, this setting implies a reference molecular Prandtl number being always $Pr_w = \frac{\mu_w c_{p,w}}{\lambda_w} = 10$. The individual DNS cases are summarized in Table 5.1. The first letter of the assigned labels indicates the type of thermal boundary condition, where "D" and "N" indicate Dirichlet (*isothermal*) and Von Neumann (*isoflux*) thermal b.c., respectively, while conjugate heat transfer cases are denoted by the initial three letter code "CHT". The second letter, next to the "D" or "N", indicates the direction of the wall heat flux, where "H" stands for heating,

and "C" for cooling. The doubling "HH" represent enhanced wall heating. This distinction between heated and cooled wall has been dropped in the labels of the constant fluid properties cases, where the non-dimensionalised thermal fields are the same for heating and cooling and have no effect on the flow field. The number at the end of each label denotes the wall friction Reynolds number at reference state $T_{w,out}$, $Re_\tau = \frac{w_\tau D \rho_w}{\mu_w}$.

Table 5.1: DNS test cases with variable fluid properties

<i>label</i>	Re_τ	fluid is	$\bar{q}_w [Wm^{-2}]$	fluid properties
DHH360	360	heated	$3.2 \cdot 10^4$	variable, v.f.p.
DH360	360	heated	$2 \cdot 10^4$	variable, v.f.p.
DC360	360	cooled	$-2 \cdot 10^4$	variable, v.f.p.
D360	360	-	$2 \cdot 10^4$	constant, c.f.p.
NH360	360	heated	$2 \cdot 10^4$	variable, v.f.p.
NC360	360	cooled	$-2 \cdot 10^4$	variable, v.f.p.
N360	360	-	$2 \cdot 10^4$	constant, c.f.p.
CHT360	360	-	$2 \cdot 10^4$	constant, c.f.p.
DHH500	500	heated	$4 \cdot 10^4$	variable, v.f.p.
DH500	500	heated	$2 \cdot 10^4$	variable, v.f.p.
DC500	500	cooled	$-2 \cdot 10^4$	variable, v.f.p.
D500	500	-	$2 \cdot 10^4$	constant, c.f.p.
DHH750	750	heated	$5 \cdot 10^4$	variable, v.f.p.
DH750	750	heated	$2 \cdot 10^4$	variable, v.f.p.
DC750	750	cooled	$-2 \cdot 10^4$	variable, v.f.p.
D750	750	-	$2 \cdot 10^4$	constant, c.f.p.

5.2 Validation and spatial resolution

In this section the accuracy of DNS simulations is addressed by firstly comparing the numerical results against the available reference data, as retrieved from literature at similar friction Reynolds number and secondly against the experiments carried out on the in house facility described in Section 3.3.

All DNS cases were carried out on a grid consisting of $256 \times 512 \times 1024$ points, respectively in radial, azimuthal and axial direction. The coarsest spatial resolution is expressed in wall units in Table 5.2 for the cases at $Re_\tau = 360, 500, 750$. The spatial resolution of the present DNS simulations was assessed by comparing the local grid size of the computational grid against the local Kolmogorov and Batchelor length scale, as introduced in Section 3.1 in Eq. (3.1) and (3.3). The estimation of these length scales is based on knowledge of the local dissipation rate of turbulent kinetic energy and of the local molecular viscosity.

Table 5.2: Grid size in DNS

Re_τ	Δr_{max}^+	$R\Delta\varphi_w^+$	Δz^+
360	1.38	2.21	1.75
500	2.08	3.07	2.44
750	3.44	4.60	3.66

The dissipation rate is computed from the gradients of the velocity fluctuations as

$$\langle \epsilon \rangle = \left\langle \nu \left(\frac{\partial u_i'}{\partial x_j} \frac{\partial u_i'}{\partial x_j} \right) \right\rangle, \quad (5.1)$$

where the averaging denoted by the operator $\langle \rangle$ is carried out along the spatial homogeneous directions and over time. This further leads to the following averaged expressions of the Kolmogorov and Batchelor length scale as function of only the local radial distance

$$\begin{aligned} \eta_K &= \left(\frac{\langle \nu \rangle^3}{\langle \epsilon \rangle} \right)^{1/4}, \\ \eta_B &= \frac{\eta_K}{\sqrt{\langle Pr \rangle}}, \end{aligned} \quad (5.2)$$

respectively, where $\langle \nu \rangle$ represents the averaged local kinematic viscosity and $\langle Pr \rangle$ the averaged molecular Prandtl number both dependent on the local material properties. The spatial resolution of velocity field in the radial, azimuthal, and axial directions, resolved by the DNS simulations is quantified by the ratios

$$\frac{\Delta r}{\eta_K}, \frac{r\Delta\varphi}{\eta_K}, \frac{\Delta z}{\eta_K}.$$

Similarly, the spatial resolution for the thermal field is represented by the ratios

$$\frac{\Delta r}{\eta_B}, \frac{r\Delta\varphi}{\eta_B}, \frac{\Delta z}{\eta_B}.$$

The radial variations of these ratios are shown in Fig. 5.1 for the simulations DC360, DC500, DC750 associated with $Re_\tau = 360, 500, 750$, respectively, $Pr_w = 10$ and a cooled pipe wall assuming variable material properties. These particular cases turned out to be the most demanding on the required spatial resolution, as the decreasing molecular viscosity towards the pipe centerline effectively leads to an enhanced turbulent small scale motion. This trend is reversed in the analogous cases with heated walls or absent in the constant fluid properties, resulting in less demanding resolution requirements.

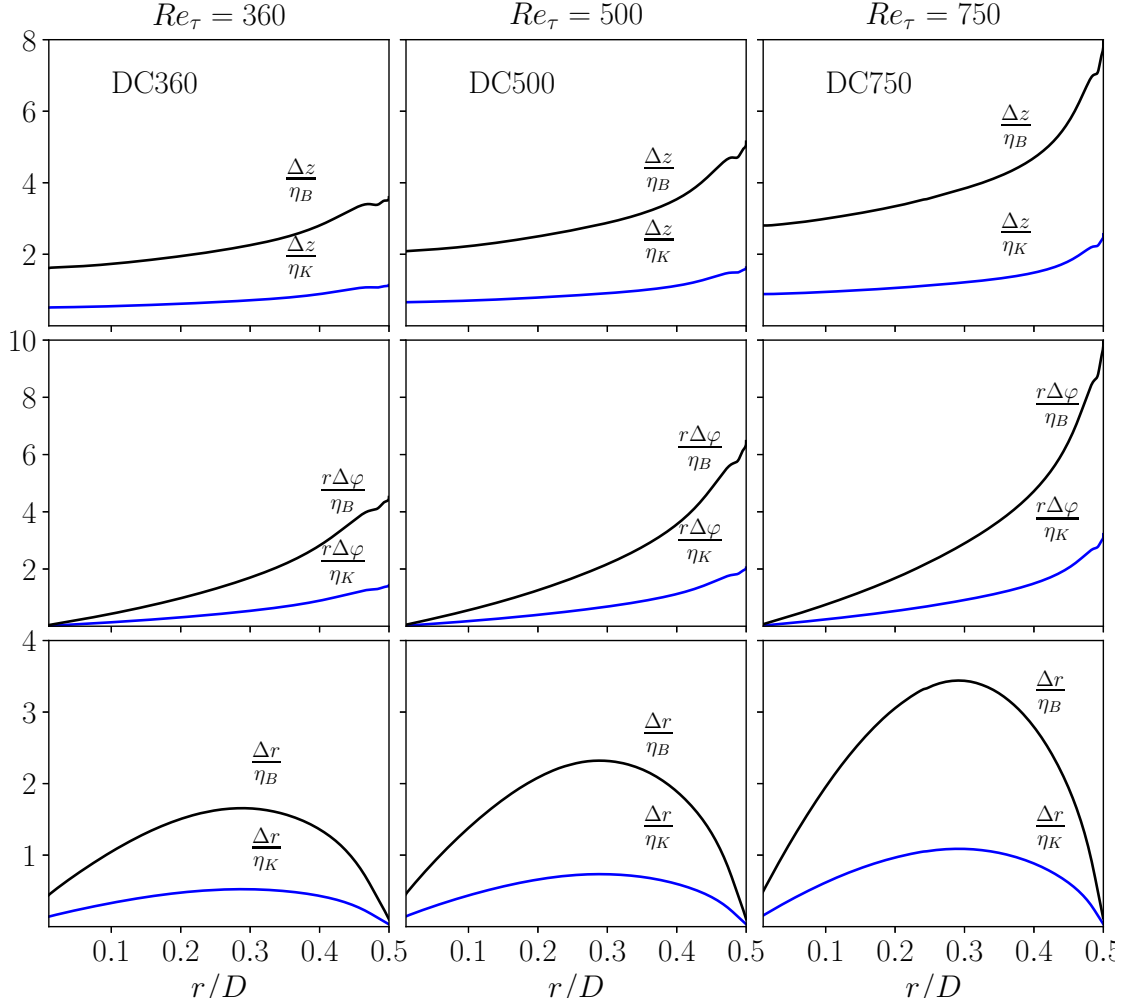


Figure 5.1: Spatial resolution normalized with the Kolmogorov length scale η_K and Batchelor length scale η_B for the DNS at $Re_\tau = 360, 500, 750$ and $Pr_w = 10$ under cooled conditions. Δr , $r\Delta\varphi$ and Δz represent the grid size in radial, azimuthal and axial directions, respectively

As expected and well illustrated in Fig. 5.1, the demand on spatial resolution increases at higher friction Reynolds numbers for both the momentum and thermal field. The azimuthal direction exhibits the highest ratios $\frac{r\Delta\varphi}{\eta_K}$, $\frac{r\Delta\varphi}{\eta_B}$ near the wall, due to the inherently increasing azimuthal span of the cells with increasing radial distance from the center line. Additionally, as an effect of the high molecular Prandtl number, the overall resolution of the thermal field is consistently lower than the resolution for momentum. At maximum, for $Re_\tau = 750$, the local grid size in azimuthal direction equals 10 times the local Batchelor length scale at the wall. Despite this notable excess over unity particularly obtained for $Re_\tau = 750$, the presently applied resolution is well comparable to similar previous DNS studies in literature, as reported in Irrenfried and Steiner (2017), Lee *et al.* (2013), Nemati and Patel (2016), Zonta *et al.* (2012).

5.2.1 Assessment against reference DNS data

Since no computational reference data were available for a fully developed heated/cooled pipe flow with the considered operating liquid, the DNS solution was rather validated against a highly resolved isothermal DNS of turbulent pipe flow with constant fluid properties at the same friction Reynolds number $Re_\tau = 360$. A comparison of the predicted mean axial velocity and the *rms* statistics of velocity components is shown in Fig. 5.2. The present predictions of 1st and 2nd-order statistics are evidently in very good agreement with the highly accurate reference data provided by Wu and Moin (2008) over the entire y^+ range.

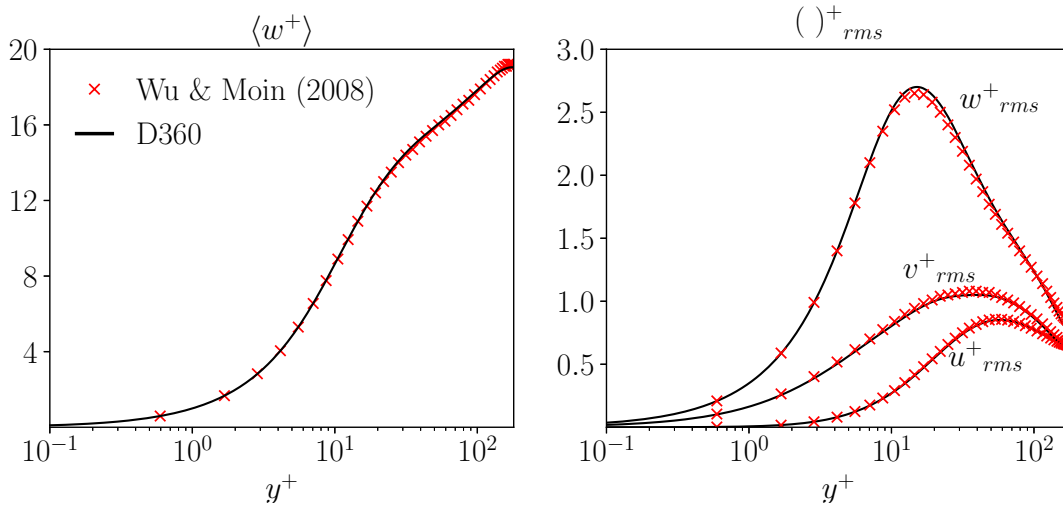


Figure 5.2: Mean axial velocity and *rms* of radial, azimuthal and axial velocity components against data of Wu and Moin (2008) with constant fluid properties

5.2.2 Assessment against experiments

The numerical results provided by DNS have been additionally validated against correspondent measurement data obtained from dedicated *in-house* experiments on fully developed pipe flows at several bulk Reynolds numbers. The comparison between numerical and experimental results was carried out for both the wall skin friction coefficient and the heat transfer coefficient, represented by the non-dimensional numbers C_f and Nu , respectively.

The assessment of the predicted momentum transfer was performed by comparing C_f predicted for the three c.f.p. cases D360, D500, D750 against measurements performed with unheated isothermal flow, where the material properties remain constant. The well-known correlation formulas developed by Konakov (1954) and Petukhov (1970) were considered as additional reference for assessing both numerics and experiments. The empirical correlations determine the skin friction coefficient dependent on the bulk Reynolds number as

$$C_{f,Konakov} = 0.25 (1.8 \log_{10}(Re_b) - 1.5)^{-2} \quad (5.3)$$

$$C_{f,Petukhov} = 0.25 (1.82 \log_{10}(Re_b) - 1.64)^{-2} \quad (5.4)$$

In Fig. 5.3, the wall skin friction coefficient in the laminar regime, $C_{f,laminar} = \frac{64}{Re_b}$, has been included for the sake of completeness, even though only a few laminar measurements have been conducted during the experimental campaign. As expected, a transition between $C_{f,laminar}$ and the correlations-based predictions of C_f is observed for $Re_b > 2300$. In the moderate and fully turbulent regime beyond $Re_b > 3000$, the experimental results turn out to fall in between the predictions of two correlations formulas, suggesting a reasonable accuracy of the measurements. This applies to the numerical results of the DNS cases D360, D500, D750 as well, which evidently show a very good agreement with both the experimental results and the correlation based predictions of C_f .

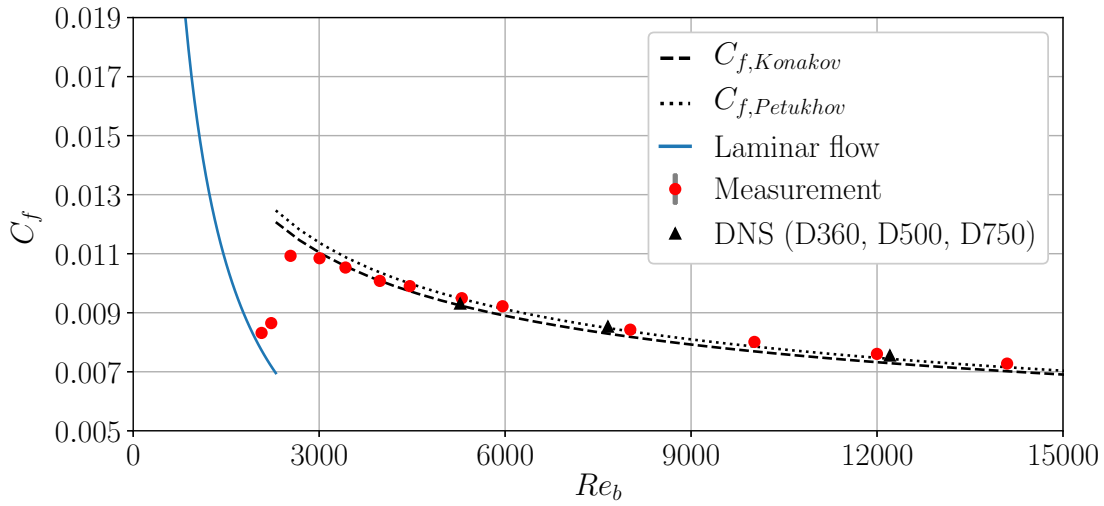


Figure 5.3: Skin friction coefficient C_f vs bulk Reynolds number Re_b

The validation of the global heat transfer coefficient Nu was carried out considering the results of DNS cases DH360, DH500, DH750.

The variation of the temperature-dependent material properties is also an important issue in the definition of reliable empirically adapted correlations for the Nusselt number, as widely used in the layout of thermal machinery involving convective pipe or channel flow. Most of them follow the proposal of Hufschmidt and Burck (1968), who correlate an “isothermal” base Nusselt number Nu_0 , dependent on a bulk Reynolds and Prandtl number, $Re_b = U_b D \rho_b / \mu_b$ and $Pr_b = \mu_b c_{p,b} / \lambda_b$, respectively, which would be approached in the theoretical limit of vanishing wall heat flux, $q_w \rightarrow 0$, and hence wall overtemperature $\Delta T = T_w - T_b \rightarrow 0$, associated with uniform material properties. This isothermal limit for zero wall heat flux is then modified by some correction factor K , which considers the temperature-dependent variation of the material properties near the wall. The correlations of Gnielinski (1975) and Petukhov (1970) are two popular representatives of this concept, which are written as

$$Nu_{Gnielinski} = Nu_0 K = \frac{(C_{f,Petukhov}/2)(Re_b - 1000)Pr_b}{1 + 12.7\sqrt{C_{f,Petukhov}/2}(Pr_b^{2/3} - 1)} K, \quad (5.5)$$

$$Nu_{Petukhov} = Nu_0 K = \frac{1/2 C_{f,Petukhov} Re_b Pr_b}{1.07 + 12.7 \sqrt{C_{f,Petukhov}/2} (Pr_b^{2/3} - 1)} K. \quad (5.6)$$

For liquids the correction factor reads

$$K = \left(\frac{Pr_b}{Pr_w} \right)^m, \quad \text{with } m = 0.11, \quad (5.7)$$

essentially representing the bulk-to-wall viscosity ratio μ_b/μ_w , which should somehow reflect the influence of varying dynamic viscosity on the turbulent transport. The input parameter $C_{f,Petukhov}$ represents the correlation-based skin friction coefficient as defined in Eq. (5.4).

In Fig. 5.4, the measured non-dimensional heat transfer coefficients at different bulk Reynolds numbers are shown and compared against the correlation-based predictions and the numerical results obtained for DH360, DH500 and DH750. The measurement uncertainty is indicated by grey vertical lines at each of the coloured spots, which represent the experimental mean values. The color of each measurement point indicates the measured wall overtemperature $\Delta T = T_w - T_b$. The black triangles refer to the Nusselt numbers predicted by the DNS with variable fluid properties (v.f.p.), where the corresponding wall overtemperatures $\Delta T = T_w - T_b$ are added as well for completeness.

The correlation of Petukhov (1970), Eq. (5.6), evidently agrees better with the experiments for the higher Reynolds number than the correlation of Gnielinski (1975), Eq. (5.5). The offset of the bulk Reynolds number in the nominator of Eq. (5.5), which was introduced to improve the predictions at the lower Reynolds numbers, is obviously rather disadvantageous for the higher Reynolds numbers near $Re_b \approx 10000$.

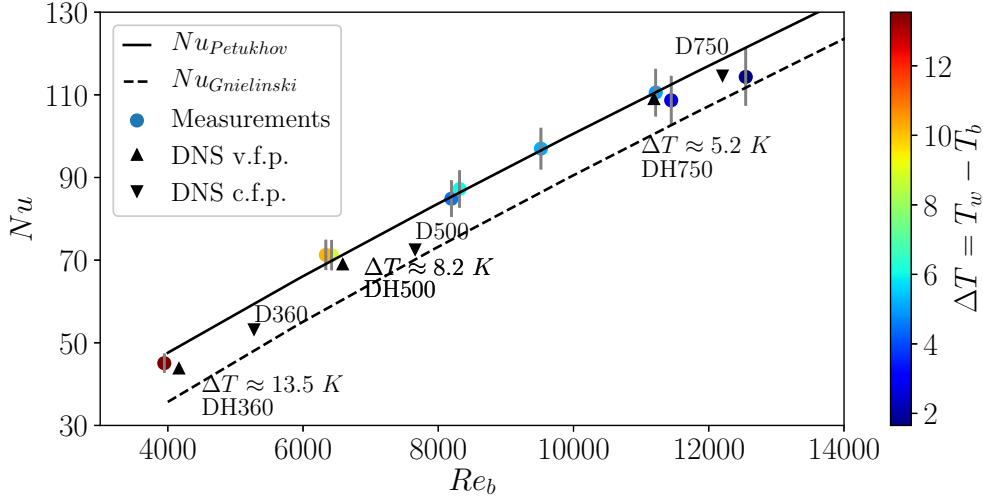


Figure 5.4: Heat transfer coefficient Nu vs bulk Reynolds number

The predictions of the v.f.p. DNS are generally in very good agreement with both the measurements and the correlation-based predictions, $Nu_{Petukhov}$. The predictions of the DNS with constant fluid properties (c.f.p.) are included as well to highlight the importance of the variation of the fluid properties in the considered cases. The locally varying viscosity

in the v.f.p. DNS always leads to a decreased bulk Reynolds number Re_b while the bulk Prandtl number Pr_b increases. The generally smaller Nusselt number, as compared to the c.f.p. results, clearly indicates a stronger influence of the variation in Re_b .

5.3 First order statistics

In the following discussion, the averaged velocity, enthalpy difference and fluid properties obtained from the different DNS cases will be examined in detail, so as to highlight in particular the effect of varying fluid properties on the first order turbulent statistics.

Statistical averaging has been performed over the homogeneous spatial directions φ , z and in time over approximatedly 30 flow-through times (FTT), where one FTT is considered to be the averaged time needed by a fluid particle to move through the entire pipe from the inlet to the outlet, being advected by the bulk velocity U_b , such that

$$1 \text{ FTT} = \frac{L}{U_b}. \quad (5.8)$$

Therefore, all statistics is only dependent on the radial distance r^* , or equivalently on the wall distance in wall units y^+ .

5.3.1 Variation of local material properties

The considered working fluid is a mixture of 50/50 Vol% glyserine and water, whose thermophysical material properties depend only on the temperature, as quantitatively described in Section 2.5. The molecular viscosity μ is most affected by the temperature, hence, undergoes the highest variations in the wall-normal direction, as compared to the other material properties. Even in the case DHH750, where the maximum difference in temperature between the wall and the centerline is achieved, variations in $\langle c_p^* \rangle$, $\langle \rho^* \rangle$, $\langle \lambda^* \rangle$ are confined within 5 % of their reference wall values, as compared to $\langle \mu^* \rangle$, which almost increases by a factor 2. This can be clearly observed in Fig. 5.5, where the averaged material properties are shown for DHH750 and DC360, which represent those cases, where the variation in fluid properties is highest considering heated and cooled walls, respectively.

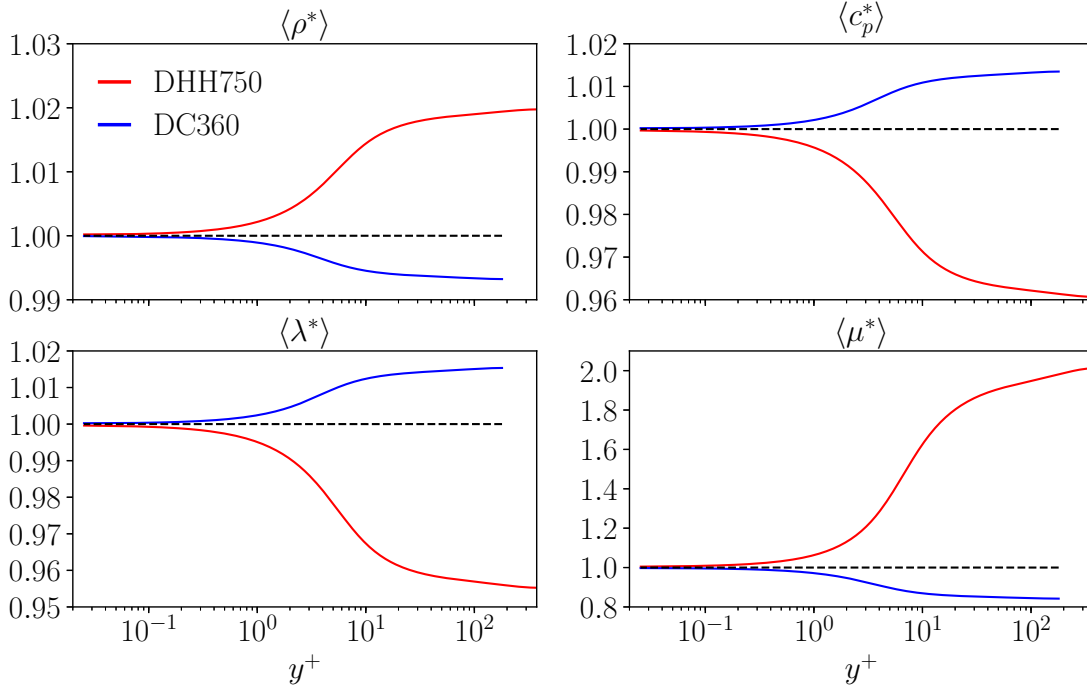


Figure 5.5: Averaged local material properties for DHH750 and DC360, dashed line representing constant fluid properties added as reference

The variation of density with respect to the assumed reference value ρ_w allows for a closer assessment of the possible influence of buoyancy which has been neglected in the governing equations presented in Eqs. (2.8)-(2.10). In line with the literature on stratified flows the analysis is based on the bulk and shear Richardson numbers, defined as

$$Ri_b = \frac{g\Delta\rho D}{\rho_w U_b^2} \quad (5.9)$$

and

$$Ri_\tau = \frac{g\Delta\rho D}{\rho_w u_\tau^2}, \quad (5.10)$$

respectively, where $\Delta\rho = |\rho_b - \rho_w|$ represents the deviation of bulk density from the wall reference value ρ_w , and $g = 9.81 \text{ m/s}^2$ the gravitational acceleration. For the case with the strongest wall heating (DHH750), where the variation of density is the highest, we obtain $Ri_b \approx 0.00077$ and $Ri_\tau \approx 0.18$. This is well below the range $0.001 < Ri_b < 0.01$ where first weak effects of buoyancy have been observed in the study of Sekimoto *et al.* (2011) for the unstably stratified conditions near the heated channel wall. Similarly, for the cooled wall, which resembles stably stratified conditions as the density increases towards the wall, the case with the largest variation of density (DC360) is associated with a bulk and shear Richardson numbers $Ri_b \approx 0.0011$ and $Ri_\tau \approx 0.26$, respectively. This falls again well below

the lower boundary of the regime of weakly/moderate stratified turbulence, which arises for shear Richardson numbers beyond $Ri_\tau \approx 5$ (Zonta and Soldati (2018)). The neglect of buoyant forces thus appears to be well justified for all considered heated and cooled cases.

When dealing with molecular Prandtl number well beyond unity, like in the considered operating conditions, steep temperature gradients occur in the vicinity of the wall, causing a strong variation in the molecular viscosity, which may significantly affect the advective and diffusive transport of momentum and heat. For a better understanding and interpretation of the computational results, it is therefore very instructive looking at the variation of the relevant characteristic parameters, the local Reynolds and molecular Prandtl number. The local mean values written as

$$\langle Re \rangle = \frac{\langle \rho \rangle w_\tau D}{\langle \mu \rangle}, \quad (5.11)$$

$$\langle Pr \rangle = \frac{\langle \mu \rangle \langle c_p \rangle}{\langle \lambda \rangle}. \quad (5.12)$$

essentially reflect the locally varying material properties. The radial variation of $\langle Re \rangle$ is quantitatively shown in Fig. 5.6, where a straight horizontal line is added to represent the constant fluid property case.

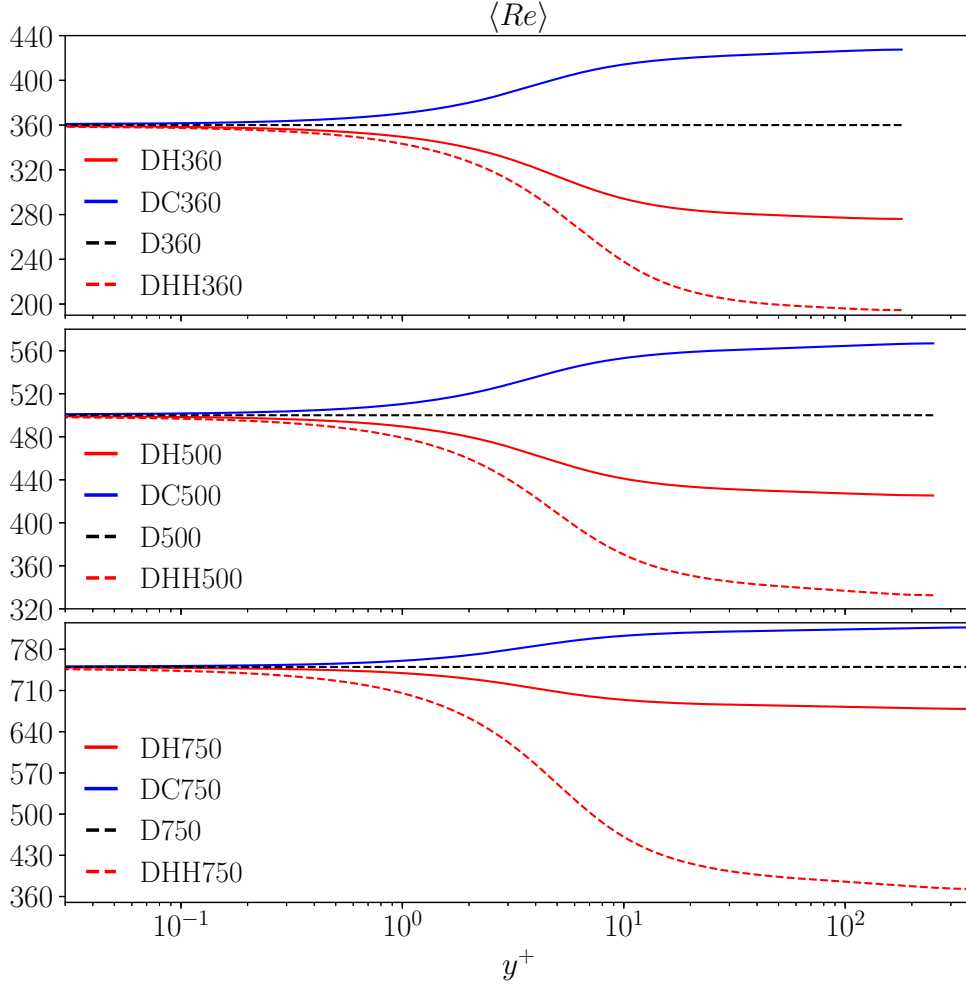


Figure 5.6: Wall normal variation of $\langle Re \rangle$ at three different reference friction Reynolds numbers $Re_\tau = 360, 500, 750$, and reference Prandtl number $Pr_w = 10$

Due to the negligible change in density, the variation of the mean molecular viscosity effectively determines the local Reynolds number. A negative mean wall heat flux corresponds to a cooled pipe and leads to an increased local Reynolds number towards the centerline, as the viscosity decreases relative to the cold wall level. This trend is realized in the cases DC360, DC500 and DC750, as seen from the blue lines. On the contrary, when the pipe is heated, a positive mean wall heat flux is applied, and the local Reynolds number drops towards the center, as the viscosity relatively increases with distance from the hot wall. The decrease in Reynolds number is more pronounced for higher wall heat fluxes, which indicates a stronger variation of the molecular viscosity.

The reverse trend is observed in the variation of local Prandtl number $\langle Pr \rangle$. Here, a cooled wall results in a decrease of $\langle Pr \rangle$ towards the centerline, whereas a heated wall leads to an increased local Prandtl number, as clearly observed in Fig. 5.7. The maximum variation

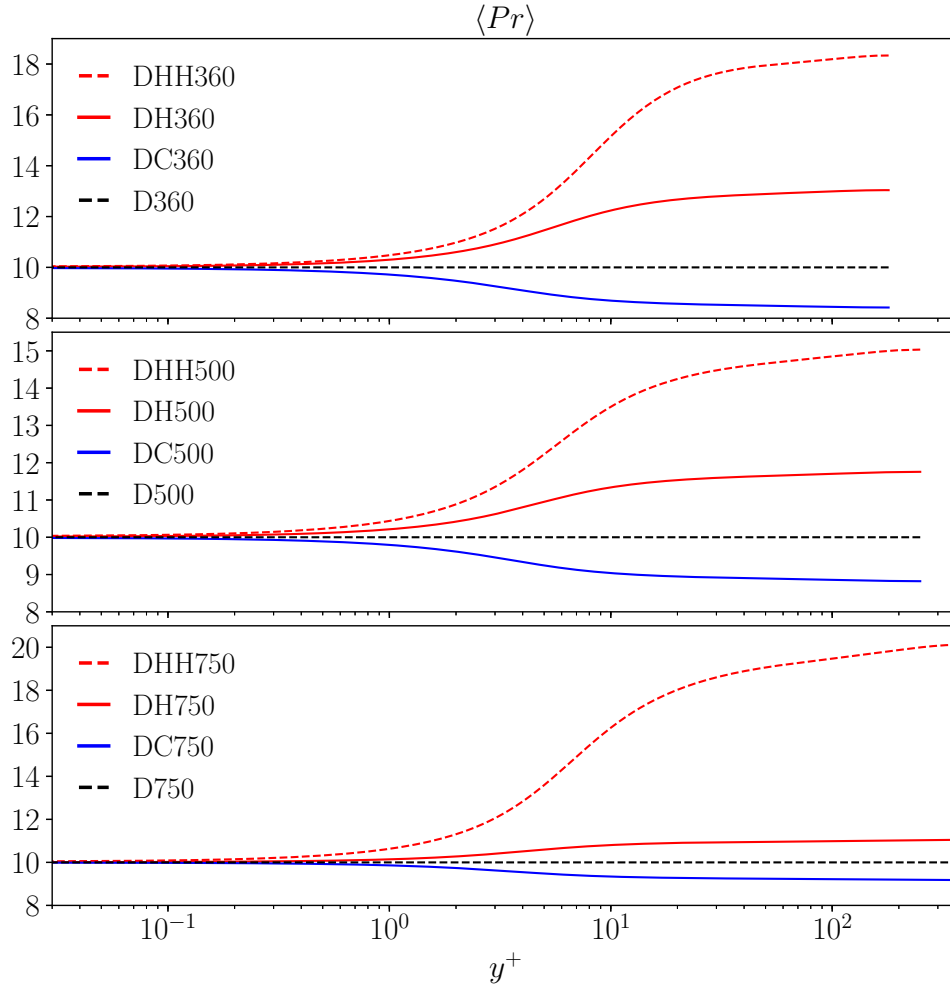


Figure 5.7: Wall normal variation of $\langle Pr \rangle$ at three different reference friction Reynolds number $Re_\tau = 360, 500, 750$ and $Pr_w = 10$

in $\langle Pr \rangle$ occurs in the case DHH750, which reflects the increase by almost 100% of the molecular viscosity relative to the wall conditions. Moreover, for the same absolute wall heat fluxes, represented by the value of $\langle q_w \rangle$, an increased friction Reynolds number always leads to a reduced variation of both $\langle Re \rangle$ and $\langle Pr \rangle$. The increased turbulent mixing associated with higher Re_τ evidently enhances the heat transfer rate, which leads to a smaller wall overtemperature $\Delta T = T_w - T_b$ for given wall heat flux $\langle q_w \rangle$. The resulting spatially more homogeneous temperature causes less variation in the material properties.

5.3.2 Axial velocity

The first order statistics of axial velocity $\langle w^+ \rangle$ exhibit markedly different trends due to the effect of local varying material properties. Figure 5.8 shows the variation of $\langle w^+ \rangle$ compared against the reference solution with constant fluid properties, represented by a dashed black line. At all considered friction Reynolds numbers, the heated cases DH360,

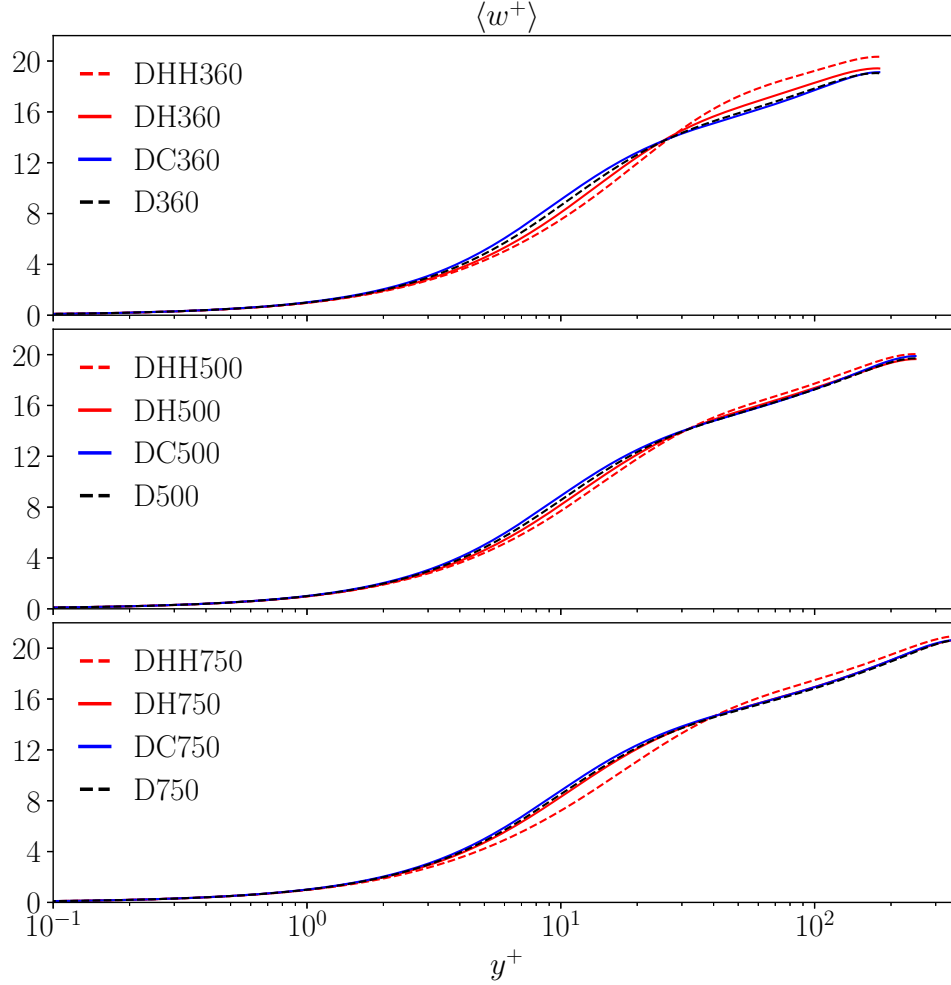


Figure 5.8: Averaged axial velocity profile at reference friction Reynolds number $Re_\tau = 360, 500, 750$

DH500, DH750 show always a lower averaged velocity profile in the wall region up to $y^+ \approx 30$. This decrease becomes more pronounced when the wall heat flux is enhanced, as seen from the profiles of the cases DHH500 and DHH750. For $Re_\tau = 360$, when approaching the centerline is approached, the averaged axial velocity in DH360 is increased well above the prediction for D360 associated with constant material properties. At the higher friction Reynolds numbers $Re_\tau = 500/750$, this excess of velocity near the centre is observed only in the strongly heated cases DHH500 and DHH750. For the less heated cases DH500 and DH750, which assume the same wall heat flux as DH360, the predictions in the core region practically collapse with the corresponding profiles of the reference cases with constant fluid properties.

Conversely, the cooled cases DC360, DC500 and DC750 (blue lines in Fig. 5.8) are characterized by a generally higher axial velocity near the wall, as compared to the corresponding profiles for the heated and constant fluid properties cases. For DC360, beyond

$y^+ \approx 30$, a slight decrease in $\langle w^+ \rangle$ is observed, as compared to the predictions for DH360 and D360. This relative decrease is not observed at higher Re_τ . At $Re_\tau = 750$ a reverse trend is rather observed, where velocity profile continuously somewhat exceeds the c.f.p. reference profile.

5.3.3 Enthalpy difference

In Fig. 5.9 the averaged enthalpy difference profiles $\langle \chi^+ \rangle$ are illustrated. The reference Pr_w well beyond unity brings about steep temperature gradients in the diffusive sublayer, which further leads to the observed markedly divergent trends of $\langle \chi^+ \rangle$ in the buffer layer. The increase/decrease of local Prandtl number $\langle Pr \rangle$ discussed above and shown in Fig. 5.7 may be related to a corresponding increase/reduction of the local thermal resistance. This, explains the strongest increase of the mean enthalpy difference towards the centerline seen

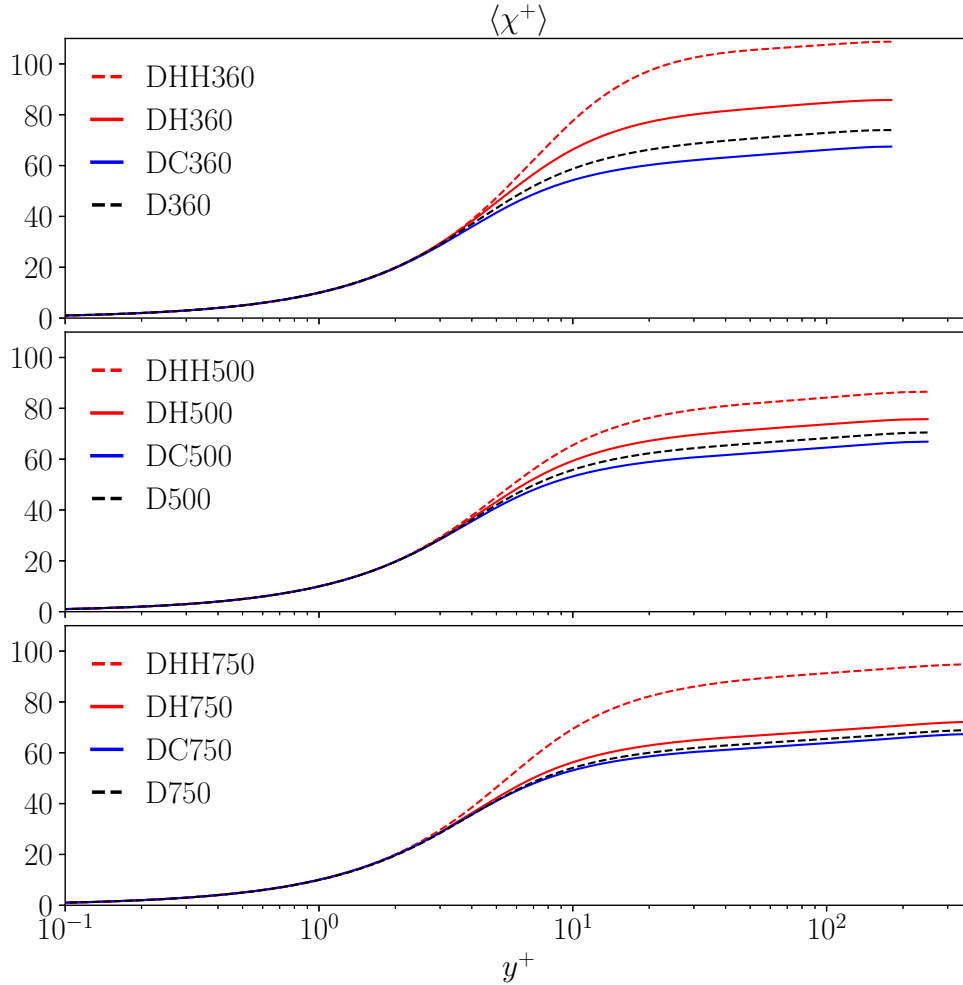


Figure 5.9: Averaged enthalpy difference profile at reference friction Reynolds numbers $Re_\tau = 360, 500, 750$

for the cases with the strongest wall heating DHH360, DHH500, DHH750, where the Prandtl number reaches the highest core levels. The opposite trend is seen for the cooled cases DC360, DC500, and DC750. Here the Prandtl number decreases with distance from the cold wall, which together with the enhanced turbulent advective mixing leads to continuously lower $\langle \chi^+ \rangle$ -profiles as compared to the c.f.p. references.

5.4 Higher order statistics

In this section the 2nd and higher order statistical moments of the turbulent fluctuating flow variables are presented and discussed. In the following analysis the density is assumed as constant, due to the observed rather limited fluctuation in density ($\rho' \approx 0$). Consequently, the Reynolds average $\langle \cdot \rangle$, introduced in Eq. (2.2), and density-weighted average can be considered equivalent, such that

$$\hat{\phi} = \frac{\langle \rho \phi \rangle}{\langle \rho \rangle} \approx \langle \phi \rangle. \quad (5.13)$$

5.4.1 Turbulent velocity fluctuations

The variation in local temperature-dependent molecular viscosity has a strong impact on the radial variation of the turbulent fluxes of momentum. The modulation of the turbulent advective motion can be closely related to the variation of the local Reynolds number, which drops towards the centerline for the heated wall cases, while it increases for the cooled wall conditions. Accordingly, turbulent mixing is mitigated towards the centerline in the first, whereas it is enhanced in the latter. A key role in turbulent mixing of both momentum and heat is played by the wall-normal velocity fluctuations, which are shown in terms of *rms*-statistics in Fig. 5.10, as obtained in the DNS cases at different wall friction Reynolds numbers.

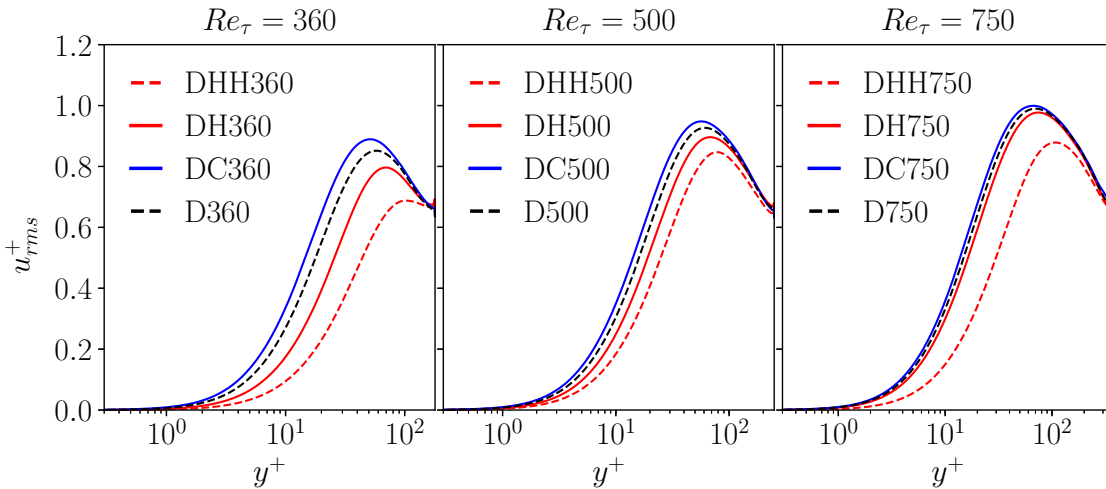


Figure 5.10: *Rms*-value of the turbulent fluctuating velocity component in radial direction for heated and cooled cases at $Re_\tau = 360, 500, 750$

A clear trend exhibited by all heated and strongly heated cases (DH and DHH, respectively) can be identified in a general dampening of wall-normal velocity fluctuations. The dampening is evidently stronger with increasing wall heat fluxes. The tendency is also more pronounced at lower Reynolds number and weaker at higher ones. The inherently stronger turbulence intensity for increasing Re_τ leads to higher heat transfer rates, which reduces the wall-to-bulk overtemperature $\Delta T = T_w - T_b$ for given wall heat flux $\langle q_w \rangle$. The resulting smaller variations of the temperature dependent molecular viscosity brings the solution closer to the constant fluid properties (c.f.p.) reference cases.

Aside from the change in magnitude, the local variation of molecular viscosity also alters the radial position of the maximum of the turbulent fluctuations. The maximum of u_{rms}^+ is always shifted towards the center for the heated cases, while it is shifted towards the wall for the cooled cases. The larger displacement is seen for the higher wall heat fluxes, which reflects the stronger variation of the molecular viscosity very next to the wall.

As shown in Fig. 5.11, the fluctuating azimuthal velocity component v'^+ exhibits essentially the same trends as seen for u'^+ .

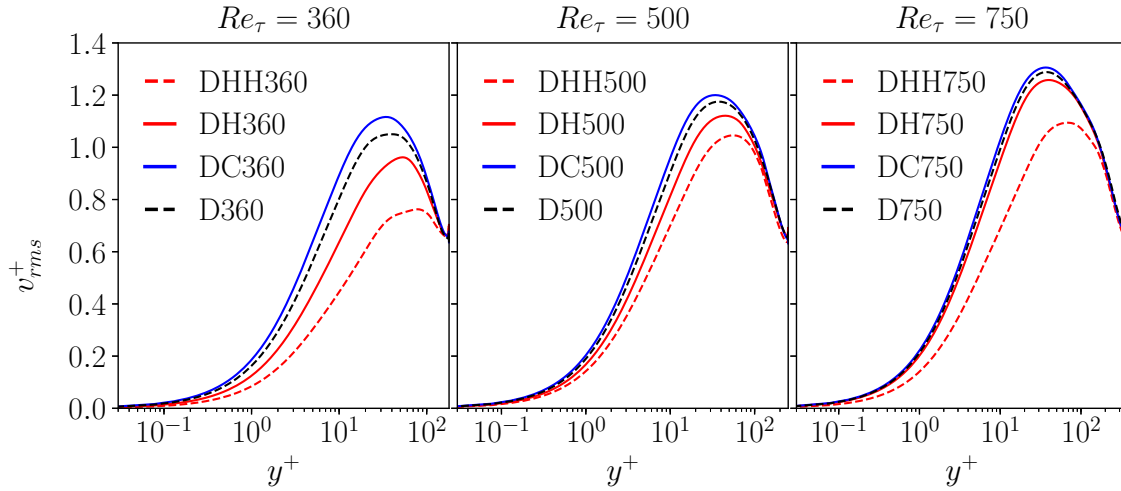


Figure 5.11: Rms -value of turbulent fluctuating velocity component in azimuthal direction for heated and cooled cases at $Re_\tau = 360, 500, 750$

A notably different behaviour is observed for the intensity of fluctuations of the axial velocity component w^+ . As seen from Fig. 5.12, the position of the peak of w_{rms}^+ is shifted again away from/towards the heated/cooled wall. However, very different to u_{rms}^+ and v_{rms}^+ , the magnitude of the peak is not notably neither decreased nor increased. It is even somewhat increased for the heated cases at lowest Reynolds number $Re_\tau = 360$, thus going into the opposite direction. Encountering, at the same time, significantly dampened velocity fluctuations in the other two flow directions, this relative increase of w_{rms}^+ effectively makes the turbulent motion more anisotropic. This aspect may become an important issue in the turbulence modelling, which is often based on the assumption of isotropic turbulence.

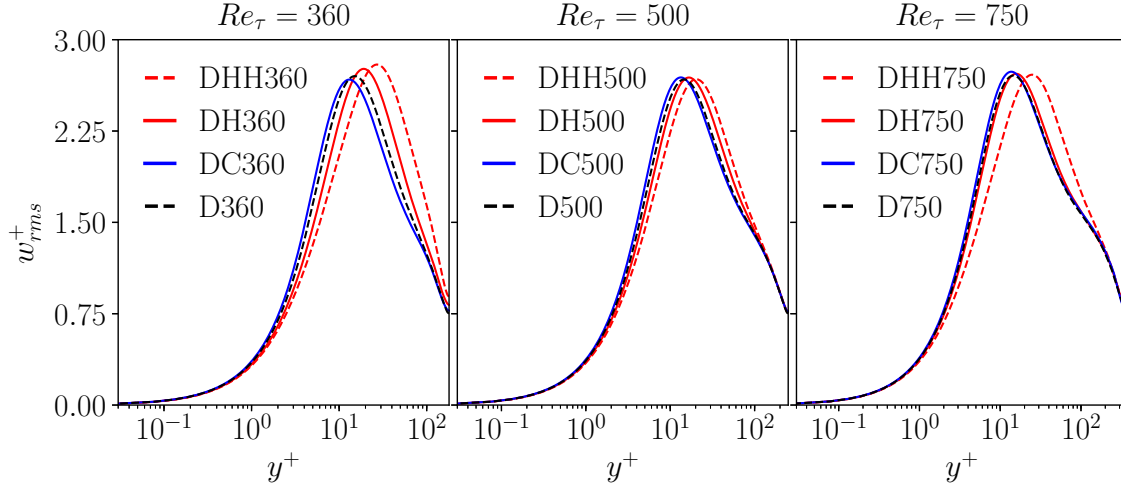


Figure 5.12: Rms -value of turbulent fluctuating velocity component in axial direction for heated and cooled cases at $Re_\tau = 360, 500, 750$

The rms -statistics in the three spatial directions affects by definition the total turbulent kinetic energy $k^+ = \frac{(u_{rms}^{+2} + v_{rms}^{+2} + w_{rms}^{+2})}{2}$. As seen in Fig. 5.13, k^+ exhibits a shift of its peak position, as generally observed for u_{rms}^+ , v_{rms}^+ and w_{rms}^+ . Only at $Re_\tau = 360$ the observed enhanced fluctuations in the axial velocity component overcompensate the drop of its radial and azimuthal counterparts, so that the peak level of k^+ is still highest for DHH360 and DH360. This is not the case for $Re_\tau = 500$ and $Re_\tau = 750$, where the peak is again spatially shifted again, but is lower in magnitude.

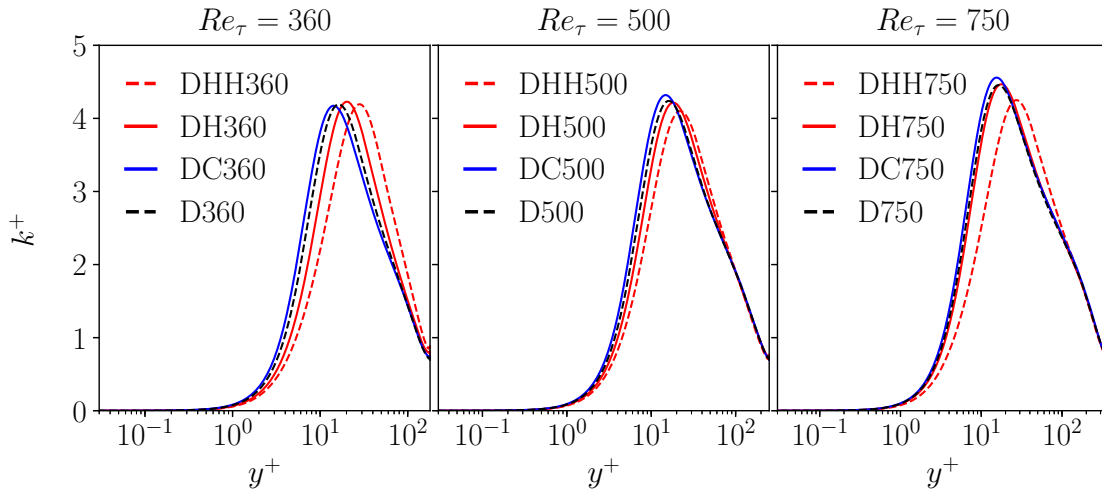


Figure 5.13: Turbulent kinetic energy k^+ for heated and cooled cases at $Re_\tau = 360, 500, 750$

5.4.2 Laminar and turbulent shear stress

Basically, three contributions to the total shear stress τ_{tot}^+ arise, when varying material properties in a turbulent pipe flow are considered:

$$\tau_{tot}^+ = \underbrace{-\langle \rho^* u'^+ w'^+ \rangle}_{\tau_{turb}^+} + \underbrace{\langle \mu^* \rangle \frac{\partial \langle w^+ \rangle}{\partial r^*}}_{\tau_{lam}^+} + \underbrace{\left\langle \mu'^* \frac{\partial w'^+}{\partial r^*} \right\rangle}_{\tau_{prop}^+}. \quad (5.14)$$

The terms on the right-hand side, τ_{turb}^+ , τ_{lam}^+ , and τ_{prop}^+ represent the transfer of momentum caused by turbulent fluctuations, by laminar diffusion, and by variation in fluid properties, respectively. Even in the cases, where the variation of the mean material properties is largest, namely for DHH750 and DHH500, the contribution τ_{prop}^+ turned out to be quite small when compared to both τ_{turb}^+ and τ_{lam}^+ . Therefore, it may be reasonably neglected in all the following analysis without a significant loss of accuracy. The aforementioned increase in viscosity towards the center line in the heated cases consistently leads to an increased laminar shear stress contribution, as shown in Fig. 5.14. This tendency becomes even more pronounced when the wall heating is enhanced, so that variation of molecular viscosity from its reference wall value is amplified. The enhanced wall heat flux conditions, represented by the cases DHH360, DHH500, DHH750, consider an average wall heat flux augmented by a factor of 1.6, 2 and 5 as compared to the cases DH360, DH500 and DH750, respectively. The increase in τ_{lam}^+ for the heated cases is coherently accompanied by a decreased contribution of the turbulent stress τ_{turb}^+ over a significant portion of the region near the wall up to $y^+ \approx 70$, as it can be observed in the left column of Fig. 5.14. On the contrary, the cooled wall conditions represented by the cases DC360, DC500 and DC750 always result in an enhancement of the turbulent stress, as compared to the respective reference lines represented by D360, D500 and D750, associated with constant fluid properties. The basic tendency, which distinguishes the heated from the cooled test cases, matches well with the general trend of $\langle Re \rangle$, discussed above. Cooled walls lead to a higher mean local Reynolds number and enhanced turbulent mixing of momentum along the wall normal direction, so that $-\tau_{turb}^+$ increases. On the contrary, the heated walls lead to a decrease in local mean Reynolds number, so that $-\tau_{turb}^+$ and the related turbulent mixing are reduced.

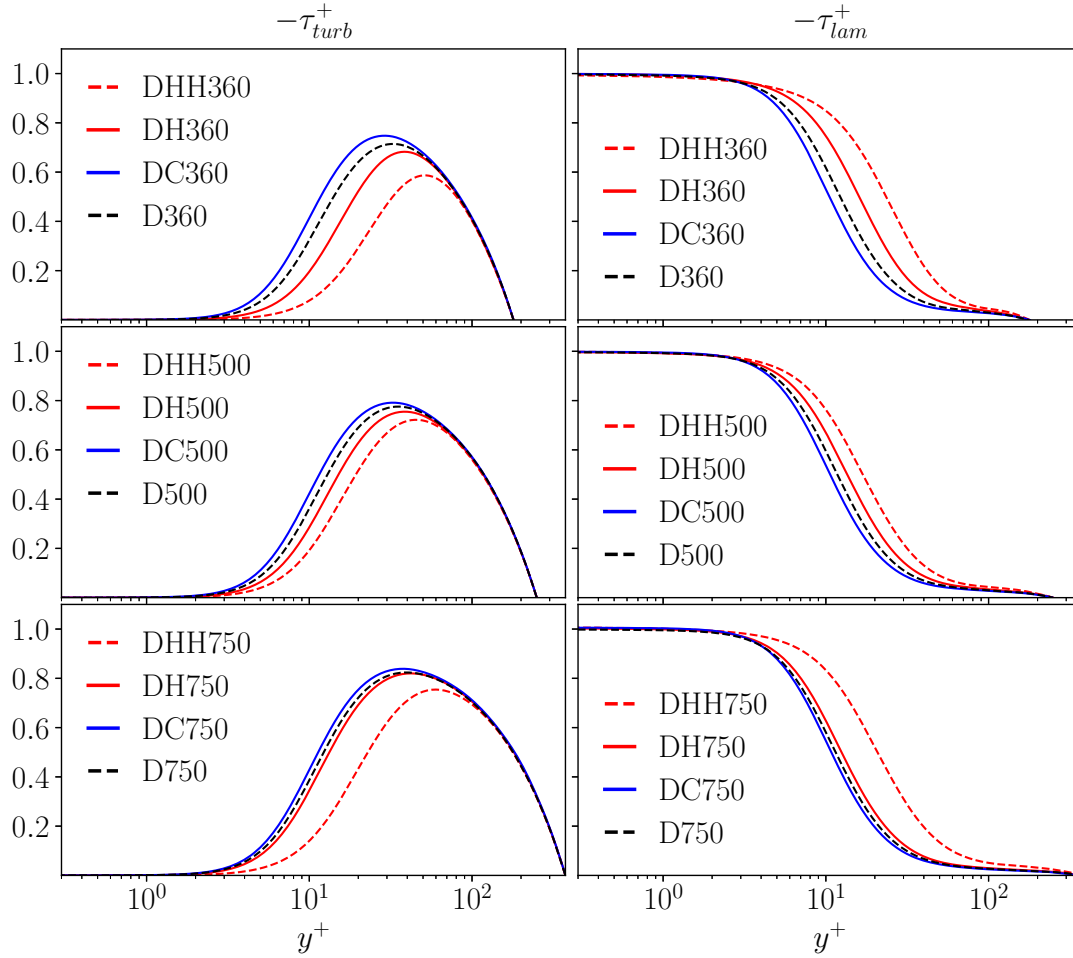
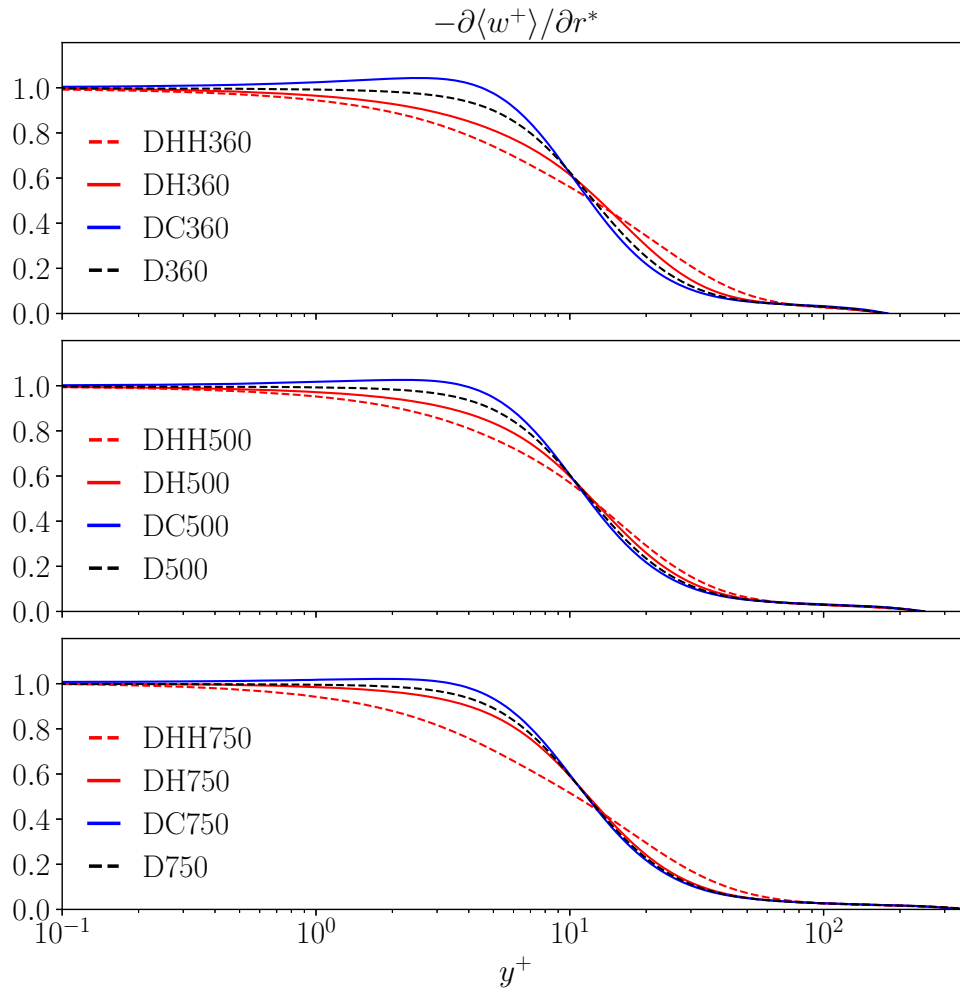


Figure 5.14: Turbulent and laminar contribution to total shear stress at reference friction Reynolds number $Re_\tau = 360, 500, 750$ for different wall heat fluxes

In all cases, the differences in τ_{lam}^+ , which arise between the cooled, heated and strongly heated conditions, can be predominantly attributed to the pronounced variation of the local molecular viscosity rather than to a modulation of the shear rate. As seen from Fig. 5.15, the shear rate $-\frac{\partial \langle w^+ \rangle}{\partial r^*}$ is, even reduced for the heated case, while it is enhanced for the cooled case in the region up to $y^+ \approx 10$. The trend is reverse further beyond. The observed decrease of $-\frac{\partial \langle w^+ \rangle}{\partial r^*}$ for the heated cases has an important effect on the production of turbulent kinetic energy, as will be discussed in the following subsection.

Figure 5.15: Mean shear rate at reference friction Reynolds numbers $Re_\tau = 360, 500, 750$

5.4.3 Budgets for turbulent kinetic energy and shear stress

The transport equation for the the turbulent stresses of momentum $\langle \rho u'_i u'_j \rangle$ can be generally written in dimensional index notation as

$$\begin{aligned}
 \frac{\partial \langle \rho u'_i u'_j \rangle}{\partial t} + \frac{\partial (\langle \rho u'_i u'_j \rangle \langle u_i \rangle)}{\partial x_i} = & \underbrace{-\langle \rho u'_j u'_k \rangle \frac{\partial \langle u_i \rangle}{\partial x_k} - \langle \rho u'_i u'_k \rangle \frac{\partial \langle u_j \rangle}{\partial x_k}}_{P_{ij}} \\
 & - \underbrace{\frac{1}{2} \frac{\partial \langle \rho u'_i u'_j u'_k \rangle}{\partial x_k}}_{T_{ij}} - \underbrace{\frac{\partial \langle p' u'_j \rangle}{\partial x_i} - \frac{\partial \langle p' u'_i \rangle}{\partial x_j}}_{\Pi_{ij}} + \underbrace{\langle p' \left[\frac{\partial u'_j}{\partial x_i} + \frac{\partial u'_i}{\partial x_j} \right] \rangle}_{\Psi_{ij}} \\
 & + \underbrace{\frac{\partial \langle \tau'_{ik} u'_j \rangle}{\partial x_k} + \frac{\partial \langle \tau'_{jk} u'_i \rangle}{\partial x_k}}_{D_{ij}} - \underbrace{\langle \tau'_{ik} \frac{\partial u'_j}{\partial x_k} \rangle - \langle \tau'_{jk} \frac{\partial u'_i}{\partial x_k} \rangle}_{\varepsilon_{ij}}.
 \end{aligned} \tag{5.15}$$

where P_{ij} represents the production, T_{ij} the turbulent diffusion, Π_{ij} the pressure diffusion, Ψ_{ij} the pressure deformation, D_{ij} the viscous diffusion, ε_{ij} the dissipation of the ij -th component of the turbulent stress of momentum. The budget for the normal turbulent stresses of momentum is obtained from Eq. (5.15) by setting $i = j = 1, 2, 3$, leading to the evolution equations for $\langle u'^{+2} \rangle$, $\langle v'^{+2} \rangle$ and $\langle w'^{+2} \rangle$, respectively. For the considered fully developed flow, a non-zero production rate term only appears in the budget for the streamwise component. The production reads in non-dimensional form

$$P_{zz}^+ = -2 \langle \rho^* u'^+ w'^+ \rangle \frac{\partial \langle w^+ \rangle}{\partial r^*}. \tag{5.16}$$

As such, this term is responsible for the production of the normal stress $\langle w'^{+2} \rangle$, which mostly contributes to the turbulent kinetic energy k^+ . The fluctuations of velocity in the streamwise component are further redistributed to the remaining spatial directions and converted into $\langle u'^{+2} \rangle$ and $\langle v'^{+2} \rangle$ through the pressure deformation term, represented by

$$\psi_{zz}^+ = - \left\langle \pi'^* \frac{\partial w'^+}{\partial r^*} \right\rangle. \tag{5.17}$$

Consistently, with the pressure deformation term acts as source term, in the budget of $\langle u'^{+2} \rangle$, where it appears as

$$\psi_{rr}^+ = - \left\langle \pi'^* \frac{\partial u'^+}{\partial r^*} \right\rangle. \tag{5.18}$$

$\langle u'^{+2} \rangle$ in turn contributes to the production of the turbulent shear stress $-\tau_{trb}^+ = \langle \rho^* w'^+ u'^+ \rangle$, through the production term

$$P_{rz}^+ = - \langle \rho^* u'^+ u'^+ \rangle \frac{\partial \langle w^+ \rangle}{\partial r^*}, \tag{5.19}$$

which appears in the budget of $\langle \rho^* u'^+ w'^+ \rangle$.

Finally, $\langle \rho^* u'^+ w'^+ \rangle$ takes part in the production of $\langle \rho^* w'^+ w'^+ \rangle$ through Eq. (5.16), closing the so called "cycle of turbulence" (Pope (2000)).

When variable fluid properties are considered, the aforementioned mechanism can be altered in such a way, that the transfer of kinetic energy from the streamwise velocity component is either dampened (heated case) or enhanced, leading to less or more pronounced isotropic turbulence, respectively. This effect can be observed in Fig. 5.16, which shows the budgets of $\langle \rho^* w'^+ w'^+ \rangle$. Here, the heated cases DH360 and DHH360 are characterized by a lower production P_{zz}^+ , which is additionally shifted towards the centerline of the pipe. The opposite trend is seen for the cooled case (DC360). The redistribution term ψ_{zz}^+ in the budget of $\langle \rho^* w'^+ w'^+ \rangle$ and its counterpart ψ_{rr}^+ in the budget of $\langle \rho^* u'^+ u'^+ \rangle$ is also dampened when heated wall conditions are considered, as seen in Figs. 5.16 and 5.17.

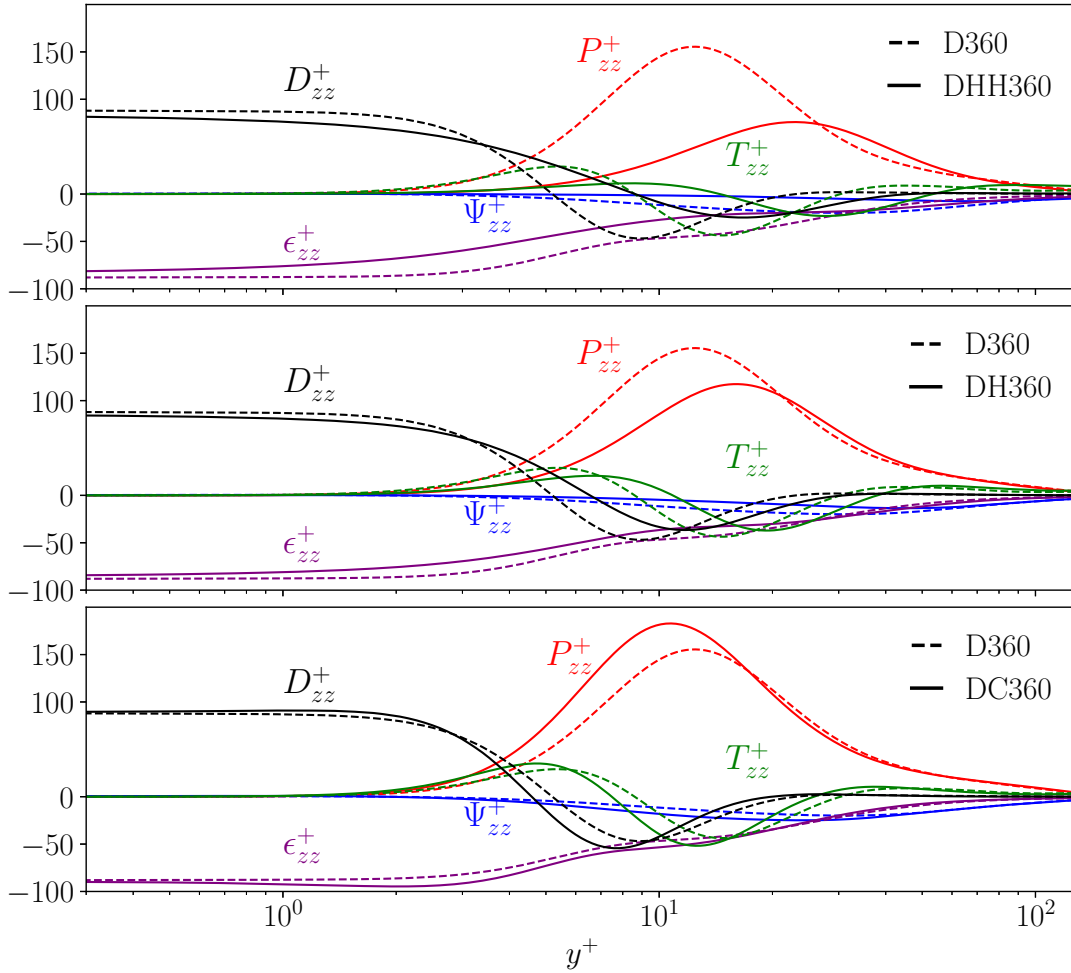
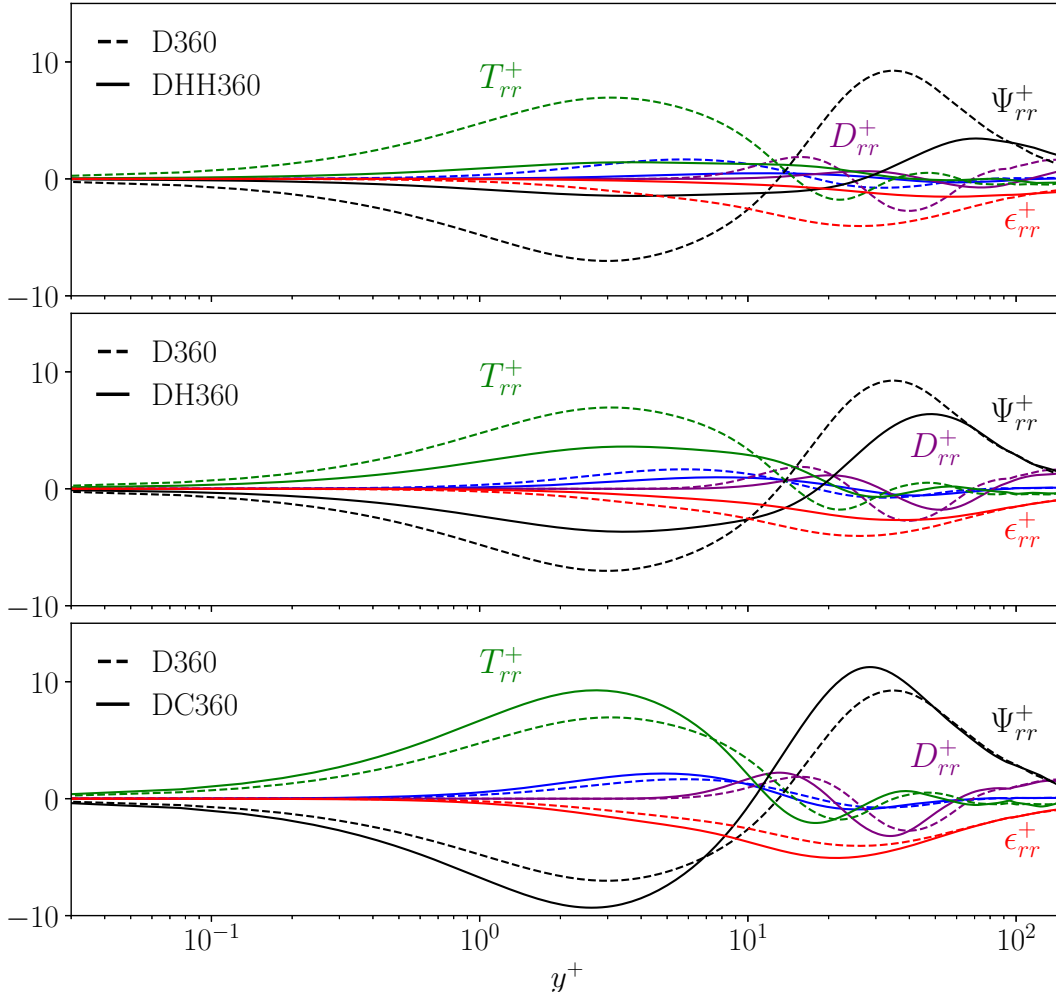


Figure 5.16: Turbulent $\langle \rho^* w'^+ w'^+ \rangle$ -budget for heated and cooled cases at $Re_\tau = 360$

Figure 5.17: Turbulent $\langle \rho^* u^+ u'^+ \rangle$ -budget for heated and cooled cases at $Re_\tau = 360$

This explains the reduced rms-values of the radial and azimuthal fluctuating velocity components, observed in Fig. 5.10, and 5.10, respectively. This dampening effectively reduces the production of turbulent shear stress, so that it becomes markedly lower near the heated wall, as shown in Fig. 5.14.

The evolution equation for the turbulent kinetic energy $k = \frac{\langle u'_i u'_i \rangle}{2}$ is obtained by contracting Eq. (5.15) to

$$\begin{aligned}
 \frac{\partial \langle \rho k \rangle}{\partial t} + \frac{\partial (\langle \rho u_i \rangle k)}{\partial x_i} = & \underbrace{-\langle \rho u'_i u'_k \rangle \frac{\partial \langle u_i \rangle}{\partial x_k}}_{P_k} - \underbrace{\frac{1}{2} \frac{\partial \langle \rho u'_j u'_i u'_i \rangle}{\partial x_j}}_{T_k} \\
 & \underbrace{-\frac{\partial \langle p' u'_i \rangle}{\partial x_i}}_{\Pi_k} + \underbrace{\frac{\partial \langle \tau'_{ij} u'_i \rangle}{\partial x_j}}_{D_k} - \underbrace{\langle \tau'_{ij} \frac{\partial u'_i}{\partial x_j} \rangle}_{\varepsilon_k}.
 \end{aligned} \tag{5.20}$$

In Eq. (5.20), the first term P_k denotes the production term and acts as a source for k . It is simply represented by the half of the production term in the budget of $\langle \rho^* w'^+ w'^+ \rangle$, such that $P_k = \frac{1}{2} P_{zz}$.

The terms \bar{D}_k , T_k and Π_k describe the laminar viscous diffusion, the diffusion due to turbulent fluctuations, and due to pressure fluctuations of k , respectively. Lastly, the dissipation term ε_k acts as a sink in Eq. (5.20), which is essentially responsible for the destruction of k . For the considered fully developed turbulent pipe flow the non-dimensional representations of the individual contributions to the budget of k^+ become

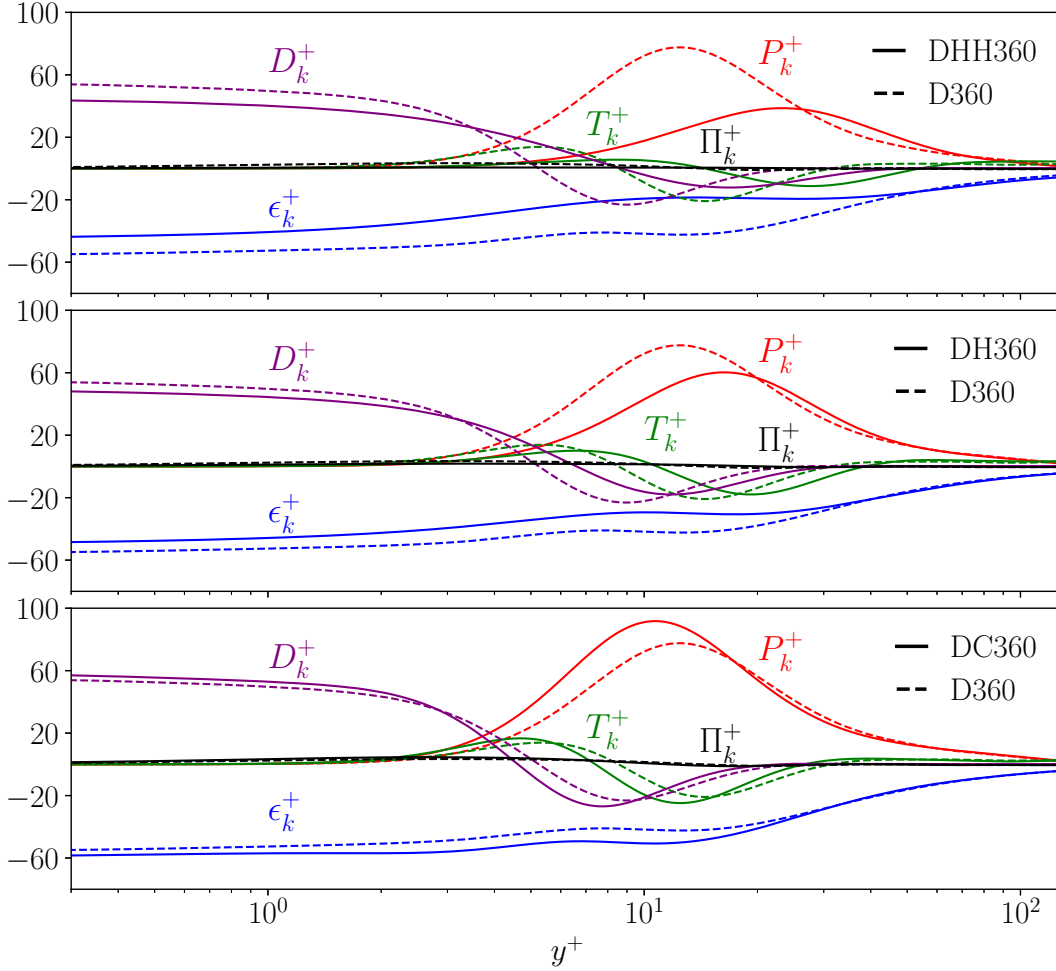
$$P_k^+ = -\langle \rho^* u'^+ w'^+ \rangle \frac{\partial \langle w^+ \rangle}{\partial r^*} \quad (5.21)$$

$$T_k^+ = -\frac{\partial \langle \rho^* k^+ u'^+ \rangle}{\partial r^*}, \quad \Pi_k^+ = -\frac{\partial \langle p'^+ u'^+ \rangle}{\partial r^*} \quad (5.22)$$

$$D_k^+ = \frac{\langle \tau_{rr}'^+ u'^+ \rangle}{\partial r^*} + \frac{\langle \tau_{\varphi r}'^+ v'^+ \rangle}{\partial r^*} + \frac{\langle \tau_{zr}'^+ w'^+ \rangle}{\partial r^*} \quad (5.23)$$

$$\begin{aligned} \varepsilon_k^+ = & -\langle \tau_{rr}'^+ \frac{\partial u'^+}{\partial r^*} + \tau_{\varphi r}'^+ \frac{\partial v'^+}{\partial r^*} + \tau_{zr}'^+ \frac{\partial w'^+}{\partial r^*} + \\ & \frac{1}{r^*} \tau_{r\varphi}'^+ \frac{\partial u'^+}{\partial \varphi} + \frac{1}{r^*} \tau_{\varphi\varphi}'^+ \frac{\partial v'^+}{\partial \varphi} + \frac{1}{r^*} \tau_{z\varphi}'^+ \frac{\partial w'^+}{\partial \varphi} + \\ & \tau_{rz}'^+ \frac{\partial u'^+}{\partial z^*} + \tau_{\varphi z}'^+ \frac{\partial v'^+}{\partial z^*} + \tau_{zz}'^+ \frac{\partial w'^+}{\partial z^*} \rangle \end{aligned} \quad (5.24)$$

The radial variation of these terms, as obtained in the simulations DHH360, DH360, and DC360 is shown in Fig. 5.18, where the case D360 associated with constant material properties is included again as a reference.

Figure 5.18: Turbulent k^+ -budget for heated and cooled cases at $Re_\tau = 360$

As a general trend, the heated cases DH360 and DHH360 are characterized by a shifting of all budgets towards the centerline as compared to D360, while cooled conditions exhibit a displacement of the budgets towards the wall. This baseline trend in the budgets can be also interpreted as an effective thickening/thinning of the viscous sublayer near the heated/cooled wall. Additionally, in the cooled case DC360, the markedly enhanced turbulent mixing reflected by a higher $-\tau_{turb}^+$ in the region up to $y^+ \approx 30$ together with the relatively highest local shear rate $-\frac{\partial \langle w^+ \rangle}{\partial r^*}$, is responsible for the higher peak of turbulent kinetic energy production term P_k^+ , as compared to D360, DH360 and DHH360. It is further interesting to see, that, although the peak of the production is significantly decreased for the heated cases, it still exceeds the levels of the c.f.p. reference and the cooled case near the core region beyond $y^+ \approx 30$. This reverse trend is mostly due to the fact that in this region, $y^+ \approx 30$, the shear rate $-\frac{\partial \langle w^+ \rangle}{\partial r^*}$ is relatively highest for the heated cases, while the turbulent momentum fluxes $-\tau_{turb}^+$ already collapsed for all the considered cases,

so that the enhanced shear stresses effectively causes the higher production term in this region. The shift of the peak of P_k^+ towards the center and the relatively highest level reached there also explains the high peaks of the axial velocity $rms\ w^+$ and turbulent kinetic energy k^+ observed for DH360 and DHH360 in Fig. 5.12 and Fig. 5.18, respectively. Finally, a notable difference in ε_k in the region up to $y^+ \approx 30$ is observed between the heated and cooled cases. The dampening/enhancement of the turbulent velocity fluctuations, and correspondingly, of their fluctuating gradients evidently dominates over the increase/decrease of the molecular viscosity with distance to the heated/cooled wall. The strongly heated case DHH360 basically follows a similar trend as DH360, but in a more pronounced way, reflecting the stronger radial variation of molecular viscosity due to the higher wall-to-bulk overtemperature.

5.4.4 Turbulent enthalpy fluctuations

The intensity of the fluctuations of the enthalpy difference is essentially determined by two effects. First, the enthalpy fluctuations need to be triggered by the turbulent fluctuating advective motion associated with the velocity fluctuations u'^+ , v'^+ , and w'^+ . Secondly, the amplitude of the enthalpy fluctuations is strongly related to the degree of thermal inhomogeneity subject to the turbulent mixing. The thermal inhomogeneity actually depends on the temperature gradients near the heated/cooled wall, which are determined by the molecular Prandtl number. Heated wall conditions are associated with steeper temperature gradients near the wall, due to the increase of the molecular Prandtl number with wall distance, thus producing a higher level of enthalpy fluctuations, whose peak is additionally shifted from the wall towards the center of the pipe. A reverse trend is seen for the cooled walls, where more intense turbulent mixing favours the thermal homogeneity, which together with decreasing Prandtl number effectively smoothens the temperature gradients near the wall. This trend is revealed in Fig. 5.19, which shows the rms of χ^+ for different friction Reynolds numbers $Re_\tau = 360, 500, 750$ under heated and cooled wall conditions, including the results obtained with constant material properties for comparison.

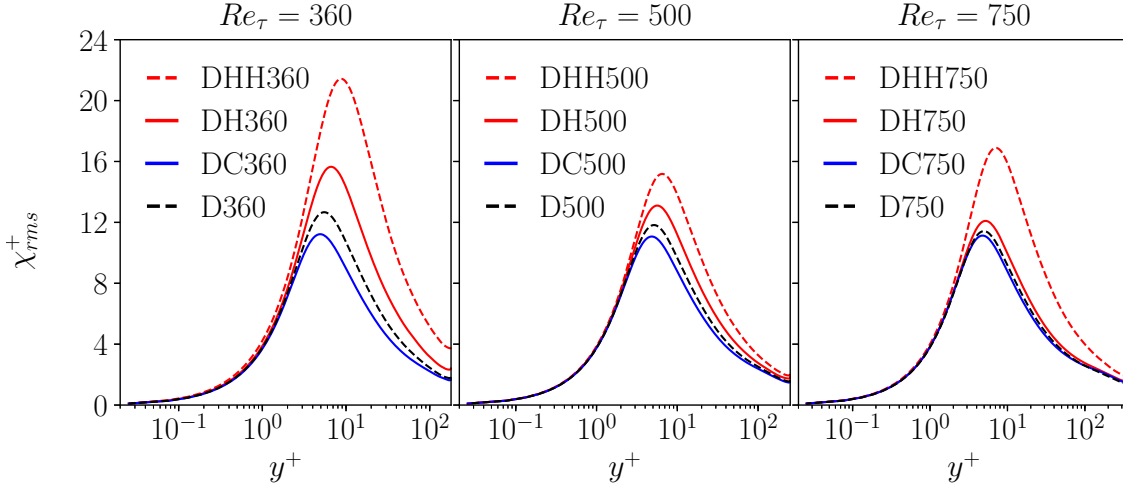


Figure 5.19: Rms -value of enthalpy difference χ_{rms}^+ for heated and cooled cases at $Re_\tau = 360, 500, 750$

The increase/decrease in the local molecular Prandtl number with distance to the heated/cooled walls clearly prevails over the dampened/enhanced turbulent advective fluctuating motion. At higher friction Reynolds numbers, the effect of variable material properties is mitigated and the differences between heated, cooled and constant fluid properties case are consistently reduced.

5.4.5 Laminar and turbulent heat flux

Similarly to the total shear stress, the total heat flux can be decomposed into

$$q_{tot}^+ = \underbrace{-\langle \rho^* u'^+ \chi'^+ \rangle}_{q_{turb}^+} + \underbrace{\frac{\langle \lambda^* \rangle}{\langle c_p^* \rangle Pr_w} \frac{\partial \langle \chi^+ \rangle}{\partial r^*}}_{q_{lam}^+} + \underbrace{\left\langle \frac{\lambda^*}{c_p^* Pr_w} \frac{\partial \chi'^+}{\partial r^*} \right\rangle}_{q_{prop}^+}, \quad (5.25)$$

where q_{turb}^+ and q_{lam}^+ denote the turbulent advective and the laminar diffusive contribution, respectively. The third contribution termed q_{prop}^+ arises from variable fluid properties. Again, this term is comparatively much smaller than q_{turb}^+ and q_{lam}^+ and, therefore, can be reasonably neglected. The radial variations of the contributions q_{turb}^+ and q_{lam}^+ are shown in Fig. 5.20, including again the c.f.p. cases as reference.

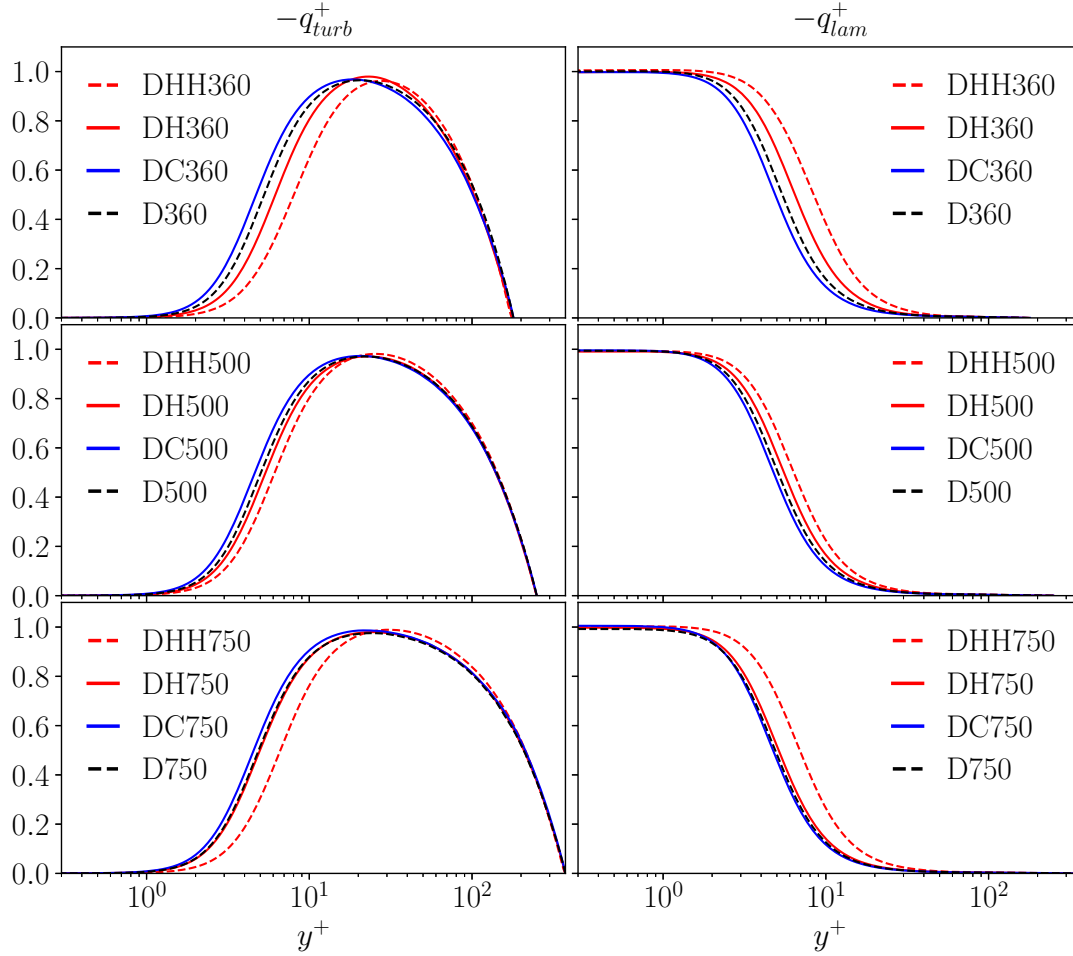


Figure 5.20: Turbulent and laminar contribution to total heat fluxes at reference wall friction Reynolds number $Re_\tau = 360, 500, 750$

The different trends of averaged enthalpy difference profiles, as observed in Fig. 5.9, can be readily explained by the variation of the shown turbulent and laminar heat fluxes considering the different dependencies of the molecular viscosity and thermal conductivity on the temperature. A marked drop in the turbulent component $-q_{turb}^+ = \langle \rho^* u'^+ \chi'^+ \rangle$ is featured by all heated cases. This unveils a dominant role of radial velocity fluctuation, which evidently outweighs the increased near wall enthalpy fluctuations triggered by the locally increased molecular Prandtl number. In turn with the decrease of $-q_{turb}^+$, the laminar counterpart $-q_{lam}^+$ increases. Due to the negligible dependence of the thermal conductivity on the temperature, the increase in $-q_{lam}^+$ is fully translated into the gradient of the temperature, or equivalently enthalpy, $\frac{\partial \langle \chi^+ \rangle}{\partial r^*}$. This explains the much steeper increase of the average $\langle \chi^+ \rangle$ -profiles seen in Fig. 5.9 for the heated cases. Analogously, the increased turbulent fluctuations in radial velocity occurring in the cooled cases, outbalance

the decreased level of enthalpy fluctuations, resulting in an increased radial turbulent heat flux, as seen from the blue lines in Fig. 5.20. The in turn decreased laminar contribution $-q_{lam}^+$ finally causes a lower rise of the average enthalpy difference $\langle \chi^+ \rangle$ with distance to the cooled wall, as shown in Fig. 5.9.

5.4.6 Budget for enthalpy difference variance and heat flux

The budget of enthalpy variance $\langle \rho \chi'^2 \rangle$ can be generally described by the following dimensional equation in index notation:

$$\begin{aligned} \frac{1}{2} \left[\frac{\partial \langle \rho \chi'^2 \rangle}{\partial t} + \frac{\partial (\langle u_j \rangle \langle \rho \chi'^2 \rangle)}{\partial x_j} \right] = & \underbrace{-\langle \rho u'_j \chi' \rangle \frac{\partial \langle \chi \rangle}{\partial x_j}}_{P_\chi} - \underbrace{\frac{1}{2} \frac{\partial \langle \rho u'_j \chi'^2 \rangle}{\partial x_j}}_{T_\chi} \\ & + \underbrace{\frac{\partial \langle q'_j \chi' \rangle}{\partial x_j}}_{D_\chi} - \underbrace{\langle q'_j \frac{\partial \chi'}{\partial x_j} \rangle}_{\varepsilon_\chi} + \frac{\langle \rho w' \chi' \rangle}{\dot{m}_b} \langle q_w \rangle D\pi \end{aligned} \quad (5.26)$$

The right-hand side of Eq. 5.26 is constituted by the several terms P_χ , T_χ , D_χ , ε_χ , representing the production, turbulent diffusion, the laminar diffusion and dissipation of $\langle \rho \chi'^2 \rangle$, respectively. Figure 5.21 shows the radial variations terms as obtained from the DNS cases DHH360, DH360, DC360, and D360. The discrepancy between the variable fluid properties cases and the c.f.p. reference baseline D360 can again be ascribed mainly to the change in local viscosity, although it does not appear explicitly in the governing equation for χ^+ . It rather acts implicitly through the local molecular Prandtl number and the underlying velocity fluctuations being both strongly determined by viscosity. The influence of the remaining material properties might be reasonably neglected, as their maximum variation remains always limited within 5% of their wall reference value.

Similar to the budget of k^+ , we observe as a general trend, that the contributions to the $\langle \rho \chi'^2 \rangle$ -budget of all heated cases are characterized by a shifting towards the core region with respect to the c.f.p. reference D360. Conversely, a displacement towards the wall is observed for the cooled case DC360. Notable differences still appear in the magnitude of the peak levels.

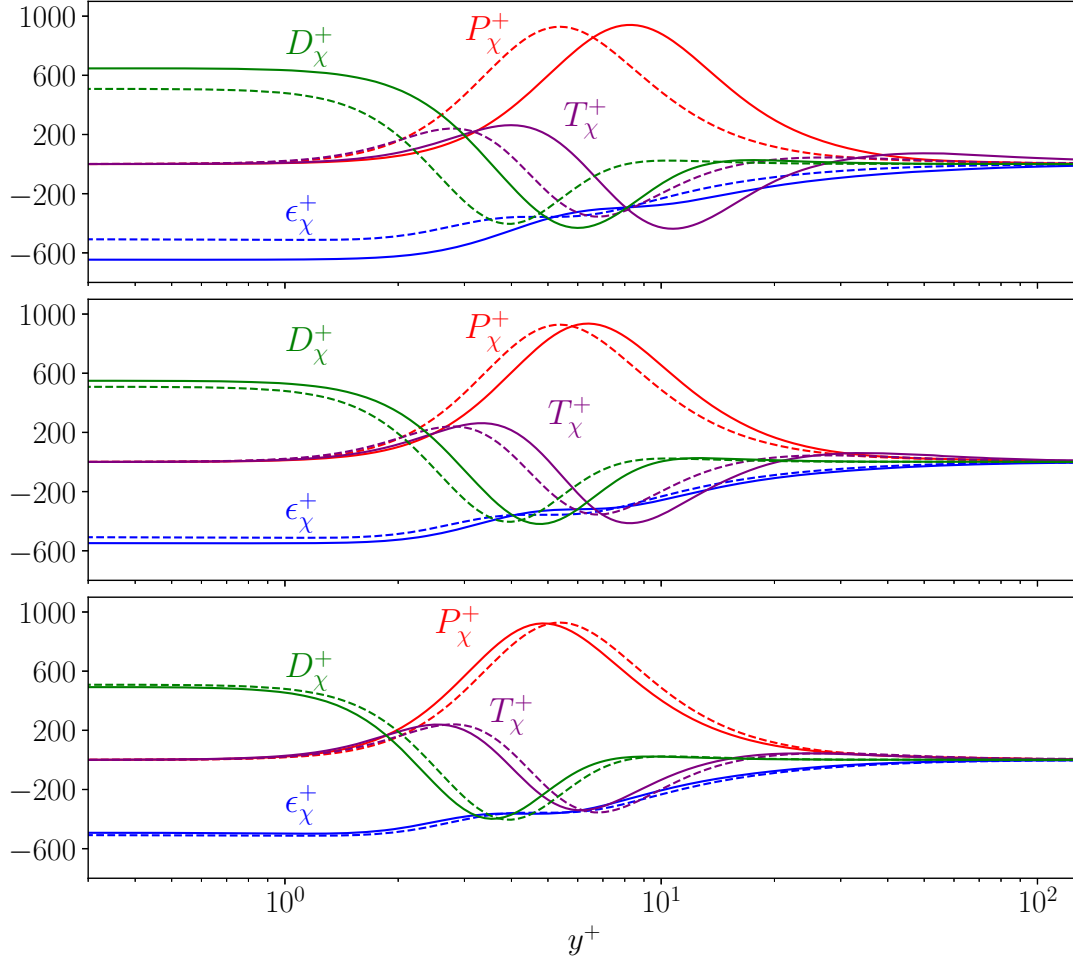


Figure 5.21: Turbulent $\langle \rho \chi'^2 \rangle$ -budget for heated and cooled cases at $Re_\tau = 360$

In particular the production term, which reads for the fully developed conditions in $(\cdot)^+$ -units

$$P_\chi^+ = \langle \rho^* u'^+ \chi'^+ \rangle \partial \langle \chi^+ \rangle / \partial y^+, \quad (5.27)$$

does not exhibit any significant variation of its maximum value. The position of the maximum is only radially shifted away from/towards heated/cooled wall, as already noted. The significant increase of $-\partial \langle \chi^+ \rangle / \partial r^*$ (or equivalently in $\partial \langle \chi^+ \rangle / \partial y^+$) in the heated cases DH360, DHH360 evidently compensates for the decrease in the turbulent heat flux $-q_{turb}^+$. The reverse trend is observed again for the cooled case DC360, where despite a decreased enthalpy gradient, the augmented turbulent heat flux evidently suffices to keep the maximum value of P_χ^+ at the same level as seen for the heated cases and D360. The enhanced/reduced fluctuations of enthalpy indicated in Fig. 5.19 for the heated/cooled cases also lead to a different behaviour of the thermal dissipation ϵ_χ^+ as compared to its dynamic

counterpart ε_k^+ . For the considered fully developed conditions it is written as

$$\varepsilon_\chi^+ = -\frac{1}{Re_\tau Pr_w \langle c_p^* \rangle} \left\langle \left(\frac{\partial \chi'^+}{\partial r^*} \right)^2 + \left(\frac{1}{r^*} \frac{\partial \chi'^+}{\partial \varphi} \right)^2 + \left(\frac{\partial \chi'^+}{\partial z^*} \right)^2 \right\rangle, \quad (5.28)$$

where the fluctuations in the material properties have been neglected again. Due to the only weak dependence of $\langle \lambda \rangle$ and $\langle c_p \rangle$ on the temperature, this quantity is mainly determined by the gradients of enthalpy fluctuations. These gradients apparently follow in magnitude the observed trends of the *rms* value of χ_{rms}^+ for most part of the domain, so that the absolute value of ε_χ^+ is higher in the heated cases and lower in the cooled cases. The change of the asymptotic value of ε_χ^+ in the limit of $y^+ \rightarrow 0$, turns out to be most pronounced for DHH360. The increased wall-to-bulk overtemperature caused by the enhanced wall heating evidently produces the most intense fluctuations in the wall heat flux.

The dimensional evolution equation for the turbulent heat flux can be generally written in index notation as

$$\begin{aligned} \frac{\partial \langle \rho u'_i \chi' \rangle}{\partial t} + \frac{\partial (\langle u_j \rangle \langle \rho u'_i \chi' \rangle)}{\partial x_j} = & \underbrace{-\langle \rho u'_j \chi' \rangle \frac{\partial \langle u_i \rangle}{\partial x_j}}_{P_{qi}} - \underbrace{\langle \rho u'_i u'_j \rangle \frac{\partial \langle \chi \rangle}{\partial x_j}}_{T_{qi}} \\ & - \underbrace{\langle \chi' \frac{\partial p'}{\partial x_i} \rangle}_{\Pi_{qi}} + \underbrace{\left[\frac{\partial \langle \tau'_{ij} \chi' \rangle}{\partial x_j} + \frac{\partial \langle q'_j u'_i \rangle}{\partial x_j} \right]}_{D_{qi}} \\ & - \underbrace{\left[\langle q'_j \frac{\partial u'_i}{\partial x_j} \rangle + \langle \tau'_{ij} \frac{\partial \chi'}{\partial x_j} \rangle \right]}_{\varepsilon_{qi}} + \frac{\langle \rho u'_i w' \rangle \langle q_w D \pi \rangle}{\dot{m}_b 4}. \end{aligned} \quad (5.29)$$

Figure 5.22 shows the radial variation of the individual contributions to the budget, appearing as production P_{qi} , turbulent diffusion T_{qi} , redistribution due to pressure fluctuations Π_{qi} , laminar diffusion D_{qi} and dissipation ε_{qi} on the right-hand side of Eq. (5.29), rewritten for the radial turbulent heat flux $q_r^+ = \langle \rho^* u'^+ w'^+ \rangle$ in wall units. The production, which is written for the considered fully developed conditions as

$$P_{qr}^+ = -\langle \rho^* u'^+ u'^+ \rangle \frac{\partial \langle \chi^+ \rangle}{\partial r^*}, \quad (5.30)$$

is significantly decreased in the heated case as compared to the c.f.p. results. The reduction of the radial turbulent stress $\langle \rho^* u'^+ u'^+ \rangle$ apparently outweighs the increased gradient of mean enthalpy. The same reasoning applies in reverse for the cooled case. The opposite tendencies seen for the enthalpy fluctuations and the turbulent heat flux in the heated/cooled case closely reflect their underlying production mechanism, represented in the corresponding budgets by the production terms P_χ and P_{qu} , respectively.

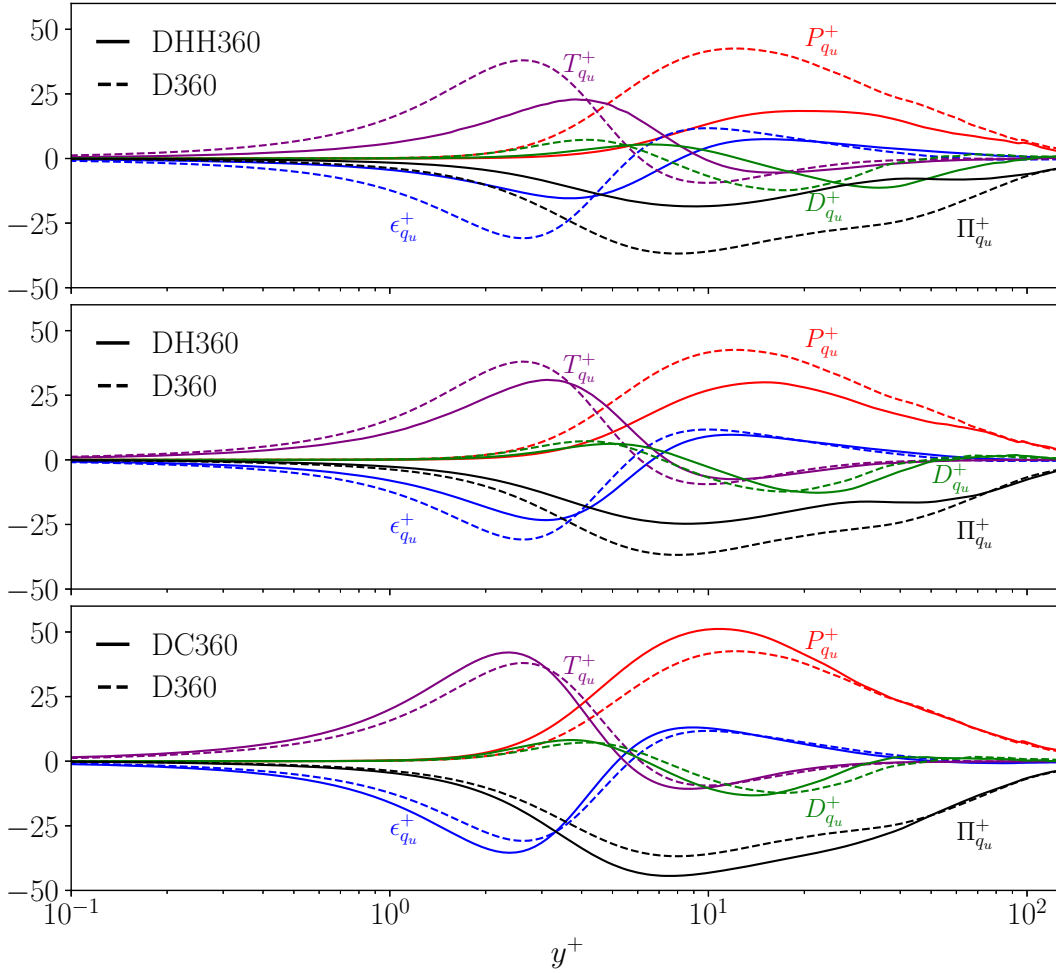


Figure 5.22: Budget of the turbulent radial heat flux $q_{turb}^+ = \langle \rho^* u'^+ \chi'^+ \rangle$ for heated and cooled cases at $Re_\tau = 360$

5.5 Turbulent Prandtl number

For the considered fully developed flow the turbulent Prandtl number reads

$$Pr_T = \frac{\langle u'^+ w'^+ \rangle}{\langle u'^+ \chi'^+ \rangle} \frac{d\langle \chi^+ \rangle / dy^+}{d\langle w^+ \rangle / dy^+} = \frac{\nu_T}{a_T}. \quad (5.31)$$

It represents an important modelling parameter, which is often introduced in the turbulence modelling of RANS when considering heat transfer. Valuable *a priori* estimates of Pr_T can be readily obtained by evaluating Eq. (5.31) with the statistics of the DNS data. A comprehensive comparison of the radial variation of these *a priori* values for the considered test cases is presented in Fig. 5.23.

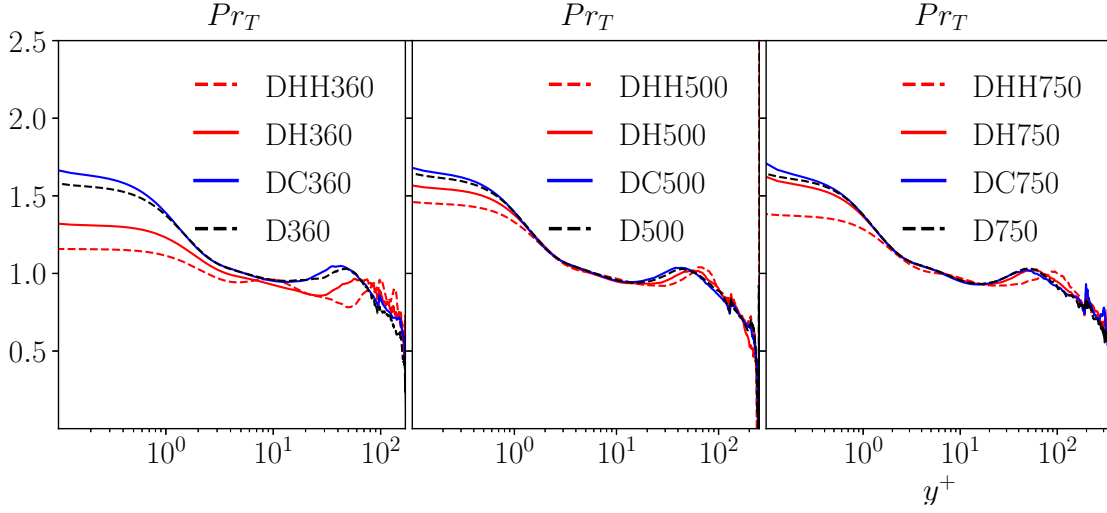


Figure 5.23: Turbulent Prandtl number Pr_T for heated and cooled cases at $Re_\tau = 360, 500, 750$

Notable discrepancies in the predicted Pr_T can be observed in the viscous sublayer for $y^+ < 5$, and in part of the core region in the range $10 < y^+ < 100$. For all considered friction Reynolds numbers the asymptotically approached near wall level $Pr_T|_{y^+ \rightarrow 0}$ is increased for the cooled wall, while it is generally decreased for all heated cases. The constant fluid properties reference cases, D360, D500, D750, always deliver asymptotic results in between. Looking across the Fig. 5.23 from left to right, it may be observed that the discrepancies in the near wall asymptotic behaviour of Pr_T are generally mitigated with increasing friction Reynolds numbers, when the same absolute wall heat flux is considered. On the other hand, enhanced wall heating lowers the near wall asymptotic limit of Pr_T for given Reynolds number. A similar spreading of the profiles is seen in the inner region beyond $y^+ > 10$, where again the cooled cases exhibit highest values, while the heated cases the lowest. Again, these differences are most pronounced for the smallest Reynolds number $Re_\tau = 360$. Recalling the definition of Pr_T , as given by Eq. (5.31), representing the ratio of eddy viscosity ν_T to eddy diffusivity α_T , it can be stated that the variation of the molecular viscosity has a stronger effect on the eddy viscosity than on the eddy diffusivity. This explains the general decrease of Pr_T as the molecular viscosity increases with distance from the heated wall, whereas Pr_T increases as the molecular viscosity decreases with distance from the cooled wall. Lastly, a general collapsing trend towards the value 0.5 in the core region is seen for all cases, regardless of heated/cooled wall conditions and the account of temperature depending material properties.

5.6 Effect of thermal boundary conditions

The heat transfer between a turbulent flow and its surrounding solid surface can be influenced by several aspects, which are related to the geometry of the boundary, its material composition and, of course, the properties of the considered working fluid. All these parameters may alter the production, diffusion and dissipation of near wall thermal fluctua-

tions in a complex fashion, which in a rigorous sense only a solution of the fully coupled problem between the heat transfer inside the wall boundary and in the fluid phase could describe. In the present analysis, the effect of the three different thermal boundary conditions introduced in subsection 2.3.4 are compared. The parameters for the conjugate heat transfer problem were chosen so as to reflect the experimental conditions in the *in-house* measurements carried out for validation. The material properties of the actually applied steel pipe together with the related parameters, which arise from the non-dimensionalized formulation of the conjugate heat transfer problem are summarized in Table 5.3. In the asymptotic limit for $K \rightarrow 0$ and $K \rightarrow \infty$, the conjugate heat transfer problem approaches the *isothermal* and *isoflux* condition, respectively.

The conduction problem in the solid domain was solved numerically, using the same axial and azimuthal resolution as used for the fluid domain, applying 1024 and 512 cells respectively. The number of nodes in the radial direction has been chosen 256, with a clustering towards the fluid-solid interface, due to the expected pronounced local temperature gradient. The radially outer solid boundaries were assumed adiabatic. The volumetric heat release (heat source) was specified so as to match the average wall heat flux into the fluid, being $\langle q_w \rangle = 20000 \text{ W/m}^2$.

Table 5.3: Geometrical and physical parameters used in the *conjugate heat transfer* analysis

<i>phase</i>	$\rho [\frac{Kg}{m^3}]$	$c_s [\frac{J}{kg \text{ K}}]$	$c_p [\frac{J}{kg \text{ K}}]$	$\lambda [\frac{W}{m^2 \text{ K}}]$	$\alpha [m^2/s]$			
solid	8000	500	-	16.3	4.075e-06	K	G	d_s
fluid	1041	-	3564.51	0.422	1.139e-09	0.155	0.028	0.0015

The near wall level of fluctuations on the fluid side resulting from the use of *Dirichlet*, *Von Neumann* thermal boundary conditions, and from the *conjugate heat transfer* analysis at $Re_\tau = 360$ are shown in detail in Fig. 5.24

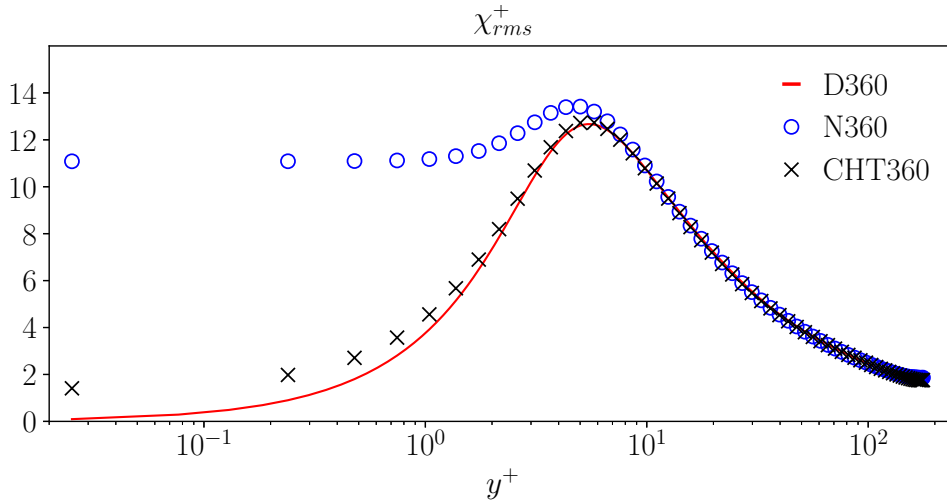


Figure 5.24: *Rms*-value of enthalpy difference as predicted by D360, N360, CHT360 at $Re_\tau = 360$ for constant fluid properties.

The three cases D360, N360, CHT360 evidently exhibit different trends in the enthalpy difference fluctuations at $y^+ < 10$. N360, which applies *Von Neumann* thermal boundary conditions, expectedly predicts the highest level of fluctuations in this region, which approach the wall on a constant plateau. The case CHT360 turns out to yield non-vanishing thermal fluctuations as well, when the solid wall is approached, but their intensity becomes very low for $y^+ < 10$. The presently obtained solution of the conjugate heat transfer problem can be indeed considered similar to the *Dirichlet* case, for the given geometrical and material parameters.

Despite the substantially altered near wall behaviour of thermal fluctuations, the overall heat transfer remains basically unchanged accross the different cases. As seen from Fig. 5.25, the averaged enthalpy profile as well as the turbulent heat flux are indeed practically unaffected by the enhanced or dampened level of thermal fluctuations below $y^+ < 10$, which proves the dominant role of the wall-normal velocity fluctuations in the turbulent heat flux. The high molecular Prandtl number $Pr = 10$, limits the enhancement of the thermal fluctuations seen for the Von Neumann b.c.s to a vary confined region, where the radial velocity fluctuations are already almost entirely dampened. The turbulent heat flux consequently remains almost negligibly affected, which further explains the almost insensitivity of the Nusselt number to the adoption of different thermal boundary conditions.

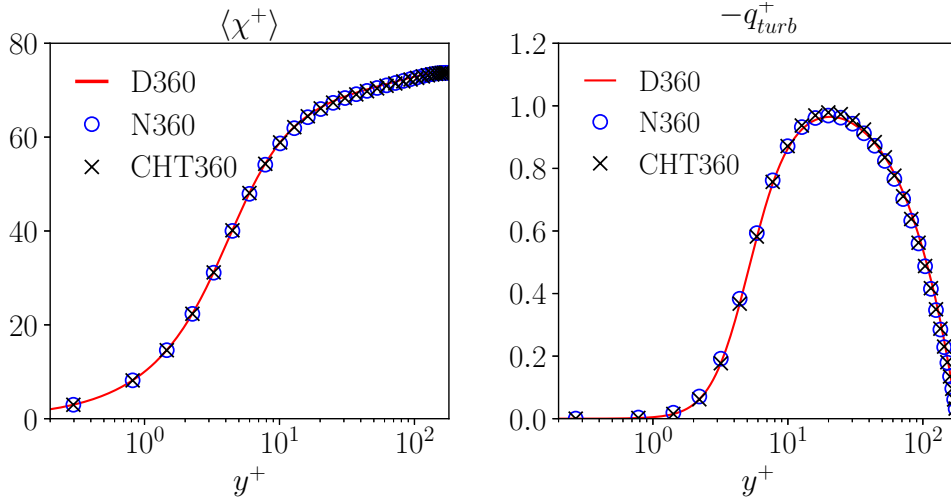


Figure 5.25: Averaged enthalpy difference and turbulent heat flux as predicted for D360, N360, CHT360 at $Re_\tau = 360$ using constant fluid properties.

A qualitative insight into the thermal structures obtained for the different boundary conditions is given by the instantaneous temperature contours in Fig. 5.26.

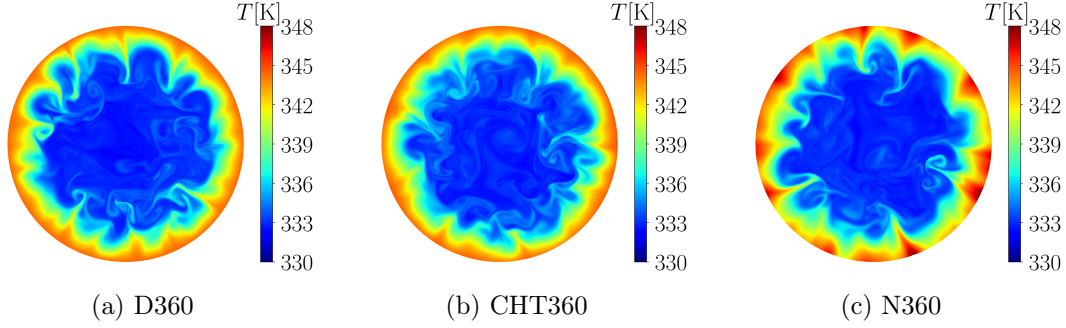


Figure 5.26: Instantaneous temperature contours from DNS using c.f.p. with different thermal boundary conditions: a) isothermal, b) conjugate Heat Transfer, c) isoflux

The turbulent thermal structures obtained for isothermal boundary condition (D360) and the conjugate heat transfer case (CHT360) do not differ significantly. More evident differences appear in comparison against the isoflux case (N360). Here, we observe a pronounced intermittency of hot and cold regions along the wall. This intermittency clearly indicates the strong enthalpy fluctuations, which remain on very high level all way down to the wall.

When variable fluid properties are considered, the marked differences observed for the thermal fluctuations using different thermal boundary conditions may also affect the transfer of momentum. The possible effect of such thermal back-coupling was therefore investigated in the present work by alternatively applying isoflux and isothermal boundary conditions in DNS of turbulent heated and cooled pipe flows at $Re_\tau = 360$, assuming temperature-dependent fluid properties as already specified for the 50/50 Vol% mixture of glysantine/water. The considered cases have already been listed in Table 5.1, labelled as NH360 and NC360 for the *isoflux* (Von Neumann) b.c.s, and DH360, DC360 for the *isothermal* (Dirichlet) b.c.s. Figure 5.27 shows the turbulent heat flux and the *rms*-value of the enthalpy difference for the different thermal b.c.s. The findings, which have been already made in the corresponding cases with constant fluid properties represented by D360 and N360, are confirmed here. Despite the strongly enhanced level of near wall enthalpy fluctuations always met with the *isoflux* b.c.s, the turbulent heat flux still remains practically unaltered. This in turn leads to negligible changes also in the averaged enthalpy difference profile as well as in the averaged axial velocity, as shown in Fig. 5.28.

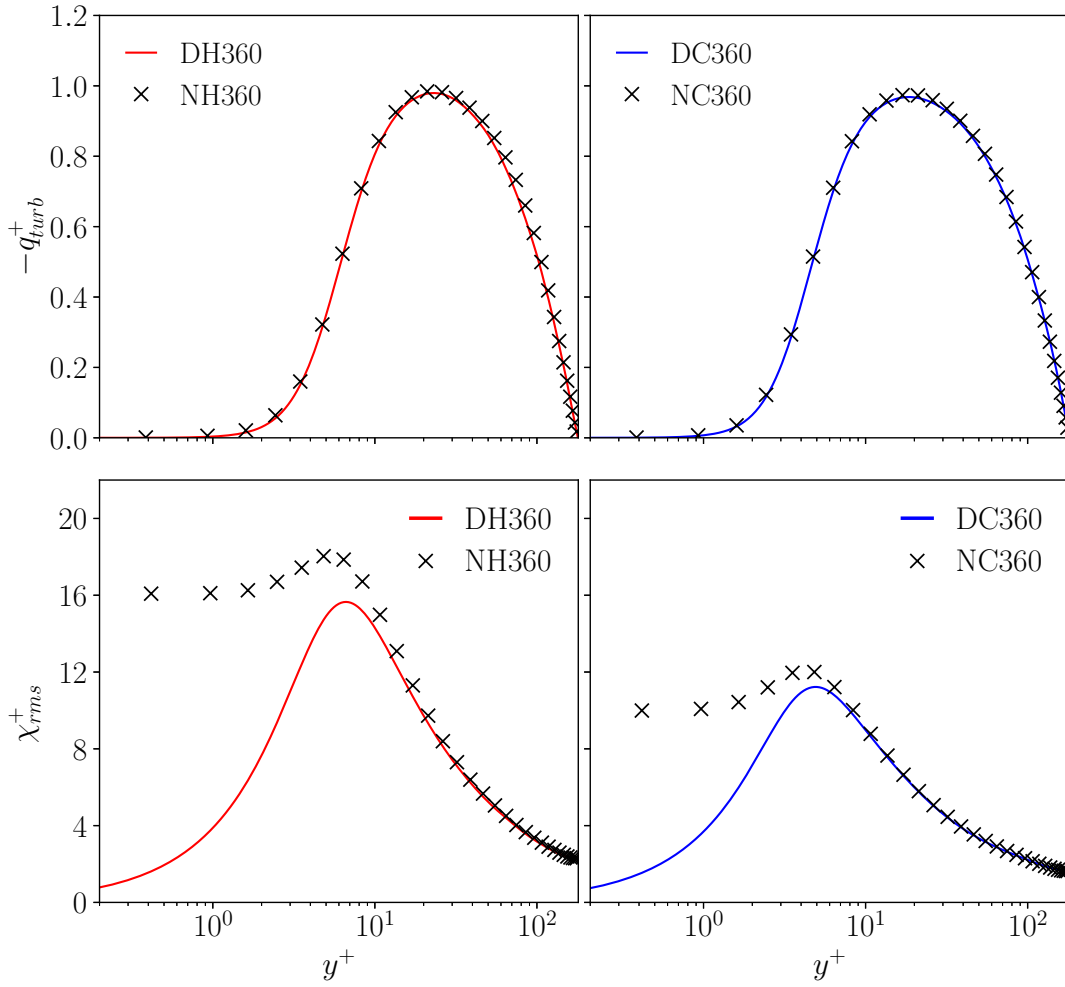


Figure 5.27: Turbulent heat flux and *rms*-value of enthalpy difference as predicted for the cases NH360, DH360, C360 at $Re_\tau = 360$ for variable fluid properties.

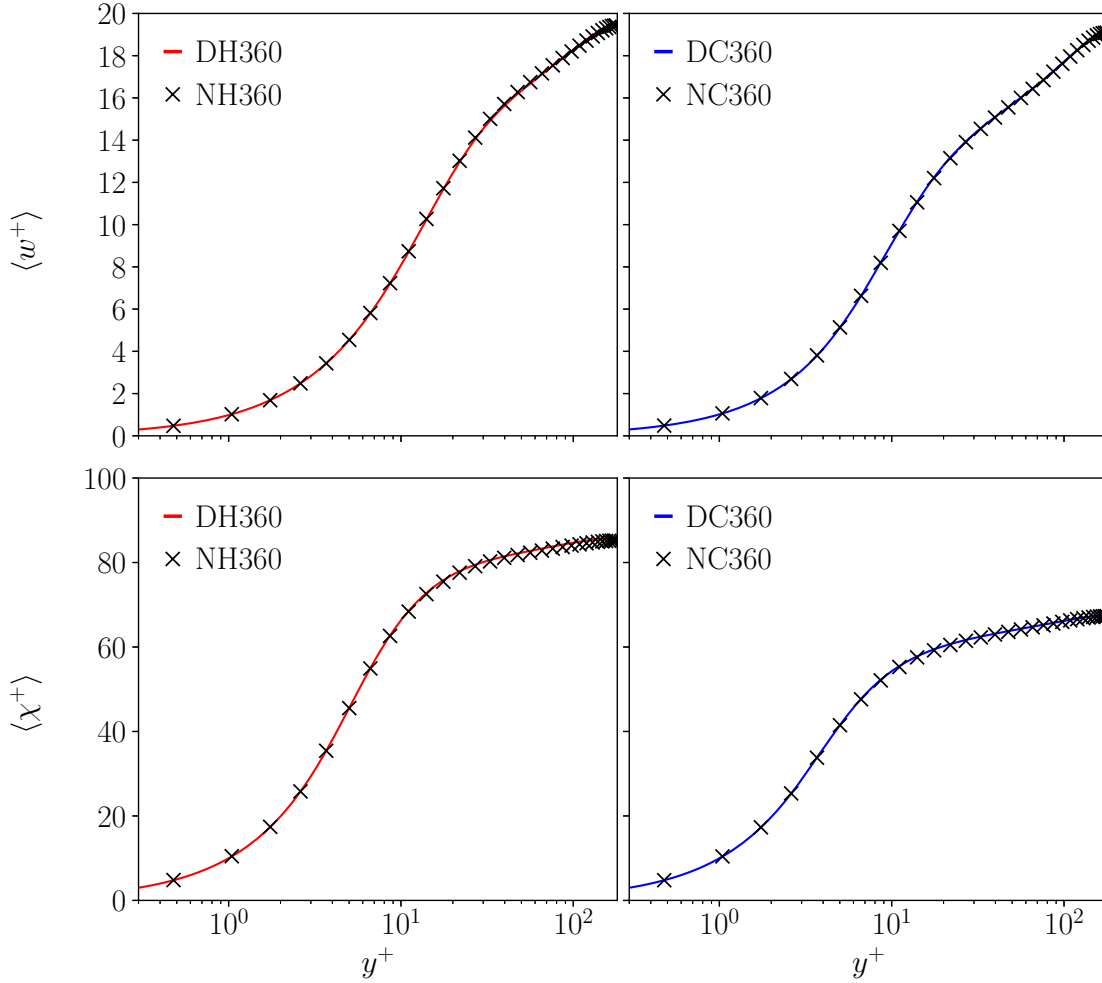


Figure 5.28: Averaged axial velocity and enthalpy difference profile as predicted for the cases NH360, DH360 and NC360, DC360 at $Re_\tau = 360$ for variable fluid properties.

The different trend of the enthalpy fluctuations associated with different thermal boundary conditions strongly affects the turbulent Prandtl number in the viscous sublayer up to the buffer layer at $y^+ < 10$. The non-vanishing high wall level of the thermal fluctuations makes the turbulent Prandtl number Pr_T drop to zero for the *isoflux* conditions, regardless of the account of material property variation. On the other hand, the vanishing of the turbulent enthalpy fluctuations at the wall produces an asymptotically approached non-zero maximum wall level of Pr_T for the *isothermal* b.c.s. These near wall trends, which are clearly seen in Fig. 5.29, can be easily proven by Taylor series expansion of the velocity and enthalpy in powers of wall distance y^+ . The profile obtained from the solution of the conjugate heat transfer problem (CHT360) with constant fluid properties is included for comparison as well. Due to the non-vanishing of the thermal fluctuations, Pr_T decays here also to zero, hereby always remaining beyond the values of the *isoflux* conditions.

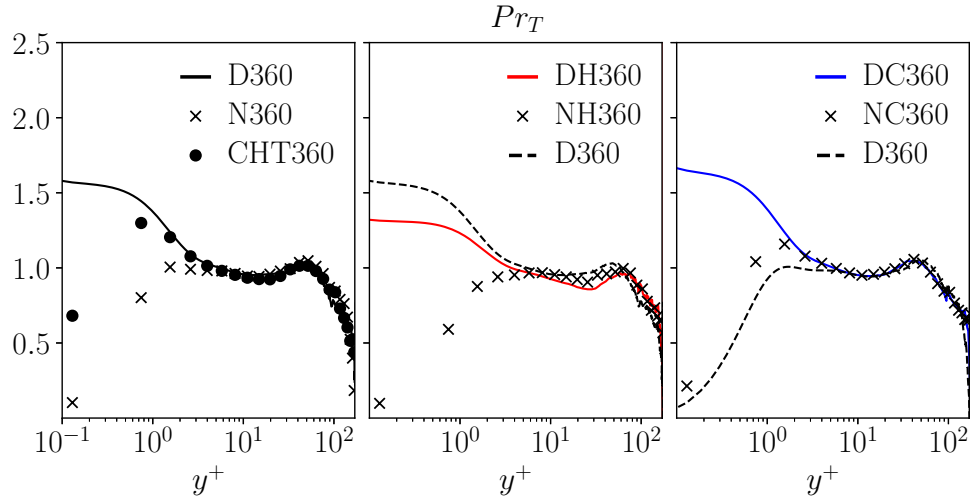


Figure 5.29: Turbulent Prandtl number Pr_T obtained for the different thermal wall b.c.s at $Re_\tau = 360$, assuming constant and variable fluid properties.

Chapter 6

LES of fully developed turbulent pipe flow

In the following section an extensive LES analysis of heated and cooled turbulent pipe flows will be presented in both *a priori* and *a posteriori* tests. The focus will be the predictive capability of the models SMAG, CSM and WALE, the role of the numerical error and the possible relevance of varying material properties in the subgrid-scale closure.

6.1 *A priori* LES and assessment of numerical error

The *a priori* analysis was carried out on fully resolved velocity and thermal fields obtained in precursor DNS simulations of heated turbulent pipe flow with constant material properties. The aim of the present *a priori* study is twofold: on one side the predictions of the selected sgs models SMAG, CSM and WALE will be assessed by comparing the unresolved modelled fluxes against the DNS based unresolved *a priori* fluxes. On the other hand, the contribution of the numerical error is identified and quantitatively assessed.

The *a priori* LES was performed considering four DNS cases at friction Reynolds number $Re_\tau = 360/500$, based on friction velocity w_τ and pipe diameter D , and molecular Prandtl number $Pr = 10/20$. The data at $Pr = 20$ are taken from fully resolved DNS, which have been previously computed by Irrenfried (2019). These simulations applied the same *isothermal* (Dirichlet) boundary conditions as the cases with $Pr = 10$, as already listed as D360, D500, in Table 5.1. The LES grid was assumed as eight times coarser in all directions as compared to the DNS grid, implying a filter size $\tilde{\Delta} = 8\Delta$.

Concerning the filtered governing equations (3.9) - (3.10), the Favre-filtering method can be replaced by the unweighted spatial filter operator defined in Eq. (3.4), so that

$$\overline{(\quad)} = (\widetilde{\quad}), \quad (6.1)$$

because the density ρ remains constant throughout the entire flow fields, like all material properties. The uniform specific heat capacity $c_p = \text{const}$ also implies that the temperature T can be equivalently used instead of enthalpy h for the advective heat transfer. Thus, assuming constant material properties the decomposition of the advective divergence term

introduced by Eq. (3.30) reads

$$\underbrace{\nabla^* \cdot (\widetilde{\mathbf{U}^+ \mathbf{U}^+})}_{A_{\mathbf{U}}^*} = \underbrace{\widetilde{\nabla}^* \cdot (\widetilde{\mathbf{U}^+} \widetilde{\mathbf{U}^+})}_{\tilde{A}_{\mathbf{U}}^*} + \underbrace{\widetilde{\nabla}^* \cdot (\widetilde{\mathbf{U}^+ \mathbf{U}^+} - \widetilde{\mathbf{U}^+} \widetilde{\mathbf{U}^+})}_{\alpha_{\mathbf{U}}^*} + \underbrace{\nabla^* \cdot (\widetilde{\mathbf{U}^+ \mathbf{U}^+}) - \widetilde{\nabla}^* \cdot (\widetilde{\mathbf{U}^+ \mathbf{U}^+})}_{\beta_{\mathbf{U}}^*}. \quad (6.2)$$

The deviatoric part of the subgrid-scale stress tensor $\tau_{sgs} = \widetilde{\mathbf{U}^+ \mathbf{U}^+} - \widetilde{\mathbf{U}^+} \widetilde{\mathbf{U}^+}$ in the unclosed contribution $\alpha_{\mathbf{U}}^*$ is modelled using the *Boussinesq*-Ansatz described in Eq. (3.15), in which the subgrid-scale eddy viscosity ν_{sgs} is delivered by the alternatively assessed candidates SMAG, CSM, and WALE. In the following, only the budget of the filtered advective momentum flux for the axial velocity component w will be discussed, as the average subgrid-scale model contribution is the highest in this direction. Accordingly, the decomposition (6.2) is rewritten for the axial component of momentum as

$$\underbrace{\nabla^* \cdot (\widetilde{\mathbf{U}^+ w^+})}_{A_w^*} = \underbrace{\widetilde{\nabla}^* \cdot (\widetilde{\mathbf{U}^+} \widetilde{w^+})}_{\tilde{A}_w^*} + \underbrace{\widetilde{\nabla}^* \cdot (\widetilde{\mathbf{U}^+ w^+} - \widetilde{\mathbf{U}^+} \widetilde{w^+})}_{\alpha_w^*} + \underbrace{\nabla^* \cdot (\widetilde{\mathbf{U}^+ w^+}) - \widetilde{\nabla}^* \cdot (\widetilde{\mathbf{U}^+ w^+})}_{\beta_w^*}. \quad (6.3)$$

Analogously, applying the assumption of constant material properties, the divergence term for the advective heat flux introduced by Eq. (3.31) reads

$$\underbrace{\nabla^* \cdot (\widetilde{\mathbf{U}^+ \theta^+})}_{A_{\theta}^*} = \underbrace{\widetilde{\nabla}^* \cdot (\widetilde{\mathbf{U}^+} \widetilde{\theta^+})}_{\tilde{A}_{\theta}^*} + \underbrace{\widetilde{\nabla}^* \cdot (\widetilde{\mathbf{U}^+ \theta^+} - \widetilde{\mathbf{U}^+} \widetilde{\theta^+})}_{\alpha_{\theta}^*} + \underbrace{\nabla^* \cdot (\widetilde{\mathbf{U}^+ \theta^+}) - \widetilde{\nabla}^* \cdot (\widetilde{\mathbf{U}^+ \theta^+})}_{\beta_{\theta}^*}. \quad (6.4)$$

The unresolved subgrid-scale heat flux in α_{θ}^* is modelled using the *gradient-diffusion*-hypothesis described in Eq. (3.16), where the sgs eddy viscosity is again supplied by the assessed sgs models, SMAG, CSM and WALE, and the subgrid-scale Prandtl number has been set to a constant value $Pr_{sgs} = 0.5$.

Figure 6.1 shows the radial variations of the statistically averaged budgets of the advective axial momentum flux divergence for the four considered cases, as obtained from the decomposition (6.3).

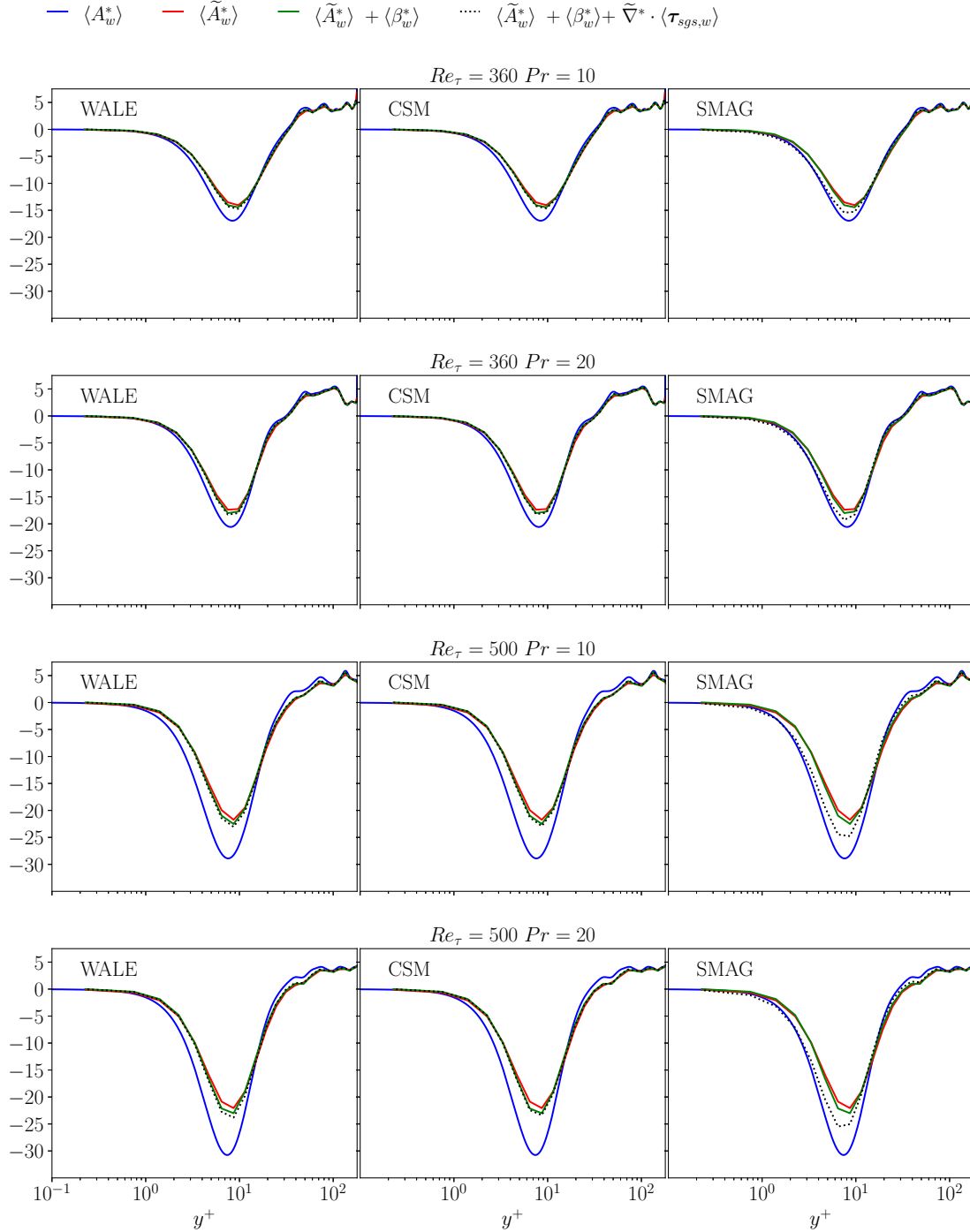


Figure 6.1: Budgets of the averaged advective divergence terms for the axial momentum transport comparing the WALE, CSM and SMAG subgrid-scale model contributions for different $Re_\tau = 360/500$, $Pr = 10/20$

The accumulated sum of the average resolved flux (red line), average numerical error,

and modelled subgrid-scale contribution (black dotted line) should best possibly agree with the blue lines in Fig. 6.1, representing the target divergence fluxes computed from the DNS-filtered data. The latter exhibits a pronounced negative peak, which gets deeper and moves towards the wall for increasing Re_τ . The considerable unresolved gap to the blue (DNS-based) target line is partly filled by the Standard Smagorinsky subgrid-scale model (SMAG). The WALE and CSM models deliver even smaller contributions, being quantitatively in the same range as the average numerical error $\langle \beta_w^* \rangle$.

The statistically averaged contributions to the budgets of the advective heat flux divergence for the four considered cases, as obtained from the decomposition (6.4), are shown in Fig. 6.2.

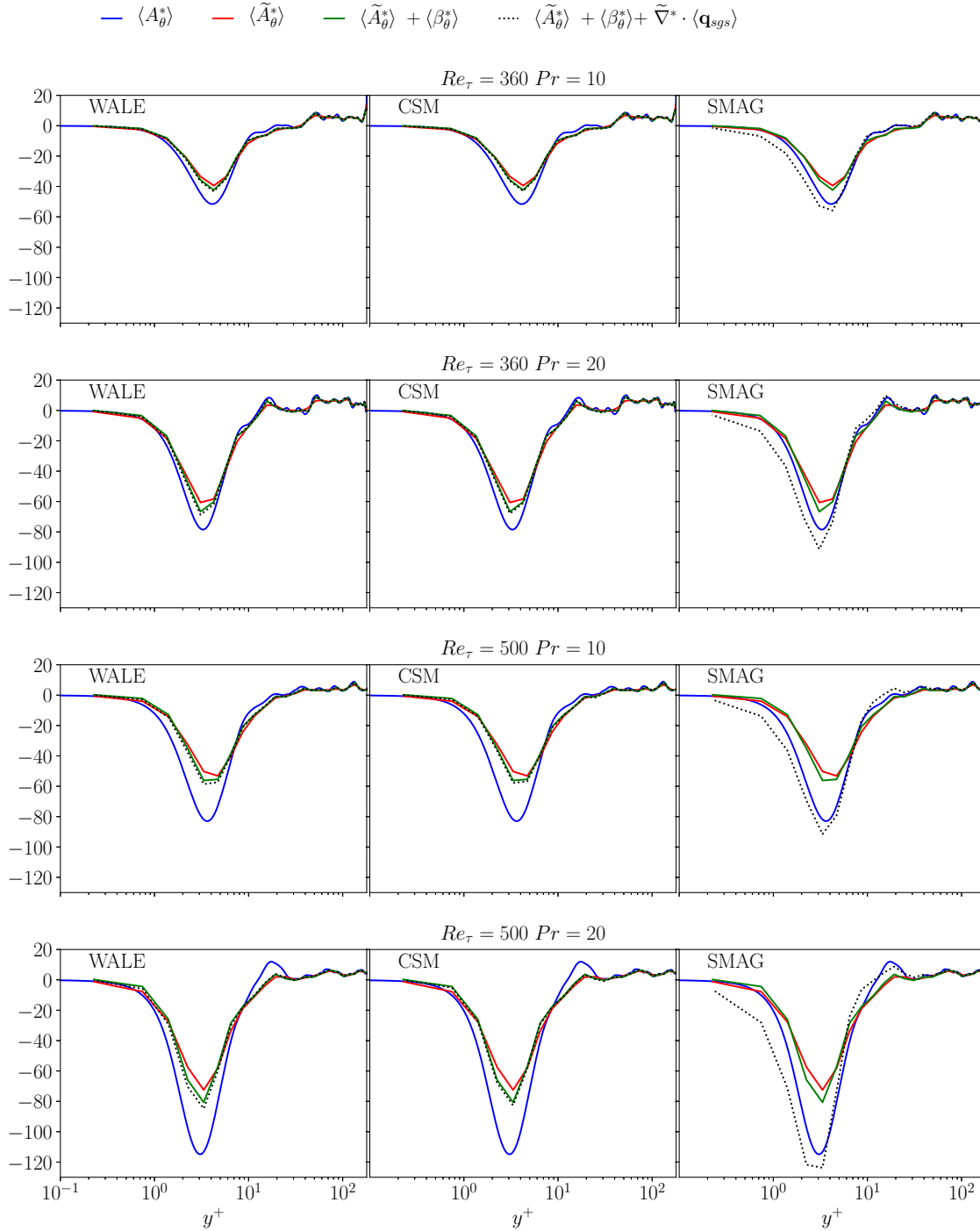


Figure 6.2: Budgets of the averaged advective divergence terms for the heat transport comparing the WALE, CSM and SMAG subgrid-scale model contributions for different $Re_\tau = 360/500$, $Pr = 10/20$

Here again a pronounced negative peak always occurs near the upper limit of the viscous

sublayer. This local minimum gets deeper for increasing Reynolds and Prandtl numbers, and it is shifted towards the wall for the higher Prandtl number. The numerical error $\langle \beta_\theta^* \rangle$ evidently adds on average very little to the resolved contribution $\langle \tilde{A}_\theta^* \rangle$. The remaining marked gap to the blue target line, represented by $\langle A_\theta^* \rangle$, is filled and even partly over-compensated only by the Standard Smagorinsky subgrid-scale model (SMAG), whereas the WALE model delivers comparatively little, and the CSM model produces even less. As follows from Eq. (3.16), the contribution from the subgrid-scale model is certainly also influenced by the choice of the subgrid-scale Prandtl number, being assumed as constant $Pr_{sgs} = 0.5$.

In contrast to the small average contribution, observed for $\langle \beta_w^* \rangle$ and $\langle \beta_\theta^* \rangle$, respectively, in Fig. 6.1 and Fig. 6.2, the instantaneous fluctuating representations of the numerical discretization error are significantly higher. This is clearly seen from Fig. 6.3 and Fig. 6.4, which show the *rms* value of the error contribution to the axial momentum transport β_w^{rms} and the error contribution to the heat transport β_θ^{rms} .

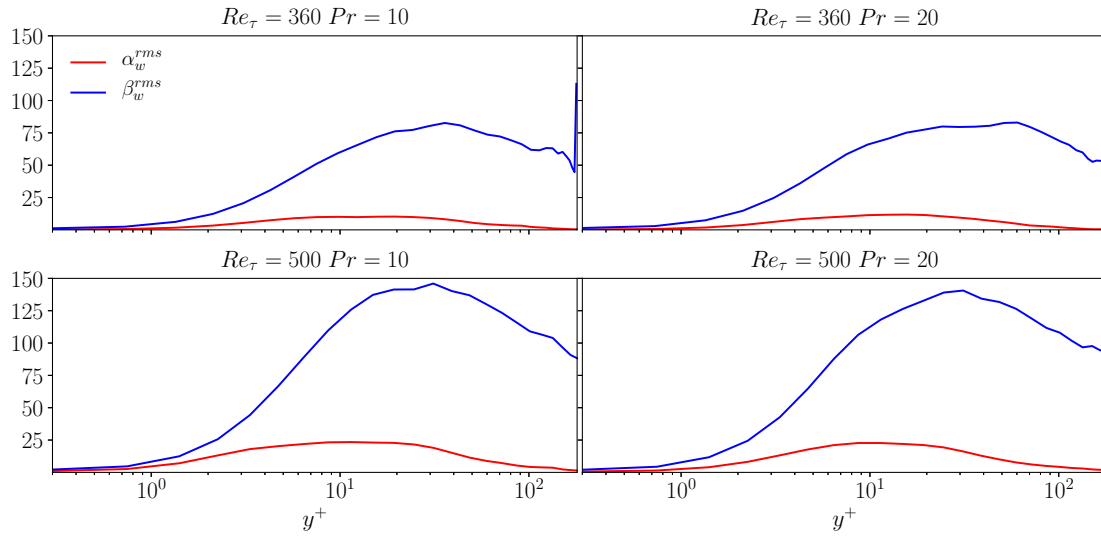


Figure 6.3: *Rms*-values of the numerical error β_w and the *a priori* sgs-contribution α_w for axial momentum equation at different Re_τ and Pr numbers

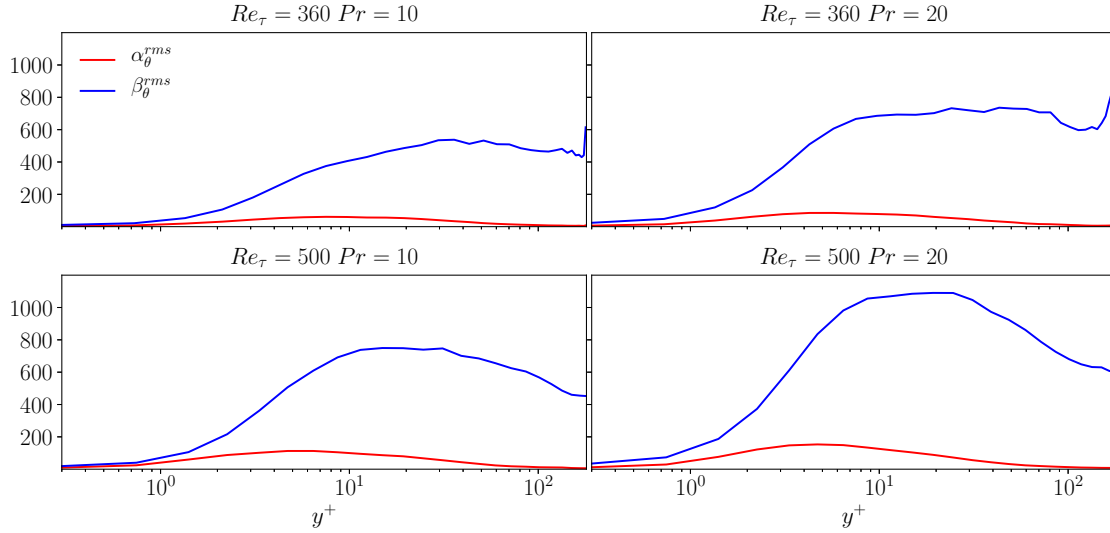


Figure 6.4: *Rms*-values of the numerical error β_θ and the *a priori* sgs-contribution α_θ for energy transport equation at different Re_τ and Pr numbers

The also shown lower red lines in Fig. 6.3 and Fig. 6.4 represent the *rms*-values of the *a priori* sgs-contributions $\alpha_w = \tilde{\nabla} \cdot \boldsymbol{\tau}_{sgs,w}$ and $\alpha_\theta = \tilde{\nabla} \cdot \mathbf{q}_{sgs}$ occurring in the budgets (6.2) and (6.4), respectively, where the *a priori* sgs-flux vectors $\boldsymbol{\tau}_{sgs,w}$ and \mathbf{q}_{sgs} are obtained from Eqs. (3.27) and (3.27), respectively, using the filtered DNS data for velocity and temperature. The instantaneous contributions from the *a priori* sgs-terms evidently tend to stay considerably below those of the numerical error. This observation confirms the findings of Vreman *et al.* (1995). Their *a priori* analysis of a turbulent mixing layer unveiled the same dominance of the numerical error over the sgs-contribution, if the filter width is equal to the mesh size of the LES-grid, which is generally assumed in implicit LES and also applies in the present study. Additionally, the intensity of the fluctuation of β_w increases at the higher friction Reynolds number $Re_\tau = 500$. On the other hand, the fluctuations in β_θ are clearly enhanced as both the friction Reynolds number Re_τ and the molecular Prandtl number Pr increase.

The mutual statistical dependence of the individual contributions is illustrated in terms of the normalized cross correlations, as shown for the advective heat flux for the considered Reynolds and Prandtl numbers in Fig. 6.5. The correlation coefficient between the resolved contribution and the numerical error becomes strongly negative towards the wall. This indicates the dissipative nature of the numerical error, which effectively dampens the resolved turbulent fluctuations in this region. On the other hand, the resolved contribution mostly appears as positively correlated with the contribution from subgrid-scale model in the diffusive sublayer and buffer layer $y^+ < 10$, implying that the applied subgrid-scale model enhances the resolved turbulent fluctuations in this region. This positive correlation is obviously most pronounced for the SMAG, which also explains the overpredicted subgrid-scale contribution of SMAG near the wall, as seen in the budgets in Fig. 6.5, right column. Basically the same trends are observed for all considered cases.

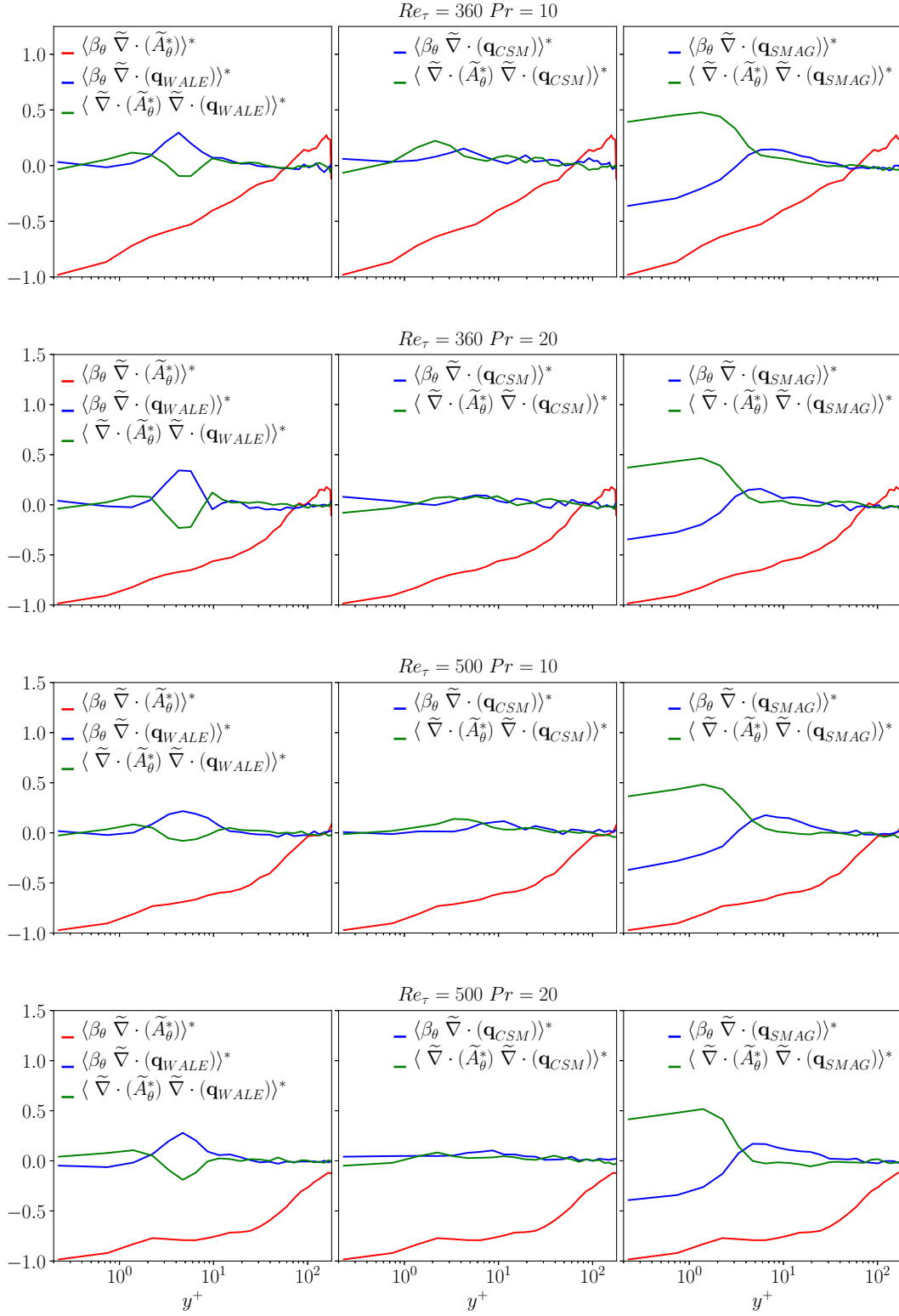


Figure 6.5: Cross correlation coefficient $\langle \cdot \rangle^*$ between numerical error and resolved contribution (red line), resolved and sgs model contribution (blue line), resolved and sgs model contribution (green line) for $Re_\tau = 360/500$ and $Pr = 10/20$

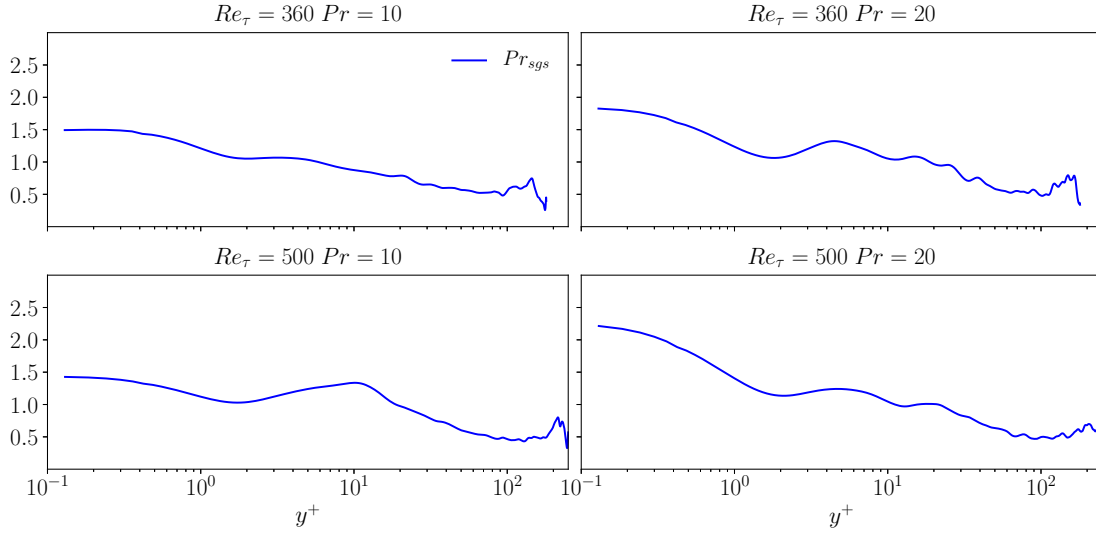


Figure 6.6: Radial variation of the subgrid-scale Prandtl number as computed from the filtered DNS data Pr_{sgs} at different Re_τ and Pr numbers

Figure 6.6 shows the radial variation of the local *a priori* value for $Pr_{sgs} = \nu_{sgs}/a_{sgs}$, as obtained from Eq. (3.32) and Eq. (3.33) using the filtered DNS results. For all considered cases, Pr_{sgs} remains evidently close to 0.5 in the fully turbulent core region. It increases towards unity in the buffer layer and further approaches higher levels above unity very next to the wall ($y^+ < 1$). As such, the *a priori* results are well in line with the findings for channel flow presented in literature by Moin *et al.* (1991), and, as particularly suggested by the observations for the turbulent inner region, they support the presently applied setting $Pr_{sgs} = 0.5$. In Fig. 6.7 the model parameters C^{SMAG} , C^{CSM} , computed from Eq. (3.20) and (3.23), respectively, are compared against the *a priori* value C^{DNS} obtained from the filtered DNS results using Eq. (3.34). The *a priori* target level identified by the black line in Fig. 6.7 is better matched by SMAG in the viscous sublayer up to the buffer layer, where, on the contrary, C^{CSM} exhibits a strong decay. The latter, however, agrees better with C^{DNS} in the core region $y^+ > 20$, where C^{SMAG} reaches the asymptotical value of 0.01, as prescribed by the analytical formulation of the Van-Driest damping function. The sgs eddy viscosity-to-laminar viscosity ratios for the selected models, shown in Fig 6.8, closely follows the trend observed in their respective Smagorinsky coefficient, previously discussed. Both the CSM and the WALE model produce evidently a markedly lower eddy-viscosity in the buffer layer and below ($y^+ < 10$), while the wall-dampened prediction of SMAG lies fairly close to the DNS-based *a priori* results. This deficit stays the same at both friction Reynolds number $Re_\tau = 360$, and 500. It explains the insignificantly small sgs-contributions of CSM and WALE observed in Fig. 6.1 and Fig. 6.2.

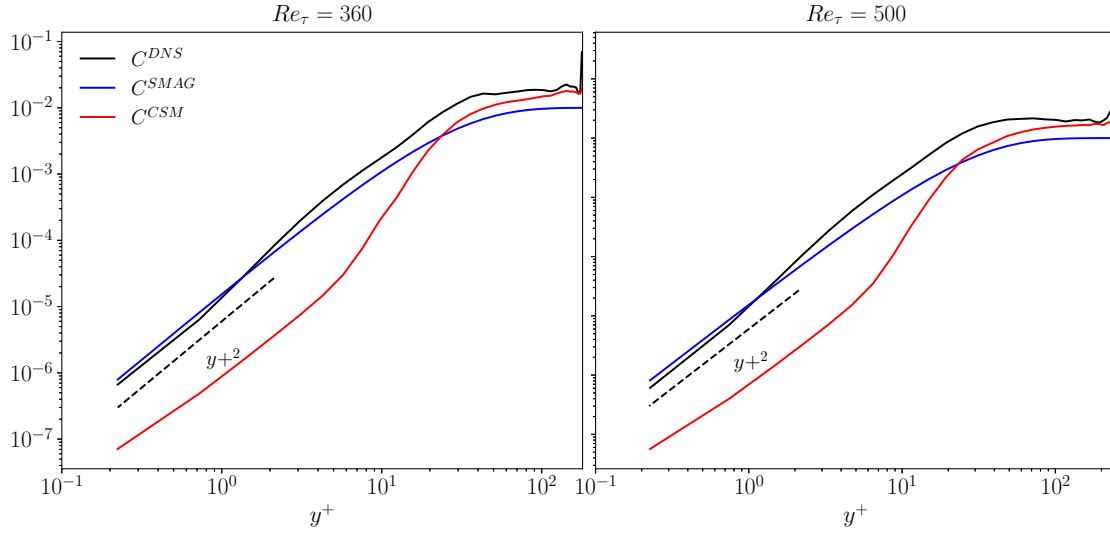


Figure 6.7: Radial variation of the Smagorinsky model coefficient C^{SMAG} , C^{DNS} , and Coherent Structure Model coefficient C^{CSM} as computed from the filtered DNS data, at different friction Reynolds numbers $Re_\tau = 360/500$

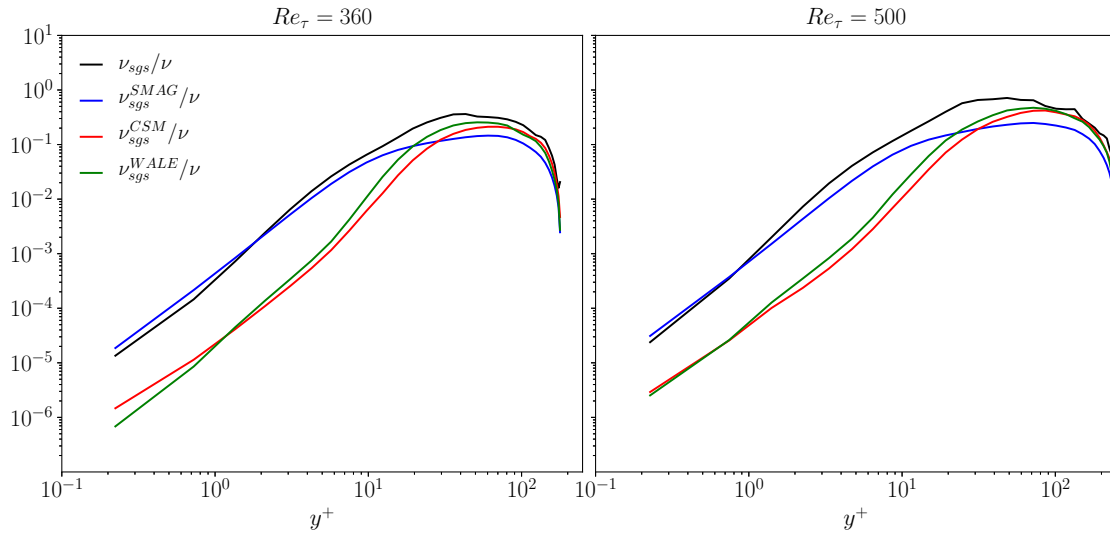


Figure 6.8: Sgs eddy viscosity predicted by CSM, WALE and SMAG sgs models compared against the *a priori* eddy viscosity retrieved from the filtered DNS data at $Re_\tau = 360/500$

6.2 *A posteriori* LES

In the *a posteriori* LES, or simply *a posteriori* test, the predictive capabilities of the three selected sgs modelling candidates SMAG, WALE, CSM are assessed in a self-sustained predictive numerical solution of the discretized governing equations on the underresolved LES-grid. The sgs models were tested in the simulation of heated and cooled turbulent pipe flow, assuming alternatively constant and temperature-dependent material properties. The subgrid-scale Prandtl number was assumed again constant, $Pr_{sgs} = 0.5$, similar to the *a priori* LES. Statistics of the flow and thermal fields was collected by averaging the instantaneous fields along the spatial homogeneous directions and in time over a total of 60 FTTs. The results were compared against corresponding DNS statistics, assumed as benchmark. The considered LES cases are summarized in Table 6.1. For the sake of comparability with the DNS data, the same labelling as for DNS cases with isothermal b.c.s, already listed in Table 5.1, has been adopted.

Table 6.1: LES test cases

<i>label</i>	Re_τ	fluid is	$\bar{q}_w [Wm^{-2}]$	fluid properties
DH360	360	heated	$2 \cdot 10^4$	variable, v.f.p.
DC360	360	cooled	$2 \cdot 10^4$	variable, v.f.p.
D360	360	-	$2 \cdot 10^4$	constant, c.f.p.
DHH500	500	heated	$4 \cdot 10^4$	variable, v.f.p.

A second order accurate Adams-Bashforth scheme for time discretization and a second order Finite Volume spatial discretization scheme was applied, as it is common practice in most available commercial CFD codes devised for real applications with complex geometries.

A *Dirichlet* thermal boundary condition was always imposed at the pipe wall, prescribing zero enthalpy difference $\chi_w = 0$.

The computational grid of the LES consists of 32, 128 and 64 elements in radial, azimuthal and axial direction, respectively. The same hyperbolic tangent stretching function, as used for DNS simulations, is adopted for radial clustering, whereas azimuthal and axial directions have been homogeneously discretized. The maximum mesh size in the different directions is shown in wall units in Table 6.2, including the DNS resolution as reference.

Table 6.2: Grid size in LES/DNS

Re_τ	Δr_{max}^+		$R\Delta\varphi_w^+$		Δz^+	
	LES	DNS	LES	DNS	LES	DNS
360	13.24	1.71	8.82	2.21	28.13	1.75
500	19.87	2.49	12.25	3.07	39.06	2.44

The quality of the resolution applied in each spatial direction was assessed by a direct

comparison between the local grid size and the respective Taylor micro scale λ_{ij} . The latter represents a reasonable measure for the smallest eddies in the inertial subrange, which an appropriate grid resolution for LES should be able to resolve directly, without the aid of any sgs model.

Based on its general mathematical definition,

$$\lambda_{ij}^2 = \frac{\langle u'_i u'_j \rangle}{\left\langle \frac{\partial u'_i}{\partial x_j} \frac{\partial u'_i}{\partial x_j} \right\rangle}, \quad (6.5)$$

the Taylor micro scale λ_{ij} is represented by a 9-component tensor, whereas the actual spatial resolution is entirely defined by the local grid size along three spatial directions. Therefore, the comparison was restricted to the diagonal components $\lambda_{11} = \lambda_{rr}$, $\lambda_{22} = \lambda_{\varphi\varphi}$, $\lambda_{33} = \lambda_{zz}$, representing the eddy size in the radial, azimuthal and axial direction, respectively. In the present analysis, λ_{rr} , $\lambda_{\varphi\varphi}$ and λ_{zz} are estimated from the available DNS data as

$$\lambda_{rr}^2 = \frac{\langle u'^{+2} \rangle}{\left\langle \frac{\partial u'^{+}}{\partial r^*} \frac{\partial u'^{+}}{\partial r^*} \right\rangle}, \quad (6.6)$$

$$\lambda_{\varphi\varphi}^2 = \frac{\langle v'^{+2} \rangle}{\frac{1}{r^{*2}} \left\langle \frac{\partial v'^{+}}{\partial \varphi} \frac{\partial v'^{+}}{\partial \varphi} \right\rangle}, \quad (6.7)$$

$$\lambda_{zz}^2 = \frac{\langle w'^{+2} \rangle}{\left\langle \frac{\partial w'^{+}}{\partial z^*} \frac{\partial w'^{+}}{\partial z^*} \right\rangle}. \quad (6.8)$$

The comparison between the local grid sizes Δr , $r\Delta\varphi$, Δz and the corresponding DNS based Taylor micro scales is shown in Fig. 6.9.

Ideally, the value of the shown ratios should be kept as high as possible or, at least well beyond unity, in order to guarantee the correct representation of a sufficiently large part of the turbulent motion on the current grid.

In Fig. 6.9, on the left side, it is noted that the ratio $\lambda_{rr}/\Delta r$ naturally vanishes, as the wall is approached. This behaviour is due to the different scaling of the numerator and denominator in Eq. (6.6), where the former scales as $\mathcal{O}(y^{+4})$ and the latter as $\mathcal{O}(y^{+2})$. A fairly good resolution is seen in azimuthal and axial directions, as the ratios $\lambda_{\varphi\varphi}/r\Delta\varphi$ and $\lambda_{zz}/\Delta z$ stay above unity over a large portion of the radial distance.

6.2.1 First order statistics

The averaged axial and enthalpy profiles predicted by the LES are compared in Fig. 6.10 against the corresponding results from DNS at $Re_\tau = 360$ for heated and cooled wall, with variable and constant fluid properties, labelled as DH360, DC360, D360, respectively. Results obtained from LES without a sgs model are included as dashed lines as well. The predictions from the LES with CSM/WALE are evidently in close agreement with the DNS

results over the whole y^+ -range, while the LES with SMAG generally overestimates the mean axial velocity over the entire core region and underestimates the enthalpy difference. This trend is repeated in all test cases, regardless of the actual thermal forcing provided by a positive or negative wall heat flux and the assumption of constant or temperature-depending material properties.

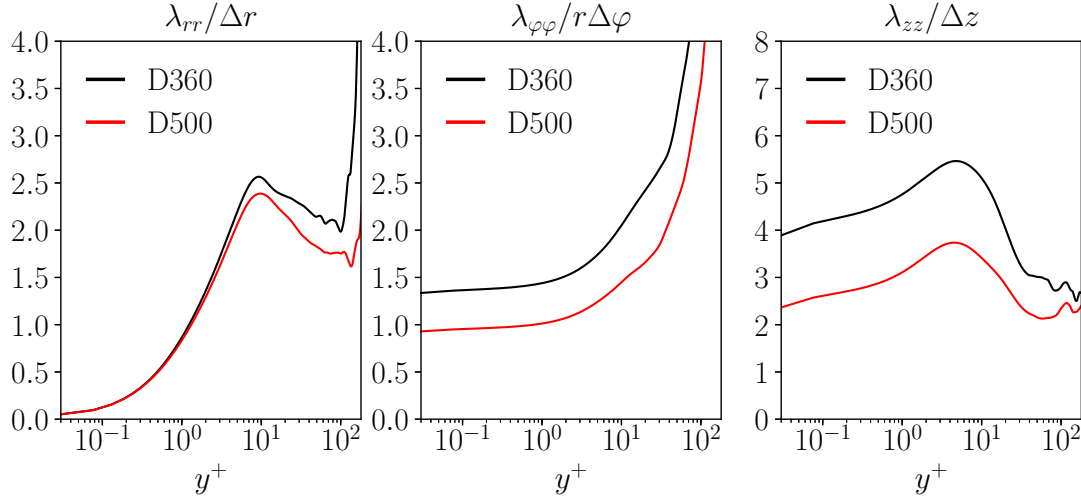


Figure 6.9: Diagonal components of Taylor micro scale tensor λ_{ij} as obtained from DNS and compared against LES grid sizes in radial, azimuthal and axial direction

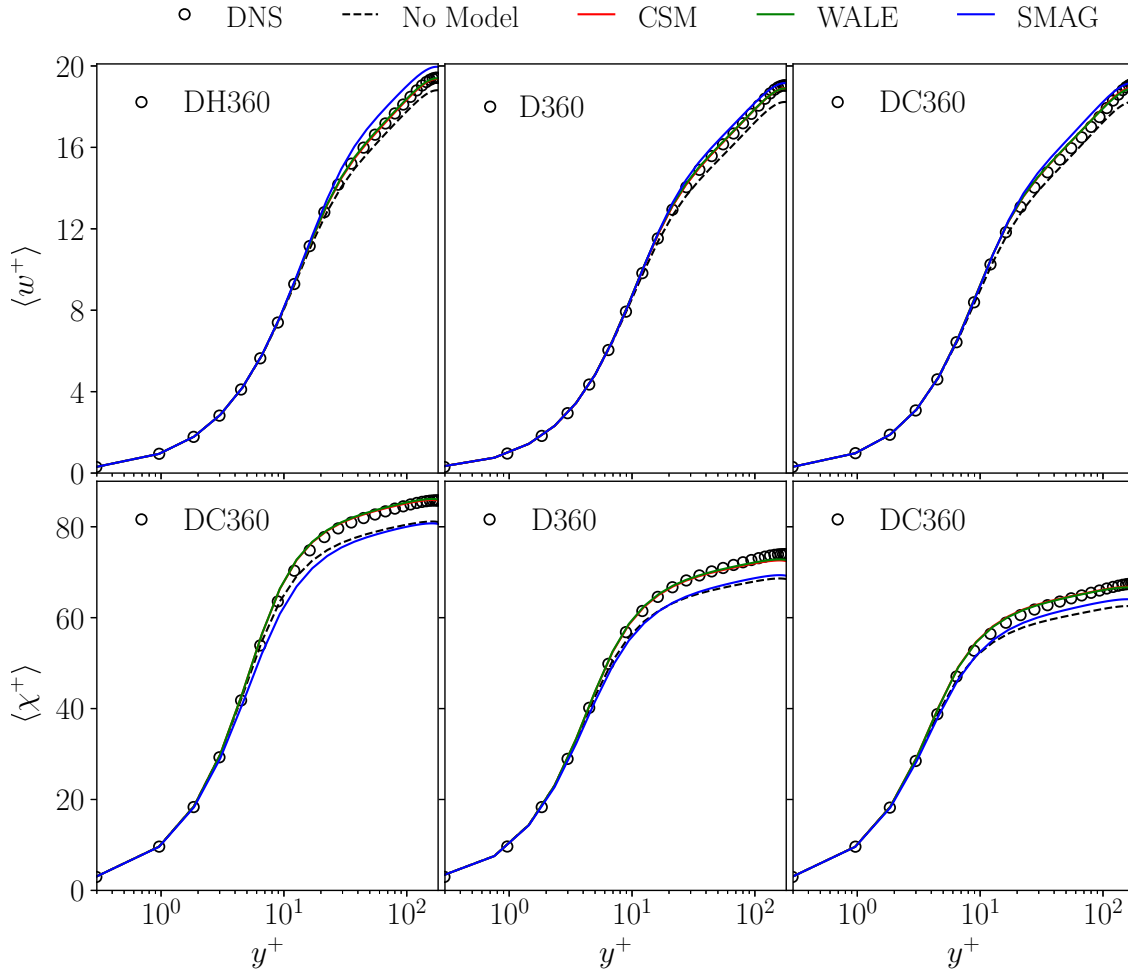


Figure 6.10: Averaged axial velocity (first row) and averaged enthalpy difference profile (second row) predicted by LES for variable fluid properties in heated/cooled conditions (DH360/DC360) and constant material properties (D360) as compared against correspondent DNS results at $Re_\tau = 360$

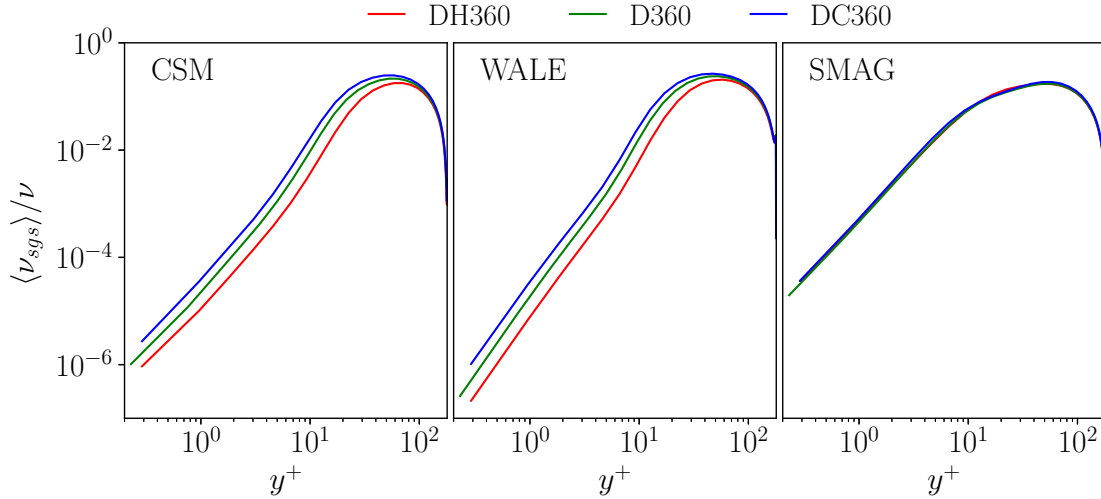
The generally observed superior performance of the subgrid-scale models WALE and CSM expectedly translates into accurate predictions for the global transfer parameters for momentum and heat, as represented by the wall skin friction coefficient C_f and Nusselt number Nu . Both parameters, which are computed with the bulk quantities of the predicted $\langle w^+ \rangle$ and $\langle \chi^+ \rangle$ according to Eqs. (2.71)-(2.73), are listed in Table 6.3. The values of C_f and Nu predicted by LES with WALE and CSM sgs models match satisfactorily the DNS predictions in all three cases. Consistently with the observations made in Fig. 6.10, SMAG overpredicts the high Nusselt number, whereas it underpredicts the wall skin friction coefficient.

Concerning the subgrid-scale eddy viscosity, SMAG appears as almost insensitive to the

Table 6.3: Wall skin friction coefficient C_f and Nusselt number Nu

Re_τ	360					
case	DH360		DC360		D360	
	C_f	Nu	C_f	Nu	C_f	Nu
DNS	0.00896	43.82	0.00941	57.01	0.00931	51.42
CSM	0.00891	43.45	0.00911	56.68	0.00921	51.80
WALE	0.00885	43.36	0.00911	56.78	0.00918	51.66
SMAG	0.00834	46.39	0.00885	59.20	0.00892	54.38

variation of the local Reynolds number in the heated and cooled v.f.p. cases. As seen from Fig. 6.11, the eddy viscosity of SMAG practically remains unaltered for all cases. On the other hand, the candidates CSM and WALE evidently capture the weaker/stronger turbulent small scale motion, yielding both lower/higher subgrid-scale viscosities in the heated/cooled case. SMAG additionally turns out to deliver the highest sgs eddy viscosity in the near wall region up to the buffer layer, where CSM and WALE, on the contrary, provide significantly lower contributions by almost one order of magnitude.

Figure 6.11: Averaged subgrid-scale eddy viscosities predicted by CSM, WALE, SMAG at $Re_\tau = 360$

6.2.2 Second order statistics

The marked differences observed in the first order statistics predicted with the different subgrid-scale models find a reasonable explanation in the turbulent fluxes of momentum and heat, as shown in Fig. 6.12 and 6.13, respectively.

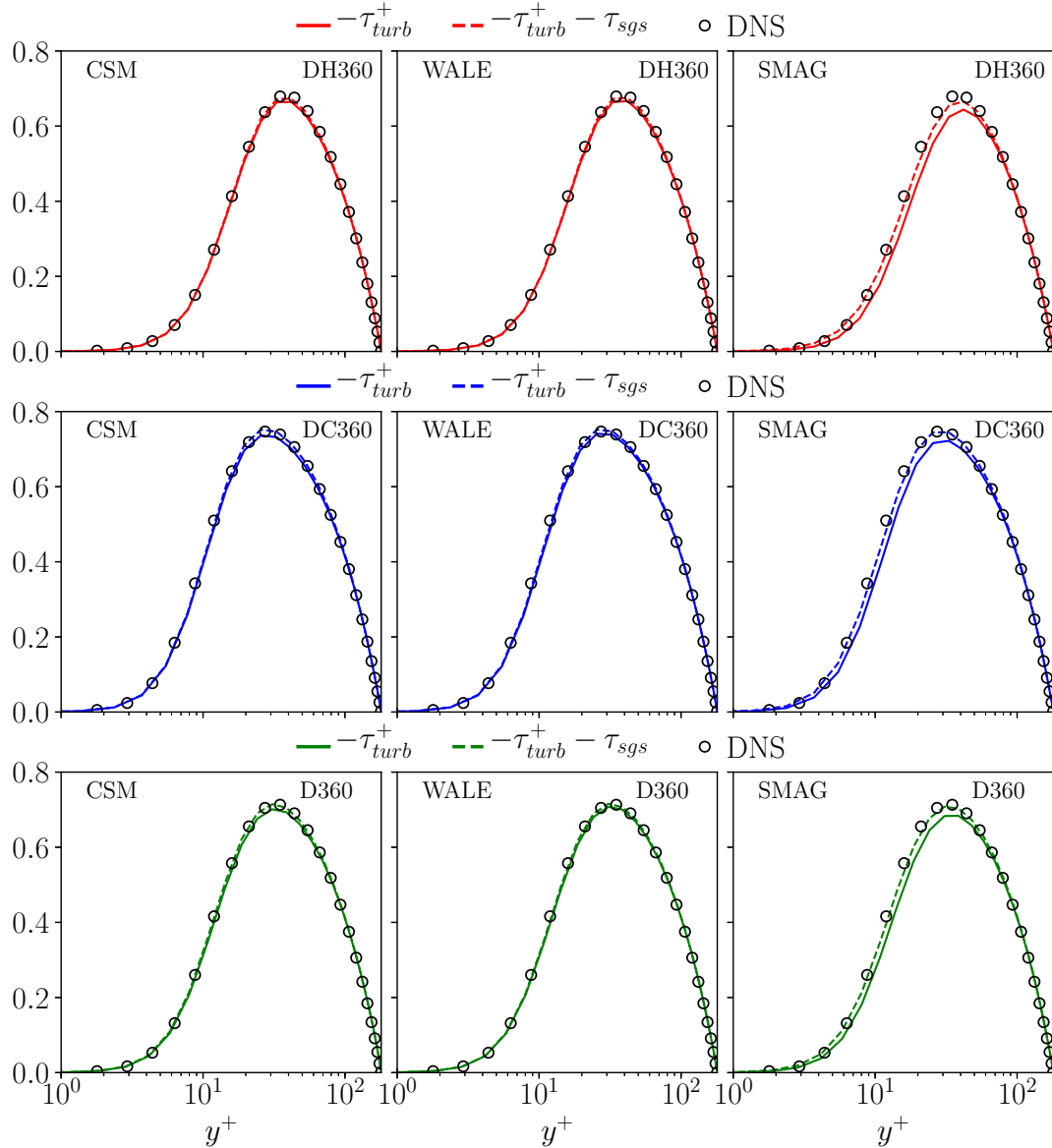


Figure 6.12: Resolved and total turbulent fluxes of momentum from CSM, WALE and SMAG compared against DNS for $Re_\tau = 360$

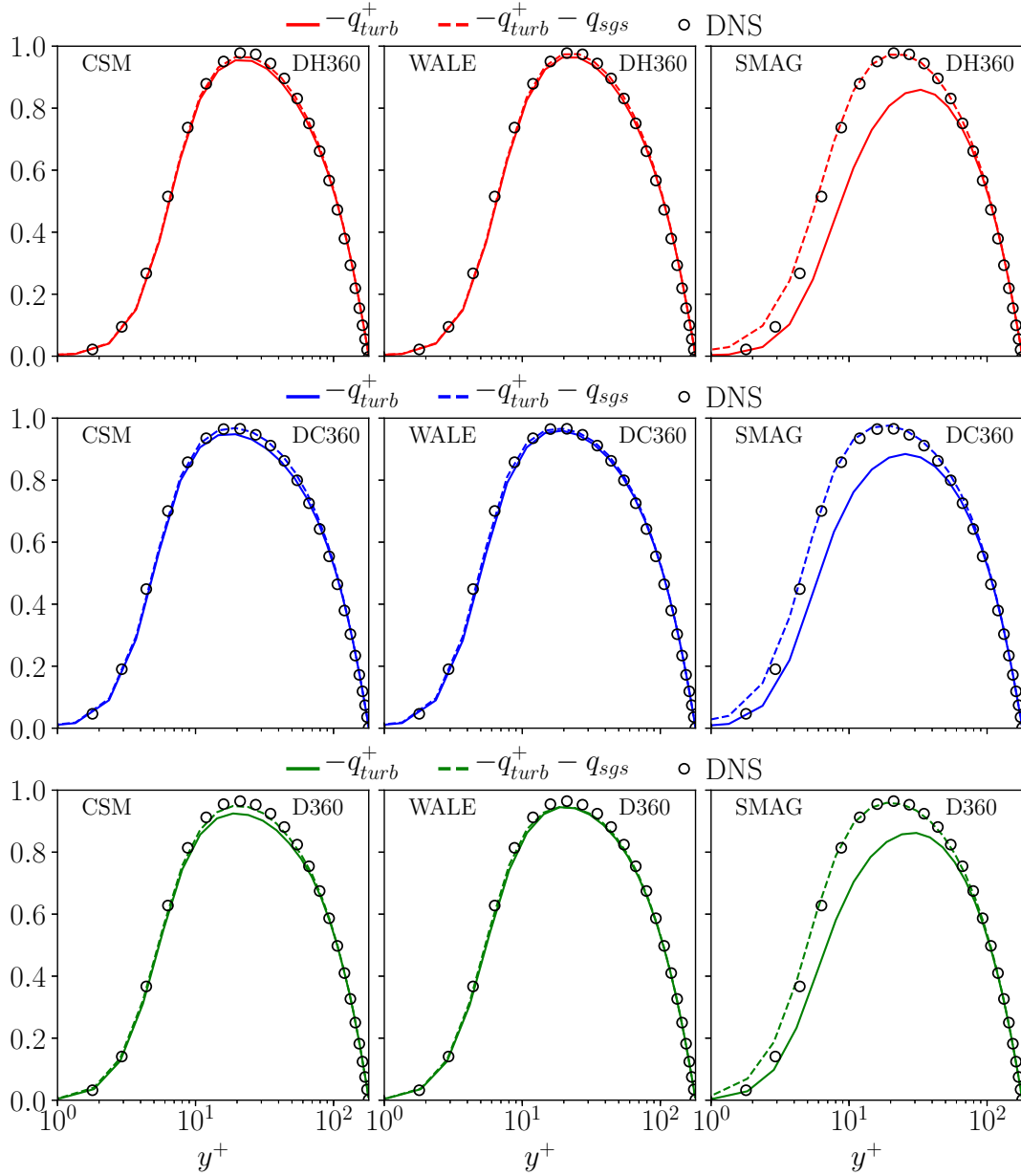


Figure 6.13: Resolved and total turbulent fluxes of heat from CSM, WALE and SMAG compared against DNS for $Re_\tau = 360$

It is seen that SMAG consistently predicts lower resolved contributions $\tau_{turb}^+ = -\langle \tilde{\rho}^* \bar{u}'^+ \bar{w}'^+ \rangle$ and $q_{turb}^+ = -\langle \tilde{\rho}^* \bar{u}'^+ \bar{\chi}'^+ \rangle$ in all considered cases across the whole near wall region. This general behaviour points at the comparatively strong dissipative nature of this model, despite the artificial wall dampening of eddy viscosity introduced by the Van Driest function. In turn, SMAG produces the relatively largest sgs-contributions, which reflects the high predicted sgs-viscosity for $y^+ < 10$, as already pointed out by Fig. 6.11. Especially in the

heated case DH360, the enhanced sgs-contribution to momentum flux still does not fully compensate for the deficit in the resolved turbulent shear stress. The consequently over-predicted laminar contribution translates into a faster increase in the axial mean velocity $\langle w^+ \rangle$, as observed in the first row of Fig. 6.10 for $y^+ > 20$. On the other hand, the sgs-contribution considerably overcompensates the gap in the turbulent heat flux very next to the wall, which in turn reduces the laminar contribution q_{lam}^+ , resulting in a notably slower increase of the mean enthalpy difference $\langle \bar{\chi}^+ \rangle$ beyond $y^+ > 3$. This underestimation also leads to a slower increase in the molecular viscosity in the heated case, which effectively further increases the overestimation of $\langle w^+ \rangle$.

As opposed to SMAG, the LES using CSM and WALE sgs models deliver consistently higher total turbulent shear stresses, despite the significantly lower eddy viscosity for the modelled contribution τ_{sgs} up to the buffer layer. The laminar contribution τ_{lam}^+ is therefore in closer agreement with DNS results. In a similar fashion, the more accurate representation of the total turbulent and laminar heat flux leads to a better prediction of the local molecular viscosity profile and, consequently, also of the shear rate $\partial \langle w^+ \rangle / \partial r^*$, granted the aforementioned correct prediction of τ_{lam}^+ .

In the cooled case (DC360), where the molecular viscosity decreases towards the centre, SMAG evidently performs better with respect to the heated case, as indicated by the closer agreement with the DNS data seen for the predicted total fluxes of momentum and heat in Figs. 6.12 and 6.13, respectively.

Despite the apparently marginal contribution of τ_{sgs} and q_{sgs} of CSM and WALE to the resolved turbulent fluxes of momentum and heat, the action of both sgs models is still very beneficial to the predictions of the first order statistics of the axial velocity and enthalpy difference. This benefit becomes evident by comparing in Fig. 6.10 the predictions obtained with CSM and WALE against the LES results predicted without sgs model, represented by the dashed line labelled with "No Model".

The *rms*-value of the fluctuating velocity components and enthalpy difference are compared against the corresponding DNS data for the heated (DH360), cooled (DC360) and constant fluid properties (D360) cases in Figs. 6.14 through 6.16, respectively. The superior performance of CSM and WALE as compared to SMAG is confirmed here again. SMAG consistently underpredicts the radial and azimuthal velocity components in the near wall region, while CSM and WALE are always very close to the DNS data. This trend is well in line with the already commented deficits of SMAG, which consistently delivers the lowest contribution in both resolved turbulent momentum and heat fluxes, as compared to CSM/WALE.

SMAG exhibits the biggest deviation from the DNS results in the resolved enthalpy fluctuations for the heated case (DH360), where the significantly underpredicted averaged enthalpy difference results in a lower local molecular Prandtl number, which effectively reduces the thermal fluctuations over the whole wall distance. A similar behaviour is seen for SMAG in the cooled (DC360) and constant fluid properties (D360) cases, albeit less pronounced, as the underlying underprediction of enthalpy difference is not as significant as in the heated case (DH360).

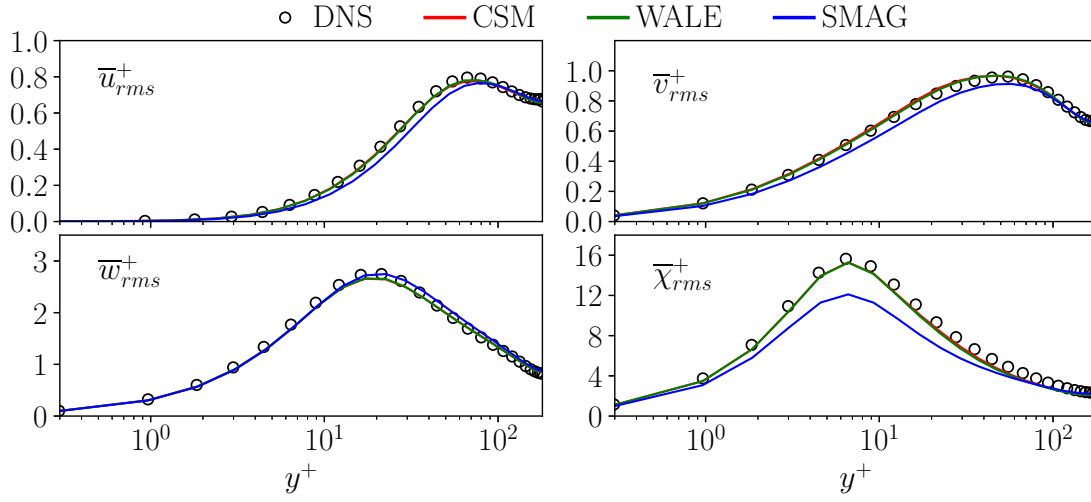


Figure 6.14: *Rms*-values of fluctuating velocity components and enthalpy difference predicted by LES with SMAG, CSM, WALE and DNS at $Re_\tau = 360$, heated variable fluid properties case DH360

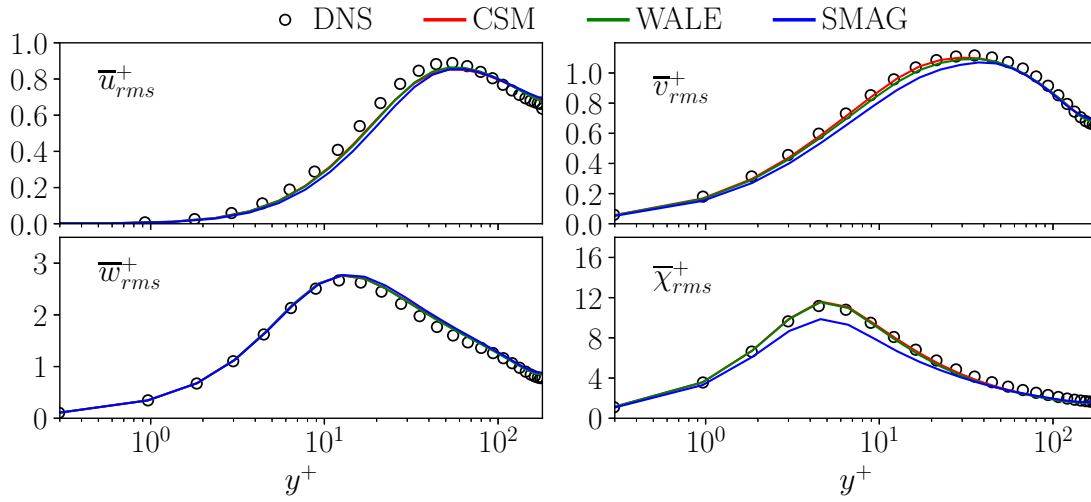


Figure 6.15: *Rms*-values of fluctuating velocity components and enthalpy difference predicted by LES with SMAG, CSM, WALE and DNS at $Re_\tau = 360$, cooled variable fluid properties case DC360

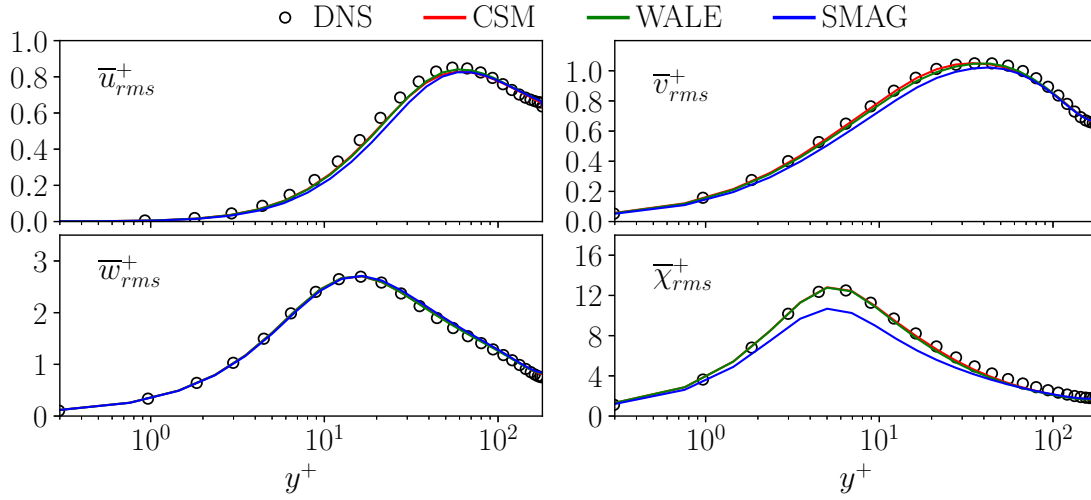


Figure 6.16: *Rms*-values of fluctuating velocity component and enthalpy difference as predicted by LES with SMAG, CSM, WALE and DNS at $Re_\tau = 360$, constant fluid property case D360

6.2.3 Assessment in strongly heated condition

The accuracy of the sgs models was further assessed in strongly heated conditions, where a higher variation in molecular viscosity is realized by a more pronounced difference between the wall and bulk temperature T_w and T_b , respectively. The considered conditions are associated with a doubled wall heat flux $\langle q_w \rangle = 40000 \text{ W/m}^2$ and a Reynolds number $Re_\tau = 500$, and they are referred to by DHH500 in Tables 5.1 and 6.1 for DNS and LES, respectively. For this particular test case, the molecular viscosity is increased up to 50% over its reference wall value, which further translates into a drop in local friction Reynolds number by a similar extent (see Fig. 5.6).

The settings of DHH500 certainly pose a higher challenge to the subgrid-scale modelling, which arises from the larger content of unresolved turbulent small scale motion due to the larger Reynolds number, and the more pronounced variation of the material properties due to the increased wall heating. The results from the LES of this more challenging test case basically confirm the findings from the assessment of the sgs models carried out with the lower Reynolds number and wall heat flux. Similar trends of deviation are seen for SMAG in the profiles of the mean axial velocity and enthalpy difference, while CSM and WALE are again in very good agreement with the DNS data, as it is shown in Fig. 6.17.

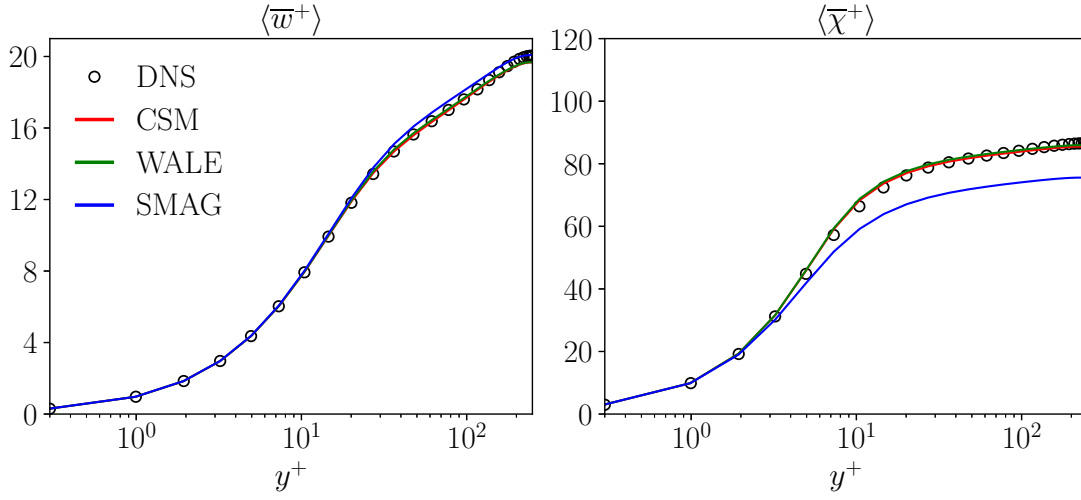


Figure 6.17: Averaged axial velocity component and enthalpy difference as predicted by LES with SMAG, CSM, WALE and DNS at $Re_\tau = 500$, strongly heated case with variable fluid properties (DHH500)

Similar to the observations in Fig. 6.14, the comparison between *rms*-statistics of the velocity components unveils again underpredicted wall normal and azimuthal velocity fluctuations for SMAG, as shown in the first row of Fig. 6.18. Enthalpy fluctuations predicted by SMAG are underestimated as well, due to the significantly lower predicted averaged enthalpy difference as compared to DNS (see the right side of Fig. 6.17), which in turn is responsible for a slower increase in local molecular Prandtl number towards the centerline.

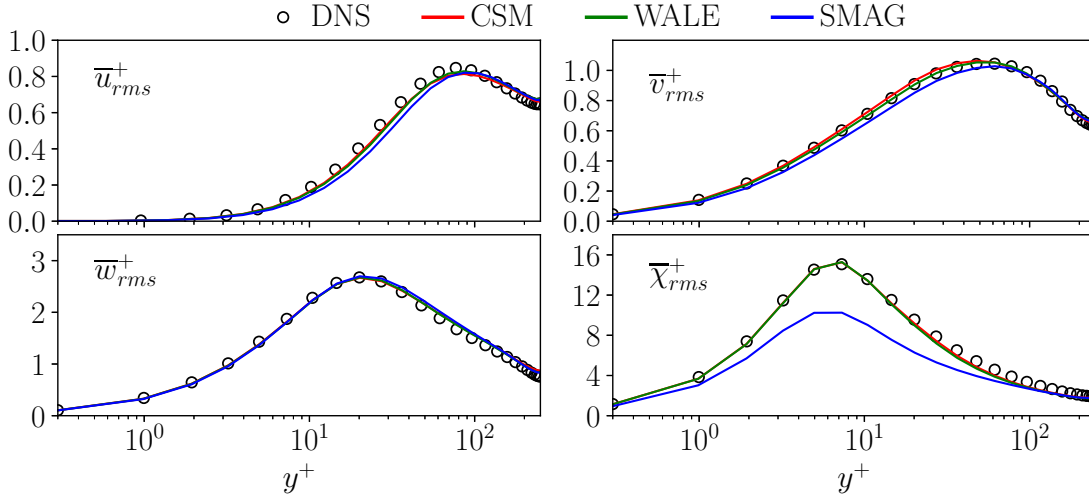


Figure 6.18: *Rms*-values of fluctuating velocity components and enthalpy difference as predicted by LES with SMAG, CSM, WALE and DNS at $Re_\tau = 500$, strongly heated case with variable fluid properties (DHH500)

Finally, the performance of CSM, WALE and SMAG is assessed by evaluating the modelled subgrid-scale contributions τ_{sgs} and q_{sgs} to total turbulent fluxes of momentum and heat, respectively. The comparison between resolved plus modelled fluxes and the DNS-based fully resolved fluxes is presented in Fig. 6.19. A closer look unveils that SMAG apparently predicts the total turbulent momentum flux better for the present higher friction Reynolds number condition than in the heated case with the lower Reynolds number (DH360), as discussed above in Fig. 6.19. The overshoot, which is still exhibited by SMAG in the mean axial velocity in Fig. 6.17, can be therefore mainly attributed to the back-coupling of the underestimated enthalpy difference on the flow through the local molecular viscosity, being predicted too low here again.

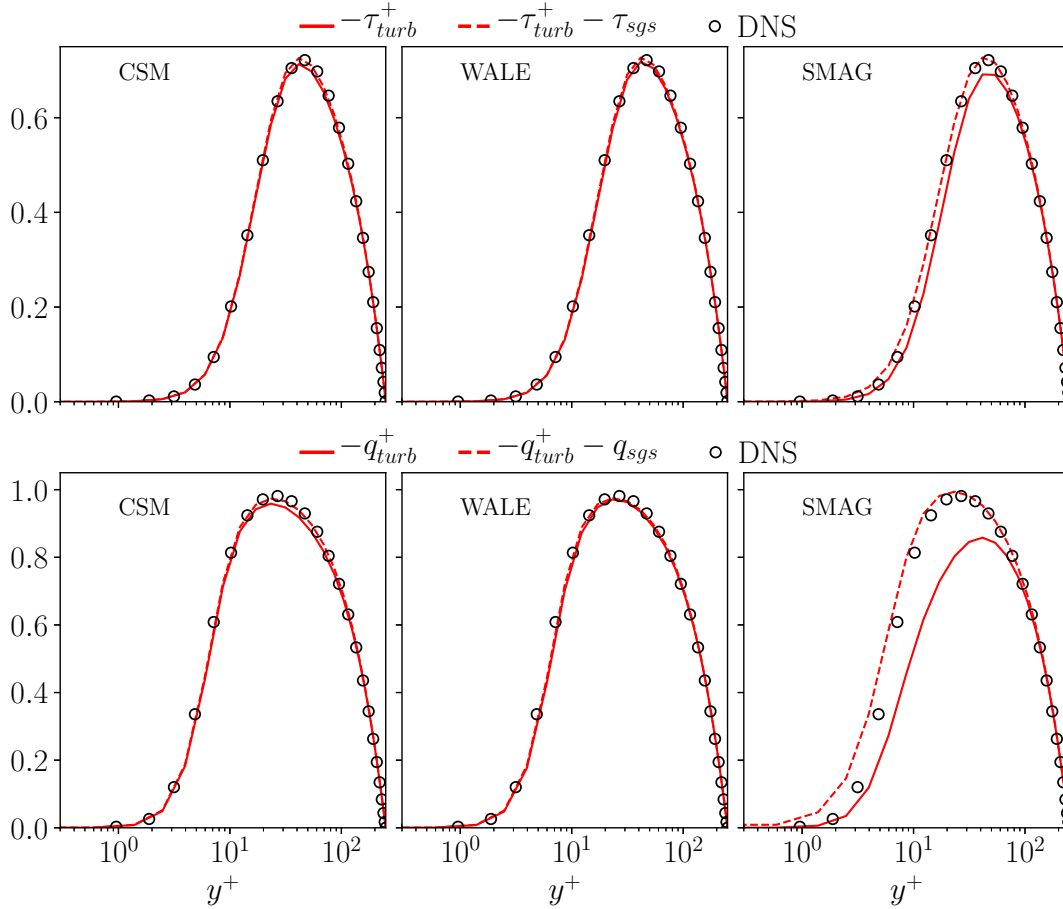


Figure 6.19: Resolved and total turbulent fluxes of momentum and heat from LES with CSM, WALE and SMAG compared against DNS at $Re_\tau = 500$, strongly heated case with variable fluid properties (DHH500)

Chapter 7

A posteriori LES of turbulent flow in pipe with abrupt circular expansion

The present section is dedicated to the analysis of heat transfer in a turbulent pipe flow which suddenly experiences an abrupt circular expansion, which causes a complete separation of the dynamic and thermal boundary layers. The separated flow region, downstream of the step-like change in the pipe diameter has already been sketched in Fig. 2.6 in chapter 2. In the presently considered geometrical configuration, the ratio between the upstream and downstream diameters is assumed as

$$ER = \frac{d}{D} = 0.533, \quad (7.1)$$

which has been chosen so as to match the conditions reported in Baughn *et al.* (1984) and Zemanick and Dougall (1970). The inlet bulk Reynolds number was always assumed as

$$Re_d = \frac{w_{b,inlet}d}{\nu_{inlet}} = 9650. \quad (7.2)$$

The length of the inlet pipe was always set to $l_{inlet} = 2d$, the length of the radially extended downstream pipe was $L = 20 D$.

The dynamic boundary condition at the inlet is prescribed by an unsteady instantaneous velocity distribution obtained at a certain cross section in a precursor DNS of fully turbulent pipe flow, so as to impose a physically reasonable turbulent motion at the considered inlet Reynolds number. The simulations considered two working fluids with different thermophysical properties:

- *air* with constant material properties
- 50/50 Vol% mixture of *glysantine-water* at with temperature-dependent molecular viscosity $\mu(T)$ as shown in Fig. 2.9, while assuming the thermal conductivity λ , the specific heat capacity c_p , and density ρ as constant.

The inlet pipe section was always assumed as unheated, so that the flow remains isothermal here and stays on its inlet temperature T_i . Different thermal boundary conditions were applied in the extended pipe section for each considered working fluid. As summarized in Table 7.1, a constant wall heat flux is imposed for air (*isoflux*), while a constant wall

Table 7.1: Thermal conditions adopted for the considered working fluids

Re_d	9650					
	$w_{\tau,inlet} [\frac{m}{s}]$	$T_i [K]$	Pr_w	<i>thermal BC</i>	$q_w [\frac{W}{m^2}]$	$T_w [K]$
<i>Air</i>	0.897	311	0.7	isoflux	400.0	-
<i>glysantine-Water</i>	0.0567	331	10.0	isothermal	-	344.7

temperature $T_w > T_i$ is imposed for glysantine-water, both prescribed along the whole length of the downstream pipe. The assumption of constant material properties implies a uniform molecular Prandtl number $Pr = Pr_w = const$ throughout the whole computational domain for air. Considering variable viscosity in the case glysantine-water, the molecular Prandtl number based on the constant heated wall temperature T_w is used as reference $Pr_w(T_w)$.

The quantitative settings for the thermal conditions represented by the inflow temperature T_i , downstream wall temperature T_w and heat flux q_w , and the reference wall molecular Prandtl number Pr_w are listed in Table 7.1. The friction velocities, which ensure the same inlet bulk Reynolds number for both fluids, are included as well.

For each of the considered working fluids three simulations (DNS, LES with CSM as sgs model, LES without sgs model) have been carried out. The resolution at the wall of both the LES and DNS cases in the radial and azimuthal directions is shown in Table 7.2, where a non-dimensional representation

$$(\cdot)^+ = \frac{(\cdot) w_{\tau,inlet}}{\nu_{inlet}} \quad (7.3)$$

based on the respective inlet wall units of the precursor DNS is adopted, with the inlet kinematic viscosity evaluated at the inlet temperature T_i as $\nu_{inlet} = \nu(T_i)$.

The grid was clustered in the axial direction in the proximity of the abrupt expansion, in order to better represent the small scales structures emerging in this region. The axial resolution for the grids employed in LES and DNS, represented again in inlet wall units $(\cdot)^+$, is shown in Fig. 7.1 and Fig. 7.2, respectively.

Table 7.2: Grid resolution in the radial and azimuthal directions for DNS/LES

	Δr_w^+	$R^+ \Delta \phi$	total number of mesh points
<i>DNS</i>	0.51	3.56	$13.12 \cdot 10^7$
<i>LES</i>	0.51	14.92	$5.59 \cdot 10^6$

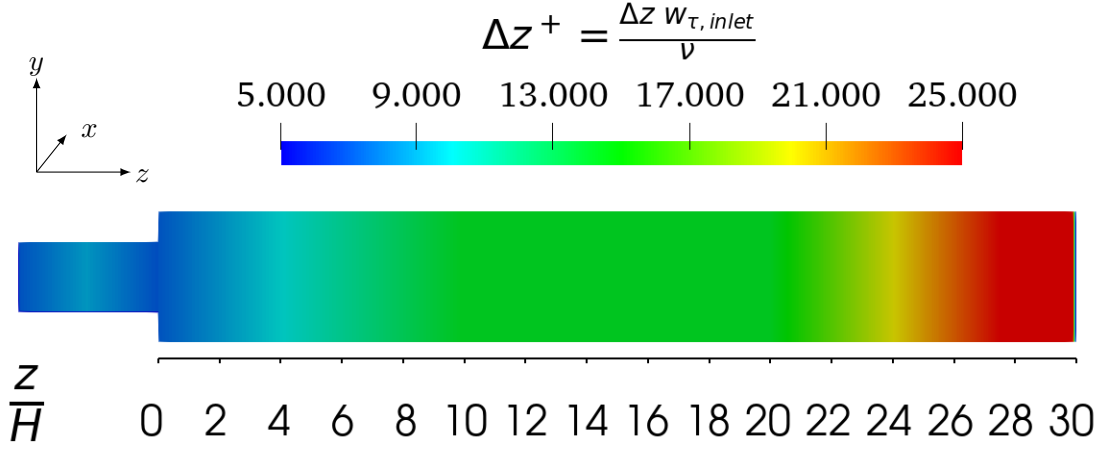


Figure 7.1: Axial resolution in LES given in inlet wall units

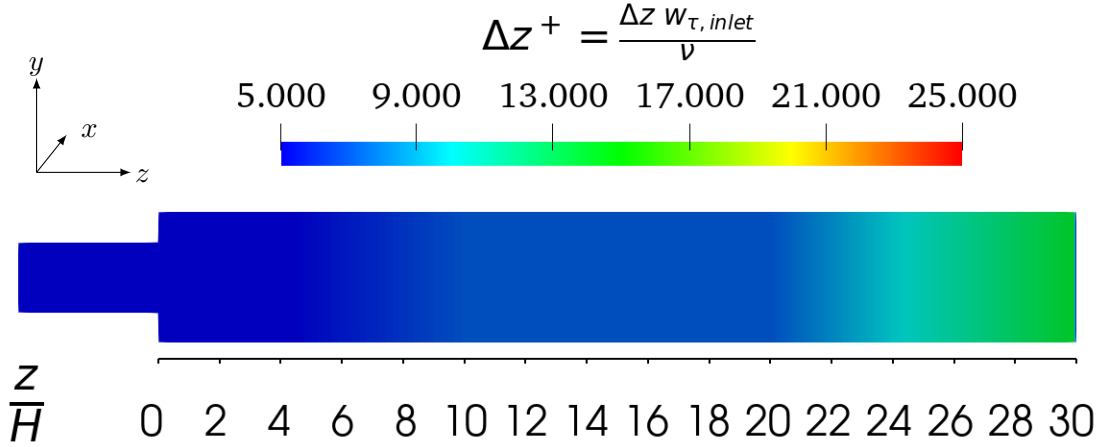
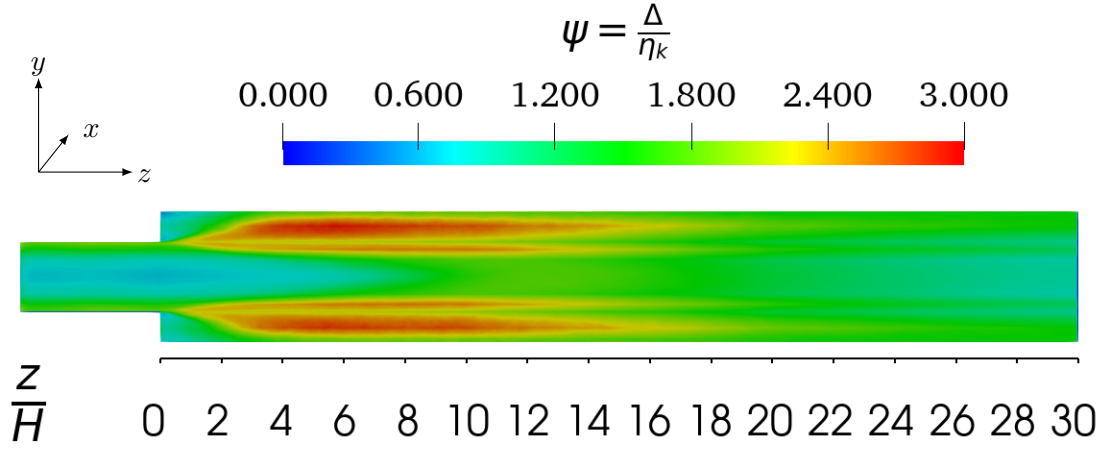


Figure 7.2: Axial resolution in DNS given in inlet wall units

The quality of the resolution of the DNS simulations was assessed by evaluating the ratio $\Psi = \frac{\Delta}{\eta_K}$, which relates the local grid size, estimated as $\Delta = (\Delta V)^{1/3}$, to the averaged local Kolmogorov scale η_K as retrieved from DNS results according to the definition given in Eq. (3.1). Contours of Ψ on a meridial cross section are shown in Fig. 7.3, which highlights the region of relatively lowest axial resolution located between $3 < \frac{z}{H} < 13$. Here, the enhanced turbulent mixing associated with the breakdown of the jet-like core flow leads to a strongly increased dissipation of turbulent kinetic energy, which effectively reduces the smallest relevant scales represented by η_K . Nevertheless, the ratio Ψ never exceeds the value three. A similar satisfactory resolution was seen for the DNS with glysantine-water.

Figure 7.3: Contours of ratio Ψ obtained for the DNS with air

7.1 Momentum transfer in separated flow condition

Although the material properties are assumed as constant for air, while the molecular viscosity can vary with temperature for glyserine-water, the spatial evolution of the turbulent velocity field past the cylindrical backward facing step is still very similar for both cases. The reason for this similarity lies, on one hand, in the same inlet bulk, or equivalently, friction Reynolds number, and on the other hand, in the fact, that the local molecular viscosity only varies inside a spatially very confined region in the case of glyserine-water. The latter is clearly indicated in Fig. 7.4, showing profiles of the the ratio between the averaged kinematic viscosity, $\langle \nu \rangle$, and its reference value at the wall, ν_w , at selected axial positions in the heated region downstream of the abrupt expansion. The intense mixing encountered in the shear layer between the inner jet-like core flow and the radially outer separated flow leads to a fairly homogeneous distribution of the molecular viscosity. For the most part, it thus remains on its inlet value ν_{inlet} and sharply drops only in close vicinity of the heated wall approaching the reference value at the higher wall temperature.

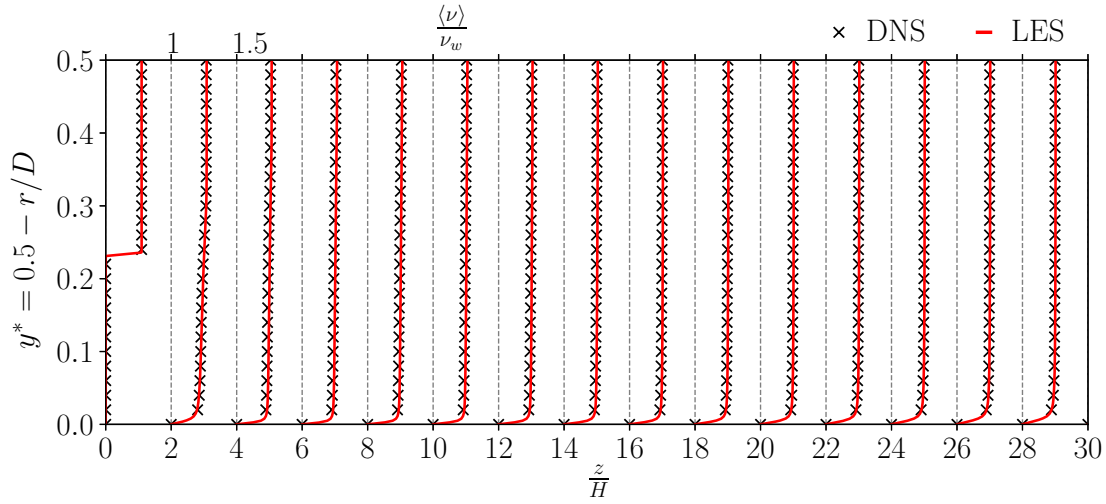


Figure 7.4: Wall normal variation of molecular kinematic viscosity with wall distance $y^* = 0.5 - r/D$ at selected positions z/H as predicted by DNS and LES using glysantine-water as working fluid

We observe here a relative decrease in $\frac{\langle \nu \rangle}{\nu_w}$ with respect to the bulk, or equivalently, inlet level of almost 30%. As this variation is confined to the very thin thermal boundary layer. The cross sectional bulk viscosity

$$\nu_b = \frac{\int_A \nu dA}{\int_A dA} \quad (7.4)$$

is not significantly decreased relative to the inlet conditions, so that there is practically no difference in the downstream bulk Reynolds number Re_D as compared to the case with air, where the viscosity is assumed constant. Thus, both cases exhibit essentially the same flow fields.

The sharp gradient in axial velocity right after the corner of the backward facing step triggers a Kelvin-Helmoltz instability. This instability typically generates small scale vortical structures producing a turbulent mixing layer which grows into the inner core region reducing the axial momentum similar to the breakdown of a free stream turbulent jet. Instantaneous snapshots of velocity field predicted by the DNS are shown in Figs. 7.5 - 7.7, where the velocity components are non-dimensionalized by rescaling with the inlet friction velocity.

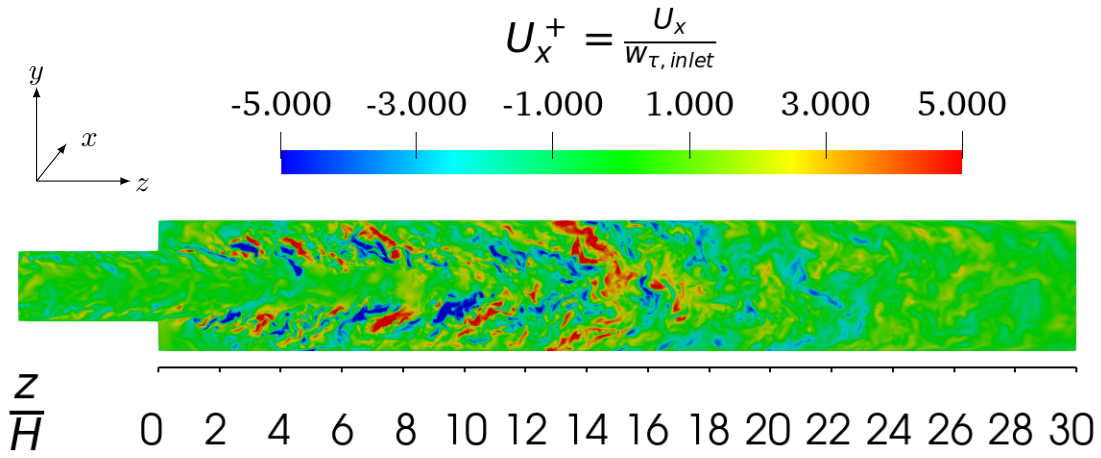


Figure 7.5: Sagittal view of instantaneous contours of spanwise velocity component predicted by DNS for air

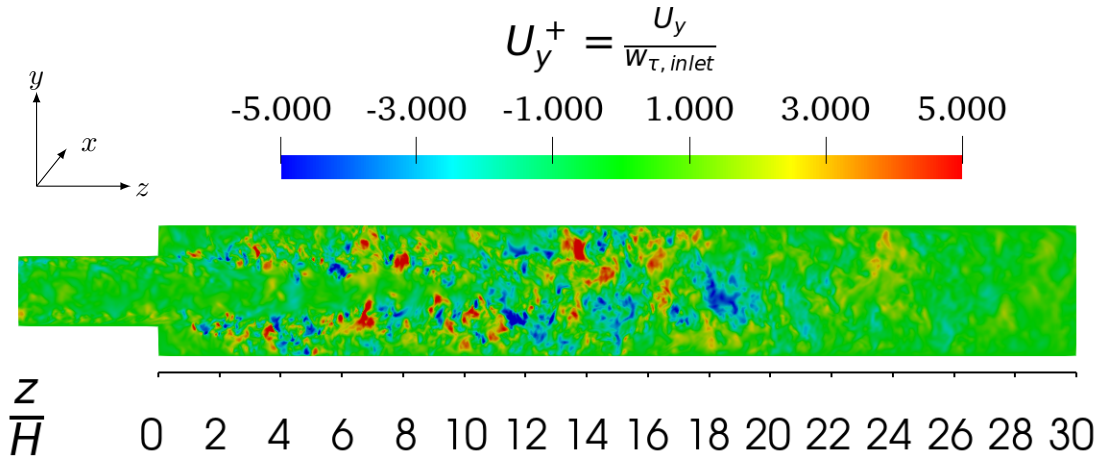


Figure 7.6: Sagittal view of instantaneous contours of wall normal velocity component predicted by DNS for air

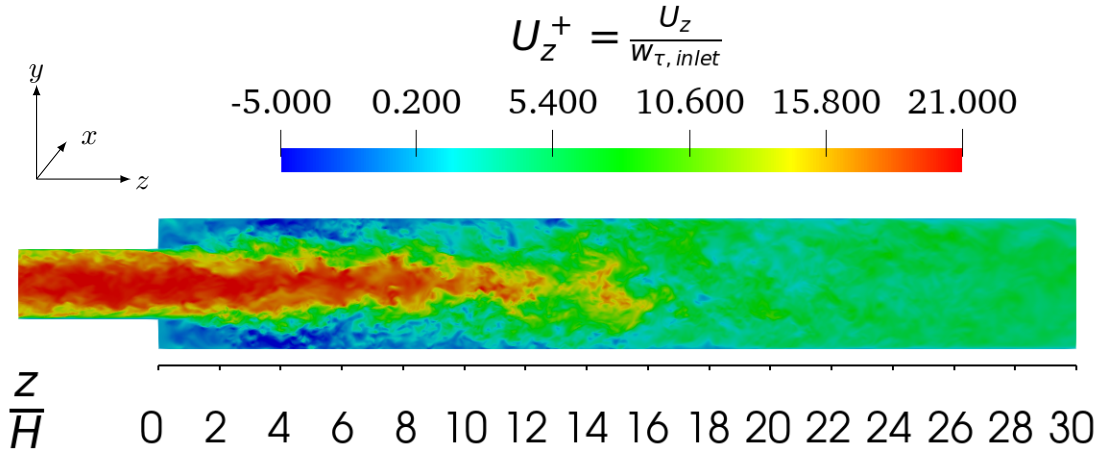


Figure 7.7: Sagittal view of instantaneous contours of axial velocity component predicted by DNS for air

The jet-like flow structure is clearly seen in Fig. 7.7. The oncoming jet-like flow breaks down past the step and preserves its central momentum up to approximately 12 step heights in the downstream pipe. The breaking down core-flow is surrounded by a large separated flow region. As seen in Fig 7.6, the abrupt circular expansion causes the formation of small eddies in the vicinity of the step, which grow in size on their way downstream. The countours of the azimuthal component U_x in Fig 7.5 further unveil the presence of helical structures, as also observed in the turbulent shear layers generated in free stream jets.

As the turbulent mixing of momentum and heat is significantly enhanced in the separated region, the correct prediction of the axial extension of the recirculation region represents a major issue for any turbulence model. In the present cases, the separation region past the step extends in the downstream pipe up to $\frac{z}{H} \approx 10$, as it may be observed from the axial position of the zero average wall friction coefficient $\langle C_f \rangle$ in Fig. 7.8. The similarity of the bulk Reynolds numbers throughout the domain, as pointed out above in the discussion of the radial variation of viscosity, evidently leads to a similar behaviour of the wall shear stress and skin friction coefficient C_f for both fluids. The reattachment length is practically the same for air and glysantine-water, being about $z/H \approx 10.5$. Both LES with CSM sgs model and without any sgs model turn out to accurately predict the location of the reattachment point, although a slight overprediction in C_f observed between $12 < \frac{z}{H} < 19$ for CSM.

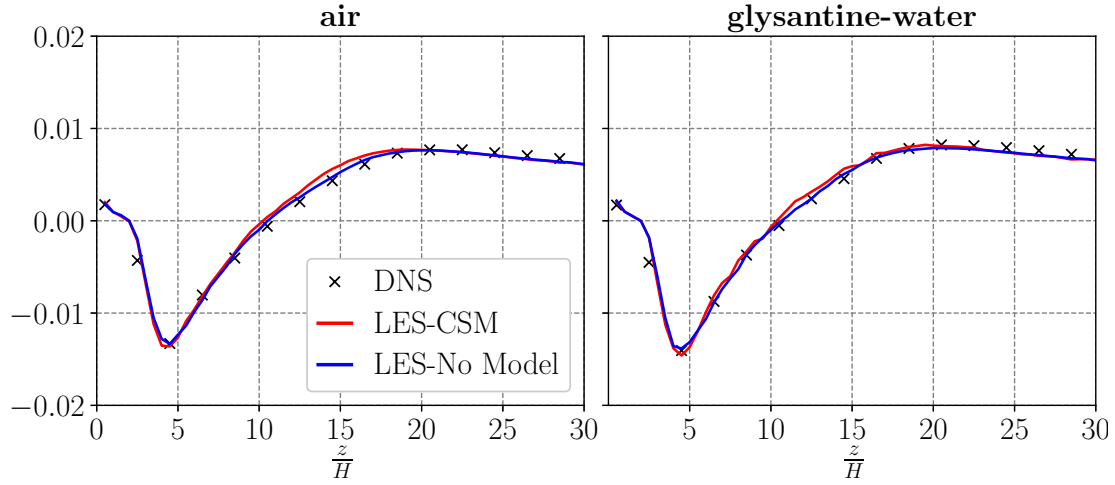


Figure 7.8: Axial variation of skin friction coefficient past the step in the downstream pipe as predicted by DNS, LES with CSM sgs model, and LES without sgs model

Inside the mixing layer between the inner jet-like core flow and the separated outer flow, the enhanced velocity fluctuations lead to an increased turbulent shear stress $\langle u'w' \rangle$. Due to the mentioned similarity in bulk Reynolds numbers, the variations of $\langle u'w' \rangle$ relative to the turbulent kinetic energy k are essentially the same for both fluid cases, as seen from Figs. 7.9 and 7.10. The LES predictions come evidently very close to the DNS results. Between $4 < z/H < 10$, the normalized turbulent shear stress $\langle u'w' \rangle / k$ exhibits a fairly flat plateau-like profile in the shear layer for both fluid cases, which is correctly predicted

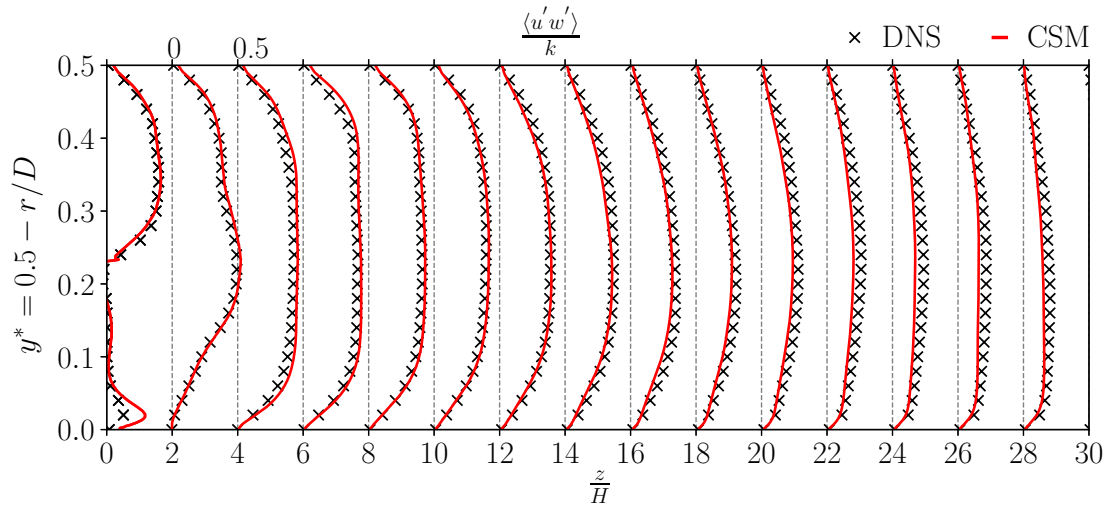


Figure 7.9: Wall normal variation of turbulent shear stress normalized with the turbulent kinetic energy in the downstream pipe past the step as predicted by DNS and LES with CSM sgs model for air

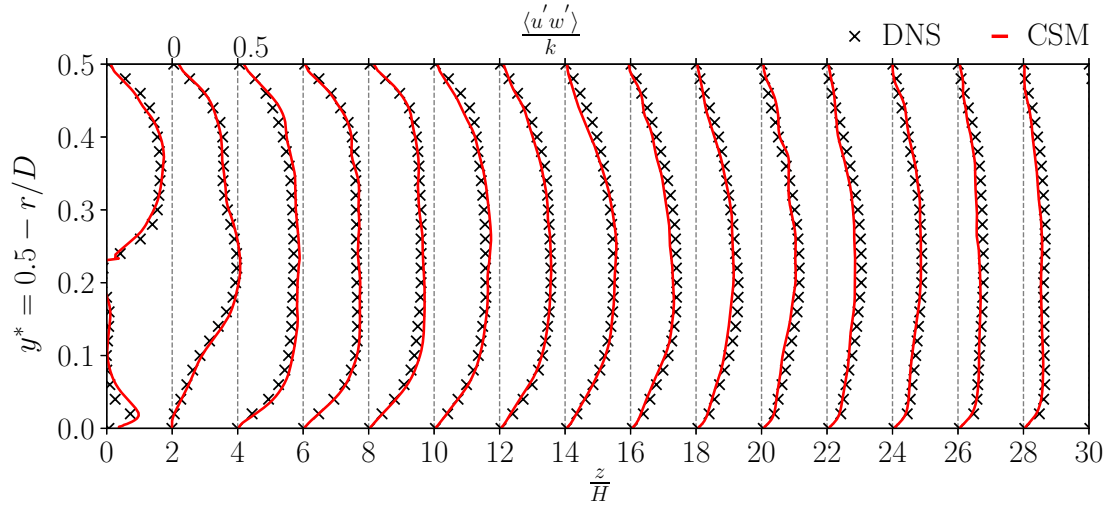


Figure 7.10: Wall normal variation of turbulent shear stress past the step in the downstream pipe as predicted by DNS, LES with CSM sgs model for glysantine-water

by LES. A moderate underprediction is seen for LES in the far downstream region for $\frac{z}{H} > 22$, where the turbulent flow is already recovering towards fully developed pipe flow conditions.

Finally, the contribution of the sgs eddy viscosity ν_{sgs} to total momentum diffusivity is assessed by evaluating the wall-normal variation of the ratio between $\langle \nu_{sgs} \rangle$ and the molecular counterpart ν at selected axial positions of the downstream pipe. As Fig. 7.11 exemplarily shows for air, the local eddy viscosity reaches its maximum of roughly 30% of the molecular counterpart at $\frac{z}{H} \approx 5$, indicating a significantly high sgs model contribution in this region. The contribution from the sgs model generally decreases further downstream. The kink at $y^* \approx 0.23$ is due to the local refinement of the grid, which is applied here for resolving the highly sheared region between the inner jet-like core flow and the outer separated flow region.

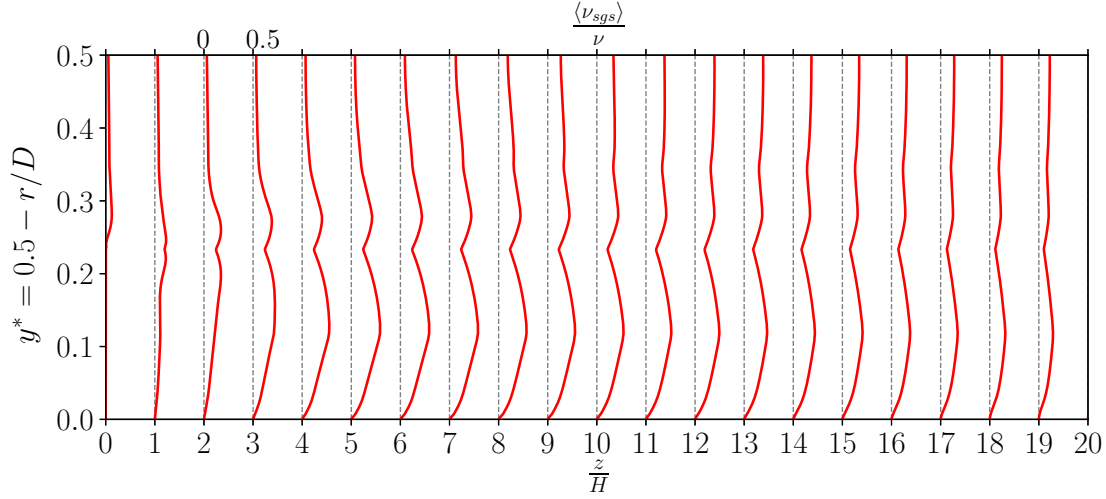


Figure 7.11: Wall normal variation of sgs eddy viscosity relative to molecular viscosity in the downstream pipe as predicted by LES with CSM sgs model for air

7.2 Heat transfer in separated flow condition

The markedly different molecular Prandtl numbers characterizing air ($Pr \approx 0.7$) and the mixture of glysantine-water 50/50 Vol% ($Pr \approx 10$) assumed as working fluids, breaks the similarity of the turbulent thermal field, as opposed to the previous observations on momentum transfer. As typical for Prandtl numbers well above unity, the thermal boundary layer near the heated wall is markedly thinner in the case with glysantine-water as compared to the case with air. The inner core flow region associated with a homogeneous (almost isothermal) distribution consistently extends closer to the wall. This behaviour is clearly seen in Figs. 7.12 and 7.13, showing contours of the instantaneous local temperature ratio $\frac{T}{T_i}$, as predicted for air and glysantine-water, respectively. In the latter case, the portion of uniformly low core flow temperature (associated with the dark blue regions) is definitely radially extended as compared to the case with air shown in Fig. 7.12.

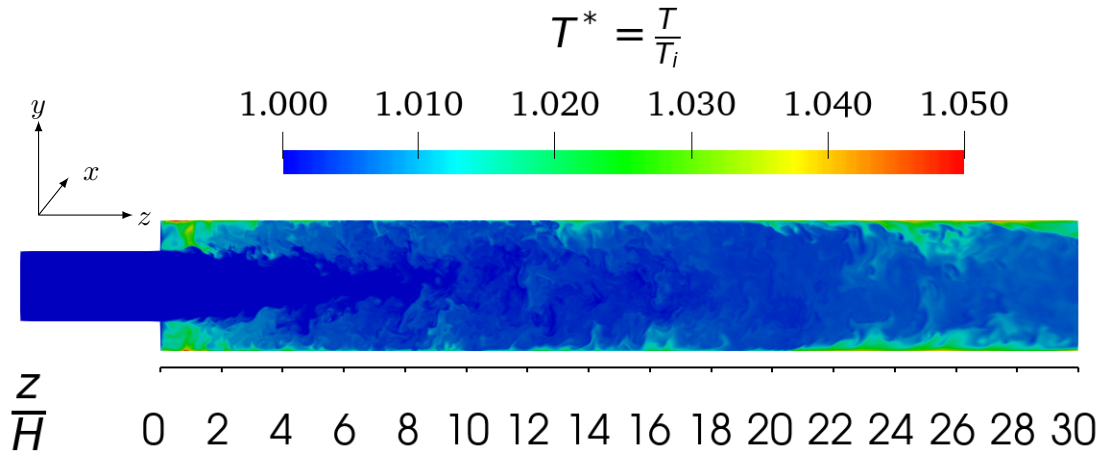


Figure 7.12: Sagittal view of instantaneous non-dimensional temperature field predicted by the DNS for air

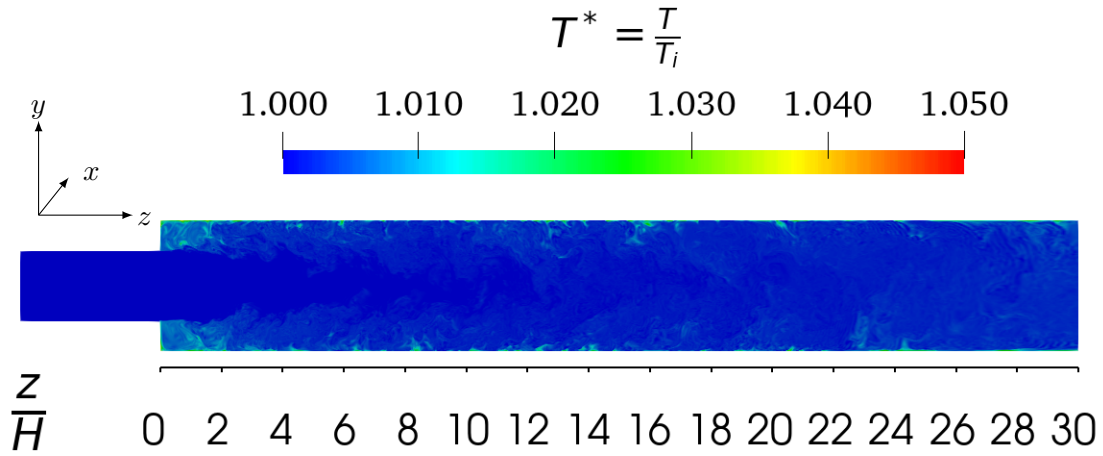


Figure 7.13: Sagittal view of instantaneous non-dimensional temperature field predicted by the DNS for glysantine-water

The thinner thermal boundary layer inherently leads to sharper temperature gradients resulting in higher turbulent temperature fluctuations. The enhanced fluctuations of the temperature next to the wall become evident in the *rms*-profiles shown in Fig. 7.14.

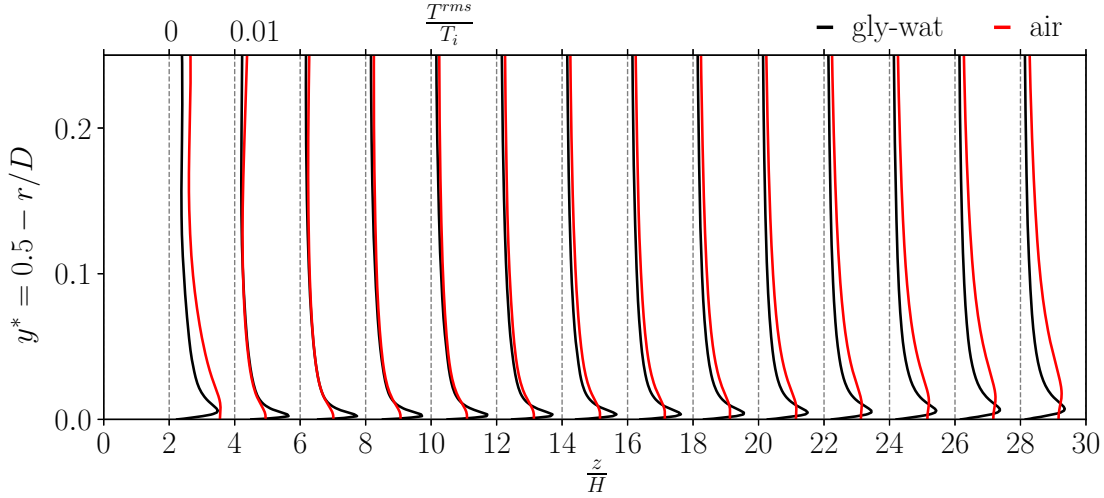


Figure 7.14: Wall normal variation of *rms*-value of non-dimensional temperature along the downstream pipe as predicted by DNS for air (red line) and glycantine-water (black line)

The intense mixing associated with the breakdown of the jet-like core flow induces a pronounced peak of the radial turbulent flux of heat $\langle u'T' \rangle$, located in the shear region at $z \approx 2H$, as shown in Figs. 7.15 and 7.16. The turbulent heat flux is rescaled here with the product $w_{\tau,inlet}\Delta T$, where

$$\Delta T = T_{bulk} - T_i = \begin{cases} 1.02 \text{ K,} & \text{for glycantine-water} \\ 2.73 \text{ K,} & \text{for air} \end{cases} \quad (7.5)$$

denotes the increase of the bulk temperature between in- and outlet. As such, $w_{\tau,inlet}\Delta T$ basically represents the total amount of heat, which is submitted to the fluid per time unit on its way through the pipe. The peak observed at the axial position $z \approx 2H$, being notably higher for the case with glycantine-water, is rapidly smeared out, due to the intense mixing in the shear layer between the core region and the separated back flow region.

The enhanced temperature fluctuations and the thinner thermal boundary layer associated with the higher Prandtl number is reflected as well in the near wall behaviour of the turbulent heat flux. The profiles for glycantine-water steeply decrease towards the wall within much smaller distance as in the case with air. In both fluid cases, the predictions obtained from LES with CSM as sgs model are in fairly good agreement with the targeted DNS based results.

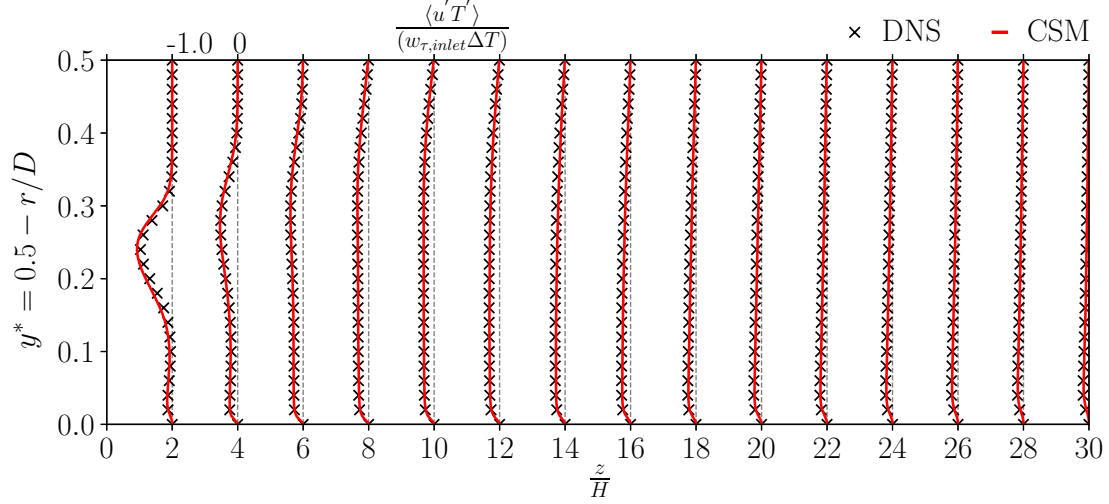


Figure 7.15: Wall normal variation of radial turbulent heat flux past the step in the downstream pipe obtained from DNS and LES with CSM sgs model for air

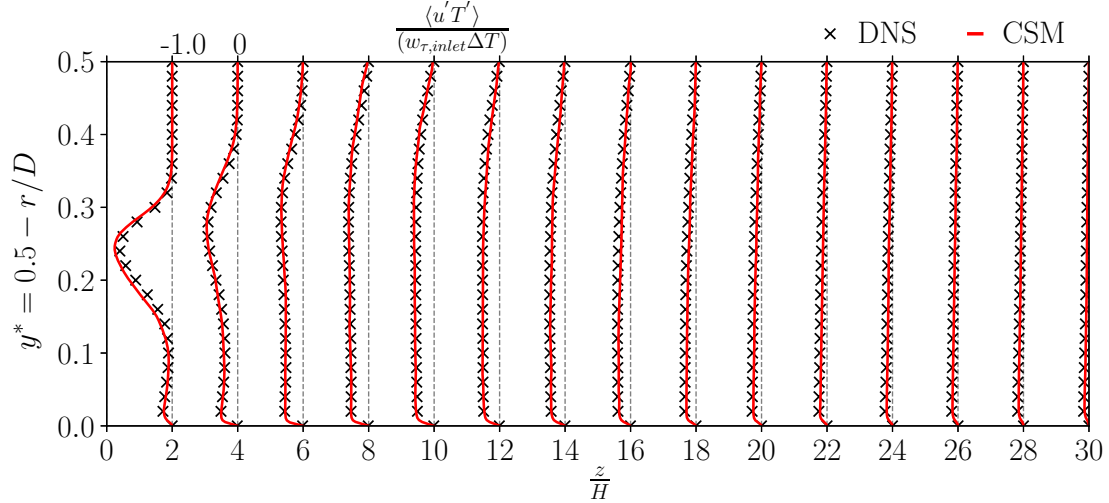


Figure 7.16: Wall normal variation of radial turbulent heat flux past the step in the downstream pipe obtained from DNS and LES with CSM sgs model for glycantine-water

The contribution of the sgs model CSM is predominantly constituted by the radial component of the modelled turbulent sgs heat flux vector specified by Eq. (3.16), depending on the gradient of temperature in wall-normal direction as prescribed by the gradient-diffusion hypothesis as

$$\frac{q_{sgs,r}}{\tilde{\rho} \tilde{c}_p} = -\frac{\nu_{sgs}}{Pr_{sgs}} \frac{\partial T}{\partial r}. \quad (7.6)$$

The radial variation of its average value is shown in Fig. 7.17.

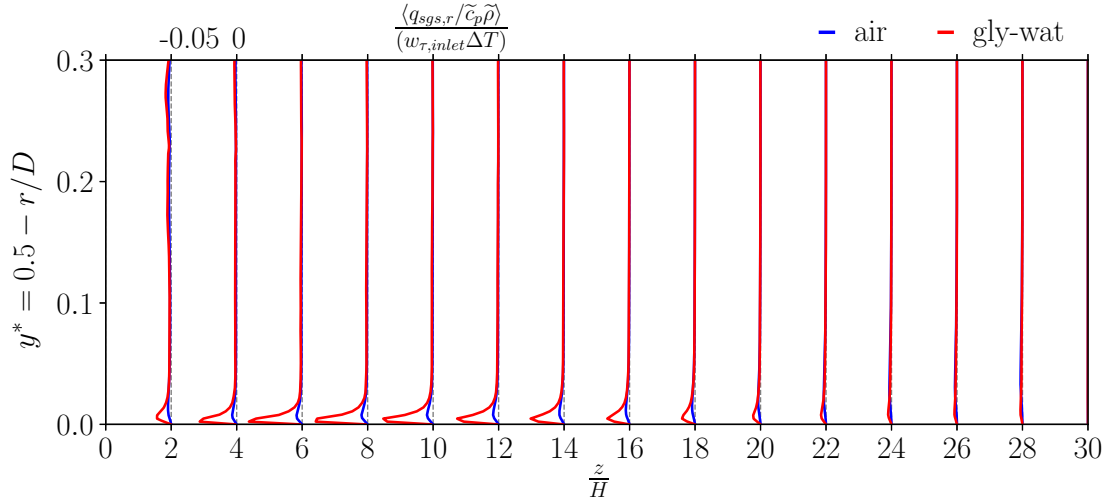


Figure 7.17: Wall normal variation of modelled sgs radial heat flux in the downstream pipe obtained from LES with CSM sgs model for glystantine-water and air

Here again, the reference quantity $w_{\tau,inlet}\Delta T$ is used for rescaling in both cases. Evidently, the sgs-contribution is generally much smaller than the resolved counterpart, already shown in Figs. 7.15 and 7.16. Only within a very confined region near the wall, where the temperature gradients become large, especially in the case with glystantine-water, we observe a notable contribution, as indicated by the peaks.

The performance of the sgs model was further assessed in the predicted heat transfer rate in terms of a relative Nusselt number defined as

$$Nu^* = \frac{Nu}{Nu_{DB}}. \quad (7.7)$$

Nu was evaluated here according to its definition

$$Nu = \frac{D \langle q_w \rangle}{\lambda_w \langle T_w - T_b \rangle}, \quad (7.8)$$

with T_b , T_w and q_w being obtained from the predicted temperature field, if not imposed as thermal wall b.c. Nu_{DB} represents the Nusselt number computed from the Dittus-Bolter formula based on the bulk molecular Prandtl number and bulk Reynolds number as

$$Nu_{DB} = 0.023 Pr_b^{0.3} Re_b^{0.4} \quad (7.9)$$

in the extended pipe.

The axial variation of Nu^* for air and glystantine-water is shown in Fig. 7.18, where the DNS based results are compared against the predictions from LES with the CSM sgs model and without any sgs model (LES-No Model).

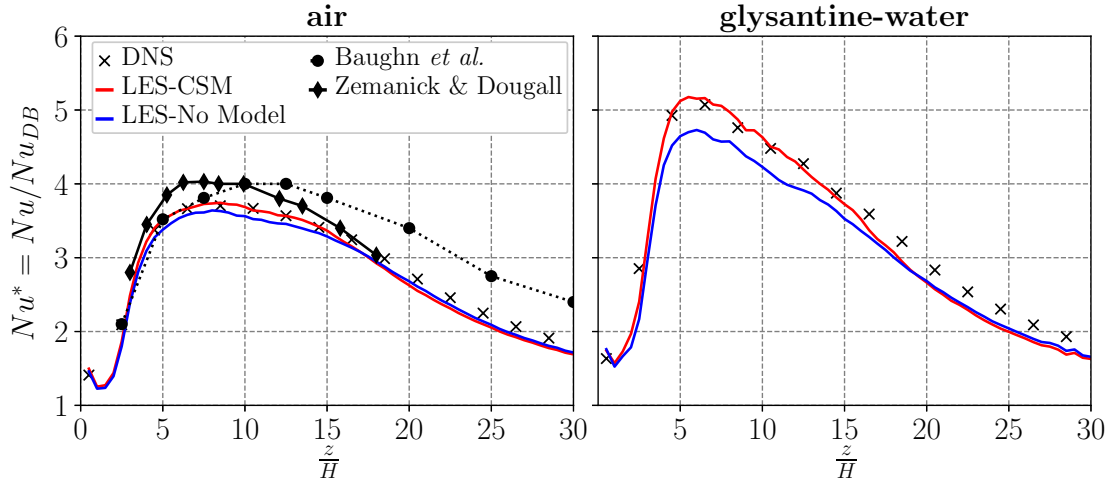
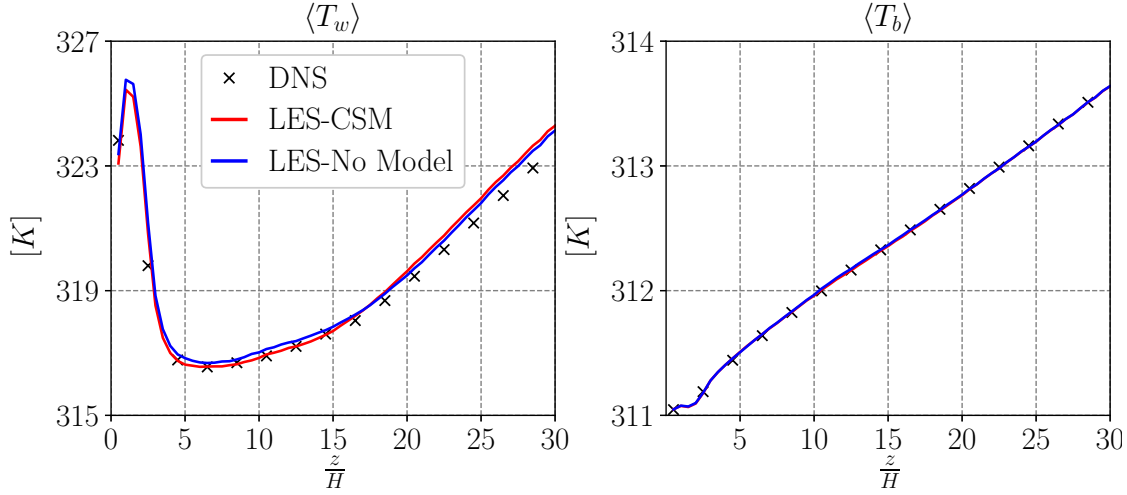
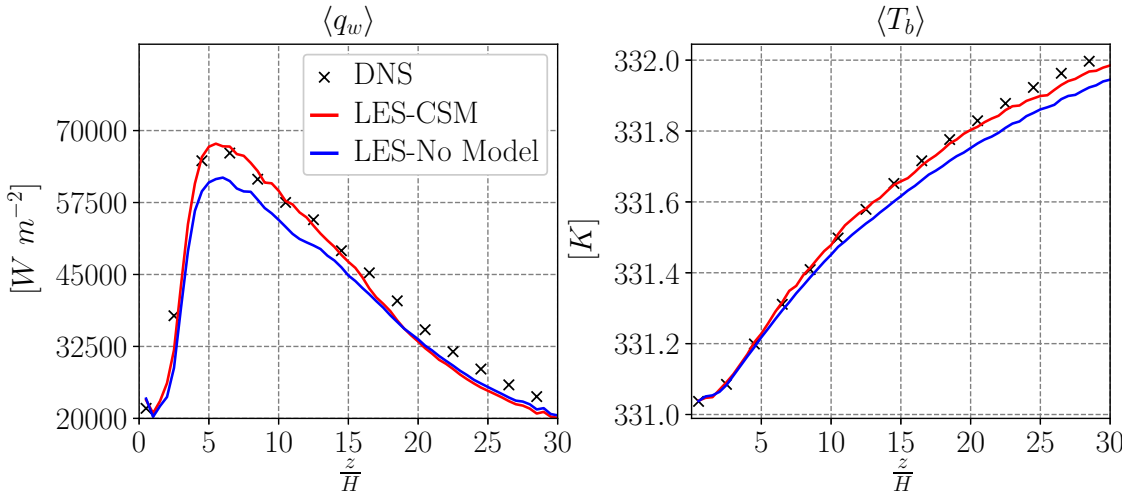


Figure 7.18: Axial variation of local Nusselt number Nu^* in the downstream pipe obtained from DNS, LES with CSM sgs model and LES without sgs model

The enhanced turbulent mixing prompted by the recirculating flow past the backward facing step results in an effective increase of Nu up to almost five times the value obtained in fully developed pipe flow at the same downstream bulk Reynolds and Prandtl numbers, represented by Nu_{DB} . The significant axial variation of Nu^* can be explained by a closer inspection of the individual constituents of Eq. (7.8) for the local Nusselt number Nu , together with the underlying flow field. Figs. 7.19 and 7.20 show the axial variations of the temperatures $\langle T_w \rangle$ and $\langle T_b \rangle$, and of the average wall heat flux $\langle q_w \rangle$ for the two fluid cases, respectively. The bulk temperature is computed as

$$\langle T_b \rangle = \frac{2\pi}{\dot{V}} \int_0^{D/2} \langle wT \rangle r dr.$$

$\langle q_w \rangle$ and $\langle T_w \rangle$ are prescribed as uniform thermal wall b.cs in the case with air and glysantine-water, respectively.

Figure 7.19: Averaged $\langle T_w \rangle, \langle T_b \rangle$ along axial coordinate z in the downstream pipe for airFigure 7.20: Averaged $\langle q_w \rangle, \langle T_b \rangle$ along axial coordinate z in the downstream pipe for glycantine-water

We can clearly see that the peak in Nu^* is associated with minimum wall temperature, $\langle T_w \rangle \rightarrow \min$, for the case with air, while it is associated with maximum wall heat flux, $\langle q_w \rangle \rightarrow \max$, in the case of glycantine-water. The position of the peak, which always occurs somewhat beyond $z/H \approx 5$, can be attributed to the action of the strong vortices emerging from the shear layer between the separated radially outer flow region and the inner core flow region. As it is indicated by the instantaneous velocity contours of the streamwise and wall normal velocities in Figs. 7.7 and 7.6, respectively, these strong vortices reach the heated wall near $z/H \approx 5$, inducing a strong axially reverse motion. Accordingly, the local wall shear stress drops to a distinct minimum around $z/H \approx 4$, as indicated by the skin friction coefficients in Fig. 7.8. This separation driven vortical motion apparently convects cold core fluid vertically downwards to the hot heated wall, which significantly increases

the local heat transfer rates, as measured by the Nusselt number. Further downstream, beyond the reattachment point around $z/H \approx 10$ this separation eddy enhanced transport fades out, and the flow field recovers towards fully developed conditions. Comparing the Nu^* -variation of air against glycantine-water, we also observe a notable Prandtl number effect. For glycantine-water, the peak of Nu^* is higher and occurs further upstream. Due to the inherently slower conductive heat up of the fluid with the higher Prandtl number, high wall temperature gradients persist further upstream, as seen in Fig. 7.21. This brings high temperature gradients into closer vicinity to the negative peak of wall shear stress, which effectively increases the heat transfer rate.

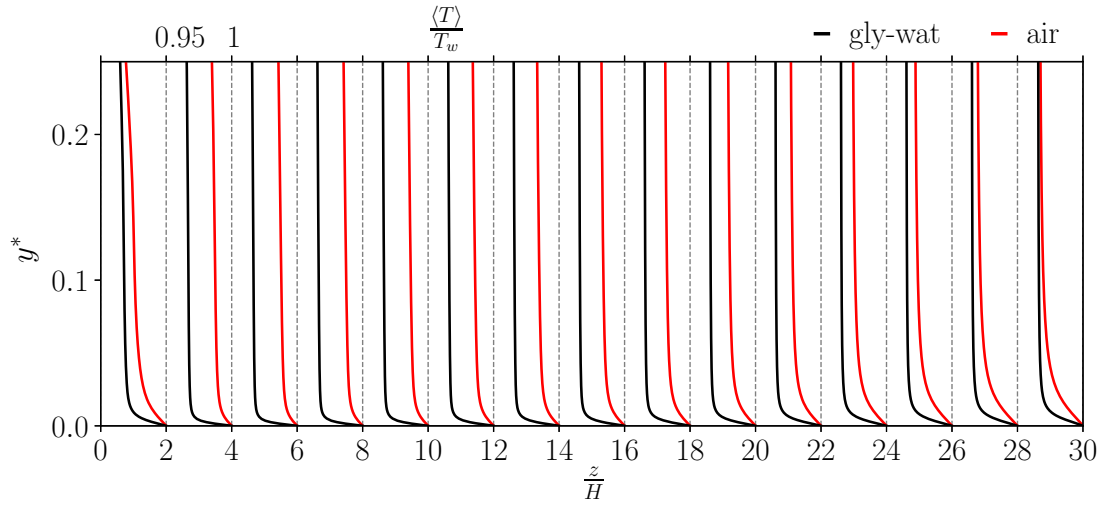


Figure 7.21: Axial variation of averaged temperature $\langle T \rangle / T_w$ along the downstream pipe as predicted by DNS for air (red line) and glycantine-water (black line)

For the case with air as working fluid, the experimental works by Baughn *et al.* (1989) and Zemanick and Dougall (1970) provide data for comparison, considering air in a pipe with similar expansion ratios $d/D = 0.533$, and inlet Re_B equal to 5300 and 4860, respectively. These data were been included in Fig. 7.18 on the left side for comparison. Both experiments report an increase by almost 4 times in the local Nusselt number within the region $8 < z/H < 11$. However, the exact position of the peak of Nu^* is not consistently reported by these two studies. Compared with the results from Baughn *et al.* (1984), the present DNS/LES underpredict the local heat transfer distribution in the far region of the downstream pipe, whereas a better agreement is observed in the region past the step for $z/H < 8$. When compared with the experiments of Zemanick and Dougall, 1970, on the other hand, a better agreement with the numerical simulations is found downstream of the reattachment point, for $z/H > 15$, whereas for $2 < z/H < 15$ the experimental results consistently exhibit a somewhat higher distribution. As opposed to the case associated with glysantine-water, the peak of Nu^* is here determined by a decreased contribution of the wall-to-bulk temperature difference $\Delta T = \langle T_w \rangle - \langle T_b \rangle$, rather than from the wall heat flux, which is imposed as constant on the whole downstream pipe's wall, as shown in Fig. 7.22.

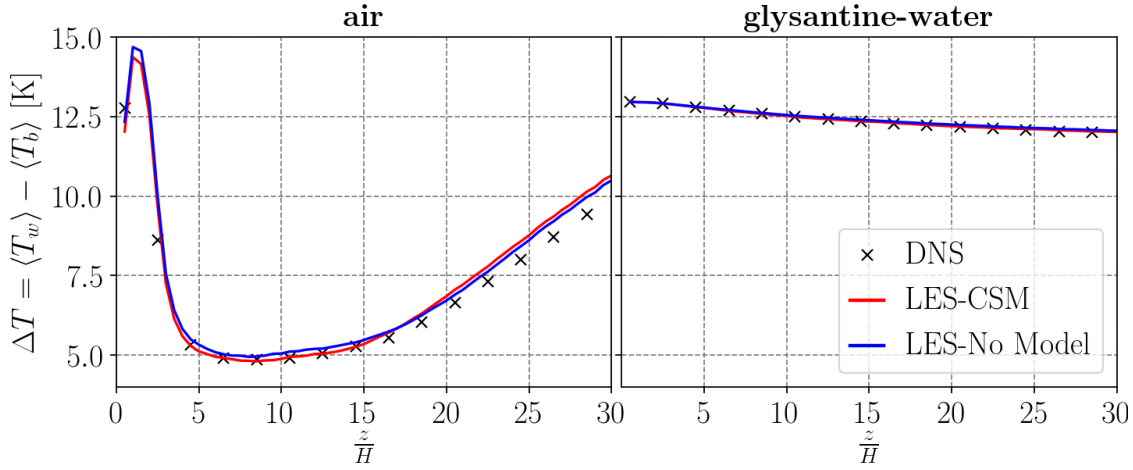


Figure 7.22: Axial variation of averaged wall-to-bulk temperature difference $\Delta T = \langle T_w \rangle - \langle T_b \rangle$ in the downstream pipe obtained from DNS, LES with CSM sgs model

Lastly, it is observed that the CSM sgs model notably improves the description of the overall heat transfer rate in the region of increased mixing between $4 < z/H < 18$. This is clearly indicated by a comparison against the predictions of the LES without sgs model, which underestimates Nu^* in this region for both cases with air and glysantine-water as working fluids.

Chapter 8

Summary and Conclusions

The convective heat transfer in periodic heated and cooled pipe flows subject to a significant variation of material fluid properties was investigated with the method of DNS. For the considered working fluid, a mixture of water and glysantine 50/50 Vol%, the molecular Prandtl number always stayed well beyond one, approaching the value $Pr \approx 10$ near the wall. The alternatively heated/cooled walls lead to a marked increase/decrease in molecular viscosity towards the centre relative to the common reference state prescribed at the wall. On the other hand, the variation of the remaining thermophysical properties was very limited, deviating at maximum by 5% from their reference wall values, even in the cases with the strongest wall heating or cooling.

The significant variation in viscosity is translated into an almost equivalent radial change in the local molecular Prandtl number, which effectively enhances/dampens the fluctuations of the enthalpy for the heated/cooled cases. Correspondingly, the local Reynolds number decreases/increases with distance to the heated/cooled wall, which effectively decreases/increases the turbulent fluctuations of velocity. This modulation of the turbulent velocity fluctuations turned out to always outweigh the opposed trend observed for the enthalpy fluctuations, so that the turbulent heat fluxes and finally the Nusselt numbers Nu are consistently lower/higher for the heated/cooled wall, at a given friction Reynolds number. This dominance of the Reynolds number effect over the effect of the molecular Prandtl number was clearly seen in all considered cases.

The influence of the thermal boundary conditions was specially investigated as well by alternatively applying isothermal (Dirichlet), isoflux (Von Neumann) conditions at the wall, and by coupling the thermal solution in the fluid phase with a heat conduction problem inside the surrounding wall (conjugate heat transfer). In spite of the completely different near wall asymptotics of the enthalpy fluctuations, no noteworthy effect on the heat transfer coefficient Nu was observed. This insensitivity to the enthalpy fluctuations further confirms the dominating role of the velocity fluctuations in the turbulent heat flux near the wall. In fact, the high local molecular Prandtl number consistently confines the region with significant enthalpy fluctuations to a narrow zone very next to the wall, where the turbulent advective mixing motion is already extremely dampened in any case.

The results from DNS of the heated/cooled test cases were further used for assessing the modelling capabilities of three popular subgrid-scale models developed for closure of the unresolved fluxes in LES, namely the Wall Adapting Local Eddy Viscosity (WALE), Coherent Structure (CSM) and Standard Smagorinsky (SMAG) models. The assessment

included *a priori* LES as well as self-sustained predictive *a posteriori* LES. The *a priori* LES was based on the DNS data obtained with constant material properties at molecular Prandtl numbers $Pr = 10/20$, filtering the data onto an eight times coarser grid in all directions. As a most salient feature, both the CSM and WALE model delivered a significantly lower sgs contribution near the wall than the SMAG approach. Below $y^+ \approx 10$ the difference runs up to almost one order of magnitude. Furthermore, the *a priori* analysis also highlighted the role of the numerical error arising from a relative coarse grid with a possibly less accurate discretization scheme. It became evident, that while the numerical error generally produces a fairly small mean contribution, it still delivers significantly high instantaneous contributions, which may even strongly exceed the modelled sgs components. The accordingly large *rms*-values of the numerical error further appeared to be consistently increased for increasing Reynolds and Prandtl numbers. The *a posteriori* LES essentially confirmed the substantially lower predicted sgs model contribution near the wall, as observed for WALE and CSM in the *a priori* LES. The global key parameters for momentum and heat transfer represented by the skin friction coefficient and Nusselt number, respectively, were predicted with CSM and WALE in very close agreement with the DNS reference data for all considered heated and cooled cases. Both candidates demonstrated very well their adequate sensitivity to the decreased/increased subgrid-scale content met near the heated and cooled wall by predicting correspondingly lower/higher sgs eddy viscosities. On the contrary, SMAG clearly revealed its known dissipative nature by predicting consistently too high subgrid-scale eddy viscosities near the wall, which further did not show any sensitivity to the decreased/increased subgrid-scale content near the heated/cooled walls. As a result, the Nusselt number is consistently overestimated with SMAG in comparison against DNS. The wall skin friction coefficient is still always somewhat underestimated with SMAG, which is due to the mispredicted molecular viscosity near the heated/cooled walls.

Lastly, the computational investigation of forced convective heat transfer was also extended to highly non-developed flow conditions, due to massive boundary layer separation, as prompted by a sudden axisymmetric expansion of the turbulent pipe. The same mixture of glysantine-water with variable temperature-dependent molecular viscosity was assumed as operating fluid. The DNS and LES were additionally carried out with air as well, to provide data well comparable with experiments from literature using air as working fluid. The numerical results from the DNS with air match the experiments of Baughn *et al.* (1984) only in the shear-driven region past the step, whereas a substantial underprediction of the local Nusselt number is observed far downstream. On the contrary, the experimental investigations of Zemanick and Dougall (1970) was better predicted by the DNS in the far downstream region, whereas near the breakdown zone of the jet-like flow a higher heat transfer rate is observed in the experiments. Despite this partial discrepancy with the considered experimental studies, the simulations clearly demonstrated, that the breakdown of the jet-like central core flow caused by the intense shear-driven vortical mixing with the surrounding separated flow region significantly enhances the heat transfer rate downstream of the circular step. The Nusselt number is thus increased up to four to five times the value, which is asymptotically reached far downstream for recovered fully developed flow conditions. The increase of the Nusselt number was generally higher for the mixture of glysantine/water than for air, which indicates the effect of the roughly ten times higher molecular Prandtl number. Aside from this difference in the thermal field,

the solutions for both fluids generally exhibited very similar flow fields as the Reynolds number remained almost the same for most part of the domain.

The results obtained with LES were also used for assessing the performance of the CSM sgs model, when applied to strongly non-developed flow conditions. The LES predictions were generally very close to the DNS data proving again the adequacy of the subgrid-scale contributions provided by this model. Albeit being in general relatively small, these contributions turned out to be still essential for providing accurate predictions. The beneficial role of the model was also demonstrated by the marked deficits of the LES results, which were computed without sgs model for comparison.

Appendix

Numerical procedure in OpenFOAM

The numerical solution of the turbulent flow in a pipe with a sudden circular expansion is based on the pressure-implicit with splitting of operators method (PISO), developed by Issa (1986), and implemented in the employed software OpenFOAM.

In all the simulations performed for this geometry the density ρ is treated as a constant. This is justified by the fact that, even in the case, where the temperature difference between the wall temperature T_w and the bulk temperature T_b is highest, the density shows a rather limited radial variation with respect to its wall values. This is not the case for the molecular viscosity, whose temperature dependence was therefore accounted for as described in Section 2.5.

The workflow in PISO starts with the solution of the equations for momentum as stated in Eqs. (2.8) - (2.9). Due to the assumption of constant density, the conservation of mass is ensured by enforcing a divergence free velocity field written as

$$\nabla \cdot \mathbf{U} = 0. \quad (\text{A.1})$$

The FV discretization of Eq. (2.9) is reformulated by integrating over the control volume V_c and applying Gauss theorem, leading to

$$\frac{\partial \mathbf{U}}{\partial t} V_c + \sum_j \mathbf{S}_j \cdot (\mathbf{U}\mathbf{U})_j = - \sum_j \mathbf{S}_j P_j / \rho + \sum_j \mathbf{S}_j \cdot (\nu_{eff}(\nabla \mathbf{U})_j), \quad (\text{A.2})$$

where the outward pointing surface area vector of the j -th face has been introduced as $\mathbf{S}_j = S_j \mathbf{n}$ and the subscript $()_j$ denotes the interpolation of the quantity $()$ at the j -th face. Introducing the volume face flux accross the j -th face of the control volume as $F_j = \mathbf{S}_j \cdot \mathbf{U}_j$, Eq. (A.2) can be rewritten as

$$\frac{\partial \mathbf{U}}{\partial t} V_c + \sum_j F_j \mathbf{U}_j = - \sum_j \mathbf{S}_j P_j / \rho + \sum_j \mathbf{S}_j \cdot (\nu_{eff}(\nabla \mathbf{U})_j). \quad (\text{A.3})$$

The method PISO applies a *predictor* step to Eq. (A.3), in order to compute an intermediate solution represented by \mathbf{U}^* , $F_j^* = \mathbf{S}_j \cdot \mathbf{U}_j^*$ and two or more *correction* steps, which enforce the mass conservation on the previously predicted field to finally obtain a corrected velocity \mathbf{U}^{**} , representing the updated solution at the new time level t^{n+1} . After the solution of the velocity field, the temperature field is advanced to the new time level by solving the equation of energy, rewritten in terms of temperature. The individual steps in the PISO work flow are described in more detail below.

predictor step

The solution at time level t^n is used to compute a predicted velocity field \mathbf{U}^* from the FV representation of Eq. (A.3) as

$$\rho \frac{\delta(\mathbf{U}^* - \mathbf{U}^n)}{\delta t} = \mathbf{H}(\mathbf{U}^*) - \nabla P^n, \quad (\text{A.4})$$

Here, the operators $\mathbf{H}(\mathbf{U}^*)$ and $\frac{\delta}{\delta t}$ denote respectively the discretized representation of the spatial convective and diffusive fluxes and of the unsteady term of the conservation equation of momentum. A second order accurate Backward-Differencing scheme (BDF2) is used for the discretization of the time derivative on the left-hand side of Eq. (A.4), Δt represents the finite time increment between two time levels t^n and t^{n+1} , and $(\)^n$ denotes the old time level.

first corrector step

The predicted solution \mathbf{U}^* is corrected by seeking a new velocity field \mathbf{U}^{**} and a new pressure field P^* such that $\nabla \cdot \mathbf{U}^{**} = 0$. To meet this requirement, the following equation is considered:

$$\rho \frac{\delta(\mathbf{U}^{**} - \mathbf{U}^n)}{\delta t} = \mathbf{H}(\mathbf{U}^*) - \nabla P^*. \quad (\text{A.5})$$

Equation (A.5) is fully explicit in \mathbf{U}^{**} but the term P^* is still unknown to this point. In order to retrieve the pressure field P^* , the constraint $\nabla \cdot \mathbf{U}^{**} = 0$ is enforced by taking the divergence of Eq. (A.5), resulting in:

$$\Delta P^* = f(\nu_{eff}^n, \mathbf{U}^*). \quad (\text{A.6})$$

Once the field P^* is computed solving the Poisson equation (A.6), the corrected field \mathbf{U}^{**} is explicitly derived from Eq. (A.5).

second corrector step

At the end of the first corrector step a second corrected velocity \mathbf{U}^{***} field associated with a second correcting pressure field P^{**} might be asked for better accuracy in time by performing an additional corrector step as

$$\rho \frac{\delta(\mathbf{U}^{***} - \mathbf{U}^n)}{\delta t} = \mathbf{H}(\mathbf{U}^{**}) - \nabla P^{**}, \quad (\text{A.7})$$

and solving for P^{**} taking the divergence of Eq. (A.7). This step can be repeated an arbitrary number of times, but after the second corrector step a sufficient time accuracy is guaranteed [Oliveira and Issa (2001)] and the corrected velocity field \mathbf{U}^{***} can be considered the best representation of the approximated solution at time t^{n+1} .

The boundary conditions at the walls for the numerical integration of temperature equation are discussed in 2.4. Concerning the physical walls, a no-penetration and no-slip boundary conditions for velocity fluxes is imposed as

$$\mathbf{U} \Big|_{wall} = 0. \quad (\text{A.8})$$

The solution of the Poisson equation for pressure arising from the corrector(s) step(s) in the PISO method is lastly solved imposing a zero gradient normal to the wall

$$\nabla P \Big|_{wall} = 0 \quad (\text{A.9})$$

At the inlet section, a turbulent velocity profile, computed from a precursor DNS simulation at the same Re_b in a periodic and fully developed pipe flow, is imposed at each time step. At the outlet section of the downstream pipe the mass flow rate is matched with its corresponding value at the inlet, allowing for possible backflows. The boundary condition for pressure is enforced by imposing a zero normal gradient on both inlet and outlet section.

Bibliography

- Abba, A. ; Cercignani, A. C. ; Valdettaro, L.: Analysis of subgrid scale models. *Computers and Mathematics With Applications* 46 (2003), pp. 521–535
- Bae, Joong H. ; Yoo, Jung Y. ; Choi, Haecheon: Direct numerical simulation of turbulent supercritical flows with heat transfer. *Physics of Fluids* 17 (2005), pp. 105–104
- Barri, M. ; El Khoury, G. K. ; Andersson, H. I. ; Pettersen, B.: DNS of backward-facing step flow with fully turbulent inflow. *International Journal for Numerical Methods in Fluids* 64 (2010), pp. 777–792
- Batchelor, G.: Small-scale variation of convected quantities like temperature in turbulent fluid Part 1. General discussion and the case of small conductivity. *Journal of Fluid Mechanics* 5 (1959), pp. 113–133
- Baughn, J. W. ; Hoffman, M. A. ; Launder, B. E. ; Lee, D. ; Yap, C.: Heat Transfer, Temperature, and Velocity Measurements Downstream of an Abrupt Expansion in a Circular Tube at a Uniform Wall Temperature. *Journal of Heat Transfer* 111 (1989), pp. 870–876
- Baughn, J. W. ; Hoffman, M. A. ; Takahashi, R. K. ; Launder, B. E.: Local Heat Transfer Downstream of an Abrupt Expansion in a Circular Channel With Constant Wall Heat Flux. *Journal of Heat Transfer* 106 (1984), pp. 789–796
- Bergman, Theodore L. ; Incropera, Frank P. ; DeWitt, David P. ; Lavine, Adrienne S.: *Fundamentals of heat and mass transfer*. John Wiley & Sons, 2011
- Brandt, T.: A priori tests on numerical errors in large eddy simulation using finite differences and explicit filtering. *International Journal for Numerical Methods in Fluids* 51 (2006), pp. 635–657
- Chieng, C. C. ; Launder, B. E.: ON THE CALCULATION OF TURBULENT HEAT TRANSPORT DOWNSTREAM FROM AN ABRUPT PIPE EXPANSION. *Numerical Heat Transfer* 3 (1980), pp. 189–207
- Chorin, A.: Numerical Solution of the Navier-Stokes Equations. *Mathematics of Computation* 22 (1968), pp. 745–762
- Dailey, L. D. ; Meng, N. ; Pletcher, R. H.: *Large eddy simulation of constant heat flux turbulent channel flow with property variations using a dynamic subgrid-scale model*. 14th Computational Fluid Dynamics Conference, 1999

- Dailey, L. D. ; Meng, N. ; Pletcher, R. H.: Large Eddy Simulation of Constant Heat Flux Turbulent Channel Flow With Property Variations: Quasi-Developed Model and Mean Flow Results . *Journal of Heat Transfer* 125 (2003), pp. 27–38
- Friedrich, R. ; Hüttl, M. ; Wagner, C.: Direct numerical simulation of incompressible turbulent flows. *Computers & Fluids* 30 (2001), pp. 555–579
- Garg, Rajat P. ; Ferziger, Joel H. ; Monismith, Stephen G. ; Koseff, Jeffrey R.: Stably stratified turbulent channel flows. I. Stratification regimes and turbulence suppression mechanism. [Garg *et al.* 2000] *Physics of Fluids* 12 (2000), , pp. 2569–2594
- Germano, M. ; Piomelli, U. ; Moin, P. ; Cabot, W.: A dynamic subgrid-scale eddy viscosity model. *Phys. Fluids A* 3 (1991), pp. 1760–1765
- Gnielinski, V.: New equations for heat and mass transfer in the turbulent flow in pipes and channels. *NASA STI/Recon Technical Report A* 41 (1975), pp. 8–16
- Hufschmidt, W. ; Burck, E.: Der Einfluss temperaturabhängiger Stoffwerte auf den wärmeübergang bei turbulenter Strömung von Flüssigkeiten in Rohren bei hohen Wärmestromdichten und Prandtlzahlen. *International Journal of Heat and Mass Transfer* 11 (1968), pp. 1041–1048
- Inagaki, M. ; Hattori, H. ; Nagano, Y.: A mixed-timescale SGS model for thermal field at various Prandtl numbers. *International Journal of Heat and Fluid Flow* 34 (2012), pp. 47–61
- Irrenfried, C.: *DNS and experimentally based modelling of convective turbulent near wall heat transfer at high Prandtl numbers*, Dissertation, 2019
- Irrenfried, C. ; Steiner, H.: DNS based analytical P-function model for RANS with heat transfer at high Prandtl numbers. *International Journal of Heat and Fluid Flow* 66 (2017), pp. 217–225
- Issa, R. I.: Solution of the implicitly discretised fluid flow equations by operator-splitting. *Journal of Computational Physics* 62 (1986), pp. 40–65
- Kasagi, N. ; Tomita, Y. ; Kuroda, A.: Direct Numerical Simulation of Passive Scalar Field in a Turbulent Channel Flow. *Journal of Heat Transfer* 114 (1992), pp. 598–606
- Kawamura, H. ; Abe, H. ; Matsuo, Y.: DNS of turbulent heat transfer in channel flow with respect to Reynolds and Prandtl number effects. *International Journal of Heat and Fluid Flow* 20 (1999), pp. 196–207
- Kim, J. ; Moin, P.: Transport of Passive Scalars in a Turbulent Channel Flow. *Turbulent Shear Flows* 6, 1989, pp. 85–96
- Kim, J. ; Moin, P. ; Moser, R.: Turbulence statistics in fully developed channel flow at low Reynolds number. *Journal of Fluid Mechanics* 177 (1987), pp. 133–166
- Kim, K. ; Lee, Y.: Prediction of turbulent heat transfer downstream of an abrupt pipe expansion. *KSME Journal* 8 (1994), pp. 248–254

- Kobayashi, H.: The subgrid-scale models based on coherent structures for rotating homogeneous turbulence and turbulent channel flow. *Physics of Fluids* 17 (2005), pp. 45–104
- Kobayashi, H. ; Ham, F. ; Wu, X.: Application of a local SGS model based on coherent structures to complex geometries. *International Journal of Heat and Fluid Flow* 29 (2008), pp. 640–653
- Konakov, P. K.: Eine neue Formel für den Reibungskoeffizienten glatter Rohre. *Bericht der Akademie der Wissenschaften der UDSSR* 51 (1954), pp. 503 – 506
- Kopera, M. ; Kerr, R. ; Blackburn, H. ; Barkley, D.: Simulation of turbulent flow over a backward-facing step at $Re = 9000$. *Physics of Fluids* in review (2017)
- Le, H. ; Moin, P. ; Kim, J.: Direct Numerical Simulation of Turbulent Flow over a Backward-Facing Step. *Journal of Fluid Mechanics* 330 (1997), pp. 349–374
- Lee, J. ; Yoon J., Seo ; Jin Sung, H. ; Zaki, T. A.: Effect of wall heating on turbulent boundary layers with temperature-dependent viscosity. *Journal of Fluid Mechanics* 726 (2013), pp. 196–225
- Lemos, E. ; Secchi, A. ; Biscaia Jr, E.: Development of a high-order finite volume method with multiblock partition techniques. *Brazilian Journal of Chemical Engineering* 29 (2012), pp. 183–201
- Lilly, D. K.: A proposed modification of the Germano subgrid-scale closure method. *Physics of Fluids A* 4 (1992), pp. 633–635
- Moin, P. ; Squires, K. ; Cabot, W. ; Lee, S.: A dynamic subgrid-scale model for compressible turbulence and scalar transport. *Physics of Fluids A: Fluid Dynamics* 3 (1991), pp. 2746–2757
- Moser, R. ; Kim, J. ; Mansour, N. N.: Direct numerical simulation of turbulent channel flow up to $Re_\tau = 590$. *Physics of Fluids* 11 (1999), pp. 943–945
- Na, Y. ; Hanratty, T.J.: Limiting behavior of turbulent scalar transport close to a wall. *International Journal of Heat and Mass Transfer* 43 (2000), pp. 1749 – 1758
- Nemati, H. ; Patel, A.: The effect of thermal boundary conditions on forced convection heat transfer to fluids at supercritical pressure. *Journal of Fluid Mechanics* 800 (2016), pp. 531–556
- Nicoud, F.: Numerical study of a channel flow with variable properties. *Center for Turbulent Research. CTR Annual Research Brief* (1998), pp. 289–310
- Nicoud, F. ; Ducros, F.: Subgrid-Scale Stress Modelling Based on the Square of the Velocity Gradient Tensor. *Flow Turbulence and Combustion* 62 (1999), pp. 183–200
- Oliveira, P. ; Issa, R.: An improved piso algorithm for the computation of buoyancy-driven flows. *Numerical Heat Transfer, Part B: Fundamentals* 40 (2001), pp. 473–493

- Patel, A. ; Peeters, J. W. R. ; Boersma, B. J. ; Pecnik, R.: Semi-local scaling and turbulence modulation in variable property turbulent channel flows. *Physics of Fluids* 27 (2015), pp. 95–101
- Petukhov, B. S.: Heat Transfer and Friction in Turbulent Pipe Flow with Variable Physical Properties. *Advances in Heat Transfer* 6 (1970), pp. 503 – 564
- Piller, M.: Direct numerical simulation of turbulent forced convection in a pipe. *International Journal for Numerical Methods in Fluids* 49 (2005), pp. 583–602
- Pirozzoli, Sergio ; Bernardini, Matteo ; Verzicco, Roberto ; Orlandi, Paolo: Mixed convection in turbulent channels with unstable stratification. *Journal of Fluid Mechanics* 821 (2017), pp. 482–516
- Pont-Vilchez, A. ; Trias, F. X. ; Gorobets, A. ; Oliva, A.: Direct numerical simulation of backward-facing step flow at $Re_\tau = 395$ and expansion ratio 2. *Journal of Fluid Mechanics* 863 (2019), pp. 341–363
- Pope, S. B.: *Turbulent Flows*. Cambridge University Press, 2000
- Prud'homme, M. ; Elghobashi, S.: Turbulent Heat Transfer Near the Reattachment of Flow Downstream of a Sudden Pipe Expansion. *Numerical Heat Transfer* 10 (1986), pp. 349–368
- Salvetti, M. V. ; Banerjee, S.: A priori tests of a new dynamic subgrid-scale model for finite difference large-eddy simulations. *Physics of Fluids* 7 (1995), pp. 2831–2847
- Sekimoto, A. ; Kawahara, G. ; Sekiyama, K. ; Uhlmann, M. ; Pinelli, A.: Turbulence- and buoyancy-driven secondary flow in a horizontal square duct heated from below. *Physics of Fluids* 23 (2011), pp. 75–103
- Serra, S. ; Toutant, A. ; Bataille, F.: Thermal Large Eddy Simulation in a Very Simplified Geometry of a Solar Receiver. *Heat Transfer Engineering* 33 (2012), pp. 505–524
- Serra, S. ; Toutant, A. ; Bataille, F. ; Zhou, Ye: High-temperature gradient effect on a turbulent channel flow using thermal large-eddy simulation in physical and spectral spaces. *Journal of Turbulence* 13 (2012), pp. N49
- Smagorinsky, J.: General Circulation Experiments with the primitive equations: I. The basic Experiment. *Monthly Weather Review* 91 (1963), pp. 99–164
- Tiselj, I. ; Bergant, R. ; Mavko, B. ; Bajsic, I. ; Hetsroni, G.: DNS of Turbulent Heat Transfer in Channel Flow With Heat Conduction in the Solid Wall. *Journal of Heat Transfer* 123 (2001), pp. 849–857
- Tiselj, I. ; Cizelj, L.: DNS of turbulent channel flow with conjugate heat transfer at Prandtl number 0.01. *Nuclear Engineering and Design* 253 (2012), pp. 153–160
- Van Driest, E. R.: On Turbulent Flow Near a Wall. *Journal of the Aeronautical Sciences* 23 (1956), pp. 1007–1011

- Vreman, A.W. ; Geurts, B. ; Kuerten, H.: A priori tests of large-eddy simulation of compressible plane mixing layer. *Journal of Engineering Mathematics* 29 (1995), pp. 299–327
- Wagner, C. ; Friedrich, R.: Turbulent Flow in a Sudden Pipe Expansion. *Advances in Turbulence V*, 1995, pp. 544–548
- Wu, X. ; Moin, P.: A direct numerical simulation study on the mean velocity characteristics in turbulent pipe flow. *Journal of Fluid Mechanics* 608 (2008), pp. 81–112
- Zemanick, P. P. ; Dougall, R. S.: Local Heat Transfer Downstream of Abrupt Circular Channel Expansion. *Journal of Heat Transfer* 92 (1970), pp. 53–60
- Zonta, F. ; Marchioli, C. ; Soldati, A.: Modulation of turbulence in forced convection by temperature-dependent viscosity. *Journal of Fluid Mechanics* 697 (2012), pp. 150–174
- Zonta, F. ; Soldati, A.: Stably Stratified Wall-Bounded Turbulence. *Applied Mechanics Reviews* 70 (2018)